

Probing Li-ion transport in Sulfide-based solid-state batteries

Yu, Chuang

Publication date

2017

Document Version

Publisher's PDF, also known as Version of record

Citation (APA)

Yu, C. (2017). Probing Li-ion transport in Sulfide-based solid-state batteries

Important note

To cite this publication, please use the final published version (if applicable). Please check the document version above.

Copyright

Other than for strictly personal use, it is not permitted to download, forward or distribute the text or part of it, without the consent of the author(s) and/or copyright holder(s), unless the work is under an open content license such as Creative Commons.

Takedown policy

Please contact us and provide details if you believe this document breaches copyrights. We will remove access to the work immediately and investigate your claim.

Probing Li-ion transport in Sulfide-based solid-state batteries

Probing Li-ion transport in Sulfide-based solid-state batteries

Proefschrift

ter verkrijging van de graad van doctor

aan de Technische Universiteit Delft,

op gezag van de Rector Magnificus prof. Ir. K. C. A. M. Luyben,

voorzitter van het College voor Promoties,

in het openbaar te verdedigen op donderdag 5 oktober 2017 om 10:00 uur

door

Chuang YU

Master in Natural Science, Physical Chemical (including Chemical Physics)

Fujian Institute of Research on the Structure of Matter, Chinese Academy of
Sciences, Fuzhou, China

geboren te Hubei, China

This dissertation has been approved by the

promotor: Prof. dr. E. H. Brück

copromotor: Dr. Ir. M. Wagemaker

Composition of the doctoral committee:

Rector Magnificus

Prof. dr. E. H. Brück

Dr. Ir. M. Wagemaker

Technische Universiteit Delft, promotor

Technische Universiteit Delft, copromotor

Independent members:

Prof. dr. F. M. Mulder,

Prof. dr. C. Masquelier

Prof. dr. Y. Yang

Dr. E. R.H. van Eck

Dr. Ir. E. M. Kelder

Technische Universiteit Delft

Université de Picardie Jules Verne

Xiamen University

Radboud University Nijmegen

Technische Universiteit Delft



The research carried out in this thesis has been financially supported by the European Research Council under the European Union's Seventh Framework Programme (FP/2007-2013)/ERC Grant Agreement No. [307161].

Copyright © 2017 by Chuang Yu

All rights reserved. No part of the material protected by this copyright notice may be produced or utilized in any form or by any means, electronic or mechanical, including photocopying, recording or by any information storage and retrieval system, without written permission from the author.

Printed in the Netherlands by ProefschriftMaken

ISBN 978-94-6186-853-4

Table of Contents

1 Introduction	1
1.1 Conventional organic liquid electrolyte	2
1.2 Solid-state batteries	3
1.2.1 Basic operation solid-state batteries	3
1.2.2 Thin film and bulk solid-state batteries	5
1.3 Inorganic solid electrolytes	6
1.3.1 Lithium oxide systems	8
1.3.2 Lithium sulfide systems	13
1.4 Thesis research motivation and objectives	21
References	23
2 Characterization Techniques, Theory and Methods	31
2.1 X-rays and neutron diffraction	32
2.2 Alternating Current (AC) impedance	36
2.3 Solid-State Nuclear Magnetic Resonance (NMR)	38
2.4 Cyclic voltammetry (CV)	51
2.5 Electrochemical Impedances Spectra (EIS)	53
References	54
3 Synthesis, Structure and Electrochemical Performance of the Argyrodite Li₆PS₅Cl Solid Electrolyte for Li-ion Solid-State Batteries	57
3.1 Introduction	58
3.2 Experimental	60
3.3 Results and discussions	62
3.3.1 Synthesis, structure and conductivity of argyrodite Li ₆ PS ₅ Cl	62
3.3.2 Preparation of all-solid-state cells and electrochemical tests	68
3.4 Conclusions	74
References	75
4 Unravelling Li-Ion Transport from Pico-seconds to Seconds, Bulk versus Interfaces in An Argyrodite Li₆PS₅Cl-Li₂S All-Solid-State Li-Ion Battery	79
4.1 Introduction	80
4.2 Experimental	83
4.3 Results and Discussion	86
4.3.1 Synthesis, Impedance spectroscopy, Electrochemical Performance	86
4.3.2 Molecular Dynamics simulations	89
4.3.3 NMR spin-lattice relaxation experiments	94
4.3.3 Li ion exchange between Li ₂ S and Li ₆ PS ₅ Cl	100
4.4 Conclusions	107
References	108

5 Revealing the Relation between the Structure, Li-ion Conductivity and Solid-State Battery Performance for the Argyrodite $\text{Li}_6\text{PS}_5\text{Br}$ Solid Electrolyte	115
5.1 Introduction	116
5.2 Experimental	118
5.3 Results and discussion.....	121
5.3.1 Impedance, diffraction and TEM characterization of $\text{Li}_6\text{PS}_5\text{Br}$	121
5.3.2 Solid-state NMR relaxation experiments.	130
5.3.3 Electrochemical performance.....	136
5.4 Conclusions	140
References	143
6 Accessing the Bottleneck in All-Solid-State Batteries, Li-ion Transport over the Interface between the Solid-Electrolyte and Electrode.....	147
6.1 Introduction	148
6.2 Experimental	151
6.3 Results and discussions	154
6.4 Conclusions	171
6.5 Supplement.....	172
References	178
Summary	187
Samenvatting.....	193
Acknowledgements	201
List of Publications	205
Curriculum Vitae.....	211

1

Introduction

1 Introduction

1.1 Conventional organic liquid electrolyte

A lithium battery is composed of four basic parts, the cathode, the anode, the electrolyte and the separator. Cathode and anode materials are separated by the electrolyte and separator, as shown in Figure 1.1. Cathode and anode are connected via a load having an internal resistance completing the circuit. The electrochemical reaction proceeds at both electrodes, typically through a Li-ion insertion and extraction process, driven by the difference in the chemical potential of lithium between the cathode and the anode. During discharge this drives the charge compensating electrons through the external circuit, powering the application, or during charge, an external voltage or current source drives the reverse process.

The role of the electrolyte is to conduct the Li-ions, and its Li-ion conductivity and design directly affect the internal resistance of Li-ion batteries. Conventional liquid electrolytes consist of a Li-salt dissolved in an organic solvent. The diversity and contradicting requirements of battery applications can hardly be met by a single solvent, i.e. both a high fluidity and a high dielectric constant are beneficial. Lithium electrolytes are based on solutions of one or more lithium salts in mixtures of two or more solvents. Typical inorganic salts include LiPF_6 , LiBF_4 , LiClO_4 , LiAsF_6 and typical solvents include propylene carbonate (PC), ethylene carbonate (EC), dimethyl carbonate (DMC), and diethyl carbonate (DEC).¹

These conventional organic electrolytes are highly volatile and flammable which have a serious safety issue for their applications. If exposed to extreme conditions of elevated voltage and temperature, these electrolytes can react with active electrode materials and result in significant heat and gas release. Gas generation will start when the cell reaches the solvent decomposition temperature, as a consequence of internal or external causes, resulting in serious safety issues.

To mitigate the above issues, several electrolyte additives are developed and applied to improve the battery performance and safety. However, it is impossible to completely eliminate the inherent problems introduced by liquid electrolytes. Because of the increasing amount of Li-ion batteries employed in our daily life, for instance in electric vehicles and mobile devices, exploring new electrolytes to replace current organic liquid electrolytes becomes increasingly urgent. Solid electrolytes are intrinsically safer because of their much higher melting temperature. Currently, many solid electrolytes are being developed aiming for a high ionic conductivity, the low energy barrier for diffusion and negligible electron conductivity. An advantage of solid electrolytes is that the transference number is typically close to unity, which implies that practically only the Li-ions are mobile, and the counter anions do not contribute to the internal resistance. Additional potential advantages of solid electrolytes are a more restricted amount of side reactions (physically confined because of the solid nature of the electrolytes), less battery packaging leading to larger practical energy densities and more design freedom because of the completely solid state system. Main challenges of solid electrolytes are the large resistance through the electrolyte bulk and over the interface between the solid electrolyte and the electrodes. Charge transport over these interfaces is most likely compromised by interfacial side reactions and volumetric changes of the electrode upon Li-ion insertion/extraction. In the next part, this thesis presents a short review about inorganic solid electrolytes.

1.2 Solid-state batteries

1.2.1 Basic operation solid-state batteries

Unlike the commercial lithium ion batteries utilizing liquid organic electrolytes, a solid-state battery is composed of cathode, solid electrolyte and anode, as shown in Figure 1.1. Solid electrolytes not only function as a lithium ion conductor, but also

1 Introduction

a separator between the cathode and anode. The absence of organic materials, electrolyte salt, separator, and binder simplifies the fabrication process of solid-state batteries. There are many advantages of solid-state batteries compared with lithium batteries using liquid electrolyte. Firstly, the replacement of the liquid electrolyte by a nonflammable solid electrolyte mitigates almost all safety issues. Secondly, the simple construction of solid-state batteries makes the stacking of many cells in one package easier, which can increase the practical energy density. Additionally, working with only solid materials opens the opportunity to design flexible solid-state batteries, which has a wide application prospect. Thirdly, unlike in liquid electrolytes of lithium batteries, only lithium ions diffuse in solid electrolytes, causing a lower internal resistance and less potential for side reactions at the interfaces with the electrodes. However, solid-state batteries still suffer many issues after decades of research. The first challenge is the power density as typically solids show smaller lithium ion diffusivity. Another fundamental challenge is the volumetric changes associated with the insertion and extraction of Li-ions in the electrodes that puts the interface with the solid electrolyte under strain, potentially leading to mechanical failure, and therefore loss of contact, and blocked Li-ion transport. Related to this is the challenge to establish good interfacial contacts between the solid electrolyte and the electrodes to provide facile lithium ion transport over the interfaces.

The working principle of solid-state batteries is the same as for lithium ion batteries using liquid electrolyte. During the charging, lithium ions are extracted from the positive electrode and inserted in the negative electrode. This is driven by the externally applied potential, while the electrolyte conducts the lithium ions. Parallel the electrons migrate from the positive to the negative electrode via the external circuit. During the discharge, the reverse process occurs, in this case spontaneously.

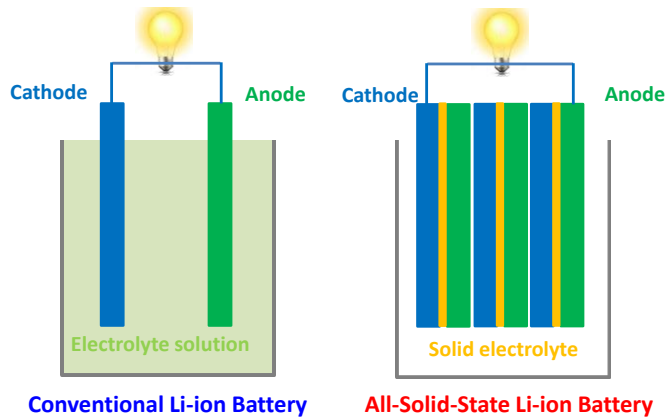


Figure 1.1: Schematic illustration of lithium batteries with liquid organic electrolyte and solid electrolyte.

1.2.2 Thin film and bulk solid-state batteries

As shown in Figure 1.2, two types of all-solid-state batteries can be distinguished, thin-film micro-batteries produced by thin film deposition techniques, such as Radio Frequency (RF) sputter, spin-coating and pulsed laser deposition (PLD), and bulk solid-state batteries constructed by cold or hot pressing the electrodes and the solid electrolyte powder together. The thickness of thin-film solid-state batteries is in the range of hundreds of nanometers to several microns, while the thickness of bulk solid-state batteries is typically hundreds of micrometers or even thicker. The application of thin-film solid-state batteries is restricted to small-scale applications, while bulk solid-state batteries are designed for both portable electronic devices and large-scale applications. Lithium-phosphorus-oxy-nitride (LiPON) is the most commonly chosen electrolyte for thin-film solid state batteries, where LiPON has a Li-ion conductivity of 10^{-6} S/cm at room temperature.² Thin-film solid-state batteries are typically deposited on an insulating substrate, such as polycrystalline alumina. The battery stack is build up by successive film deposition of the metal current collectors, cathode, electrolyte, and anode, plus a multilayer protective coating of Ti and parylene-C permitting the battery to be exposed to the air for up

1 Introduction

to 1-3 months. These thin film systems typically have large power densities because of the short diffusion distances between the positive and negative electrode materials. To achieve practical power densities, the conductivity of the solid electrolyte in bulk solid-state batteries requires being in the range of 10^{-4} - 10^{-3} S/cm, which approaches the conductivity of liquid electrolytes.

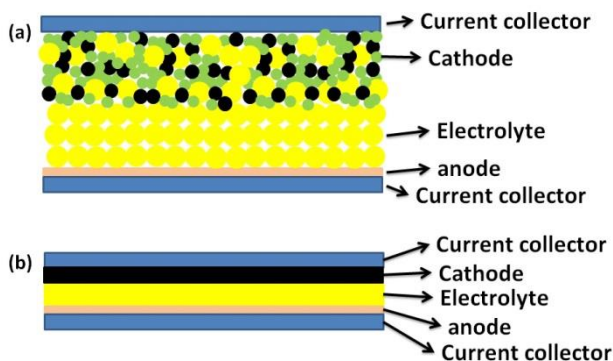


Figure 1.2: Schematic illustration of (a) bulk solid-state batteries and (b) thin film solid-state batteries.

1.3 Inorganic solid electrolytes

Two groups of solid electrolytes are distinguished, inorganic and organic polymer solid electrolytes having very distinct mechanical properties. Currently, polymer electrolytes are commercially well developed, partially because they are easier to manufacture compared to that of inorganic solid electrolytes. Polymer lithium electrolytes are produced by dissolving a lithium salt, such as LiX (X=Cl, Br, I), LiTFSI, in a polymer matrix, such as Poly(ethylene oxide) (PEO), to form a lithium ion conductor with a Li-ion conductivity in the order of 10^{-8} to 10^{-4} S/cm at room temperature. In this system, Li-ions move between complex sites assisted by the segmental motion of the PEO matrix. In PEO-based polymer electrolytes, the Li-ion conductivity is largest when the structure is amorphous. Therefore, lithium ion

conductivity can be promoted by reducing the crystallization of PEO and/or weakening the interaction between Li ions and PEO chains. The application of polymer electrolytes is generally limited by its cost, low lithium ion conductivities at room temperature and demanding protection requirements. Overcharge and overdischarge will destroy the reversible active material and thus shorten the life time of the batteries.

This thesis focuses on inorganic solid electrolytes. Ionic conductivity in inorganic ceramic compounds occurs through diffusion of ionic point defects, the creation and/or movement of which requires overcoming the energy barrier for diffusion.³ Several families of inorganic solid electrolytes for lithium batteries can be distinguished, including lithium nitrides, lithium iodides, lithium phosphate, lithium oxide and lithium sulfide solid electrolytes, as shown in Figure 1.3. In the following part, lithium oxides, lithium phosphates, and lithium sulfide systems are chosen to be reviewed because they are currently considered to be the most promising candidates based on the combination of their promising lithium-ion conductivity, electrochemical, and chemical stability.

1 Introduction

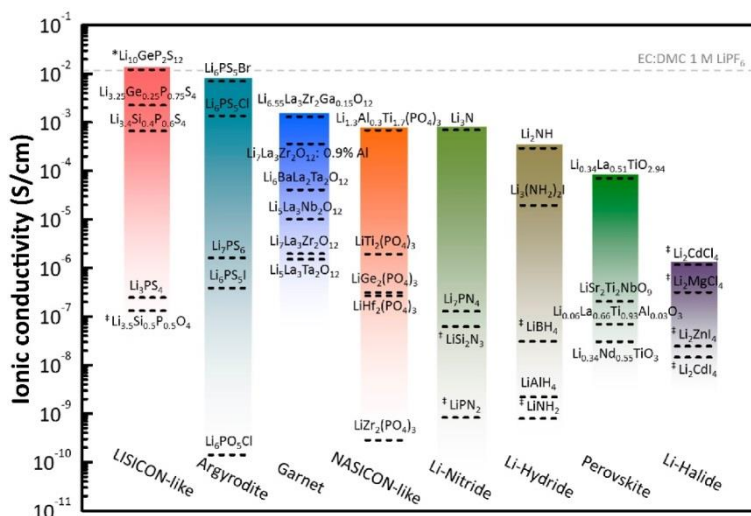


Figure 1.3: Lithium ion conductivity for published lithium-ion conductors.⁴

1.3.1 Lithium oxide systems

The most well-known and studied lithium oxide solid electrolytes are lithium oxysalts (Li_2SO_4 and Li_3PO_4), perovskite-type lithium oxides $(Li, La)TiO_3$, garnet-type lithium oxides and NASICON-type lithium phosphates $(LiA_{2-x}B_x(PO_4)_3)$. These lithium oxide electrolytes either show a high Li-ion conductivity or a high electrochemical stability.

Lithium oxysalts

Specific lithium oxysalts, such as Li_4SiO_4 , have the potential to be used as an electrolyte for solid-state cells owing to the high conductivity of their high-temperature phases reaching conductivities in the order of 10^{-3} S/cm at 300 °C. Much efforts have been devoted to obtaining these highly conducting high-temperature phases at room temperature.⁵⁻⁶ Research shows that combining these phases with Li_3PO_4 , to form a solid solution between Li_4SiO_4 and Li_3PO_4 , can further enhance the Li-ion conductivity towards 10^{-2} S/cm at 300 °C with an

activation energy of 0.55 eV.⁷ Recently, Deng *et al.* have used a powerful multi-technical approach, combining diffraction, AC impedance, NMR spectroscopy and atomistic modeling, to obtain understanding of the diffusion mechanism of the $(1-z)\text{Li}_4\text{SiO}_4-z\text{Li}_3\text{PO}_4$ system, which shows excellent Li-ion conductivity at lower temperatures, $\sim 10^{-3}$ S/cm at 200 °C when $z=0.25, 0.50,$ and 0.75 .⁸

Perovskite-type lithium oxides (Li, La)TiO₃

The general formula of perovskite-type electrolytes is ABO_3 which belongs to the cubic $Pm\bar{3}m$ space group. The perovskite-type electrolytes family have alkaline or rare earth metal ions at the *A* sites and transition metal ions at the *B* sites, with a 6-fold and 12-fold coordinated oxygen anion towards the *B* and *A* cations, respectively.⁴ The conductivity of these perovskite lithium oxides can be improved by substituting *A* by other cations, which affects the lithium ion diffusion channels in the structure. The most famous perovskite-type lithium ion conductor is $\text{Li}_{3x}\text{La}_{2/3-x}\text{TiO}_3$ (LLTO) and its analogues, showing high bulk Li-ion conductivity in the order of 10^{-3} S/cm at room temperature.⁹ However, there are several issues that impede their applications. The first issue is the extremely high sintering temperature for synthesis and the evaporation of Li during the annealing process, which makes it difficult to obtain target perovskite lithium oxides with high lithium ion conductivity. The second issue is the large grain boundaries resistance that reduces the Li-ion conductivity.¹⁰ Finally, LLTO is unstable towards lithium metal, which makes it unsuitable as electrolyte for solid-state batteries using a Li-metal anode. This is the consequence of the reduction of Ti^{4+} in contact with Li metal. More generally, the Ti^{4+} oxidation state makes LLTO not suitable in combination with reducing negative electrodes.^{4,9}

NASICON-type Li ion conductors $\text{Li}_{1+x}\text{A}_{2-x}\text{B}_x^{\text{IV}}(\text{PO}_4)_3$

NASICON (sodium (Na) super (S) ionic (I) conductor (CON)) refers to modifications of $\text{Na}_{1+x}\text{Zr}_2\text{Si}_x\text{P}_{3-x}\text{O}_{12}$ ($0 < x < 3$), which exhibits high Na-ion

1 Introduction

conductivity.¹¹ NASICON lithium conductors have a general formula of $AM_2(BO_4)_3$, where the A site is occupied by Li^+ , and the M site is occupied by tetravalent ions (Ge^{4+} , Ti^{4+} , Zr^{4+}) or one trivalent (B^{3+} , Al^{3+} , Ga^{3+}) and pentavalent (P^{5+} , As^{5+} , Sb^{5+}) ions. Its framework consists of O shared MO_6 octahedra and BO_4 tetrahedra that form a three-dimensional structure.⁴ Lithium ions jump between octahedra and tetrahedra vacancies yielding a highly conductive 3D diffusion network in NASICON-type lithium oxide electrolytes. Li-ion conductivity depends strongly on the size of the three-dimensional framework. Matching the channel size with the Li-ion radius is important to achieve a good Li-ion conductivity. Partial occupancies of Li-ions on octahedral and tetrahedra positions are another determining factor for fast Li-ion conduction. Vacancies at the intersection of the conduction pathways in the three-dimensional structure promote Li-ion diffusion. This leads to two important routes to improve the Li-ion conductivity in NASICON-type $Li_{1+x}A_{2-x}B_xIV(PO_4)_3$ structures. One is tailoring the size of the framework structure by using A ions with different sizes. The other is aliovalent substitution of A , such as using M^{3+} ions, which can increase the mobile lithium concentration and mobility, thereby enhancing the Li-ion conductivity.⁴ Several NASICON-type $Li_{1+x}A_{2-x}B_xIV(PO_4)_3$ electrolytes display a high Li-ion conductivity, excellent chemical stability, and a wide electrochemical window. Cyclic voltammograms indicates that $Li_{1.5}Al_{0.5}Ge_{1.5}(PO_4)_{3-x}Li_2O$ has an electrochemical window reaching up to 6 V versus Li metal.¹² However, first principle calculations suggest that the stability window versus Li metal for this NASICON-type electrolyte and its analogues are much smaller, *i.e.* 2.9 ~ 4.2 V for $LiGe_2(PO_4)_3$ and $Li_{1.5}Al_{0.5}Ge_{1.5}(PO_4)_3$, and 2.17 ~ 4.2 V for $Li_{1.3}Ti_{1.7}Al_{0.3}(PO_4)_3$.¹³⁻¹⁴ Moreover, it should be noted that some of its analogues containing Ti^{4+} are unstable in contact with Li-metal similar to the perovskite-type LLTO electrolyte, due to the reduction of Ti^{4+} to Ti^{3+} . It is worthwhile mentioning that $Li_{1+x}Al_xGe_{2-x}$

$x(\text{PO}_4)_3$ has also been used as electrolyte for solid-state Li-air batteries, showing excellent initial discharge and charge capacity properties of 1700 and 900 mAh/g.¹⁵

Garnet-type lithium oxides

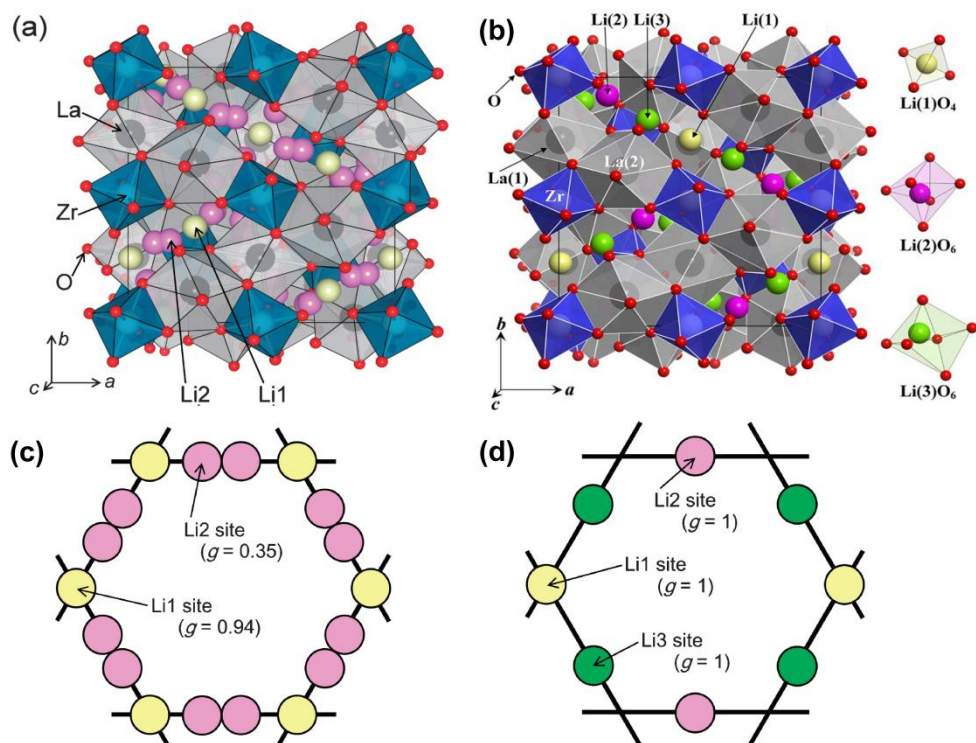


Figure 1.4: Crystal structure of (a) cubic¹⁶ and (b) tetragonal¹⁷ $\text{Li}_7\text{La}_3\text{Zr}_2\text{O}_{12}$. The corresponding loop structures constructed by Li atomic arrangement in (c) cubic and (d) tetragonal $\text{Li}_7\text{La}_3\text{Zr}_2\text{O}_{12}$. The occupancy value g for each site is noted in parenthesis.¹⁶ Note: The structure information of the low temperature phase cubic $\text{Li}_7\text{La}_3\text{Zr}_2\text{O}_{12}$ is currently not clear.

Lithium oxides with the garnet structure and the nominal chemical compositions $\text{Li}_5\text{La}_3\text{M}_2\text{O}_{12}$ ($\text{M}=\text{Ta}, \text{Nb}$) were first reported by Thangadurai and Weppner¹⁸. In these structures, Li occupies the tetrahedral $24d$ position and the octahedral $48g$

1 Introduction

position. Garnet $\text{Li}_5\text{La}_3\text{M}_2\text{O}_{12}$ displays a Li-ion conductivity of 10^{-6} S/cm at room temperature and appears to be stable towards lithium metal and towards large positive potentials.¹⁹ A new family of the garnet structure lithium oxide electrolytes with the general formula $\text{Li}_7\text{La}_3\text{Zr}_2\text{O}_{12}$ was discovered by replacing M with Zr^{4+} in $\text{Li}_5\text{La}_3\text{M}_2\text{O}_{12}$ (M=Ta, Nb).²⁰ These structures have higher lithium ion concentrations and yield larger Li-ion conductivities, reaching $3 \cdot 10^{-4}$ S/cm at room temperature with an activation energy of 0.3 eV.¹⁹ Interestingly, $\text{Li}_7\text{La}_3\text{Zr}_2\text{O}_{12}$ has two possible structures, tetragonal with a space group of $I4_1acd$ (no. 142) and cubic with a space group of $Ia3d$ (no. 230), having a different lithium ion conduction framework and conductivity.²¹ The cubic $\text{Li}_7\text{La}_3\text{Zr}_2\text{O}_{12}$ has an ionic conductivity of $\sim 10^{-4}$ S/cm at room temperature, which is two orders of magnitude higher than that of tetragonal $\text{Li}_7\text{La}_3\text{Zr}_2\text{O}_{12}$, $\sim 10^{-6}$ S/cm.²¹ Li-ion occupancy over the tetrahedral and octahedral sites is ordered in tetragonal $\text{Li}_7\text{La}_3\text{Zr}_2\text{O}_{12}$, while a complicated Li-vacancy disordering on the tetrahedral and octahedral sites is found for the cubic $\text{Li}_7\text{La}_3\text{Zr}_2\text{O}_{12}$, as shown in Figure 1.4.¹⁶ Using a classic solid state synthesis route, the phase formation temperatures for the tetragonal and the cubic phase of $\text{Li}_7\text{La}_3\text{Zr}_2\text{O}_{12}$ are 725 and 1200 °C, respectively. The tetragonal $\text{Li}_7\text{La}_3\text{Zr}_2\text{O}_{12}$ is stable at room temperature and transforms into another cubic structure between 100 and 150 °C.²²⁻²³ Although this new cubic phase $\text{Li}_7\text{La}_3\text{Zr}_2\text{O}_{12}$ shows the same X-ray diffraction pattern compared to the high-temperature synthesized cubic $\text{Li}_7\text{La}_3\text{Zr}_2\text{O}_{12}$, it delivers a Li-ion conductivity about two orders magnitude smaller.²⁴ Because of the larger Li-ion conductivity of the cubic $\text{Li}_7\text{La}_3\text{Zr}_2\text{O}_{12}$, this material has been investigated most intensively. Two approaches have been followed to improve the conductivity of the high-temperature synthesized cubic $\text{Li}_7\text{La}_3\text{Zr}_2\text{O}_{12}$ phase. Firstly, replacing Zr^{4+} with pentavalent or hexavalent cations, such as Ta^{5+} , Nb^{5+} , and Te^{6+} , can greatly promote the Li-ion conductivity due to an increase of the vacancy concentration and a decrease in the local Li ordering.²⁵⁻²⁷ The second approach is decreasing the grain boundary

resistance for Li-ion transport. There are several solutions proposed to achieve this goal, such as adding sintering additives and using advanced synthesis technology.²⁸⁻²⁹ Early research reported that $\text{Li}_7\text{La}_3\text{Zr}_2\text{O}_{12}$ has a decomposition voltage exceeding 5.5 V against Li metal, which is confirmed by current research with multiple experimental techniques and first-principles calculations.^{20, 30} Recently, Nb^{5+} was chosen to replace Zr^{4+} in cubic $\text{Li}_7\text{La}_3\text{Zr}_2\text{O}_{12}$ which improved the Li-ion conductivity of cubic $\text{Li}_{6.75}\text{La}_3\text{Zr}_{1.75}\text{Nb}_{0.25}\text{O}_{12}$ towards $8 \cdot 10^{-4}$ S/cm at 25 °C.²⁷ Ohta *et al.* combined this garnet solid electrolyte with LiCoO_2 as cathode and Li metal as anode to assemble bulk solid-state batteries exhibiting excellent capacity and cycling properties. The initial discharge capacity of this solid-state battery was 129 mAh/g, which was maintained up to 100 cycles.³¹ This electrochemical performance of solid-state battery is even comparable with that of lithium ion battery using LiCoO_2 as cathode with liquid electrolyte.³²

1.3.2 Lithium sulfide systems

In this short review, we classify lithium sulfide electrolytes into three types, lithium sulfide glasses, lithium sulfide glass-ceramics and crystalline lithium sulfides.

Lithium sulfide glasses

Lithium sulfide glassy electrolytes have many notable advantages, such as high Li-ion conductivities in the range of $10^{-5} \sim 10^{-3}$ S/cm at room temperature, isotropic ionic conduction, relatively small grain boundary resistances, an easy film manufacturing process, all of which make lithium sulfide glasses a good candidate for bulk solid-state batteries.³³ The high Li-ion conductivity of this glassy sulfide electrolytes is a consequence of the so-called open structure and the high polarizability of sulfur ions which weakens the interaction between anions and lithium ions. Two of the most intensively studied sulfide glass systems are $\text{Li}_2\text{S-SiS}_2$ and $\text{Li}_2\text{S-P}_2\text{S}_5$ and their analogues. Due to the easy crystallization of sulfide glassy materials during the synthesis, there are two synthesis routes towards these

1 Introduction

glassy electrolytes, melting followed by rapid quenching and the mechanical milling method. The extremely high Li-ion conductivity and low density for lithium sulfide glasses make it suitable candidates for constructing bulk solid-state batteries by simple cold pressing with the anode and cathode materials. However, the sulfide materials have poor chemical stability and as a consequence, they cannot be stored in the open air or in a humid environment as the reaction with water produces H_2S , which complicates the manufacturing process. The relatively low electrochemical stability is expected to result in stability issues when applied in combination with well-established cathode materials such as LiFePO_4 and LiCoO_2 . To improve the stability, partial replacement of sulfur with oxygen atoms was adopted to suppress the generation of H_2S .³⁴ Two strategies have been developed to improve the Li-ion conductivity of lithium sulfide glass electrolytes. One is to introduce new anions. Mixing two different anions in the glassy system can improve the Li-ion conductivity, which is referred to as the ‘mixed anion effect’.³⁵ Another is mixing with lithium salts, such as lithium halides (LiX , $\text{X}=\text{Cl}$, Br , I),³⁶⁻³⁷ lithium borohydride (LiBH_4)³⁸ and lithium ortho-oxosalts (Li_3PO_4),³⁹ which is helpful to enhance the Li-ion conductivity by increasing the lithium concentration and decreasing the energy barrier for Li-ion diffusion.

Lithium sulfide glass-ceramics

Lithium sulfide glass-ceramics are metastable phases displaying a high Li-ion conductivity ($>10^{-3}$ S/cm), which can be synthesized by annealing glassy lithium sulfide materials beyond the crystallization temperature.⁴⁰ Like the sulfide glasses, the superionic conduction of lithium sulfide glass-ceramics is associated with the large ionic radius and the high polarizability of the sulfur ions in the system.³³ Moreover, the crystalline domains in the glass-ceramics electrolytes are surrounded by amorphous phases, which appear to decrease the grain boundaries resistance of the electrolyte, thereby promoting the Li-ion conduction.³³ $\text{Li}_7\text{P}_3\text{S}_{11}$ is one of the

most researched glass-ceramics electrolytes in the $\text{Li}_2\text{S}-\text{P}_2\text{S}_5$ system, with a Li-ion conductivity reaching up to $3.2 \cdot 10^{-3}$ S/cm at room temperature in combination with an activation energy of 0.187 eV.⁴⁰ Previous research shows that $\text{Li}_7\text{P}_3\text{S}_{11}$ crystallizes in the triclinic unit cell indexed by the $P-1$ space group which provides three types of Li positions, located at the sites around the P_2S_7 and PS_4 groups and surrounded by 3, 4 or 5 sulfur atoms.⁴¹ The atomic positions (especially Li^+) were previously determined by combined X-ray/neutron Rietveld analysis, showing a network of neighboring Li^+ cations (composed of Li-Li chains), demonstrating the Li-ion diffusion pathway.⁴² The increment of the local conduction pathway of Li^+ ions from a LiS_4 unit to the neighboring LiS_4 units by the transformation from $(\text{Li}_2\text{S})_{70}(\text{P}_2\text{S}_5)_{30}$ glass to $\text{Li}_7\text{P}_3\text{S}_{11}$ metastable crystal strongly contributes to the excellent conductivity.⁴³ In addition to diffraction and calculation methods used in these studies,^{41, 44-45} solid state NMR was applied to probe the Li-ion dynamics and diffusion mechanism. Hayamizu *et al.* measured the lithium diffusion in the crystallized $(\text{Li}_2\text{S})_7(\text{P}_2\text{S}_5)_3$ by pulsed-gradient spin-echo ^7Li NMR spectroscopy and showed that the observed D_{Li} was consistent with the value evaluated from the ionic conductivity using the Nernst-Einstein relation.⁴⁶ Wohlmuth *et al.* also quantitatively probed the short-range as well as long-range diffusion parameters for $\text{Li}_7\text{P}_3\text{S}_{11}$ by spin-lattice relaxation (SLR) NMR, suggesting a multi-step decay behavior indicating the presence of at least three different relaxation rates in $\text{Li}_7\text{P}_3\text{S}_{11}$ glass-ceramics electrolytes.⁴⁷ Additionally, ^6Li and ^{31}P solid-state NMR was used by Murakami *et al.* to study the dynamical origin of high ionic conductivity of $\text{Li}_7\text{P}_3\text{S}_{11}$, showing that the high Li-ion conductivity above 310 K is attributed to the significant motional fluctuation of the P_2S_7 ditetrahedra units, which allows facile diffusive motion of lithium ions.⁴⁸ Although the Li-ion conductivity of $\text{Li}_7\text{P}_3\text{S}_{11}$ is sufficient for the use as an electrolyte in solid-state batteries, it can be further enhanced by optimizing the heat treatment process. Seino *et al.* prepared $\text{Li}_7\text{P}_3\text{S}_{11}$ with a Li-ion conductivity of $1.7 \cdot 10^{-2}$ S/cm at room

1 Introduction

temperature by tailoring the heat treatment process, which appears to reduce the grain boundary resistance of $\text{Li}_7\text{P}_3\text{S}_{11}$.⁴⁹ The main disadvantages of $\text{Li}_7\text{P}_3\text{S}_{11}$ glass-ceramics are the instability towards air and moisture, the narrow electrochemical stability window¹⁴, including its incompatibility with Li metal negative electrodes.⁵⁰

Crystalline lithium sulfide

The glass-ceramics obtained after crystallization show a higher Li-ion conductivity compared with that of the corresponding precursor glass materials, suggesting that the crystalline phases have a higher Li-ion conductivity and a smaller activation energy compared to the amorphous phases.³ Crystalline lithium sulfide conductors can be classified into thio-LISICON (thio-lithium superionic conductor)-type sulfides and argyrodite structured sulfides.

Thio-LISICON-type sulfide crystalline

Kanno discovered pure $\text{Li}_{3.25}\text{Ge}_{0.25}\text{P}_{0.75}\text{S}_4$ with a structure similar to LISICON, which is named thio-LISICON, showing a high ionic conductivity of $2.2 \cdot 10^{-3}$ S/cm at 25 °C with negligible electronic conductivity in combination with a high electrochemical stability.⁵¹ Since the discovery of $\text{Li}_{3.25}\text{Ge}_{0.25}\text{P}_{0.75}\text{S}_4$, $\text{Li}_{3.25}\text{Ge}_{0.25}\text{P}_{0.75}\text{S}_4$ and its analogous, these systems have been intensively investigated. Among these structures, the most attractive electrolytes appear to be thio-LISICON compounds based on Li silicon sulfides with a formula of $\text{Li}_{3.4}\text{Si}_{0.4}\text{P}_{0.6}\text{S}_4$, displaying a larger phase stability and a slightly lower conductivity ($6.4 \cdot 10^{-4}$ S/cm at 25 °C).⁵² The most intensively researched sulfide crystalline electrolyte is $\text{Li}_{10}\text{GeP}_2\text{S}_{12}$ with a three-dimensional framework that delivers an extremely high Li-ion conductivity of $1.2 \cdot 10^{-2}$ S/cm at 25 °C, comparable to that of current liquid organic electrolytes.⁵³ *Ab initio* calculations for $\text{Li}_{10}\text{GeP}_2\text{S}_{12}$ show that the Li-ion conductivities in the *c*-direction and in the *ab* plane are $4 \cdot 10^{-2}$ and

$9 \cdot 10^{-4}$ S/cm, respectively, resulting in an overall conductivity of $9 \cdot 10^{-3}$ S/cm. The corresponding activation energies for the diffusion in the *c*-direction and in the *ab* plane are 0.17 and 0.28 eV, respectively.⁵⁴ The agreement between ionic conductivity obtained by calculations and experiments suggests a three-dimensional conduction mechanism for $\text{Li}_{10}\text{GeP}_2\text{S}_{12}$ rather than on one-dimensional conduction mechanism. The one-dimensional conducting pathway along the *c*-direction is composed of sharing a common edge for LiS_4 tetrahedra at the *16h* and *8f* sites. The *ab* plane framework is constructed by connecting $(\text{Ge/P})\text{S}_4$ tetrahedra to LiS_6 octahedra.^{4, 54} Experimental results suggest that $\text{Li}_{10}\text{GeP}_2\text{S}_{12}$ has a wide electrochemical stability window up to 4 V versus Li/Li^+ .⁵³ However, recent studies questioned the reported electrochemical window for $\text{Li}_{10}\text{GeP}_2\text{S}_{12}$ due to the reversible reduction oxidization at 0-1.7 and 2-2.5 V versus Li metal, suggesting an electrochemical window 0.0-5.0 V.⁵⁵⁻⁵⁶ The chemical stability and electrode compatibility for $\text{Li}_{10}\text{GeP}_2\text{S}_{12}$ are quite complicated due to the potential oxidation of germanium and the instability towards moisture in the atmosphere. For its applications in all-solid-state batteries, $\text{Li}_{10}\text{GeP}_2\text{S}_{12}$ appears to be suitable in combination with LiCoO_2 as a cathode and Li-In alloy as an anode.⁵⁷ Additionally, all-solid-state batteries with LiFePO_4 ,⁵⁸ $\text{LiMn}_{1/3}\text{Ni}_{1/3}\text{Co}_{1/3}\text{O}_2$,⁵⁹ or $\text{LiNi}_{0.5}\text{Mn}_{1.5}\text{O}_4$ ⁵⁸ as the positive electrode in combination with $\text{Li}_{10}\text{GeP}_2\text{S}_{12}$ as electrolyte and Li metal as negative electrode show promising capacities. Although $\text{Li}_{10}\text{GeP}_2\text{S}_{12}$ appears to be an excellent solid electrolyte, the price of germanium is expected to limit its applications. Replacing Ge with other elements, such as Si, Sn and Al, can promote the development of practical solid electrolytes in this structural family. As mentioned earlier, matching the diffusion channel size with the Li-ion radius is vital to achieve high ionic conductivities for Li-ion conductors.⁴ Cation substitution is a possible strategy to tailor the ionic conductivity of $\text{Li}_{10}\text{GeP}_2\text{S}_{12}$. Replacing Ge^{4+} with Sn^{4+} , which has a larger radius, results in large bulk conductivities amounting $7 \cdot 10^{-3}$ S/cm for the bulk conductivity and $4 \cdot 10^{-3}$ S/cm for the total Li-ion

1 Introduction

conductivity at 27 °C.⁶⁰ Replacing Ge^{4+} by Si^{4+} , having a smaller radius, can form $\text{Li}_{10}\text{SiP}_2\text{S}_{12}$. Calculations⁵⁶ suggested that $\text{Li}_{10}\text{SiP}_2\text{S}_{12}$ has a Li-ion conductivity of $2.3 \cdot 10^{-2}$ S/cm at 300 K with an activation energy of 0.20 eV. Experimental results show that a maximum ionic conductivity up to $8.6 \cdot 10^{-3}$ S/cm is achieved for a composition of $\text{Li}_{10}\text{Ge}_{0.95}\text{Si}_{0.05}\text{P}_2\text{S}_{12}$.⁶¹ However, the high-pressure treatment and higher demands on sintering make the synthesis processes more costly for Si substitution in $\text{Li}_{10}\text{GeP}_2\text{S}_{12}$, which limits its application. Calculations suggest that heterovalent substitution of Ge^{4+} by Al^{3+} forms $\text{Li}_{11}\text{AlP}_2\text{S}_{12}$ which is predicted to enhance the ionic conductivity and decrease the energy barrier for diffusion.⁵⁶ In reality the $\text{Li}_{11}\text{AlP}_2\text{S}_{12}$ materials show a Li-ion conductivity of $8.02 \cdot 10^{-4}$ S/cm at 25°C, much smaller than the result predicted by calculations, $3.3 \cdot 10^{-2}$ S/cm at the same temperature.⁶² The heterovalent cation substitution of Ge^{4+} with Al^{3+} increases the Li^+ concentration, but it has a small effect on the Li-ion conductivity in this structure. Anion substitution is another strategy to modify the ionic conductivity of $\text{Li}_{10}\text{GeP}_2\text{S}_{12}$. The oxygen-substituted $\text{Li}_{10}\text{GeP}_2\text{O}_{12}$ compounds with much lower Li-ion conductivities ($3 \cdot 10^{-5}$ S/cm at 300 K) are predicted to be unstable, while the selenium-substituted $\text{Li}_{10}\text{SnP}_2\text{Se}_{12}$ compounds show a remarkable improvement of ionic conductivity ($2.4 \cdot 10^{-2}$ S/cm at 300 K), which comes along with a reduced electrochemical stability.⁵⁶

Recently, two new members of this crystalline lithium sulfide family showing highly ionic conductivity ($2.5 \cdot 10^{-2}$ S/cm for $\text{Li}_{9.54}\text{Si}_{1.74}\text{P}_{1.44}\text{S}_{11.7}\text{Cl}_{0.3}$ at 25 °C) and excellent electrochemical stability (~ 0 V versus Li metal for $\text{Li}_{9.6}\text{P}_3\text{S}_{12}$) were reported by Kato *et al.*⁶³ The three dimensional conduction pathway of the $\text{Li}_{9.54}\text{Si}_{1.74}\text{P}_{1.44}\text{S}_{11.7}\text{Cl}_{0.3}$ electrolyte was revealed by analyzing the anisotropic thermal displacement of lithium and nuclear density distribution, displaying 1D diffusion along the *c*-axis and 2D diffusion in the *ab* plane.⁴

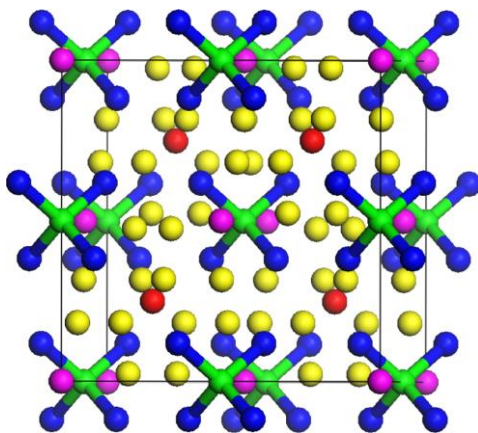


Figure 1.5: Crystal structure of $\text{Li}_6\text{PS}_5\text{X}$ ($\text{X}=\text{Cl}, \text{Br}, \text{I}$). The yellow represents Li-sites (48h), green represents phosphorus, blue represents bonded sulfur, pink represents 4a sites, and red represents 4c sites.⁶⁴

Argyrodite electrolytes

Another important family of crystalline lithium sulfide solid electrolytes is the argyrodites described by the chemical formula of $\text{Li}_6\text{PS}_5\text{X}$ ($\text{X}=\text{Cl}, \text{Br}, \text{I}$), showing promising Li-ion conductivities in the range of 10^{-3} to 10^{-2} S/cm at room temperature.⁶⁵ The ionic conductivity of Li-argyrodites is slightly smaller than that of the $\text{Li}_{10}\text{GeP}_2\text{S}_{12}$ family, while their costs are much lower making this family of electrolytes attractive for the application in all-solid-state batteries. The $\text{Li}_6\text{PS}_5\text{X}$ ($\text{X}=\text{Cl}, \text{Br}, \text{I}$) structures exhibit the high-symmetry argyrodite framework indexed by the $F-43m$ space group. In the $\text{Li}_6\text{PS}_5\text{X}$ ($\text{X}=\text{Cl}, \text{Br}, \text{I}$) structure, phosphorus atoms occupy the tetrahedral interstices, forming a framework of isolated PS_4 tetrahedra while lithium ions are randomly distributed over the remaining tetrahedral interstices (48h and 24g sites), as shown in Figure 1.5.⁶⁶ Among $\text{Li}_6\text{PS}_5\text{X}$ ($\text{X}=\text{Cl}, \text{Br}, \text{I}$), the highest ionic conductivities have been achieved for $\text{Li}_6\text{PS}_5\text{Br}$ and $\text{Li}_6\text{PS}_5\text{Cl}$ reaching up to 10^{-3} S/cm at room temperature.⁶⁷⁻⁶⁸ $\text{Li}_6\text{PS}_5\text{I}$ shows a much lower ionic conductivity due to the different distribution of I and

1 Introduction

Br/Cl ions over the $4a$ and $4c$ sites.^{64, 69} The disorder of the S^{2-}/Br^- and the S^{2-}/Cl^- distributions has been suggested to promote the Li-ion diffusivity, while the exchange between S^{2-} and I is impeded due to its larger ionic radius, resulting in an anion-ordered Li_6PS_5I with a low Li-ion conductivity.⁶⁹ The structural studies and bond-valence model results show that the packing determined by the PS_4^{3-} anions has great influence on the lithium ion transport in the argyrodites Li_6PS_5X ($X=Cl, Br, I$).⁶⁶ NMR results show that there are a variety of jump processes in the Li-argyrodite,⁷⁰ which is associated with macroscopic Li-ion conductivity. Moreover, density functional theory (DFT) based on molecular dynamics (MD) simulations was applied to reveal the diffusion mechanism for Li-argyrodite Li_6PS_5X ($X=Cl, Br, I$).⁶⁴ The calculation results show that there are three types of Li jumps in Li-argyrodite: the transition between the paired $48h$ sites, the transition within the cages between the different $48h$ pairs, and the transitions interconnecting the four cages in each unit cell. These three transitions built up the 3D diffusion pathway through the crystal, and the slowest transition limits the macroscopic diffusion. Improvement of the ionic conductivity for Li-argyrodite Li_6PS_5X ($X=Cl, Br, I$) is suggested to be achieved by optimization of the halogen distribution over the $4a$ and $4c$ sites and the increase of the halogen content in the material.⁶⁴ The common synthesis route of argyrodite Li_6PS_5X ($X=Cl, Br, I$) is mechanical milling followed by annealing. In-situ neutron diffraction and impedance measurement results show that heat treatment is vital to achieving a large Li-ion conductivity.⁶⁷ To obtain a Li_6PS_5X ($X=Cl, Br, I$) electrolyte with a high room temperature conductivity of $1 \cdot 10^{-3}$ S/cm and low activation energy of 0.16 eV, the samples need to be annealed above 250 °C.⁶⁷ Besides the excellent ionic conductivity, Li_6PS_5X ($X=Cl, Br$) electrolytes initially were suggested to have a wide electrochemical window up to 7 V versus Li/Li^+ .⁶⁸ However, recent computational studies indicate that the stability window of Li_6PS_5Cl is about 2.0 to 2.5 V.¹³ Other issues that may limit its application in all-solid-state batteries are the reactivity with air and moisture in the

atmosphere and the incompatibility with Li-metal. Recently, various cathode materials (LiCoO_2 ,^{68, 71} S ,⁷²⁻⁷³ $\text{Cu-Li}_2\text{S}$,⁷⁴ CuS ,⁷⁵ MoS_2 ⁷⁶) and anode ($\text{Li}_4\text{Ti}_5\text{O}_{12}$,^{71, 77} Li-In , In ,⁶⁸ Li-Al ⁷⁷) were combined together with the argyrodite $\text{Li}_6\text{PS}_5\text{X}$ ($\text{X}=\text{Cl}$, Br) solid electrolytes to investigate the electrochemical properties.

1.4 Thesis research motivation and objectives

The main aim of this thesis is to gain more understanding of the performance of all-solid-state lithium batteries employing argyrodite sulfide as electrolytes, in particular, related to the charge transport. The research questions can be divided into three groups:

(1) Synthesis and electrochemical performance of sulfide solid electrolytes

(**Chapter 3** and **4**)

Despite intensive investigations of the synthesis routes of sulfide-based solid electrolytes, there appears much room for optimization and simplification of the preparation of these materials. In this thesis, the synthesis of argyrodite $\text{Li}_6\text{PS}_5\text{X}$ ($\text{X}=\text{Br}$ and Cl) has been investigated, aiming at the correlation between the structure and impedance as a function of the mechanical milling process. Further, the influence of post-treatment, such as annealing and milling, and the (dis)charge voltage window in the electrochemical performances are investigated. Thereby, these studies aim at formulating optimal preparation routes for these sulfide solid electrolyte materials.

(2) Li-ion bulk dynamics in sulfide solid electrolytes (**Chapter 4** and **5**)

AC impedance spectroscopy is the most commonly employed technique used to characterize the Li-ion mobility in solid electrolytes. However, the measurement of Li-ion conductivity with impedance is potentially hindered by electrode porosity, grain boundaries and effects introduced by the electrodes in contact with the solid

1 Introduction

electrolyte during the measurement. To obtain accurate values of the Li-ion mobility and a fundamental understanding of the Li-ion charge transport, solid-state nuclear magnetic resonance (NMR) spectroscopy is employed. NMR is a non-destructive method, which has been shown to be a powerful approach to unravel the different Li-ion diffusion processes from small up to large time scales and giving quantitative and mechanistic insight into Li-ion mobility. In this thesis, both AC impedance and Solid-State NMR are employed and compared, aiming to establish the Li-ion diffusion mechanism in sulfur-based solid electrolytes.

(3) Li-ion exchange between electrode and electrolyte in the solid-solid interface (Chapter 4 and 6)

One of the biggest challenges for the development of solid-state batteries is the interfaces between the solid electrolyte and the electrode materials. These interfaces should allow facile Li-ion charge transfer, which is potentially challenged by chemical and electrochemical reactions at the interfaces, resulting in poor local conductivity and by a loss of contact due to the volumetric changes of the electrodes. In particular, in bulk solid-state batteries, these interfaces are very difficult to characterize and the even more challenging thing is to selectively measure the Li-ion transport over the interfaces. This is highly relevant as it is anticipated that the charge transport over the electrode-electrolyte interfaces dominates the internal resistance in all-solid-state batteries. One of the key questions is, how the charge transfer over these interfaces is affected by the material preparation conditions and the electrochemical cycling. Electrochemical impedance spectroscopy (EIS) is commonly used to estimate the interface resistance between the electrode and electrolyte materials. However, the complex electrode morphology and the many interfaces present in bulk solid-state batteries make it difficult to study the charge transfer over the interfaces between solid electrolytes and electrodes by EIS. In this thesis, one-dimensional (1D) and two-

dimensional (2D) ^7Li NMR are used for the first time in all-solid-state batteries to characterize the Li-ion transport over the solid electrolyte-electrode interface, in this work between argyrodite sulfide solid electrolytes and Li_2S positive electrodes. In addition to quantifying the interfacial transport, this study aims at gaining insight into the role of the electrode preparation conditions and electrochemical cycling on the charge transfer. With this knowledge, we hope to enable the design of better solid electrolyte-electrode interfaces as required for future all-solid-state batteries.

References

1. Kalkhoff, J.; Eshetu, G. G.; Bresser, D.; Passerini, S., Safer Electrolytes for Lithium-Ion Batteries: State of the Art and Perspectives. *ChemSusChem* **2015**, *8* (13), 2154-2175.
2. Hayashi, A., Development of new glassy materials for all-solid-state lithium secondary batteries: a review. *Glass Technology-European Journal of Glass Science and Technology Part A* **2008**, *49* (5), 213-220.
3. Fergus, J. W., Ceramic and polymeric solid electrolytes for lithium-ion batteries. *Journal of Power Sources* **2010**, *195* (15), 4554-4569.
4. Bachman, J. C.; Muy, S.; Grimaud, A.; Chang, H.-H.; Pour, N.; Lux, S. F.; Paschos, O.; Maglia, F.; Lupart, S.; Lamp, P., Inorganic Solid-State Electrolytes for Lithium Batteries: Mechanisms and Properties Governing Ion Conduction. *Chemical reviews* **2015**, *116* (1), 140-162.
5. Pizzini, S., Ionic conductivity in lithium compounds. *Journal of Applied Electrochemistry* **1971**, *1* (3), 153-161.
6. West, A., Ionic conductivity of oxides based on Li_4SiO_4 . *Journal of Applied Electrochemistry* **1973**, *3* (4), 327-335.
7. Hu, Y. W.; Raistrick, I.; Huggins, R. A., Ionic Conductivity of Lithium Orthosilicate-Lithium Phosphate Solid Solutions. *J. Electrochem. Soc.* **1977**, *124* (8), 1240-1242.
8. Deng, Y.; Eames, C.; Chotard, J.-N. I.; Lalère, F.; Seznec, V.; Emge, S.; Pecher, O.; Grey, C. P.; Masquelier, C.; Islam, M. S., Structural and mechanistic insights into fast lithium-ion conduction in $\text{Li}_4\text{SiO}_4\text{-Li}_3\text{PO}_4$ solid electrolytes. *J. Am. Chem. Soc.* **2015**, *137* (28), 9136-9145.
9. Fortal'nova, E.; Gavrilencov, O.; Belous, A.; Politova, E., Lithium-ion conducting oxides: Synthesis, structure, and electroconducting properties. *Russ J Gen Chem+* **2009**, *79* (9), 1987-1997.

1 Introduction

10. Alexander, K. C.; Ganesh, P.; Chi, M.; Kent, P.; Sumpter, B. G., Grain boundary stability and influence on ionic conductivity in a disordered perovskite-a first-principles investigation of lithium lanthanum titanate. *MRS Communications* **2016**, 6 (4), 455-463.
11. Bayard, M.; Barna, G., A complex impedance analysis of the ionic conductivity of $\text{Na}_{1+x}\text{Zr}_2\text{SixP}_{3-x}\text{O}_{12}$ ceramics. *Journal of Electroanalytical Chemistry and Interfacial Electrochemistry* **1978**, 91 (2), 201-209.
12. Xu, X.; Wen, Z.; Wu, X.; Yang, X.; Gu, Z., Lithium Ion-Conducting Glass-Ceramics of $\text{Li}_{1.5}\text{Al}_{0.5}\text{Ge}_{1.5}(\text{PO}_4)_{3-x}\text{Li}_2\text{O}$ ($x=0.0-0.20$) with Good Electrical and Electrochemical Properties. *Journal of the American Ceramic Society* **2007**, 90 (9), 2802-2806.
13. Richards, W. D.; Miara, L. J.; Wang, Y.; Kim, J. C.; Ceder, G., Interface Stability in Solid-State Batteries. *Chem Mater* **2016**, 28 (1), 266-273.
14. Zhu, Y. Z.; He, X. F.; Mo, Y. F., Origin of Outstanding Stability in the Lithium Solid Electrolyte Materials: Insights from Thermodynamic Analyses Based on First-Principles Calculations. *Acs Appl Mater Inter* **2015**, 7 (42), 23685-23693.
15. Kitaura, H.; Zhou, H., Electrochemical performance and reaction mechanism of all-solid-state lithium-air batteries composed of lithium, $\text{Li}_{1+x}\text{Al}_y\text{Ge}_{2-y}(\text{PO}_4)_3$ solid electrolyte and carbon nanotube air electrode. *Energy & Environmental Science* **2012**, 5 (10), 9077-9084.
16. Awaka, J.; Takashima, A.; Kataoka, K.; Kijima, N.; Idemoto, Y.; Akimoto, J., Crystal Structure of Fast Lithium-ion-conducting Cubic $\text{Li}_7\text{La}_3\text{Zr}_2\text{O}_{12}$. *Chem Lett* **2011**, 40 (1), 60-62.
17. Awaka, J.; Kijima, N.; Hayakawa, H.; Akimoto, J., Synthesis and structure analysis of tetragonal $\text{Li}_7\text{La}_3\text{Zr}_2\text{O}_{12}$ with the garnet-related type structure. *Journal of Solid State Chemistry* **2009**, 182 (8), 2046-2052.
18. Thangadurai, V.; Kaack, H.; Weppner, W. J., Novel Fast Lithium Ion Conduction in Garnet-Type $\text{Li}_5\text{La}_3\text{M}_2\text{O}_{12}$ ($\text{M} = \text{Nb}, \text{Ta}$). *Journal of the American Ceramic Society* **2003**, 86 (3), 437-440.
19. Cussen, E. J., Structure and ionic conductivity in lithium garnets. *Journal of Materials Chemistry* **2010**, 20 (25), 5167-5173.
20. Murugan, R.; Thangadurai, V.; Weppner, W., Fast Lithium Ion Conduction in Garnet-Type $\text{Li}_7\text{La}_3\text{Zr}_2\text{O}_{12}$. *Angewandte Chemie International Edition* **2007**, 46 (41), 7778-7781.
21. Buschmann, H.; Dölle, J.; Berendts, S.; Kuhn, A.; Bottke, P.; Wilkening, M.; Heitjans, P.; Senyshyn, A.; Ehrenberg, H.; Lotnyk, A., Structure and dynamics of the fast lithium ion conductor “ $\text{Li}_7\text{La}_3\text{Zr}_2\text{O}_{12}$ ”. *Phys. Chem. Chem. Phys.* **2011**, 13 (43), 19378-19392.

22. Matsui, M.; Sakamoto, K.; Takahashi, K.; Hirano, A.; Takeda, Y.; Yamamoto, O.; Imanishi, N., Phase transformation of the garnet structured lithium ion conductor: $\text{Li}_7\text{La}_3\text{Zr}_2\text{O}_{12}$. *Solid State Ionics* **2014**, *262*, 155-159.
23. Geiger, C. A.; Alekseev, E.; Lazic, B.; Fisch, M.; Armbruster, T.; Langner, R.; Fechtelkord, M.; Kim, N.; Pettke, T.; Weppner, W., Crystal chemistry and stability of “ $\text{Li}_7\text{La}_3\text{Zr}_2\text{O}_{12}$ ” garnet: A fast lithium-ion conductor. *Inorganic chemistry* **2010**, *50* (3), 1089-1097.
24. Toda, S.; Ishiguro, K.; Shimonishi, Y.; Hirano, A.; Takeda, Y.; Yamamoto, O.; Imanishi, N., Low temperature cubic garnet-type CO_2 -doped $\text{Li}_7\text{La}_3\text{Zr}_2\text{O}_{12}$. *Solid State Ionics* **2013**, *233*, 102-106.
25. Adams, S.; Rao, R. P., Ion transport and phase transition in $\text{Li}_{7-x}\text{La}_3(\text{Zr}_{2-x}\text{M}_x)\text{O}_{12}$ ($\text{M} = \text{Ta}^{5+}, \text{Nb}^{5+}$, $x = 0, 0.25$). *Journal of Materials Chemistry* **2012**, *22* (4), 1426-1434.
26. Deviannapoorani, C.; Dhivya, L.; Ramakumar, S.; Murugan, R., Lithium ion transport properties of high conductive tellurium substituted $\text{Li}_7\text{La}_3\text{Zr}_2\text{O}_{12}$ cubic lithium garnets. *J. Power Sources* **2013**, *240*, 18-25.
27. Ohta, S.; Kobayashi, T.; Asaoka, T., High lithium ionic conductivity in the garnet-type oxide $\text{Li}_{7-x}\text{La}_3(\text{Zr}_{2-x}, \text{Nb}_x)\text{O}_{12}$ ($X = 0-2$). *J. Power Sources* **2011**, *196* (6), 3342-3345.
28. Rangasamy, E.; Wolfenstine, J.; Sakamoto, J., The role of Al and Li concentration on the formation of cubic garnet solid electrolyte of nominal composition $\text{Li}_7\text{La}_3\text{Zr}_2\text{O}_{12}$. *Solid State Ionics* **2012**, *206*, 28-32.
29. Wolfenstine, J.; Sakamoto, J.; Allen, J., Electron microscopy characterization of hot-pressed Al substituted $\text{Li}_7\text{La}_3\text{Zr}_2\text{O}_{12}$. *JMatS* **2012**, *47* (10), 4428-4431.
30. Thompson, T.; Yu, S. H.; Williams, L.; Schmidt, R. D.; Garcia-Mendez, R.; Wolfenstine, J.; Allen, J. L.; Kioupakis, E.; Siegel, D. J.; Sakamoto, J., Electrochemical Window of the Li-Ion Solid Electrolyte $\text{Li}_7\text{La}_3\text{Zr}_2\text{O}_{12}$. *Acs Energy Lett* **2017**, *2* (2), 462-468.
31. Ohta, S.; Kobayashi, T.; Seki, J.; Asaoka, T., Electrochemical performance of an all-solid-state lithium ion battery with garnet-type oxide electrolyte. *J. Power Sources* **2012**, *202*, 332-335.
32. Zhu, S.; Qin, Y.; Zhang, J., Renovation of Lithium Cobalt Oxide from Spent Lithium Ion Batteries by an Aqueous Pulsed Discharge Plasma. *Int J Electrochem Sc* **2016**, *11* (7), 6403-6411.
33. Cao, C.; Li, Z.-B.; Wang, X.-L.; Zhao, X.-B.; Han, W.-Q., Recent advances in inorganic solid electrolytes for lithium batteries. *Frontiers in Energy Research* **2014**, *2*, 25.
34. Ohtomo, T.; Hayashi, A.; Tatsumisago, M.; Kawamoto, K., Characteristics of the $\text{Li}_2\text{O-Li}_2\text{S-P}_2\text{S}_5$ glasses synthesized by the two-step mechanical milling. *Journal of Non-Crystalline Solids* **2013**, *364*, 57-61.

1 Introduction

35. Minami, T.; Hayashi, A.; Tatsumisago, M., Recent progress of glass and glass-ceramics as solid electrolytes for lithium secondary batteries. *Solid State Ionics* **2006**, *177* (26-32), 2715-2720.
36. Ujiie, S.; Inagaki, T.; Hayashi, A.; Tatsumisago, M., Conductivity of $70\text{Li}_2\text{S}\cdot 30\text{P}_2\text{S}_5$ glasses and glass-ceramics added with lithium halides. *Solid State Ionics* **2014**, *263*, 57-61.
37. Ujiie, S.; Hayashi, A.; Tatsumisago, M., Preparation and ionic conductivity of $(100-x)(0.8\text{Li}_2\text{S}\cdot 0.2\text{P}_2\text{S}_5)\cdot x\text{LiI}$ glass-ceramic electrolytes. *J Solid State Electrochem* **2013**, *17* (3), 675-680.
38. Yamauchi, A.; Sakuda, A.; Hayashi, A.; Tatsumisago, M., Preparation and ionic conductivities of $(100-x)(0.75\text{Li}_2\text{S}\cdot 0.25\text{P}_2\text{S}_5)\cdot x\text{LiBH}_4$ glass electrolytes. *J. Power Sources* **2013**, *244*, 707-710.
39. Takada, K.; Aotani, N.; Kondo, S., Electrochemical behaviors of Li^+ ion conductor, $\text{Li}_3\text{PO}_4\text{-Li}_2\text{S-SiS}_2$. *J. Power Sources* **1993**, *43* (1), 135-141.
40. Mizuno, F.; Hayashi, A.; Tadanaga, K.; Tatsumisago, M., New, Highly Ion-Conductive Crystals Precipitated from $\text{Li}_2\text{S-P}_2\text{S}_5$ Glasses. *Adv Mater* **2005**, *17* (7), 918-921.
41. Yamane, H.; Shibata, M.; Shimane, Y.; Junke, T.; Seino, Y.; Adams, S.; Minami, K.; Hayashi, A.; Tatsumisago, M., Crystal structure of a superionic conductor, $\text{Li}_7\text{P}_3\text{S}_{11}$. *Solid State Ionics* **2007**, *178* (15), 1163-1167.
42. Onodera, Y.; Mori, K.; Otomo, T.; C. Hannon, A.; Kohara, S.; Itoh, K.; Sugiyama, M.; Fukunaga, T., Crystal structure of $\text{Li}_7\text{P}_3\text{S}_{11}$ studied by neutron and synchrotron X-ray powder diffraction. *Journal of the Physical Society of Japan* **2010**, *79* (Suppl. A), 87-89.
43. Onodera, Y.; Mori, K.; Otomo, T.; Sugiyama, M.; Fukunaga, T., Structural Evidence for High Ionic Conductivity of $\text{Li}_7\text{P}_3\text{S}_{11}$ Metastable Crystal. *Journal of the Physical Society of Japan* **2012**, *81* (4), 044802.
44. Onodera, Y.; Mori, K.; Otomo, T.; Arai, H.; Uchimoto, Y.; Ogumi, Z.; Fukunaga, T., Structural origin of ionic conductivity for $\text{Li}_7\text{P}_3\text{S}_{11}$ metastable crystal by neutron and X-ray diffraction. *Journal of Physics: Conference Series* **2014**, *502* (1), 012021.
45. Mori, K.; Ichida, T.; Iwase, K.; Otomo, T.; Kohara, S.; Arai, H.; Uchimoto, Y.; Ogumi, Z.; Onodera, Y.; Fukunaga, T., Visualization of conduction pathways in lithium superionic conductors: $\text{Li}_2\text{S-P}_2\text{S}_5$ glasses and $\text{Li}_7\text{P}_3\text{S}_{11}$ glass-ceramic. *Chem Phys Lett* **2013**, *584*, 113-118.
46. Hayamizu, K.; Aihara, Y., Lithium ion diffusion in solid electrolyte $(\text{Li}_2\text{S})_7\cdot(\text{P}_2\text{S}_5)_3$ measured by pulsed-gradient spin-echo ^7Li NMR spectroscopy. *Solid State Ionics* **2013**, *238*, 7-14.
47. Wohlmuth, D.; Epp, V.; Wilkening, M., Fast Li Ion Dynamics in the Solid Electrolyte $\text{Li}_7\text{P}_3\text{S}_{11}$ as Probed by $^6,7\text{Li}$ NMR Spin-Lattice Relaxation. *Chemphyschem* **2015**, *16* (12), 2582-2593.

48. Murakami, M.; Shimoda, K.; Shiotani, S.; Mitsui, A.; Ohara, K.; Onodera, Y.; Arai, H.; Uchimoto, Y.; Ogumi, Z., Dynamical origin of ionic conductivity for $\text{Li}_7\text{P}_3\text{S}_{11}$ metastable crystal as studied by ^6Li and ^{31}P solid-state NMR. *The Journal of Physical Chemistry C* **2015**, *119* (43), 24248-24254.
49. Seino, Y.; Ota, T.; Takada, K.; Hayashi, A.; Tatsumisago, M., A sulphide lithium super ion conductor is superior to liquid ion conductors for use in rechargeable batteries. *Energ Environ Sci* **2014**, *7* (2), 627-631.
50. Tatsumisago, M.; Nagao, M.; Hayashi, A., Recent development of sulfide solid electrolytes and interfacial modification for all-solid-state rechargeable lithium batteries. *Journal of Asian ceramic societies* **2013**, *1* (1), 17-25.
51. Kanno, R.; Murayama, M., Lithium Ionic Conductor Thio-LISICON: The $\text{Li}_2\text{S}\cdot\text{GeS}_2\cdot\text{P}_2\text{S}_5$ System. *J. Electrochem. Soc.* **2001**, *148* (7), A742-A746.
52. Murayama, M.; Kanno, R.; Irie, M.; Ito, S.; Hata, T.; Sonoyama, N.; Kawamoto, Y., Synthesis of new lithium ionic conductor thio-LISICON-lithium silicon sulfides system. *Journal of Solid State Chemistry* **2002**, *168* (1), 140-148.
53. Kamaya, N.; Homma, K.; Yamakawa, Y.; Hirayama, M.; Kanno, R.; Yonemura, M.; Kamiyama, T.; Kato, Y.; Hama, S.; Kawamoto, K.; Mitsui, A., A lithium superionic conductor. *Nature Materials* **2011**, *10* (9), 682-686.
54. Mo, Y.; Ong, S. P.; Ceder, G., First principles study of the $\text{Li}_{10}\text{GeP}_2\text{S}_{12}$ lithium super ionic conductor material. *Chem. Mater.* **2011**, *24* (1), 15-17.
55. Han, F.; Zhu, Y.; He, X.; Mo, Y.; Wang, C., Electrochemical Stability of $\text{Li}_{10}\text{GeP}_2\text{S}_{12}$ and $\text{Li}_7\text{La}_3\text{Zr}_2\text{O}_{12}$ Solid Electrolytes. *Advanced Energy Materials* **2016**, *6* (8), 1501590-n/a.
56. Ong, S. P.; Mo, Y.; Richards, W. D.; Miara, L.; Lee, H. S.; Ceder, G., Phase stability, electrochemical stability and ionic conductivity of the $\text{Li}_{10\pm 1}\text{MP}_2\text{X}_{12}$ (M = Ge, Si, Sn, Al or P, and X = O, S or Se) family of superionic conductors. *Energ Environ Sci* **2013**, *6* (1), 148-156.
57. Yuki, K.; Kawamoto, K.; Kanno, R.; Hirayama, M., Discharge performance of all-solid-state battery using a lithium superionic conductor $\text{Li}_{10}\text{GeP}_2\text{S}_{12}$. *Electrochemistry* **2012**, *80* (10), 749-751.
58. Hassoun, J.; Verrelli, R.; Reale, P.; Panero, S.; Mariotto, G.; Greenbaum, S.; Scrosati, B., A structural, spectroscopic and electrochemical study of a lithium ion conducting $\text{Li}_{10}\text{GeP}_2\text{S}_{12}$ solid electrolyte. *J. Power Sources* **2013**, *229*, 117-122.
59. Whiteley, J. M.; Woo, J. H.; Hu, E.; Nam, K.-W.; Lee, S.-H., Empowering the lithium metal battery through a silicon-based superionic conductor. *J. Electrochem. Soc.* **2014**, *161* (12), A1812-A1817.
60. Bron, P.; Johansson, S.; Zick, K.; Schmedt auf der Günne, J. r.; Dehnen, S.; Roling, B., $\text{Li}_{10}\text{SnP}_2\text{S}_{12}$: an affordable lithium superionic conductor. *J. Am. Chem. Soc.* **2013**, *135* (42), 15694-15697.

1 Introduction

61. Kato, Y.; Saito, R.; Sakano, M.; Mitsui, A.; Hirayama, M.; Kanno, R., Synthesis, structure and lithium ionic conductivity of solid solutions of $\text{Li}_{10}(\text{Ge}_{1-x}\text{M}_x)\text{P}_2\text{S}_{12}$ (M= Si, Sn). *J. Power Sources* **2014**, *271*, 60-64.
62. Zhou, P.; Wang, J.; Cheng, F.; Li, F.; Chen, J., A solid lithium superionic conductor $\text{Li}_{11}\text{AlP}_2\text{S}_{12}$ with a thio-LISICON analogous structure. *Chemical Communications* **2016**, *52* (36), 6091-6094.
63. Kato, Y.; Hori, S.; Saito, T.; Suzuki, K.; Hirayama, M.; Mitsui, A.; Yonemura, M.; Iba, H.; Kanno, R., High-power all-solid-state batteries using sulfide superionic conductors. *Nature Energy* **2016**, *1*, 16030.
64. de Klerk, N. J.; Rosłoń, I.; Wagemaker, M., Diffusion Mechanism of Li Argyrodite Solid Electrolytes for Li-Ion Batteries and Prediction of Optimized Halogen Doping: The Effect of Li Vacancies, Halogens, and Halogen Disorder. *Chem Mater* **2016**, *28* (21), 7955-7963.
65. Deiseroth, H. J.; Kong, S. T.; Eckert, H.; Vannahme, J.; Reiner, C.; Zaiß, T.; Schlosser, M., $\text{Li}_6\text{PS}_5\text{X}$: A Class of Crystalline Li-Rich Solids With an Unusually High Li^+ Mobility. *Angew. Chem. Int. Ed.* **2008**, *47* (4), 755-758.
66. Rao, R. P.; Adams, S., Studies of lithium argyrodite solid electrolytes for all-solid-state batteries. *physica status solidi (a)* **2011**, *208* (8), 1804-1807.
67. Rao, R. P.; Sharma, N.; Peterson, V.; Adams, S., Formation and conductivity studies of lithium argyrodite solid electrolytes using in-situ neutron diffraction. *Solid State Ionics* **2013**, *230*, 72-76.
68. Boulineau, S.; Courty, M.; Tarascon, J.-M.; Viallet, V., Mechanochemical synthesis of Li-argyrodite $\text{Li}_6\text{PS}_5\text{X}$ (X= Cl, Br, I) as sulfur-based solid electrolytes for all-solid-state batteries application. *Solid State Ionics* **2012**, *221*, 1-5.
69. Rayavarapu, P. R.; Sharma, N.; Peterson, V. K.; Adams, S., Variation in structure and Li^+ -ion migration in argyrodite-type $\text{Li}_6\text{PS}_5\text{X}$ (X= Cl, Br, I) solid electrolytes. *J Solid State Electr* **2012**, *16* (5), 1807-1813.
70. Epp, V.; Gün, O. z. I.; Deiseroth, H.-J. r.; Wilkening, M., Highly mobile ions: low-temperature NMR directly probes extremely fast Li^+ hopping in argyrodite-type $\text{Li}_6\text{PS}_5\text{Br}$. *The Journal of Physical Chemistry Letters* **2013**, *4* (13), 2118-2123.
71. Boulineau, S.; Tarascon, J.-M.; Leriche, J.-B.; Viallet, V., Electrochemical properties of all-solid-state lithium secondary batteries using Li-argyrodite $\text{Li}_6\text{PS}_5\text{Cl}$ as solid electrolyte. *Solid State Ionics* **2013**, *242*, 45-48.
72. Chuang Yu, L. v. E., Swapna Ganapathy, Marnix Wagemaker, Synthesis, structure and electrochemical performance of the argyrodite $\text{Li}_6\text{PS}_5\text{Cl}$ solid electrolyte for Li-ion solid state batteries. *Electrochim Acta* **2016**, *215*, 93-99.
73. Chen, M.; Adams, S., High performance all-solid-state lithium/sulfur batteries using lithium argyrodite electrolyte. *J Solid State Electr* **2015**, *19* (3), 697-702.

74. Chen, M.; Rao, R. P.; Adams, S., High capacity all-solid-state Cu-Li₂S/Li₆PS₅Br/In batteries. *Solid State Ionics* **2014**, *262*, 183-187.
75. Chen, M.; Rao, R. P.; Adams, S., The unusual role of Li₆PS₅Br in all-solid-state CuS/Li₆PS₅Br/In-Li batteries. *Solid State Ionics* **2014**, *268*, 300-304.
76. Chen, M.; Yin, X.; Reddy, M.; Adams, S., All-solid-state MoS₂/Li₆PS₅Br/In-Li batteries as a novel type of Li/S battery. *Journal of Materials Chemistry A* **2015**, *3* (20), 10698-10702.
77. Stadler, F.; Fietzek, C., Crystalline Halide Substituted Li-Argyrodites as Solid Electrolytes for Lithium Secondary Batteries. *ECS Transactions* **2010**, *25* (36), 177-183.

2

Characterization Techniques, Theory and Methods

2.1 X-rays and neutron diffraction

Crystalline materials are characterized by a periodic atomic lattice structure. When the wavelength of X-rays or neutrons is in the order of magnitude of the separation between the lattice planes, typically in the order of 10^{-10} m (1 Å), the lattice acts as a diffraction grating. X-rays and neutrons will be scattered coherently by lattice planes in specific directions that satisfy Bragg's law, leading to constructive interference, as shown in Figure 2.1. Bragg's law is expressed as follows:

$$2d\sin\theta = n\lambda \quad (2.1)$$

where d is the distance between the lattice planes, θ is the scattering angle between the incident radiation and the lattice plane, n is an integer and λ is the wavelength of the incident X-rays or neutrons.¹

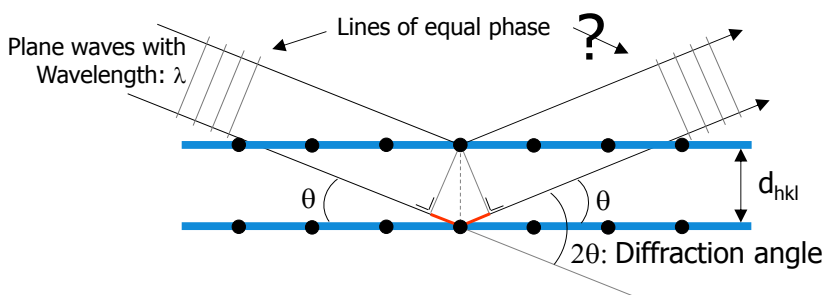


Figure 2.1: Schematic representation of Bragg's law for diffraction.

Crystalline materials are built up by repeating a unit cell that contains all the symmetry information of the lattice. A unit cell can be uniquely defined by specifying the unit cell dimensions (a , b , c), the angles between these cell edges (α , β , γ) and the atom positions within the cell. To specify the lattice plane orientation, Miller indices are introduced. A lattice vector passing from the origin to a lattice point can be expressed as:

$$\mathbf{r} = h \cdot \mathbf{a} + k \cdot \mathbf{b} + l \cdot \mathbf{c} \quad (2.2)$$

where \mathbf{a} , \mathbf{b} , \mathbf{c} are the basic vectors and (hkl) are the Miller indices. The index value of 0 for Miller indices means parallel to an axis.

Diffraction of an incident beam (X-rays or neutrons) on the crystal lattice results in a diffraction pattern, the diffracted intensity as a function of the diffraction angle. From this pattern, it is possible to deduce the crystalline structure. The periodic arrangement of atoms in a crystal results in a diffracted intensity from a lattice plane, characterized by the Miller indices (hkl) can be expressed as follows:

$$I_{(hkl)} = s \mathbf{p}_{(hkl)} \cdot L_{\theta} \mathbf{A}_{\theta} \cdot \mathbf{P}_{(hkl)} \cdot |F_{(hkl)}|^2 \quad (2.3)$$

where s is the scale factor, p is the multiplicity, L_{θ} is the Lorentz-polarization, A is the absorption correction, P is the preferred orientation, and $F_{(hkl)}$ is the structure factor which can be expressed by the following equation:

$$F_{(hkl)} = \sum f_j \exp[2\pi i(hx_j + ky_j + lz_j)] \exp[-B_j \sin^2 \theta / \lambda^2] \quad (2.4)$$

where the sum runs over the atoms within the unit cell and the first term, f_j , is the form factor, which is determined by the atomic species. The second term determines if a diffracted reflection is allowed, which is directly related to the contents of the unit cell characterized by the fractional atomic positions, x , y , z . The final item in equation 2.3 is the temperature factor determined by the thermal motions of the atoms characterized by the thermal parameter B .²

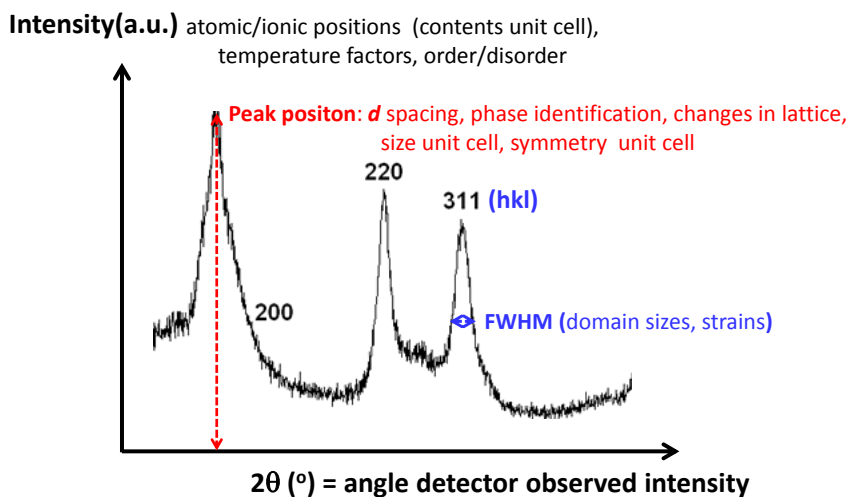


Figure 2.2: X-ray diffractogram.

From the X-ray and neutron diffraction patterns, the symmetry and phase composition can be deduced. Additionally, from each phase one can determine the unit cell dimensions, characterized by the lattice parameters, the atomic positions and the average crystallite size and strain, as schematically summarized in Figure 2.2. The peak positions are determined by the size and shape of the unit cell, whereas the contents of the unit cell, the atomic positions, and occupancies, determine the diffracted intensities. The broadening of the reflections is determined by both the crystalline size and strain which have a different dependence on the diffraction angle θ .

X-rays are scattered by the electrons, which makes them highly attenuated by matter resulting in small penetration depths from micro to millimeters, as shown in Figure 2.3a. In contrast, neutrons only interact with the nucleus of the atom, and as a result, the penetration depth of neutrons is in the order of centimeters to decimeters. As a consequence, neutron diffraction typically probes the entire sample, which makes it less susceptible to surface and absorption effects and more

suitable to handle thick sample environments. However, for powder neutron diffraction, a larger amount of samples is needed compared to X-ray diffraction, in order to obtain sufficient scattered intensity. An advantage of neutron diffraction is that the more localized form factor results at large diffracted angles in relatively large intensities are relatively large compared to X-ray diffraction. There is no useful information for X-ray diffraction at high 2θ angle, while high-intensity peaks are detected at a high angle by neutron diffraction to give more reliable structure information. Neutrons have an intrinsic magnetic moment, while X-rays have no magnetic moment, which makes neutron diffraction suitable to determine ordered magnetic structures, such as occurring in Ferro-, Ferri-, and Antiferromagnetic materials. Additionally, the X-ray cross section monotonically increases with atomic number, as shown in Figure 2.3b, which makes it difficult to distinguish elements next to each other in the periodic table, such as Cl and S. However, the neutron cross section for elastic scattering varies apparently irregularly with both atomic number and mass number, which often provides the possibility to distinguish atoms that are difficult to distinguish using X-rays. Moreover, the relatively large neutron cross sections for protons and lithium in Figure 2.3b shows that neutron diffraction is a powerful tool to investigate materials containing lithium and/or protons. In some cases, we need to combine X-ray and neutron diffraction together to resolve the detailed crystal structure, especially when there are more than two atomic species on one crystallographic site.

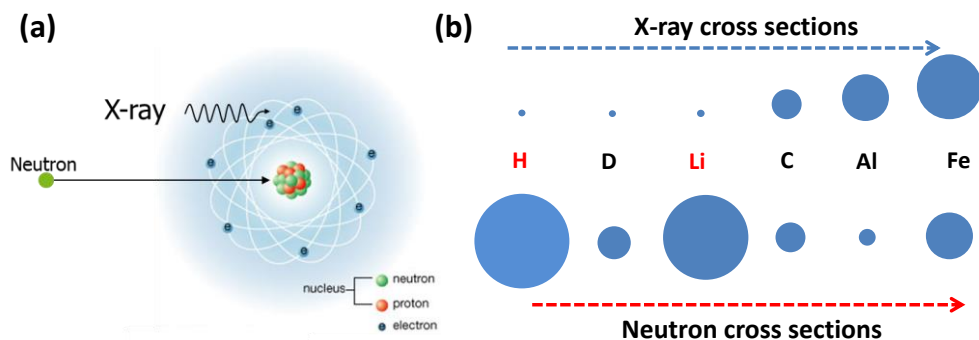


Figure 2.3: (a) Schematic representation of X-ray and neutron scattering. (b) Cross sections of X-ray and neutron elastic scattering for a number of elements. The area of the circles indicates qualitatively the size of the cross section.

In practice, when the symmetry of a crystalline material is known, the detailed structural parameters are obtained by Rietveld refinement of a model structure towards the measured diffraction pattern. This allows refinement of all structural parameters, including phase fractions, lattice parameters, atomic positions and occupancies, thermal parameters, crystallite size, and crystallite strain. The most frequently applied Rietveld refinement software packages are GSAS (General Structure Analysis System)³ and FullProf⁴. In this thesis, GSAS was applied to refine the X-ray and neutron diffraction patterns.

2.2 Alternating Current (AC) impedance

In this thesis, the ionic conductivities of lithium ion conductors are investigated by Alternating Current (AC) impedance spectroscopy. This method allows in principle to separate the grain-boundary from the bulk contribution to the overall conductivity. The conductivity σ of the sample can be obtained by measuring the resistance R , the diffusion length L and the cross-section area A . Then the conductivity can be calculated as follows:

$$\sigma = L/(R \cdot A) \quad (2.5)$$

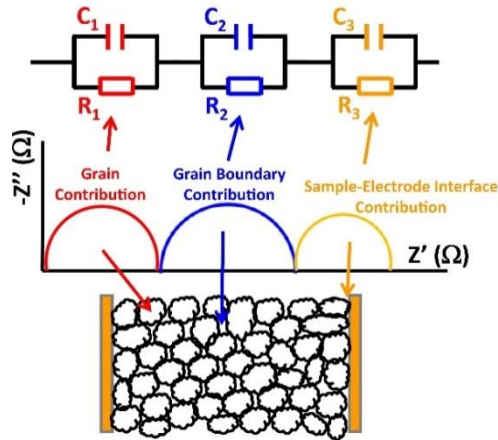


Figure 2.4: Schematic representation of an equivalent circuit model, and resulting impedance spectrum, for a solid powder sample.

As shown in Figure 2.4, a pellet of a solid ionic conductor, sandwiched between two Pt (or Au, Ag) electrodes, results in an AC impedance spectrum from which in principle the different semicircles and arcs can be related to different resistances and capacities of the solid ionic conductor. In general, the AC impedance spectra for ionic conductors are built up by a bulk semicircle, a grain-boundary semicircle, and an electrode-process arc (or a tail), corresponding to the high, medium and low frequency part of the plots.⁵ The bulk semicircles correspond to a parallel circuit composed of R_1 and C_1 , where R_1 represents the bulk resistance and C_1 is the related capacitance. R_1 is obtained from the intersection of this semicircle with the real axis, while C_1 can be calculated from the relationship $\omega_p R_1 C_1 = 1$, where ω_p is the peak frequency of the bulk semicircle. Typically, another semicircle located at medium frequencies represents the grain-boundary impedance. The arc (or tail) at the low-frequency part represents processes occurring at the pellet/Pt paste

interfaces.⁵ In most cases, the bulk contribution and grain boundary contribution can be separated only if the applied frequency is high enough. In this thesis, the AC impedance measurements are not able to distinguish between them due to the limitation in the high frequency of the employed instrument (Autolab PGSTAT302N, maximum frequency 1MHz).

2.3 Solid-State Nuclear Magnetic Resonance (NMR)

Nuclear Magnetic Resonance (NMR) spectroscopy offers a direct probe of the environment of magnetic moments of nuclear spins under the influence of an external magnetic field. Solid-state NMR is a powerful short-range analysis technique, which can be applied to probe microscopic interactions (1-100 Å) and enables the study of structure and dynamics of solid materials.

The generation of an NMR spectrum

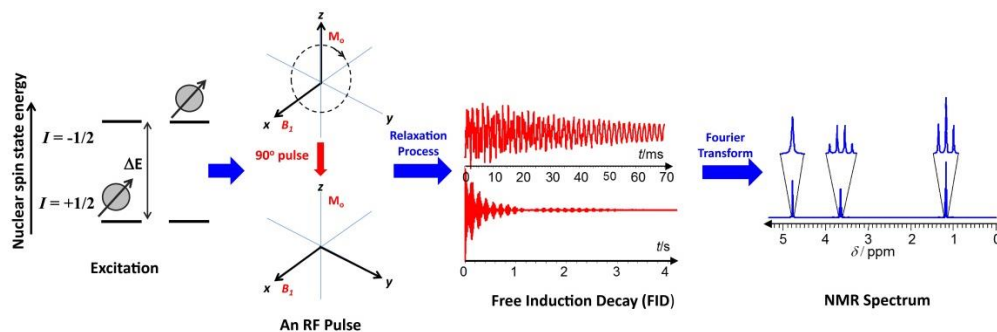


Figure 2.5: Schematic of the generation of an NMR spectrum.

A nucleus with $I = \frac{1}{2}$ in a static magnetic field B_0 results in two energy levels associated with the quantum numbers $m = -\frac{1}{2}$ and $\frac{1}{2}$. Excitation will occur if the energy of the radio-frequency radiation matches the energy for a nuclear spin transition between those two levels, as shown in Figure 2.5. The magnetic nuclear spins in a sample are detected through rotating the macroscopic nuclear spin

polarization by a radio-frequency pulse which is generated by the probe coil in a suitable resonance circuit. This radio-frequency pulse introduces an oscillating magnetic field, $\mathbf{B}_1(t)$, into the spin system. The time dependence of the magnetic field in this case means that both the eigenstates of the spin systems and their energies are time-dependent. The consequence of the radio-frequency pulse is that the macroscopic magnetization rotates away from the static magnetic field. The rotation angle can be set directly by adjusting the duration of the radio-frequency pulse. Typically, a 90° pulse is applied, which rotates the magnetization by 90° with respect to the z -axis as shown in Figure 2.5. The solid-state NMR signal is detected in the xy -plane. The precession of the macroscopic magnetization in the xy -plane induces a current in the coil around the sample, which is referred to as the free induction decay (FID). The solid-state NMR spectrum can be obtained by Fourier Transformation of the FID, which transforms the time-scale into frequency-scale. Typically NMR spectra are shown as a function of the chemical shift, which is defined as the relative ppm $\delta = 10^6 \cdot (\nu_{\text{sample}} - \nu_{\text{ref}}) / \nu_{\text{Larmor}}$. The reference frequency, ν_{ref} , is defined by measuring a reference compound for the nuclei of interest, for instance, the solution of LiCl for ^7Li and ^6Li NMR. The ^7Li NMR spectrum is typically dominated by quadrupolar interactions and the dipolar coupling, resulting in a broad spectrum, which makes ^7Li suitable to study the local environment and dynamics. For ^6Li , weaker quadrupolar and dipolar interactions result in more narrow spectra, providing better resolution towards the different local Li environments, allowing studies of the role of defects in ionic conduction and changes in the structure of a material.

Nuclear spin interactions

2 Characterization Techniques, Theory and Methods

Nuclear spin is quantified by the spin angular momentum vector (\mathbf{I}) which is related to the magnetic moment vector ($\boldsymbol{\mu}$) of the nucleus as well as the nuclear gyromagnetic ratio (γ_N), and can be expressed as:

$$\boldsymbol{\mu} = \gamma_N \hbar \mathbf{I} = g_N \mu_N \mathbf{I} \quad (2.6)$$

Where γ_N may also be expressed by the nuclear g factor (g_N) and the nuclear magneton (μ_N). The values for \mathbf{I} and μ_N are unique to a given nucleus and allow nuclei to be distinguished from one another spectroscopically.

The electric and magnetic fields experienced by a nuclear spin may originate from the external apparatus which is referred to as external spin interaction, or from the sample itself which is referred to as internal spin interaction. External spin interaction is purely magnetic and results from the applied magnetic fields which can be used to manipulate the nuclear spins. The interaction between an external magnetic field \mathbf{B}_0 and the magnetic moments of the spin system or a collection of spins results in the Zeeman interaction, which determines the position in frequency of the resonance line. When an atom is placed in an external magnetic \mathbf{B}_0 , electronic motions will generate an induced magnetic field, which will shield the local magnetic field experienced by the nucleus, shifting the resonance frequency of the nucleus slightly from the Larmor frequency. An interaction between the spins of two nuclei (\mathbf{I} and \mathbf{S}) in the system represents the dipole-dipole coupling between the corresponding magnetic moments, the strength of which depends on the orientation and spatial separation. The effect of this dipole-dipole coupling is to broaden the NMR spectrum. When the spin of the nucleus is larger than $1/2$, for instance, ${}^7\text{Li}$ ($\mathbf{I} = 3/2$), there is an interaction between a spin of the nucleus and the electric field gradient produced by the surrounding electrons. This interaction between the nuclear electric quadrupole moment and the electric field gradient is known as the quadrupolar interaction, which broadens the central transition of an

NMR spectrum. Besides the above-mentioned interactions, there are also other interactions in solids, such as J-coupling and Knight shift.

Magic Angle Spinning (MAS)

In solutions, rapid isotropic tumbling typically averages several interactions to zero, resulting in narrow NMR resonances. For solid powders, a single crystal gives a high solid-state NMR resolution. However, in a powder a large number of randomly oriented crystallites, results in a broad distribution of spectra, effectively generating a broad spectrum. In addition, e.g. the dipolar interaction broadens the spectrum, which is expressed as the interaction Hamiltonian of a spin S with another spin I :

$$H_{IS} = -d(3\cos^2 \theta - 1)I_z S_z, \quad (2.7)$$

Where θ is the angle between the applied field \mathbf{B}_0 and the inter-nuclear distance (r_{IS}). The dipole constant is dependent on the distance between the nuclear spins and their gyromagnetic ratios, which is expressed as follows:

$$d = \left(\frac{\mu_o}{4\pi}\right) \frac{\hbar\gamma_I\gamma_S}{r_{IS}^3} \quad (2.8)$$

Then the dipolar coupling between spins S and I can be obtained by combining equations 2.7 and 2.8 which lead to:

$$H_{IS} = -\left(\frac{\mu_o}{4\pi}\right) \frac{\hbar\gamma_I\gamma_S}{r_{IS}^3} (3\cos^2 \theta - 1)I_z S_z, \quad (2.9)$$

As shown in the above Hamiltonian, the dipolar coupling provides both information on the distance (r) between nuclei and their orientation (θ).

2 Characterization Techniques, Theory and Methods

Another internal interaction in powder materials is the Chemical Shift Anisotropy (CSA), a consequence of the orientation dependence of chemical shift, leading to an extensive line-width broadening in the NMR spectra of powder samples.

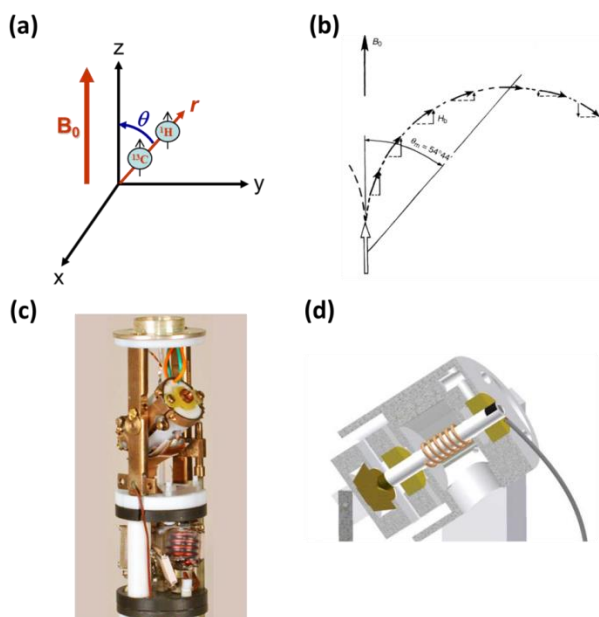


Figure 2.6: (a) The dipolar coupling between C and H. (b) Simulate a uniform distribution of magnetic moments in a powder by spinning the sample very fast at 54.74° . (c) MAS probe. (d) The rotor in an MAS probe.

To eliminate the dipolar coupling and chemical shift anisotropy interactions in powders, Magic Angle Spinning (MAS) has been developed to improve the resolution of the NMR spectrum. A nucleus with the magnetic moment (μ) will create a field at a second nucleus at a distance r , which will have a z component (B_z) in the direction of B_0 . The magnitude of B_z will depend on the angle of the magnetic moment relative to B_0 , as shown in Figure 2.6. B_z can be expressed as follows:

$$B_z = \frac{K\mu}{r^3}(3\cos^2\theta - 1), \quad (2.10)$$

The condition to eliminate this magnetic field is $(3\cos^2\theta - 1) = 0$, which leads to an angle of $\theta = \arccos(1/\sqrt{3}) \approx 54.74^\circ$. When the powder sample is spinning at the ‘magic angle’ of 54.74° with respect to \mathbf{B}_0 , this averages out both dipolar coupling and the chemical shift anisotropy. In addition, this may also reduce the quadrupole interaction. When spinning the sample under the magic angle, the internal interactions become time-dependent, resulting in spectra that contain spinning sidebands separated by the spinning rate. If the spinning rate is larger than the line broadening, these can be averaged out efficiently on the NMR time-scale. Otherwise, spinning side bands become visible if the spinning rate is lower than the magnitude of the interaction. With MAS, small spinning sidebands can be separated from the central line, and solid-state NMR spectra with high resolution can be obtained.

NMR line-shape analysis

Temperature-dependent NMR can be applied to estimate ionic motion in conductors. As discussed above, dipolar interactions cause solid-state NMR lines to broaden, and this property can be used to monitor the Li-motion in the crystal lattice. At low temperatures, the ions can be frozen and the NMR resonances are broadened by the dipolar interactions, resulting in a Gaussian shaped resonance. The jump rate of ions increases with increasing temperature. When the temperature reaches a given value, the jump rate of the Li-ion becomes comparable to the dipolar coupling constant. When the dipolar interaction is increasingly averaged, this results in the so-called motional narrowing of the NMR line. Under these conditions, the NMR line becomes Lorentzian shaped. At an intermediate temperature range, the NMR spectrum of Li-ion conductor is a combination of a

broad and a narrow component, which can be assigned to ${}^7\text{Li}$ populations with higher and lower ion mobility. The fraction of fast and slow Li-ions in the lithium ion conductor can be determined by fitting the spectra as the sum of the narrow and broad components respectively.

Spin-lattice relaxation NMR measurement

At thermal equilibrium, the magnetic field split states are populated according to the Boltzmann distribution at the temperature of the molecular environment. When a RF-pulse disturbs the equilibrium of the spin system, the population of different states will deviate from their equilibrium values. Relaxation is the process by which equilibrium is regained, through an interaction of the spin system with the thermal molecular environment. This Relaxation is divided roughly into two types, spin-lattice relaxation and spin-spin relaxation, as shown in Figure 2.7. The former is a longitudinal relaxation which is concerned with the movement of spin populations back to their Boltzmann distribution values. While the latter is known as a transverse relaxation which is concerned with the decay of coherences. For an ensemble of isolated spin- $\frac{1}{2}$, two time constants are employed to characterize the relaxation process, T_1 and T_2 . T_1 is the spin-lattice relaxation time constant for the equilibration of populations, and T_2 is the spin-spin relaxation time constant for the decay of single-quantum coherences. For spin- $\frac{1}{2}$ nuclei, relaxation is caused by fluctuating magnetic fields at the sites of the nuclear spins, caused by thermal motion of the molecules. For spins $> \frac{1}{2}$, electric quadrupole coupling is also involved. Spin-spin relaxation processes are typically much faster than spin-lattice relaxation, making T_2 smaller than T_1 . The spin-lattice relaxation time T_1 depends on temperature due to the random field fluctuation originating from the molecular environment, and the correlation time τ_c is temperature-dependent. Heating the

sample makes the fluctuations faster, reducing the correlation time, while cooling down the sample slows down the fluctuations, lengthening the correlation time.

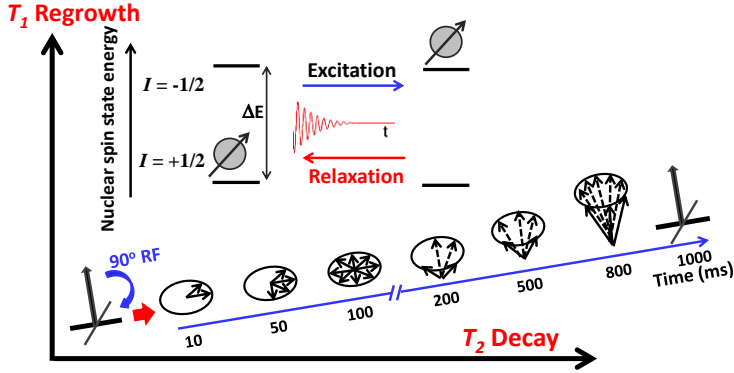


Figure 2.7: The evolution of the magnetization after it has been flipped by 90° pulse. The longitudinal and transverse are the regrowth process of the T_1 and the T_2 decay.

For liquid-like random diffusion of nuclei with $I = \frac{1}{2}$ and $I > \frac{1}{2}$, Bloembergen, Purcell and Pound⁶ derived:

$$\frac{1}{T_1} = \frac{2}{5} \gamma^4 \hbar^2 N I(I+1) \int_a^{+\infty} \frac{1}{r^6} \left[\frac{\tau_c}{1 + \omega_o^2 \tau_c^2} + \frac{2\tau_c}{1 + 4\omega_o^2 \tau_c^2} \right] 4\pi^2 r^2 dr, \quad (2.11)$$

where N is the number of nuclei per unit volume and the r -integration assumes a homogenous distribution of nuclear dipoles starting from the minimum nuclear distance a . The above-described model is named as the BPP model.

If only the effect of the first neighbors (with a distance of a) is incorporated in equation 2.11, then the result is:

$$\frac{1}{T_1} = \frac{2\gamma^4 \hbar^2 I(I+1)}{5a^6} \left[\frac{\tau_c}{1 + \omega_o^2 \tau_c^2} + \frac{2\tau_c}{1 + 4\omega_o^2 \tau_c^2} \right], \quad (2.12)$$

2 Characterization Techniques, Theory and Methods

The first item depends on which fluctuating interaction (dipolar, quadrupolar, or chemical shift) governs the relaxation process. It can be determined numerically from the Hamiltonian parameters governing the static lineshape in the rigid lattice limit. In principle, equation 2.12 allows detailed insight into dynamical processes via temperature- and frequency-dependent measurements of T_1 .

Holcomb *et al.*⁷ have shown that the BPP model is not only suitable for the liquid like diffusion, but also works quite well for atomic diffusion in solids. The self-diffusion coefficient of ions in solids can be calculated by the relationship between the correlation time and the diffusion coefficient. Assuming random translational jump diffusion of atoms in a lattice, the self-diffusion coefficient can be expressed as follows:

$$D = a^2/K\tau_c \quad (2.13)$$

where a is the hopping distance (nearest neighbor distance) and K is the number of possible jump directions. For a solid, K is 6. Commonly, the diffusion process for an ionic conductor is a thermally activated process, following the Arrhenius behavior, which can be expressed as:

$$D = D_0 \cdot e^{-E_a/kT} \quad (2.14)$$

where E_a is the activation energy for diffusion. The relation between the relaxation rate and the diffusion coefficient can be obtained by combining equation 2.13 and 2.14 that leads to a direct relation between the relaxation rate and the diffusion coefficient.

On the high-temperature side, $\omega_0^2 \cdot \tau_c^2 \ll 1$, combining equation 2.12 and 2.13 leads to:

$$\frac{1}{T_1} = \frac{6\gamma^4 \hbar^2 I(I+1)}{5KD a^6} = \frac{6\gamma^4 \hbar^2 I(I+1) e^{E_a/kT}}{5KD_o a^6} \quad (2.15)$$

Then equation 2.15 simplifies to:

$$\ln(T_1^{-1}) = \ln\left[\frac{6\gamma^4 \hbar^2 I(I+1)}{5KD_o a^6}\right] + E_a / kT \quad (2.16)$$

On the low-temperature side, $\omega_o^2 \cdot \tau_c^2 \gg 1$, one obtains:

$$\frac{1}{T_1} = \frac{3\gamma^4 \hbar^2 I(I+1)KD}{5\omega_o^2 a^8} \quad (2.17)$$

$$\ln(T_1^{-1}) = \ln\left[\frac{3\gamma^4 \hbar^2 I(I+1)KD_o}{5\omega_o^2 a^8}\right] - E_a / kT \quad (2.18)$$

Thus, symmetrical curves of $\ln(T_1^{-1})$ vs inverse temperature are expected, with a maximum at the temperature for which $\tau_c \omega_o \approx 1$. In the high-temperature limit, $\tau_c \cdot \omega_o \ll 1$, the SLR rates are proportional to the Li-ion residence time τ_c and in the low-temperature limit, $\tau_c \cdot \omega_o \gg 1$, the SLR rates are proportional to $\tau_c^{-1} \cdot \omega_{o(p)}^{-\beta}$ (with $1 < \beta \leq 2$). In either case, the slopes of the high- and low-temperature regimes of the SLR rates are related to the activation energy for the Li-ion motional process. The original BPP behavior predicts symmetric peaks, *i.e.* $\beta = 2$, in the SLR rate as a function of temperature which does not taking into account correlation effects and disorder in diffusion. Asymmetry of the SLR rates in the high- and low-temperature regimes results from of Li-ion diffusional processes taking place at different length scales. To evaluate this, the value of β can be deduced from the activation energies obtained from the high- and low-temperature flanks.

Additionally, the Li-ion conductivity can be converted from the diffusivity based on the Nernst-Einstein equation⁸:

$$\sigma = \frac{ne^2z^2D}{kT}, \quad (2.19)$$

where n is the charge carrier density of Li-ions, e the elementary charge, z the ionic charge, D the diffusivity, k Boltzmann constant and T the temperature. Thereby, solid-state NMR provides an ion-specific and direct way to determine the bulk mobility of ions in solids, for instance, Li-ions.

Two-dimension (2D) and one-dimension (1D) exchange NMR

Multi-dimensional NMR spectroscopy is a versatile method for characterizing structure and mobility of a variety of chemical systems in the solid state, since the first introduction of 2D NMR measurements.⁹⁻¹² The two-dimensional exchange spectroscopy (EXSY) experiment, which was first reported by Jeener *et al.*¹³, is a powerful tool for observing the atomic and molecular dynamics on the time scales ranging from T_2 to T_1 , allowing to probe the timescales and energy barrier of the ion hopping processes, giving a better insight of the structural constraints that promote or inhibit ionic mobility. Specifically, in this thesis, it provides quantitative information on the Li-ion dynamics between the Li-containing cathode and Li-ion solid electrolytes, providing important information for the development of solid-state batteries. The basic principle of this 2D NMR is the measurement of two time variables (t_1 and t_2), constituting the observed signal, s , which is Fourier transformed to yield a 2D spectrum with two frequency dimensions (ω_1 and ω_2), respectively.¹¹ Specifically, the first $\pi/2$ pulse places the magnetization in the xy -plane where it will precess around the static field at the Larmor frequency. When there are two distinct Li-environments A and B, resonances along the diagonal will

correspond to Li that remains in the same environment, whereas off diagonal resonances will correspond to Li that has moved from A to B and vice versa during the time period of $t = 0$ to $t = t_{\text{mix}}$, as shown in Figure 2.8. Thus 2D-NMR enables to detect changes in the environment of the resonance nucleus between the spectrum before (t_1 -dimension) and after (t_2 -dimension) the mixing time.¹¹ In this way, nuclear mobility can result in off-diagonal intensity. To determine the timescale of chemical exchange from 2D Exchange Spectroscopy (EXSY) measurements in systems undergoing fast ion exchange, the mixing time is varied over a series of experiments and the volume of the crosspeak is measured. An exponential build-up of the crosspeak volume as a function of mixing time is fit to yield a correlation time (τ_c) of the exchange process. An Arrhenius analysis of the inverse correlation time over a variable temperature range produces the energy barrier for the exchange process. Compared with 1D NMR, 2D EXSY provides convincing visual evidence of ion exchange between two sites within a material or between two different materials. To probe the ion exchange by 2D NMR, there are two basic requirements: the spin-relaxation times should be long enough for exchange to take place and there should be a difference in the chemical shift that separates the two resonances. In this thesis, 2D ^7Li NMR was employed to probe the lithium ion exchange between a Li_2S cathode and a $\text{Li}_6\text{PS}_5\text{Br}$ solid electrolyte.

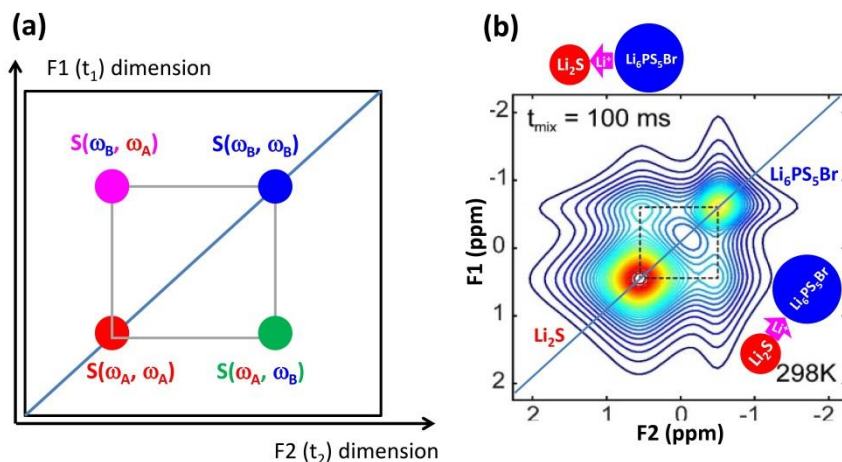


Figure 2.8: (a) Schematic of the 2D EXSY spectrum for two sites, A and B. Diagonal peaks of the A and B signals stored during t_1 are shown as red and blue circles. Crosspeaks evolving from $B \rightarrow A$ and $A \rightarrow B$ exchange are shown as pink and green. (b) The 2D EXSY spectrum for the Li-ion exchange between Li_2S and $\text{Li}_6\text{PS}_5\text{Br}$ at 298 K.

When there is an insufficient difference in chemical shift, 2D EXSY fails. However, if there is a significant difference in linewidth, for instance, due to different dipolar and chemical shift anisotropy, this provides the possibility to perform 1D EXSY NMR. In this case, the broad resonance, reflecting one Li-ion environment, can be filtered away, and this effectively labels the other environment with magnetization. The timescale of depopulation for this environment and population of the other environment is now a direct measure of the ionic transport between the two environments, provided that spin diffusion is excluded. Specifically, in this thesis, Li-ion diffusion from the $\text{Li}_6\text{PS}_5\text{Cl}$ solid electrolyte to the Li_2S positive electrode phase is monitored by the transfer of the magnetization as a function of the mixing time t_{mix} using 1D EXSY NMR, as shown in Figure 2.9. This provides quantitative parameters for the dynamics of the exchange process, such as the exchange diffusion rate D and energy barrier E_a . Similar to the 2D

EXSY NMR experiment, the basic requirement for 1D EXSY NMR is that the spin-lattice relaxation times (T_1) for both resonances is long enough for the exchange to occur.

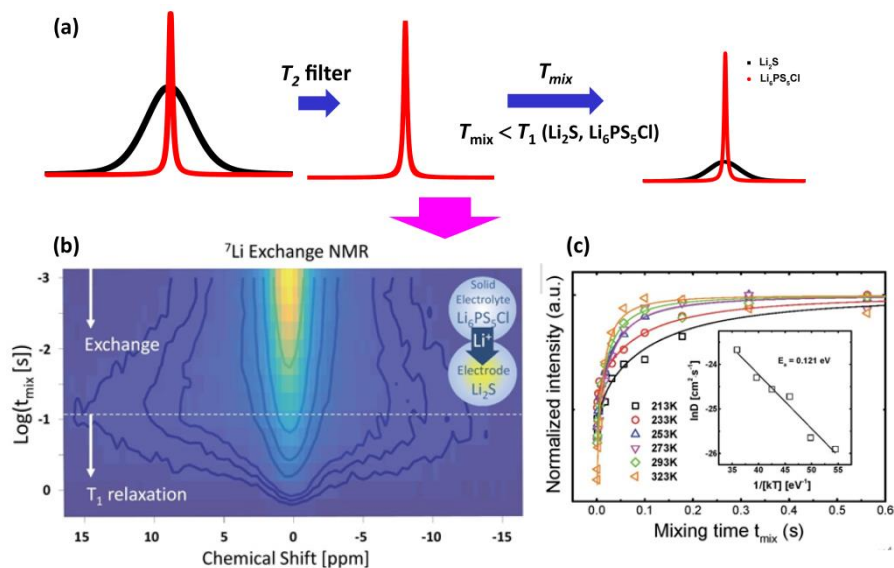


Figure 2.9: (a) Schematic of the 1D EXSY NMR spectra for Li_2S and $\text{Li}_6\text{PS}_5\text{Cl}$ mixture. (b) 1D ${}^7\text{Li}$ - ${}^7\text{Li}$ NMR exchange experiment probing the Li-ion transport from the electrolyte $\text{Li}_6\text{PS}_5\text{Cl}$ phase to the electrode Li_2S phase at room temperature. (c) Normalized intensity of the static Li_2S ${}^7\text{Li}$ NMR spectrum, T_1 corrected, as a function of mixing time at different temperatures. The inset shows the temperature dependence of the diffusion parameter D , derived from the fits representing the diffusion model, see text. An Arrhenius law is used to fit the activation energy, E_a , representing the diffusion process over the boundary between the $\text{Li}_6\text{PS}_5\text{Cl}$ solid electrolyte and the Li_2S phases.

2.4 Cyclic voltammetry (CV)

Cyclic voltammetry is a very versatile electrochemical technique which allows probing the mechanics of redox and transport properties of an electrochemical system, such as batteries, supercapacitors and fuel-cells.¹⁴ Cyclic voltammogram is

2 Characterization Techniques, Theory and Methods

obtained by measuring the current of the system as a response to the potential scan. The voltammogram displays the current (vertical axis) versus the potential (horizontal axis), as shown in Figure 2.10. The important parameters of a cyclic voltammogram are the magnitudes of the anodic and the cathodic peak currents (i_{peak}), the anodic and the cathodic peak potentials (E_{peak}), and the anodic and cathodic peak areas (A_{peak}). The (dis)charge capacity corresponding to the electrochemical processes of, for instance, Li-ion batteries, can be deduced from the peak areas (A_{peak}).¹⁵ The current and voltage difference between the oxidation peaks and reduction peaks is an important parameter to evaluate the reversibility of the electrochemical reactions. The optimal (dis)charge voltage window means that the profiles show the maximum oxidation and reduction areas with excellent reversibility. To reveal the optimum electrochemical window, the same battery should be scanned varying from a narrow to a wide voltage range. In this thesis, cyclic voltammetry is mainly applied to investigate the optimum electrochemical (dis)charge voltage window for the assembled solid-state cells.

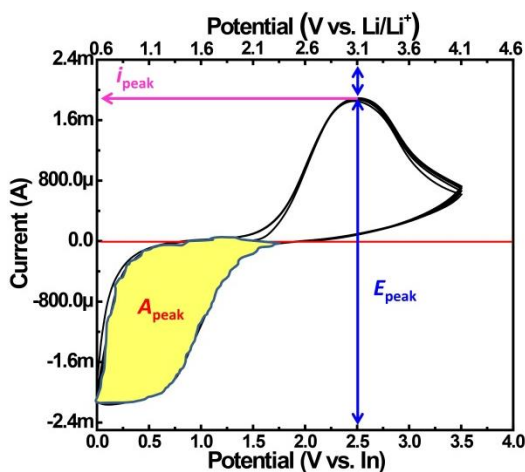


Figure 2.10: CV profiles of $\text{Li}_2\text{S}/\text{Li}_6\text{PS}_5\text{Br}/\text{In}$ all-solid-state lithium batteries with a scan rate of 0.5 mV/s at room temperature.

2.5 Electrochemical Impedances Spectra (EIS)

Electrochemical impedance spectroscopy (EIS) is a perturbative characterization method for the kinetics of electrochemical processes, for instance in Li/Na-ion batteries. It works with first polarizing the battery at a fixed voltage and then applying a small additional voltage to perturb the system. The perturbing voltage oscillates harmonically in time to create an alternating current. The response of the lithium battery is an alternating current having the same frequency and specific amplitude. EIS is a powerful technique to obtain insight into the kinetics in batteries with liquid and solid electrolytes. To analyze the EIS data, a circuit of resistances and capacities is required to represent the charge resistance and capacitive effects of the battery. Thereby, it can be used to evaluate the different resistances against charge transport in batteries. In liquid electrolyte lithium-ion battery system, as shown in Figure 2.11(a), the EIS figure typically consists of two semicircles at the higher frequency side and a tail at the low frequency side. R_b represents the resistance contribution from the electrolyte and cell components, R_{sei} is the resistance of the surface film between electrolyte and electrode, and R_{ct} is related to the resistance of the charge transfer from both the cathode and Li anode, W is the Warburg impedance that is directly related to the Li-ion diffusion process in the electrode and C_i and C_{dl} are the constant phase elements (CPE).¹⁶ The Constant Phase Element (CPE) is a non-intuitive circuit element that was discovered (or *invented*) while looking at the response of real-world systems. For solid-state batteries, impedance spectra typically show two intersection points with the horizontal axis in the high (R_1) and low (R_2) frequency range, as shown in Figure 2.11(b). R_1 reflects the resistance of the solid electrolyte, and (R_2-R_1) reflects the electrode-solid electrolyte interface.¹⁷

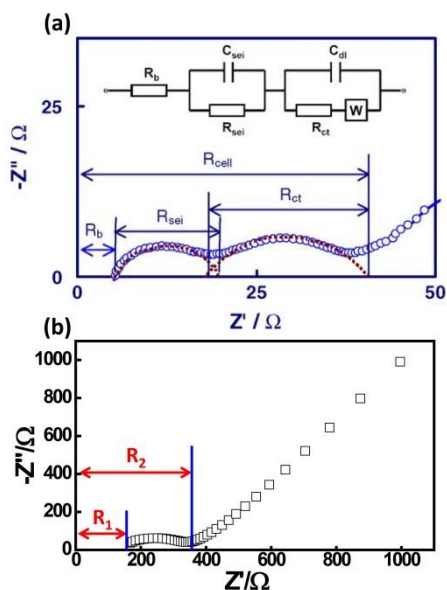


Figure 2.11: (a) Typical EIS spectrum of a lithium ion battery using a liquid electrolyte, including the equivalent circuit used to fit the EIS.¹⁸ (b) Typical EIS spectrum of an all-solid-state lithium ion battery.

References

1. Bragg, W. H.; Bragg, W. L., The Structure of the Diamond. *Proceedings of the Royal Society of London. Series A* **1913**, 89 (610), 277-291.
2. Warren, B. E., *X-ray Diffraction*. Courier Corporation: 1969.
3. Larson, A. C.; Von Dreele, R. B., Gsas. *General Structure Analysis System. LANSCE, MS-H805, Los Alamos, New Mexico* **1994**.
4. Rodriguez-Carvajal, J. In *FULLPROF: a program for Rietveld refinement and pattern matching analysis*, satellite meeting on powder diffraction of the XV congress of the IUCr, Toulouse, France: [sn]: 1990.
5. Irvine, J. T.; Sinclair, D. C.; West, A. R., Electroceramics: characterization by impedance spectroscopy. *Adv Mater* **1990**, 2 (3), 132-138.
6. Bloembergen, N.; Purcell, E. M.; Pound, R. V., Relaxation effects in nuclear magnetic resonance absorption. *Physical review* **1948**, 73 (7), 679.
7. Holcomb, D.; Norberg, R., Nuclear spin relaxation in alkali metals. *Physical Review* **1955**, 98 (4), 1074.
8. Kuhn, A.; Choi, J.-Y.; Robben, L.; Tietz, F.; Wilkening, M.; Heitjans, P., Li Ion Dynamics in Al-Doped Garnet-Type $\text{Li}_7\text{La}_3\text{Zr}_2\text{O}_{12}$ Crystallizing with Cubic

Symmetry. *Zeitschrift für Physikalische Chemie International journal of research in physical chemistry and chemical physics* **2012**, 226 (5-6), 525-537.

9. Wagemaker, M.; Kentgens, A.; Mulder, F., Equilibrium lithium transport between nanocrystalline phases in intercalated TiO₂ anatase. *Nature* **2002**, 418 (6896), 397-399.

10. Wagemaker, M., *Structure and Dynamics of Lithium in Anatase TiO₂*. TU Delft, Delft University of Technology: **2003**.

11. Davis, L. J. Multinuclear NMR Studies of Ion Mobility Pathways in Cathode Materials for Lithium Ion Batteries. **2012**.

12. Aue, W.; Bartholdi, E.; Ernst, R. R., Two-dimensional spectroscopy. Application to nuclear magnetic resonance. *The Journal of Chemical Physics* **1976**, 64 (5), 2229-2246.

13. Jeener, J.; Meier, B.; Bachmann, P.; Ernst, R., Investigation of exchange processes by two-dimensional NMR spectroscopy. *The Journal of chemical physics* **1979**, 71 (11), 4546-4553.

14. Yu, D. Y. W.; Fietzek, C.; Weydanz, W.; Donoue, K.; Inoue, T.; Kurokawa, H.; Fujitani, S., Study of LiFePO₄ by cyclic voltammetry. *J Electrochem Soc* **2007**, 154 (4), A253-A257.

15. Kissinger, P. T.; Heineman, W. R., Cyclic voltammetry. *J. Chem. Educ* **1983**, 60 (9), 702.

16. Yu, C.; Wang, H.; Guan, X.; Zheng, J.; Li, L., Conductivity and electrochemical performance of cathode xLi₂MnO₃·(1-x)LiMn_{1/3}Ni_{1/3}Co_{1/3}O₂ (x= 0.1, 0.2, 0.3, 0.4) at different temperatures. *Journal of Alloys and Compounds* **2013**, 546, 239-245.

17. Huang, B. X.; Yao, X. Y.; Huang, Z.; Guan, Y. B.; Jin, Y.; Xu, X. X., Li₃PO₄-doped Li₇P₃S₁₁ glass-ceramic electrolytes with enhanced lithium ion conductivities and application in all-solid-state batteries. *J Power Sources* **2015**, 284, 206-211.

18. Zhang, S. S.; Xu, K.; Jow, T. R., Electrochemical impedance study on the low temperature of Li-ion batteries. *Electrochim Acta* **2004**, 49 (7), 1057-1061.

3

Synthesis, Structure and Electrochemical Performance of the Argyrodite $\text{Li}_6\text{PS}_5\text{Cl}$ Solid Electrolyte for Li-ion Solid-State Batteries

This chapter is based on the published paper: “*Synthesis, structure and electrochemical performance of the argyrodite $\text{Li}_6\text{PS}_5\text{Cl}$ solid electrolyte for Li-ion solid-state batteries*”, Chuang Yu, Lambert van Eijck, Swapna Ganapathy and Marnix Wagemaker*, [Electrochimica Acta](#), **215**, 93 (2016).

3.1 Introduction

The demand for safe electrical energy storage technologies with high energy density for electric vehicle applications is emerging.¹ Li-ion batteries with organic liquid electrolytes have safety issues due to the potential electrolyte leakage and the inherent flammability.² Unlike liquid electrolytes, solid electrolytes are non-flammable, mitigating most safety issues and in addition, the reduced packaging demands potentially improves the gravimetric and volumetric energy density. However, one of the biggest obstacles for the commercialization of solid electrolytes in all-solid-state batteries is their low ionic conductivity compared to conventional organic liquid electrolytes.²

Numerous efforts have been devoted to finding solid Li-ion conductors with high ionic conductivities, wide electrochemical stability window and excellent chemical stability. For practical battery application, the conductivity of the solid electrolyte needs to exceed 10^{-3} S/cm near room temperature. Intensive research has led to several families of electrolytes, including the sulphides ($\text{Li}_2\text{S-P}_2\text{S}_5$, $\text{Li}_2\text{S-SiS}_2$, $\text{Li}_2\text{S-GeS}_2$)³, the oxides ($\text{Li}_7\text{La}_3\text{Zr}_2\text{O}_{12}$ and $\text{Li}_{3x}\text{La}_{2/3-3x}\text{TiO}_3$)⁴⁻⁵ and the phosphates (LiPON , $\text{Li}_{1+x}\text{Al}_x\text{Ge}_{2-x}(\text{PO}_4)_3$, $\text{Li}_{1+x}\text{Ti}_{2-x}\text{Al}_x(\text{PO}_4)_3$)⁶⁻⁸. Among them, oxides and phosphates display relatively low ionic conductivities, mainly attributed to the high grain boundary resistances.² More recently, there has been a renewed interest in $\text{Li}_{10}\text{GeP}_2\text{S}_{12}$, having a very high ionic conductivity of 10^{-2} S/cm at room temperature.⁹ However, the high costs of the starting material GeS_2 limits its large scale applications. Another important emerging family of solid electrolytes is the Li-argyrodites $\text{Li}_6\text{PS}_5\text{X}$ ($\text{X}=\text{Cl}$, Br and I) with Li-ion conductivities in the range of 10^{-2} - 10^{-3} S/cm at room temperature.¹⁰ In addition to high Li-ion conductivity, $\text{Li}_6\text{PS}_5\text{Cl}$ is reported to have a wide electrochemical window up to 7.0 V vs. Li/Li^+ .¹¹ The conductivities of these materials are comparable to that of $\text{Li}_{10}\text{GeP}_2\text{S}_{12}$. Besides, the much cheaper precursors give this family of materials a

3 Synthesis, Structure and Electrochemical Performance

large potential to be applied in all-solid-state batteries. Boulineau *et al.*¹¹⁻¹² assembled solid state cells using $\text{Li}_6\text{PS}_5\text{Cl}$ as the electrolyte, LiCoO_2 as the cathode, and spinel $\text{Li}_4\text{Ti}_5\text{O}_{12}$ as an anode, exhibiting excellent electrochemical performance. The theoretical capacity of LiCoO_2 , however, is relatively small, motivating research on high capacity electrode materials. Among them, sulphur has attracted much attention in past years because of its high theoretical capacity of 1672 mAh/g, giving a theoretical specific energy of 2500 Wh/kg, making it one of the most promising anode materials for next generation lithium batteries.¹³ However, Li-ion batteries with sulphur in combination with a liquid electrolyte has many problems including short cycle life, low charging efficiency, poor safety, and a high self-discharge rate, all of which are related to the dissolution of lithium polysulfide, the series sulphur reduction intermediates in liquid electrolyte and resulting parasitic reactions.¹⁴⁻¹⁶ By combining sulphur with solid electrolytes, such as Li_3PS_4 ¹⁷ and $\text{Li}_2\text{S-P}_2\text{S}_5$ ¹⁸, the high capacities of sulphur may be better utilized, making this a promising system for future applications. Chen *et al.*¹⁹ combined S with $\text{Li}_6\text{PS}_5\text{Br}$ to construct a solid-state cell, showing an initial discharge capacity of 1355 mAh/g and reversible capacity of 1080 mAh/g after 50 cycles. They attributed the excellent electrochemical performance of the solid-state battery to the small particle size of the active materials.

Rao *et al.*²⁰ reported on the synthesis protocols for argyrodite $\text{Li}_6\text{PS}_5\text{X}$ (X=Cl, Br, I) using high-speed mechanical milling followed by an annealing treatment, resulting in crystalline materials with Li-ion conductivities on the order of 10^{-3} S/cm at room temperature. Using neutron powder diffraction during annealing Rao *et al.*²¹ were able to establish a clear correlation between the annealing temperature and the ionic conductivity. It was concluded that an annealing temperature of at least 250 °C is required to obtain ionic conductivities reaching 10^{-3} S/cm.²¹ With the combined refinement of XRD and Neutron

3 Synthesis, Structure and Electrochemical Performance

Diffraction patterns, Rayavarapy *et al.*²² showed that besides the disorder in the lithium distribution the disorder in the S^{2-}/Cl^- or S^{2-}/Br^- distribution promotes the Li-ion mobility, which is also supported by recent bond-valence analysis calculations.²³ Various studies have been performed to obtain the ionic conductivity in Li_6PS_5X ($X=Cl, Br, I$) using impedance spectroscopy^{10-11, 20-22, 24-25} reporting conductivities varying between 10^{-7} and 10^{-2} S/cm and activation energies varying between 0.11 and 0.56 eV.

Considering the structure and conductivity as a function of the ball mill synthesis route, the present work aims at an optimal synthesis route of Li_6PS_5Cl . Batteries combining Li_2S as the positive electrode, Li_6PS_5Cl as the electrolyte and In as the negative electrode were assembled to determine the optimal dis(charge) window, showing high initial capacities approaching 1500 mAh/g degrading over 20 cycles towards 400 mAh/g.

3.2 Experimental

Reagent-grade Li_2S (99.98%, Sigma-Aldrich), P_2S_5 (99%, Sigma-Aldrich), and $LiCl$ (99.0%, Sigma-Aldrich) crystalline powders were used as starting materials. The required amount of starting materials were ball milled in a WC coated (inner) stainless steel jar with 10 WC balls (8 g/ball) in an Argon filled glovebox ($H_2O, O_2 < 0.3$ ppm) because of the reactivity with oxygen and moisture. The total weight of the mixture was almost 2.0 grams, and the ball milling speed was fixed at 550 rpm. The milling duration was varied to find the optimal milling time. After different milling times, a small amount of powder was collected to perform powder XRD. After the ball milling process, the mixture was sealed in a quartz tube and annealed at 550 °C for 5 hours to obtain the final Li_6PS_5Cl solid electrolyte.

Powder XRD patterns were collected over a 2θ range of 10-160° to identify the crystalline phases of the prepared materials using $Cu_{K\alpha}$ X-rays (1.5406 Å at 45

3 Synthesis, Structure and Electrochemical Performance

kV and 40 mA) on an X'Pert Pro X-ray diffractometer (PANalytical). To prevent reaction with moisture and oxygen the powders were sealed in an airtight XRD sample holder in an Argon filled glove box.

The neutron data were collected on the new neutron powder diffractometer PEARL of the TU Delft.²⁶ Data were collected at room temperature using the (533) reflection of the germanium monochromator ($\lambda = 1.665\text{\AA}$). The sample was loaded under Argon in a 6 mm diameter air-tight vanadium sample can. The sample was measured for 18 hours from 10.4-160 degrees 2θ . The sample is under vacuum during the data collection. The data treatment consisted of a relative correction for detection efficiency of (each of) the 1408 detector pixels and a subtraction of the background, caused by the instrument and the sample can. Rietveld refinement was performed using GSAS.²⁷

Ionic conductivities of the ball-milled powders and the final $\text{Li}_6\text{PS}_5\text{Cl}$ solid electrolyte were measured by preparing pellets of the powder with a diameter of 10 mm. Stainless-steel disks were attached on both faces of the pellets. AC impedance measurements were performed on an Autolab (Autolab PGSTAT302N) in the frequency range of 0.1 Hz to 1 MHz with an applied voltage of 0.05 V.

Laboratory-scale solid-state Li-S batteries were fabricated in the following manners: The S-C composite was obtained firstly by mixing S at 450 rpm for 6 h, Active carbon (Super P, TIMCAL) was added with a weight ratio of 1:1, and the composite was mixed at 500 rpm for 3 h. After that, the ball-milled S-C mixture was sealed in a quartz tube and annealed at 155 °C for 12 h.²⁸ Finally, the obtained S-C composite was mixed with $\text{Li}_6\text{PS}_5\text{Cl}$ and super P with a weight ratio of 4:4:2 and a rotation speed of 450 rpm for 1 h. Then, a two-layer pellet ($d=10\text{mm}$), consisting of 12 mg of the described cathode mixture and 88 mg $\text{Li}_6\text{PS}_5\text{Cl}$ solid electrolyte was pressed together using 6 tons of pressure. After that, a piece of Li-

3 Synthesis, Structure and Electrochemical Performance

In alloy foil (or Li metal, Li-Al alloy) was attached on the other side, this triple-pellet was pressed with 2 tons of pressure for 30 s. The Li-In and Li-Al electrodes were obtained by pressing a piece of Li metal ($\phi = 8$ mm) and a piece of In or Al foil ($\phi = 6$ mm) together. The assembled cell was charged and discharged under a current density of 0.064 mA/cm^2 between 0.4 and 3.0 V to evaluate the electrochemical performance. The test cell was cathode-limited, which means that there was a lithium excess in the Li-In alloy anode. The obtained capacity was normalized by the weight of S in the cathode electrode. The cyclic voltammetry (CV) measurements of the solid-state battery were performed at different voltage windows with a sweep speed of 0.5 mV/s . The electrochemical impedance spectroscopy (EIS) measurements were conducted with an Autolab (Autolab PGSTAT302N) before and after the charge/discharge process in the frequency range of 0.1 Hz and 1 MHz with an applied voltage of 0.05 V.

3.3 Results and discussions

3.3.1 Synthesis, structure and conductivity of argyrodite $\text{Li}_6\text{PS}_5\text{Cl}$

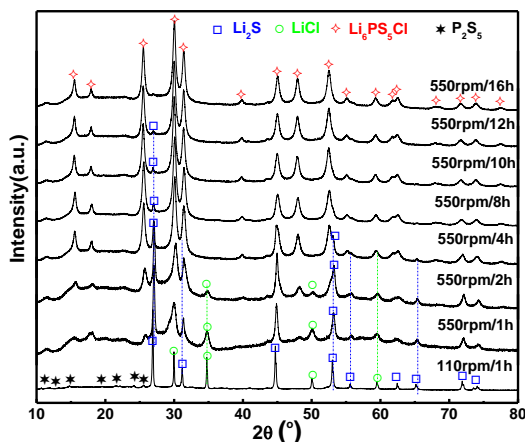


Figure 3.1: XRD patterns of the mixture of Li_2S , P_2S_5 and LiCl powders milled with different times.

Figure 3.1 shows XRD patterns for the mixture prepared by mechanically milling Li_2S , P_2S_5 and LiCl powders from 1 to 16 h. The raw materials were mixed and ball milled at 110 rpm for 1 h to achieve a homogenous mixture. The reflections of the mixture after 1 h milling at 110 rpm are attributable to the starting materials. Subsequently, the ball milling speed was fixed at 550 rpm which was expected to be sufficient for the synthesis, and the mixture was mechanically milled with increasing durations. The intense diffraction peaks at 27.0° , 31.1° , 45.0° , 53.2° , 56.1° , 65.0° , 72.1° and 74.1° can be indexed by the Li_2S structure, while the other diffraction peaks of the pattern are attributed to LiCl . The intensity of diffraction peaks of Li_2S and LiCl gradually decrease with increasing milling durations. After 550 rpm for 4 h, the major peaks of the pattern can be indexed to the $\text{Li}_6\text{PS}_5\text{Cl}$ crystal structure, although a small additional reflection is still visible at 27° which disappears when the milling time is 16 h. No obvious halo pattern was detected, indicating that no significant glassy phase was formed during the milling process. Therefore, the XRD patterns indicate that pure $\text{Li}_6\text{PS}_5\text{Cl}$ was obtained directly by precipitation of the raw materials using mechanical milling. The above XRD results indicate that the $\text{Li}_6\text{PS}_5\text{Cl}$ phase is formed after milling at 550 rpm for 4 h, after which the patterns remain almost unchanged. The impedance spectra and resulting conductivities in Figure 3.2 show that the resistance of the pressed pellet decreases with increasing milling time resulting in a higher Li^+ conductivity of the mixture as shown in Figure 3.2b.

3 Synthesis, Structure and Electrochemical Performance

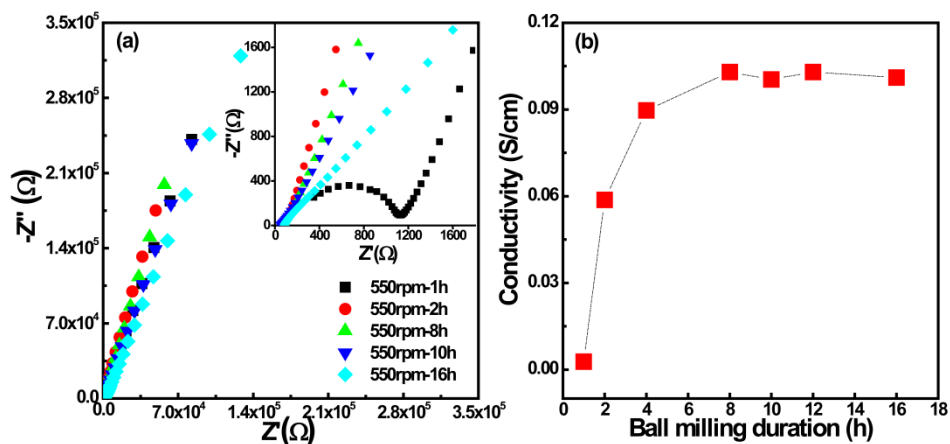


Figure 3.2: (a) Complex impedance plots for the sample ball milled for different durations. The inset shows the results at small Ω (0 to 1700 Ω). (b) The conductivity of the ball-milled samples vs. the milling times.

As shown in Figure 3.2b, the mixture displays very low ionic conductivity after milling for less than 2 hours, most likely caused by the poor ionic conductivity of the starting materials. The XRD results indicate that after 1 and 2 hours milling at 550 rpm a considerable amount of Li_2S is present. Longer milling times increase the conductivity until the conductivity remains almost unchanged after 8 hours of milling. The present results show that the ionic conductivity does not improve after 8 hours of milling, which is shorter than the durations Boulineau *et al.*¹¹ reported. Interestingly, Boulineau *et al.*¹¹ report that the conductivity of the mixture decreases after an optimum milling duration of 10 hours whereas the present results show an unchanged conductivity between 8 and 16 hours of milling. A possible explanation is that during the milling process in the present work the jar was opened every hour to grind the mixture by hand to promote the homogeneity of the mixture. This may also explain the relative short milling time to obtain the $\text{Li}_6\text{PS}_5\text{Cl}$ phase which is also much shorter than reported by Rao *et al.*²⁰, applying the same rotating speed during milling.

3 Synthesis, Structure and Electrochemical Performance

For the present research, the mixture milled for 16h was chosen as the material for further research, the Li^+ ion conductivity of which is 1.0×10^{-3} S/cm. To improve the conductivity further this material was annealed at 550°C for 5 h to increase the crystallinity and to create better grain boundary contact between the $\text{Li}_6\text{PS}_5\text{Cl}$ particles. The XRD pattern of the annealed $\text{Li}_6\text{PS}_5\text{Cl}$ material indicates a more crystalline argyrodite phase compared to the material prepared by direct precipitation (see Figure 3.3(a)). Due to the annealing, the Li^+ ion conductivity as measured by impedance spectroscopy increases to 1.1×10^{-3} S/cm (see Figure 3.3(b)), a value close to that reported by Boulineau *et al.*¹¹ and Rao *et al.*²⁰

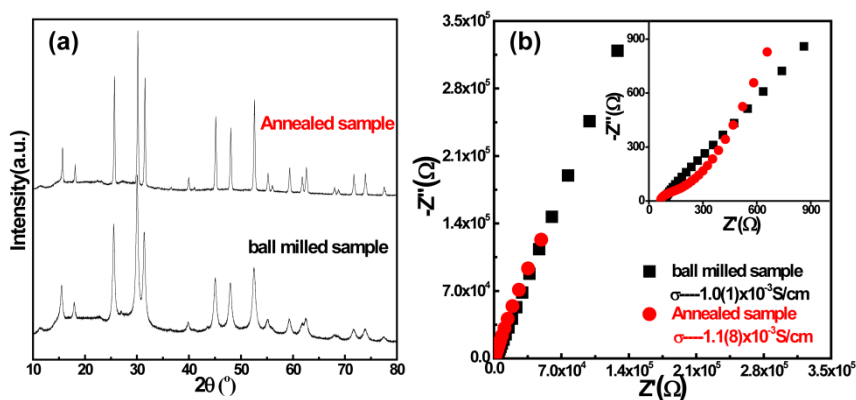


Figure 3.3: (a) XRD patterns of the ball milled mixture and the sample after heat treatment. (b) Room temperature AC impedance results of $\text{Li}_6\text{PS}_5\text{Cl}$ before and after heat treatment.

The X-ray powder diffraction and Neutron diffraction powder patterns of $\text{Li}_6\text{PS}_5\text{Cl}$ (after annealing at 550°C for 5 h) were simultaneously refined using the Rietveld method as implemented in GSAS²⁹⁻³⁰, the patterns and fits are shown in Figure 3.4. Refinement to the cubic $F-43m$ phase results in excellent fits. The resulting atomic parameters are listed in Table 3.1. During the simultaneous Rietveld refinement of the XRD and ND patterns both the sum of the occupancies

3 Synthesis, Structure and Electrochemical Performance

on the $4a$ site (S and Cl) and on the $4c$ sites (S and Cl) was constraint to 1, thereby assuming no vacancies on these sites, and the mean square displacement (U_{iso}) of both atoms on the same site was coupled. The occupancies on the $4b$ and $16e$ sites were not fitted and set to its stoichiometric value. The Li-ion occupancy and isotropic displacement parameters on the $48h$ site were fitted without constraints. The resulting large isotropic displacement parameter reflects the high room temperature mobility of the Li-ion. The results of the Rietveld refinement in Table 3.1 indicate a stoichiometry of $\text{Li}_{5.6}\text{PS}_{4.8}\text{Cl}_{1.2}$, having a slightly larger degree of substitution of S with Cl, consistently leading to more charge compensated Li-ion vacancies compared to the intended $\text{Li}_6\text{PS}_5\text{Cl}$ stoichiometry. In agreement with Rao *et al.*²⁰⁻²¹ a larger Cl occupancy is found on the Cl(1) site, with almost 60% of the Cl occupying the Cl(1) site, the distribution of the Cl dopant over the two sites has been suggested to be a prerequisite for the high conductivity along with the crystallinity.²⁰

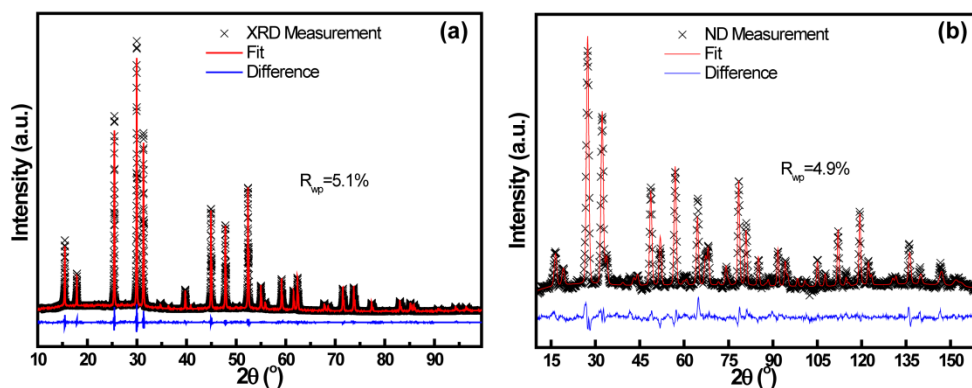


Figure 3.4: (a) X-ray Powder and (b) Neutron Powder diffraction pattern of $\text{Li}_6\text{PS}_5\text{Cl}$ at room temperature (after annealing at $550\text{ }^\circ\text{C}$ for 5 h) simultaneously refined by Rietveld refinement.

3 Synthesis, Structure and Electrochemical Performance

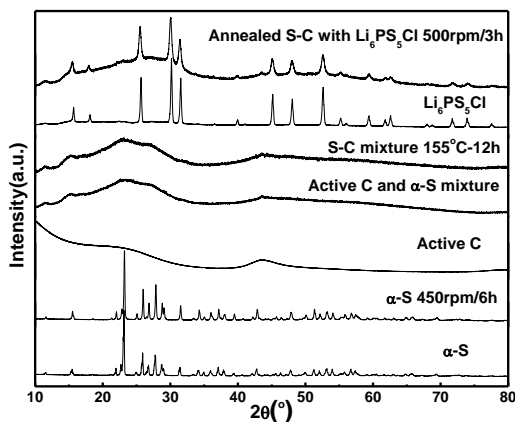


Figure 3.5: XRD patterns of pristine sulphur, active C, ball-milled sulphur, S-C composite and S-C- $\text{Li}_6\text{PS}_5\text{Cl}$ composite.

Table 3.1: Lattice parameter, fractional atomic coordinates, isotropic atomic displacement parameters (U_{iso}) and site occupancies resulting from the simultaneous Rietveld refinement of cubic $\text{Li}_6\text{PS}_5\text{Cl}$ at room temperature.

	Atom	Fractional coordinates			Wyckoff	Occupancy	U_{iso} (\AA^2)
		X	Y	z			
	Li	0.1766	0.1766	0.0224	48h	0.47	0.0666
$\text{Li}_6\text{PS}_5\text{Cl}$	P	0.5	0.5	0.5	4b	1.00	0.0181
$F-43m$	S(1)	0.6205	0.6205	0.6205	16e	1.00	0.0310
$a=9.8290 \text{ \AA}$	S(2)	0.25	0.25	0.25	4c	0.29	0.0382
	Cl(2)	0.25	0.25	0.25	4c	0.71	0.0382
	S(3)	0.0	0.0	0.0	4a	0.48	0.0383
	Cl(1)	0.0	0.0	0.0	4a	0.52	0.0383

3.3.2 Preparation of all-solid-state cells and electrochemical tests

For sulphide solid electrolytes, such as $\text{Li}_7\text{P}_3\text{S}_{11}$ and argyrodite $\text{Li}_6\text{PS}_5\text{X}$ ($\text{X}=\text{I}, \text{Cl}, \text{Br}$), In is typically applied as negative electrode material because of the electrochemical instability of sulphide electrolytes towards Li-metal.³¹⁻³² To investigate the influence of different negative electrode materials, Li metal, Li-Al alloy and Li-In were prepared in combination with the prepared $\text{Li}_6\text{PS}_5\text{Cl}$ solid electrolyte and C-S positive electrode mixtures, respectively. Figure 3.5 shows the XRD patterns of the pristine sulphur, sulphur-carbon composite and the mixture of $\text{Li}_6\text{PS}_5\text{Cl}$ and sulphur-carbon composite. The diffraction peaks of the pristine sulphur and ball milled sulphur can be indexed by the orthorhombic α -S phase. Active carbon was selected based on its high BET surface. The XRD patterns of the ball milled mixture of active carbon and α -S before and after annealing at 155 °C reflect the highly amorphous nature of the mixture. The low viscosity of sulphur at 155 °C makes it easily penetrate into the channels of the active carbon.²⁸ Subsequent annealing most likely improves the contact of the active carbon with the sulphur, improving the conductivity of the composite. The carbon-sulphur composite and the $\text{Li}_6\text{PS}_5\text{Cl}$ powder material were mixed and mechanically milled to form a homogenous composite cathode mixture where XRD indicates no other crystalline phases after mixing. To explore the electrochemical stability of the negative electrode-electrolyte combinations and the cyclability of the solid-state cells, the CV measurements were performed between different voltage sweep windows. For Li-metal as negative electrode, it is observed that when the voltage exceeds 2.2 V vs. Li/Li^+ , the current stabilizes with increasing voltage, as shown in Figure 3.6(a), indicating that the Li- $\text{Li}_6\text{PS}_5\text{Cl}$ interface is electrochemically unstable. To verify this is indeed caused by an electrochemical reaction, the chemical stability between Li metal and $\text{Li}_6\text{PS}_5\text{Cl}$ was also investigated. Li-metal and $\text{Li}_6\text{PS}_5\text{Cl}$ was mixed by hand with a mortar and pestle in an Argon glovebox, with the same weight ratio as the solid-state cell, and the mixture was subjected to

XRD in an airtight holder. The diffraction peaks of the mixture are attributed to Li-metal and $\text{Li}_6\text{PS}_5\text{Cl}$, suggesting that Li metal is chemically stable with the $\text{Li}_6\text{PS}_5\text{Cl}$ solid electrolyte at room temperature (Figure 3.6(b)). This implies that the Li- $\text{Li}_6\text{PS}_5\text{Cl}$ is electrochemically unstable above 2.2 V vs. Li/Li^+ thereby restricting the application of Li-metal in combination with $\text{Li}_6\text{PS}_5\text{Cl}$ to low potential positive electrode materials such as spinel $\text{Li}_4\text{Ti}_5\text{O}_{12}$ and Si, and excluding high potential positive electrode materials such as olivine-type, spinel-type, layered-type, S and Li_2S .

3 Synthesis, Structure and Electrochemical Performance

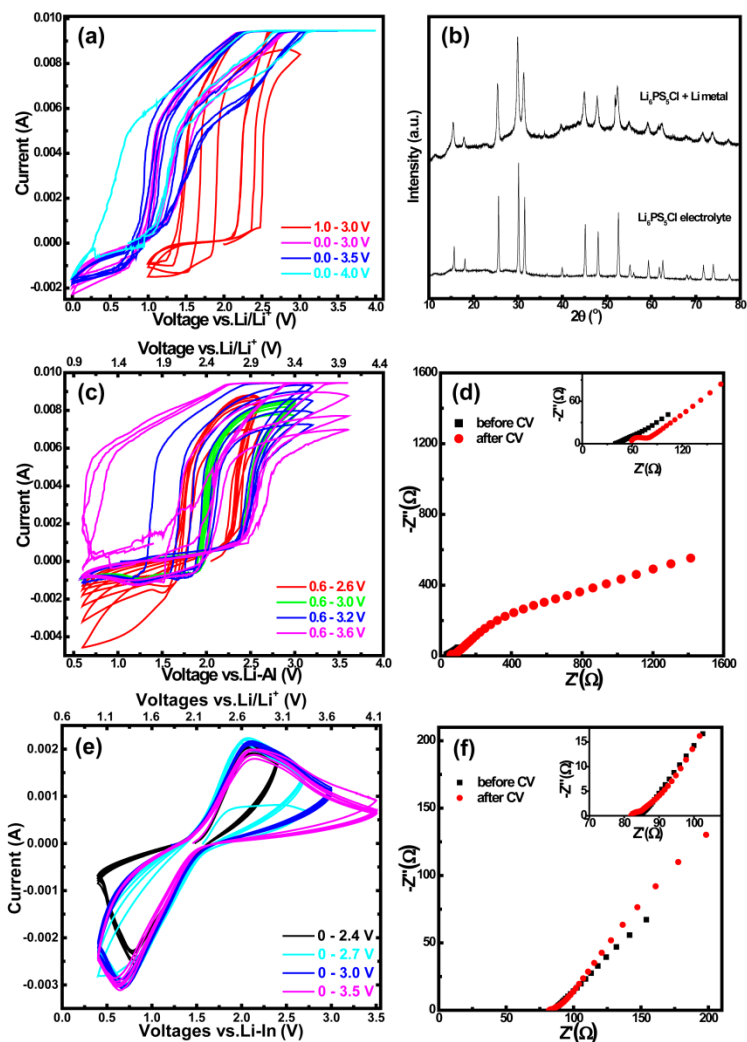


Figure 3.6: (a) The Cyclic voltammograms of the all-solid-state $S/Li_6PS_5Cl/Li$ batteries in voltage ranges from 1.0 to 3.0, 0 to 3.0 V, 0 to 3.5 V, and 0 to 4.0 V (vs. Li/Li^+) at a scanning rate of 0.5 mV/s. (b) XRD patterns of Li_6PS_5Cl electrolyte and the mixture of Li_6PS_5Cl and Li metal prepared by hand grinding. (c) Cyclic voltammograms of the all-solid-state $S/Li_6PS_5Cl/Li-Al$ batteries in voltage ranges from 0.6 to 2.6, 3.0, 3.2 and 3.6 V (vs. $Li-Al$) at a scanning rate of 0.5 mV/s. (d) Room temperature impedances of solid-state Li battery with $Li-Al$ anode before and after a CV measurement. (e) The Cyclic

3 Synthesis, Structure and Electrochemical Performance

voltammograms of the S-C/Li₆PS₅Cl/Li-In all-solid-state batteries for different voltage cut-off ranges 0.4 to 2.4, 2.7, 3.0 and 3.5 V (vs. Li-In), at a scanning rate of 0.5 mV/s. The bottom voltage axis shows the values of the voltage versus Li-In, the top voltage axis shows the corresponding values of voltage versus Li/Li⁺. (f) Room temperature impedance of a solid-state Li battery with Li-In anode before and after a CV measurement.

Additionally, a Li-Al alloy was used as a negative electrode where the CV tests display no obvious cathodic and anodic peaks, as shown in Figure 3.6(c). The intensity of the oxidation and reduction peaks decreased dramatically with increasing cycling numbers except when setting a sweep potential window between 0.6 and 3.0 V (vs. Li-Al). Impedance spectroscopy of the S-C/Li₆PS₅Cl/Li-Al battery before and after the CV experiments with the best performing potential window of 0.6 and 3.0 V (vs. Li-Al) shows a dramatic increase in the internal resistance (Figure 3.6(d)). Figure 3.6(e) shows the CV curves of the solid-state S/Li₆PS₅Cl battery using the Li-In alloy as negative electrode material for 6 cycles with various potential windows at a scan rate of 0.5 mV/s. An anodic peak can be observed around 2.0 V (vs. Li-In), corresponding to 2.62 V (vs. Li/Li⁺) representing the oxidation of Li₂S to lower order poly-sulphides and the cathodic peak at 0.75 V (vs. Li-In), corresponding to 1.35 V (vs. Li/Li⁺) representing the reduction of S to higher order poly-sulphides. The intensity of the cathodic and anodic peaks can be attributed to the discharge and charge capacities, and the differences between the two are an indication of the cycling efficiency. From Figure 3.6(e), it is observed that the potential window of 0.4 to 3.0 V (vs. Li-In) results in the best cycling performance. With increasing sweep potential window, the differences between the cathodic and anodic peak becomes larger, indicating an increasing polarization of the solid-state Li-S battery. In contrast to the results for the Li-Al negative electrode shown in Figure 3.6(d), the comparison of the impedance spectroscopy before and after the CV experiments in the optimal voltage window 0.4 - 3.0 V (vs. Li-In) suggests that the charge transport kinetics is

3 Synthesis, Structure and Electrochemical Performance

hardly affected by the cycling, as shown in Figure 3.6(f). In combination with the better cyclability, this indicates that Li-In is a more suitable negative electrode for a solid-state battery combining $\text{Li}_6\text{PS}_5\text{Cl}$ and S-C.

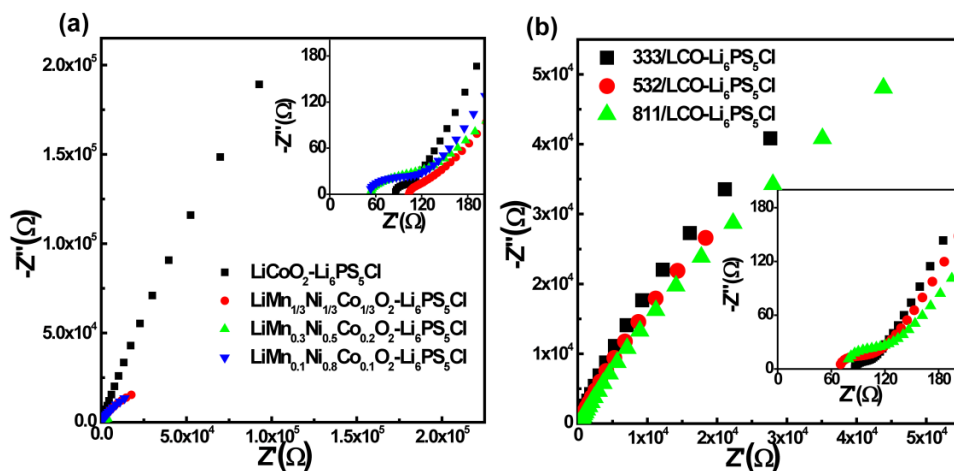


Figure 3.7: Room temperature impedances of $\text{Li}_6\text{PS}_5\text{Cl}$ with various kinds of layered-type cathode materials.

Finally, the potential application of $\text{Li}_6\text{PS}_5\text{Cl}$ with other common cathode materials was also investigated, which is shown in Figure 3.7. Layered-type $\text{LiNi}_x\text{Mn}_y\text{Co}_{1-x-y}\text{O}_2$ ($0 < (x, y) < 1$) and its analogues were mixed with $\text{Li}_6\text{PS}_5\text{Cl}$ and then measured with impedance spectroscopy. The mixture shows an extremely low resistance, indicating that $\text{Li}_6\text{PS}_5\text{Cl}$ is an excellent candidate solid electrolyte by combining it with layered cathode materials in an all-solid-state cell.

To test the cyclability, the S-C/ $\text{Li}_6\text{PS}_5\text{Cl}$ /Li-In solid state battery was galvanostatically cycled, with a current of 0.064 mA/cm^2 , between the optimal potential window of 0.4 and 3.0 V (vs. Li-In) as shown in Figure 3.8(a-b). After an initial activation cycle, the discharge capacities of the second and third cycles result in 1388.5 and 1459.0 mAh/g respectively, slightly below the theoretical

capacity of Sulphur 1600 mAh/g¹³. The charge capacities of the second and third cycle are larger than the discharge capacities potentially, indicating that the cathode mixture also participates in the electrochemical reaction during the initial cycles, which was also observed by Nagao *et al.*³³ After the very high capacities during the first few cycles, it decreases quickly in the subsequent cycles towards 389 mAh/g after 20 cycles. Comparison of the impedance spectrum between the fresh cell and after 20 cycles, shown in Figure 3.8(c), it exhibits two intersections with the Z' axis, R_1 at the high frequency side (left side of horizontal axis), and R_2 at the low frequency side (right side of horizontal axis) representing the resistance of the solid electrolyte and the total resistance of the solid-state cell (solid electrolyte and electrode-solid electrolyte interface), respectively. The resistance from the electrode-solid electrolyte interface part can be calculated by subtracting R_1 from R_2 .³⁴ For pristine, uncycled, solid-state cell this results in 82.7 and 4.5 Ω for the solid electrolyte interface and the resistance of the electrode-solid electrolyte interface, respectively. The corresponding values for the cell after 20 cycles increase towards 178.8 and 31.2 Ω , respectively. In particular, the large increase in the resistance of the electrode-solid electrolyte interface may indicate a loss in contact of the electrode with the solid electrolyte due to the large changes in electrode volume of both sulphur and Li-In.

3 Synthesis, Structure and Electrochemical Performance

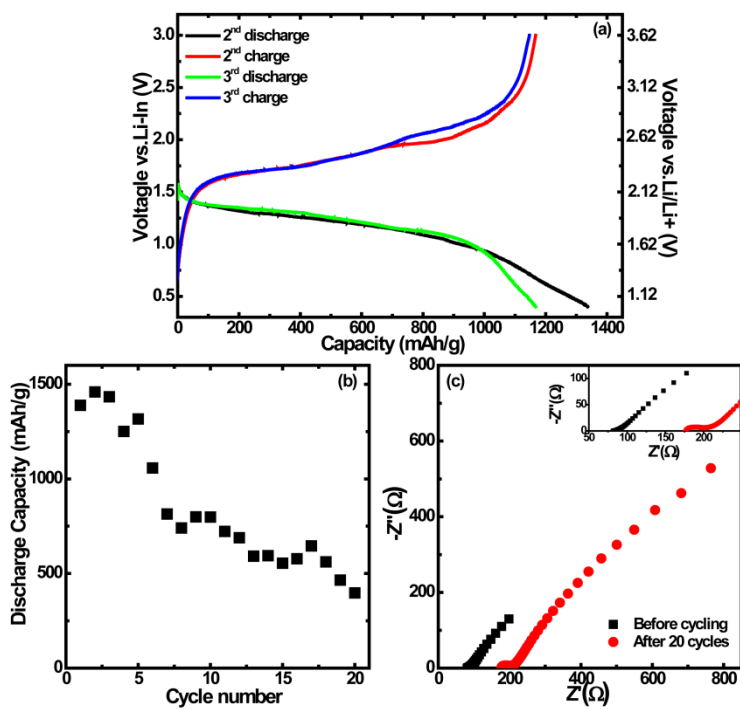


Figure 3.8: (a) The 2nd and 3rd charge/discharge galvanostatic voltage curves for the assembled all-solid-state C-S/Li₆PS₅Cl/Li-In battery. The initial cycle to activate the battery is not shown here. The (dis)charge current density is 0.064 mA/cm² and the cut-off potentials are set at 0.4 and 3.0 V (vs. Li-In). (b) Evolution of the capacity as a function of cycle number. (c) The electrochemical impedance spectra of the pristine solid-state C-S/Li₆PS₅Cl/Li-In cell and after 20 cycles.

3.4 Conclusions

The excellent Li-ion conductor Li₆PS₅Cl, reaching an ionic conductivity of 10⁻³ S/cm at room temperature, was obtained directly from mechanical milling at room temperature at 550 rpm for 8 hours. After heat-treatment at 550 °C, the Li₆PS₅Cl material displays a slightly higher ionic conductivity most likely due to the improved crystallinity. Cyclic voltammetry measurements demonstrate that Li metal is not suitable as negative electrode material for the Li₆PS₅Cl based solid-

state cells displaying unstable electrochemical reactions above 2.2 V (vs. Li/Li⁺). Also, Li-Al results in poor electrochemical performance as the internal resistance quickly rises upon cycling. The best negative electrode candidate tested is Li-In displaying relatively good reversibility and cyclability. The pressed C-S/Li₆PS₅Cl/Li-In cell delivers initial capacities above 1300 mAh/g decreasing below 400 mAh/g after 20 cycles. Impedance spectroscopy indicates that the poor cyclability of the solid-state cell is mainly caused by the increase of interface resistance between the solid-electrolyte and cathode mixture during cycling, which is most likely a consequence of the large volume changes of the sulphur and Li-In electrodes.

References

1. Etacheri, V.; Marom, R.; Elazari, R.; Salitra, G.; Aurbach, D., Challenges in the development of advanced Li-ion batteries: a review. *Energ Environ Sci* **2011**, *4* (9), 3243-3262.
2. Fergus, J. W., Ceramic and polymeric solid electrolytes for lithium-ion batteries. *J Power Sources* **2010**, *195* (15), 4554-4569.
3. Murayama, M.; Sonoyama, N.; Yamada, A.; Kanno, R., Material design of new lithium ionic conductor, thio-LISICON, in the Li₂S-P₂S₅ system. *Solid State Ionics* **2004**, *170* (3), 173-180.
4. Thangadurai, V.; Narayanan, S.; Pinzaru, D., Garnet-type solid-state fast Li ion conductors for Li batteries: critical review. *Chemical Society Reviews* **2014**, *43* (13), 4714-4727.
5. Ihlefeld, J. F.; Clem, P. G.; Doyle, B. L.; Kotula, P. G.; Fenton, K. R.; Apblett, C. A., Fast Lithium-Ion Conducting Thin-Film Electrolytes Integrated Directly on Flexible Substrates for High-Power Solid-State Batteries. *Adv Mater* **2011**, *23* (47), 5663-5667.
6. Jacke, S.; Song, J.; Dimesso, L.; Brötz, J.; Becker, D.; Jaegermann, W., Temperature dependent phosphorous oxynitride growth for all-solid-state batteries. *J Power Sources* **2011**, *196* (16), 6911-6914.
7. Mariappan, C. R.; Yada, C.; Rosciano, F.; Roling, B., Correlation between micro-structural properties and ionic conductivity of Li_{1.5}Al_{0.5}Ge_{1.5}(PO₄)₃ ceramics. *J Power Sources* **2011**, *196* (15), 6456-6464.

8. Wang, S.; Ben, L.; Li, H.; Chen, L., Identifying Li⁺ ion transport properties of aluminum doped lithium titanium phosphate solid electrolyte at wide temperature range. *Solid State Ionics* **2014**, *268*, Part A, 110-116.
9. Kamaya, N.; Homma, K.; Yamakawa, Y.; Hirayama, M.; Kanno, R.; Yonemura, M.; Kamiyama, T.; Kato, Y.; Hama, S.; Kawamoto, K.; Mitsui, A., A lithium superionic conductor. *Nature Materials* **2011**, *10* (9), 682-686.
10. Deiseroth, H.-J.; Kong, S.-T.; Eckert, H.; Vannahme, J.; Reiner, C.; Zaiß, T.; Schlosser, M., Li₆PS₅X: A Class of Crystalline Li-Rich Solids With an Unusually High Li⁺ Mobility. *Angewandte Chemie International Edition* **2008**, *47* (4), 755-758.
11. Boulineau, S.; Courty, M.; Tarascon, J.-M.; Viallet, V., Mechanochemical synthesis of Li-argyrodite Li₆PS₅X (X = Cl, Br, I) as sulfur-based solid electrolytes for all solid state batteries application. *Solid State Ionics* **2012**, *221*, 1-5.
12. Boulineau, S.; Tarascon, J.-M.; Leriche, J.-B.; Viallet, V., Electrochemical properties of all-solid-state lithium secondary batteries using Li-argyrodite Li₆PS₅Cl as solid electrolyte. *Solid State Ionics* **2013**, *242*, 45-48.
13. Manthiram, A.; Chung, S. H.; Zu, C., Lithium-Sulfur Batteries: Progress and Prospects. *Adv Mater* **2015**, *27* (12), 1980-2006.
14. Choi, J.-W.; Kim, J.-K.; Cheruvally, G.; Ahn, J.-H.; Ahn, H.-J.; Kim, K.-W., Rechargeable lithium/sulfur battery with suitable mixed liquid electrolytes. *Electrochim Acta* **2007**, *52* (5), 2075-2082.
15. Zhang, S. S., Liquid electrolyte lithium/sulfur battery: Fundamental chemistry, problems, and solutions. *Journal of Power Sources* **2013**, *231*, 153-162.
16. Wild, M.; O'Neill, L.; Zhang, T.; Purkayastha, R.; Minton, G.; Marinescu, M.; Offer, G. J., Lithium sulfur batteries, a mechanistic review. *Energy & Environmental Science* **2015**, *8* (12), 3477-3494.
17. Lin, Z.; Liu, Z.; Dudney, N. J.; Liang, C., Lithium Superionic Sulfide Cathode for All-Solid Lithium-Sulfur Batteries. *ACS Nano* **2013**, *7* (3), 2829-2833.
18. Agostini, M.; Aihara, Y.; Yamada, T.; Scrosati, B.; Hassoun, J., A lithium-sulfur battery using a solid, glass-type P₂S₅-Li₂S electrolyte. *Solid State Ionics* **2013**, *244*, 48-51.
19. Chen, M.; Adams, S., High performance all-solid-state lithium/sulfur batteries using lithium argyrodite electrolyte. *J Solid State Electr* **2015**, *19* (3), 697-702.
20. Rao, R. P.; Adams, S., Studies of lithium argyrodite solid electrolytes for all-solid-state batteries. *physica status solidi (a)* **2011**, *208* (8), 1804-1807.
21. Rao, R. P.; Sharma, N.; Peterson, V. K.; Adams, S., Formation and conductivity studies of lithium argyrodite solid electrolytes using in-situ neutron diffraction. *Solid State Ionics* **2013**, *230*, 72-76.

22. Rayavarapu, P.; Sharma, N.; Peterson, V.; Adams, S., Variation in structure and Li⁺-ion migration in argyrodite-type Li₆PS₅X (X = Cl, Br, I) solid electrolytes. *J Solid State Electr* **2012**, *16* (5), 1807-1813.
23. Chen, H. M.; Maohua, C.; Adams, S., Stability and ionic mobility in argyrodite-related lithium-ion solid electrolytes. *Physical Chemistry Chemical Physics* **2015**, *17* (25), 16494-16506.
24. Deiseroth, H.-J.; Maier, J.; Weichert, K.; Nickel, V.; Kong, S.-T.; Reiner, C., Li₇PS₆ and Li₆PS₅X (X: Cl, Br, I): Possible Three-dimensional Diffusion Pathways for Lithium Ions and Temperature Dependence of the Ionic Conductivity by Impedance Measurements. *Zeitschrift für anorganische und allgemeine Chemie* **2011**, *637* (10), 1287-1294.
25. Pecher, O.; Kong, S.-T.; Goebel, T.; Nickel, V.; Weichert, K.; Reiner, C.; Deiseroth, H.-J.; Maier, J.; Haarmann, F.; Zahn, D., Atomistic Characterisation of Li⁺ Mobility and Conductivity in Li_{7-x}PS_{6-x}I_x Argyrodites from Molecular Dynamics Simulations, Solid-State NMR, and Impedance Spectroscopy. *Chemistry-a European Journal* **2010**, *16* (28), 8347-8354.
26. van Eijck, L.; Cussen, L.; Sykora, J.; Schooneveld, E.; Rhodes, N.; van Well, A. A.; Pappas, C., Design and Performance of a Novel Neutron Powder Diffractometer: PEARL at TU Delft. *Journal of Applied Crystallography* **2016**, *Submitted*.
27. Larson, A. C. *GSAS*; Los Alamos National Laboratory: 1994.
28. Li, G.-C.; Li, G.-R.; Ye, S.-H.; Gao, X.-P., A Polyaniline-Coated Sulfur/Carbon Composite with an Enhanced High-Rate Capability as a Cathode Material for Lithium/Sulfur Batteries. *Advanced Energy Materials* **2012**, *2* (10), 1238-1245.
29. Rietveld, H., Line profiles of neutron powder-diffraction peaks for structure refinement. *Acta Crystallographica* **1967**, *22* (1), 151-152.
30. Rietveld, H., A profile refinement method for nuclear and magnetic structures. *Journal of Applied Crystallography* **1969**, *2* (2), 65-71.
31. Takada, K., Progress and prospective of solid-state lithium batteries. *Acta Materialia* **2013**, *61* (3), 759-770.
32. Wenzel, S.; Randau, S.; Leichtweiß, T.; Weber, D. A.; Sann, J.; Zeier, W. G.; Janek, J., Direct Observation of the Interfacial Instability of the Fast Ionic Conductor Li₁₀GeP₂S₁₂ at the Lithium Metal Anode. *Chemistry of Materials* **2016**, *28* (7), 2400-2407.
33. Nagao, M.; Hayashi, A.; Tatsumisago, M., High-capacity Li₂S-nanocarbon composite electrode for all-solid-state rechargeable lithium batteries. *Journal of Materials Chemistry* **2012**, *22* (19), 10015-10020.
34. Huang, B.; Yao, X.; Huang, Z.; Guan, Y.; Jin, Y.; Xu, X., Li₃PO₄-doped Li₇P₃S₁₁ glass-ceramic electrolytes with enhanced lithium ion conductivities and

3 Synthesis, Structure and Electrochemical Performance

application in all-solid-state batteries. *Journal of Power Sources* **2015**, *284*, 206-211.

4

Unravelling Li-Ion Transport from Pico-seconds to Seconds, Bulk versus Interfaces in An Argyrodite $\text{Li}_6\text{PS}_5\text{Cl-Li}_2\text{S}$ All-Solid-State Li-Ion Battery

This chapter is based on the published paper: “*Unravelling Li-ion transport from pico-seconds to seconds, bulk versus interfaces in an argyrodite $\text{Li}_6\text{PS}_5\text{Cl-Li}_2\text{S}$ all-solid-state Li-ion battery*”, Chuang Yu, Swapna Ganapathy, Niek J. J. de Klerk, Irek Roslon, Ernst R. H. van Eck, Arno P. M. Kentgens and Marnix Wagemaker*, [Journal of The American Chemical Society](#), **138**, 11192(2016).

4.1 Introduction

The demand for safe electrical energy storage technologies with high energy density for electric vehicle applications is rapidly increasing.¹ All-solid-state Li-ion batteries are appealing because replacing the flammable organic electrolyte in Li-ion batteries with a solid electrolyte will inherently improve battery safety.²⁻⁹ This has the additional advantage of less stringent packaging demands, potentially leading to higher energy densities and allowing more design freedom.^{2-3, 6, 8} The challenge is to develop solid electrolyte materials combining a high conductivity with large chemical and electrochemical stability.^{2-6, 9-10} Current liquid electrolytes have conductivities around 10^{-2} S/cm with a transference number close to 0.5. For solid electrolytes having a transference number close to unity, this means that a bulk conductivity between 10^{-2} and 10^{-3} S/cm is required. In addition to a high electrolyte conductivity, another prerequisite is a facile charge transfer reaction of the Li-ion over the electrolyte-electrode interface.¹⁰ Compared to the electrode - liquid electrolyte interface in Li-ion batteries this poses a considerable challenge, not only due to potential chemical and electrochemical instabilities, but also establishing a good contact and maintaining this during the volumetric changes of the electrode materials upon battery cycling. In addition, space charges driven by the potential difference between the positive electrode and electrolyte may lead to local Li-ion depletion of the electrolyte, posing an additional hurdle for Li-ion transport over the solid-solid electrode-electrolyte interface.^{6, 11-12}

Intensive research efforts have led to several families of excellent solid Li-ion conductors including the sulphides ($\text{Li}_2\text{S-P}_2\text{S}_5$, $\text{Li}_2\text{S-SiS}_2$, $\text{Li}_2\text{S-GeS}_2$)¹³⁻²⁰, oxides ($\text{Li}_7\text{La}_3\text{Zr}_2\text{O}_{12}$ and $\text{Li}_{3x}\text{La}_{2/3-3x}\text{TiO}_3$)²¹⁻²³ and phosphates (LiPON , $\text{Li}_{1+x}\text{Al}_x\text{Ge}_{2-x}(\text{PO}_4)_3$, $\text{Li}_{1+x}\text{Ti}_{2-x}\text{Al}_x(\text{PO}_4)_3$)²⁴⁻²⁹. Generally, the chemically stable oxides and phosphates display relatively low ionic conductivity and high grain boundary resistances.⁴ Sulphides generally offer higher conductivities¹⁰ and their relatively low melting temperatures compared to the oxides and phosphates

apparently leads to a relatively low grain boundary resistance.^{6, 9, 30} The downside of sulphides is their sensitivity to air, however, replacing S with Se shows improved mobility.³¹⁻³² An important family of solid electrolytes are the Li-argyrodites $\text{Li}_6\text{PS}_5\text{X}$ (X=Cl, Br and I) with Li-ion conductivities in the range of 10^{-2} - 10^{-3} S/cm at room temperature.¹⁶ The conductivities of these materials are comparable to $\text{Li}_{10}\text{GeP}_2\text{S}_{12}$, however, the much cheaper precursors gives this family of materials a large advantage for application in all-solid-state batteries. In addition to high Li-ion conductivities, $\text{Li}_6\text{PS}_5\text{Cl}$ is reported to have a wide electrochemical window up to 7.0 V vs. Li/Li^+ .³³ Boulineau *et al.*³³⁻³⁴ assembled solid-state cells using $\text{Li}_6\text{PS}_5\text{Cl}$ as the electrolyte, LiCoO_2 as the cathode, and spinel $\text{Li}_4\text{Ti}_5\text{O}_{12}$ as the anode, exhibiting excellent electrochemical performance. Chen *et al.*³⁵ combined S with $\text{Li}_6\text{PS}_5\text{Br}$ to construct a solid-state cell, also showing excellent performance with an initial discharge capacity of 1355 mAh/g and reversible capacity of 1080 mAh/g after 50 cycles. They attributed the excellent electrochemical performance of the solid-state battery to the small particle size of the active materials. Rao *et al.*³⁶ reported on the synthesis protocols for argyrodite $\text{Li}_6\text{PS}_5\text{X}$ (X=Cl, Br, I) using high-speed mechanical milling resulting in a room temperature conductivity in the order of 10^{-3} S/cm. And using neutron powder diffraction during annealing Rao *et al.*³⁷ were able to establish a clear correlation between the disorder in the $\text{S}^{2-}/\text{Cl}^-$ or $\text{S}^{2-}/\text{Br}^-$ distribution with the conductivity, also supported by recent bond-valence analysis³¹. In $\text{Li}_6\text{PS}_5\text{Cl}$ Li-ion mobility occurs at different time- and length-scales, three types of transitions were distinguished based on calculations in the argyrodite structure³⁸⁻³⁹, of which two do not contribute to the macroscopic conductivity. These transitions have activation energies in the range of 0-0.2 eV, while the transition responsible for macroscopic conductivity has an activation energy close to 0.3 eV. Based on this, the initially reported fast Li-ion diffusion probed by ^7Li NMR appears to be due to one of the local diffusion mechanisms^{31, 40}. Confusingly, activation energies for the macroscopic conductivity

4 Unravelling Li-Ion Transport from Pico-seconds to Seconds

measured by impedance spectroscopy are reported to be as low as 0.11 eV ranging up to 0.56 eV^{16, 33, 36-38, 40-41} making it difficult to gain insight into the various diffusion processes in $\text{Li}_6\text{PS}_5\text{Cl}$ and their role in the performance of all-solid-state batteries.

This makes unravelling the different aspects of the Li-ion mobility and conductivity, ranging from short range vibrations, at a timescale in the order of 10^{13} seconds, up to transport over grain boundaries and electrode interfaces, at a timescale potentially reaching seconds, an important experimental challenge. Using conductivity spectroscopy, it is not trivial to establish the bulk Li-ion bulk conductivity and underlying diffusion mechanism due to the influence of porosity, grain boundaries and effects introduced by the electrodes in contact with the solid electrolyte under investigation. An even greater challenge is to separate the influence of grain boundaries that need to be crossed from one solid electrolyte grain to the other, and the charge transfer reaction over the electrolyte-electrode interface from the bulk conductivity. This would give direct insight in the bottleneck for Li-ion transport, one of the major limitations of all-solid-state batteries, potentially giving a pivotal direction towards improved power performance of all-solid-state batteries. In this context Nuclear magnetic resonance (NMR) spectroscopy offers unique complementary information to impedance spectroscopy, offering high sensitivity to the atomic mobility of the ^7Li nucleus and being a non-destructive contactless probe in battery materials⁴²⁻⁴⁵. The value of NMR spectroscopy for solid electrolyte battery research is demonstrated by recent NMR research giving quantitative and mechanistic insight in the Li-ion and Na-ion bulk mobility mechanism due to the large dynamic range that can be probed.⁴⁶⁻⁵⁶ An additional opportunity of solid state NMR in multi-phase battery materials, either consisting of multiple electrode phases or a mixture of electrode and electrolyte phases, is the ability to probe the spontaneous Li-ion exchange between

different phases, giving unique selectivity for charge transfer over phase boundaries.⁵⁷⁻⁵⁸

In the present work, we aim at a detailed understanding of the conductivity in the argyrodite $\text{Li}_6\text{PS}_5\text{Cl}$ solid electrolyte from local Li-ion mobility, to bulk diffusion, up to the impact of grain boundaries and the charge transfer kinetics over the interface with the Li_2S electrode. This combination is shown to maintain capacities above 300 mAh/g for 40 cycles. Understanding of the bulk diffusion mechanism is achieved by detailed comparison of NMR spin-lattice relaxation experiments with Molecular Dynamics simulations based on DFT. Comparison with the room temperature conductivity based on impedance spectroscopy gives insight into the role of solid electrolyte grain boundaries. Moreover, NMR exchange spectroscopy is used to probe the Li-ion transport over the interface between the $\text{Li}_6\text{PS}_5\text{Cl}$ solid electrolyte and the Li_2S positive electrode, giving a unique insight into the charge transfer reaction, which appears vital for the power performance of all-solid-state batteries.

4.2 Experimental

Reagent-grade Li_2S (99.98%, Sigma-Aldrich), P_2S_5 (99%, Sigma-Aldrich), and LiCl (99.0%, Sigma-Aldrich) crystalline powders were used as starting materials. The required amount of starting materials, according to the molar ratios of stoichiometric $\text{Li}_6\text{PS}_5\text{Cl}$, were ball milled in a WC coated (inner) stainless steel jar with 10 WC balls (8 g/ball) filled in an Argon filled glovebox (H_2O , $\text{O}_2 < 0.3$ ppm) to prevent reactivity with oxygen and moisture. The total weight of the mixture was almost 2.0 g and the ball milling rotation speed was fixed at 550 rpm and different milling durations were applied. After various milling times, the jar was transferred to the glove box and an amount of powder was collected to perform powder XRD. After the ball milling process, the mixture was sealed in a quartz tube and annealed at 550 °C for 5 hours to obtain the final $\text{Li}_6\text{PS}_5\text{Cl}$ solid electrolyte.

4 Unravelling Li-Ion Transport from Pico-seconds to Seconds

Powder XRD patterns were collected over a two-theta range of 10-160° to identify the crystalline phases of the prepared materials using $\text{Cu}_{\text{K}\alpha}$ X-rays (1.5406 Å at 45 kV and 40 mA) on an X'Pert Pro X-ray diffractometer (PANalytical). To prevent reaction with moisture and oxygen the powder materials were sealed in an airtight XRD sample holder in an Argon filled glove box.

Ionic conductivities of the ball-milled powder and the final $\text{Li}_6\text{PS}_5\text{Cl}$ solid electrolyte were measured by pelletizing the powder applying a diameter of 10 mm. Stainless-steel disks were attached on both faces of the pellets and AC impedance measurements were performed for the cell by an Autolab (PGSTAT302N) in the frequency range of 0.1 Hz to 1 MHz with an applied voltage of 0.05 V.

Solid state NMR measurements were performed on a Chemagnetics 400 Infinity spectrometer ($B_0=9.4$ T), operating at a ^7Li resonance frequency of 155.506 MHz. The $\pi/2$ pulse length was determined to be 3.1 μs with an RF field strength of 85 kHz. Chemical shifts were referenced with respect to a 0.1M LiCl solution. The air sensitive $\text{Li}_6\text{PS}_5\text{Cl}$ solid electrolyte sample and the Li_2S electrode - $\text{Li}_6\text{PS}_5\text{Cl}$ solid electrolyte mixture (described in detail in the next section) were sealed in custom-made Teflon tubes in an Argon filled glove box (H_2O , $\text{O}_2 < 0.3$ ppm). Variable temperature measurements were performed using a 5 mm static goniometer probe. For the $\text{Li}_6\text{PS}_5\text{Cl}$ sample, a temperature range of -120 °C to +180 °C was probed. T_1 relaxation times were determined at various temperatures using a saturation recovery experiment. Corresponding $T_{1\rho}$ measurements were performed using the spin-lock method at three different lock frequencies *i.e.* $\omega_1/2\pi \approx 11, 42$ and 84 kHz respectively. Additional single pulse experiments were performed at different temperatures to determine the evolution of linewidth as a function of temperature. In each case a recycle delay of $3T_1$ was used. For the mixture, additional one-dimensional (1D) exchange experiments were performed at

4 Unravelling Li-Ion Transport from Pico-seconds to Seconds

temperatures ranging from 213 to 323 K. The pulse sequence used has been described in detail elsewhere with the appropriate phase cycle for cancellation of direct magnetization that may occur after T_1 relaxation.⁵⁷⁻⁵⁸ Briefly, the sequence consists of $\pi/2$, τ , π , τ , $-\pi/2$, t_{mix} , $+\pi/2$, acquisition. An echo time τ ranging from 200-400 μs was utilized so as to preserve the intensity of the narrow $\text{Li}_6\text{PS}_5\text{Cl}$ resonance and filter out the broad Li_2S resonance, effectively functioning as a T_2 filter. These 1D exchange experiments were performed for a range of mixing times, t_{mix} , to follow the spontaneous equilibrium exchange of Li between the $\text{Li}_6\text{PS}_5\text{Cl}$ and Li_2S phases.

Laboratory-scale solid-state $\text{Li}_2\text{S}/\text{Li}_6\text{PS}_5\text{Cl}/\text{Li-In}$ batteries were fabricated. Commercial Li_2S was first milled with a rotation speed of 500 rpm for 3 h, and then milled with $\text{Li}_6\text{PS}_5\text{Cl}$ and super P with a weight ratio of 4:4:2 using a rotation speed of 400 rpm for 3 h to obtain the final cathode mixture. A two-layer pellet, 10 mm in diameter, consisting of 12 mg of the described cathode mixture and 88 mg $\text{Li}_6\text{PS}_5\text{Cl}$ solid electrolyte, was obtained by pressing the powder electrode and electrolyte together under 6 tons. After that, a piece of In alloy foil was attached to the other side. Subsequently, the whole solid-state battery pellet was pressed under 2 tons for 30 s. The assembled cell was charged and discharged applying a current density of $0.064 \text{ mA}/\text{cm}^2$ between 0.4 and 3.5 V to evaluate the electrochemical performances. The obtained capacity was normalized by the weight of Li_2S in the cathode electrode. Cyclic voltammetry (CV) measurements of the solid-state battery were performed at different voltage windows applying a sweep speed of 0.5 mV/s. Electrochemical impedance spectroscopy measurements were conducted on an Autolab PGSTAT302N before and after electrochemical cycling process in the frequency range of 0.1 Hz and 1 MHz with an applied voltage of 0.05 V.

4.3 Results and Discussion

4.3.1 Synthesis, Impedance spectroscopy, Electrochemical Performance

The present synthesis, 16 h ball milling at 550 rpm followed by annealing at 550 °C for 5 hours results in the argyrodite cubic structure (space group $F-43m$), as confirmed by the Rietveld refinement of the XRD data in Figure 4.1(a), resulting in a lattice parameter $a=9.8290 \text{ \AA}$ and comparable S/Cl disorder as reported by Rao *et al.*^{36,37}. Room temperature impedance spectroscopy, shown in Figure 4.1(b), indicates a conductivity of $1.18 \times 10^{-3} \text{ S/cm}$ for the prepared $\text{Li}_6\text{PS}_5\text{Cl}$ material, a value similar to that reported by Boulineau *et al.*³³ and Rao *et al.*^{36,37}

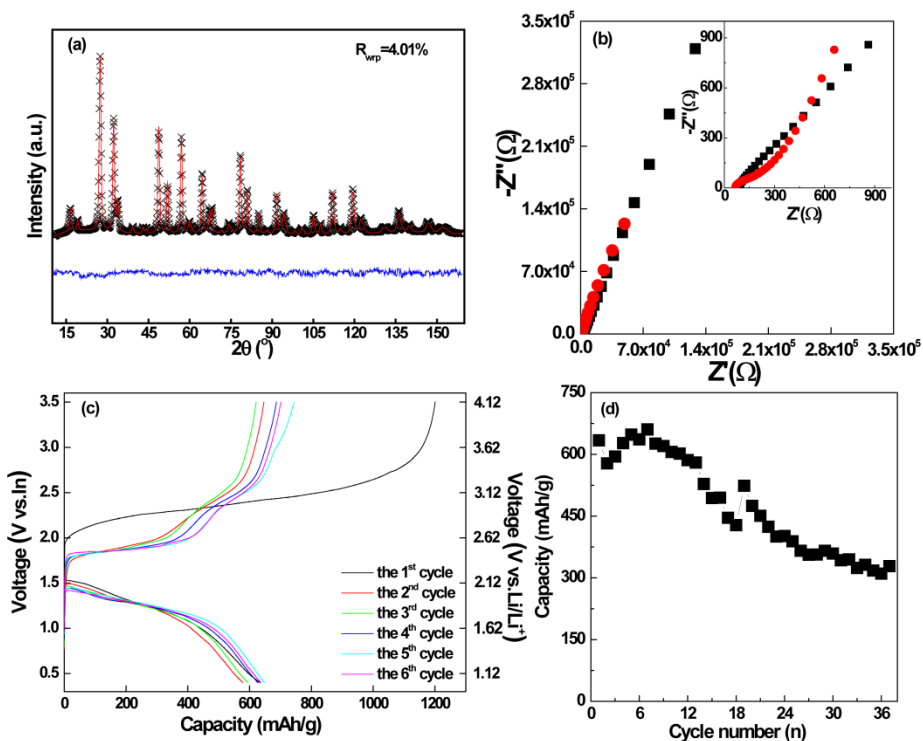


Figure 4.1: (a) XRD refinement of the prepared $\text{Li}_6\text{PS}_5\text{Cl}$ material. (b) Room temperature Impedance spectroscopy of the solid-state battery before and after electrochemical cycling. (c) Galvanostatic voltage curves during the first 6 cycles of the assembled $\text{Li}_2\text{S}/\text{Li}_6\text{PS}_5\text{Cl}/\text{In}$

4 Unravelling Li-Ion Transport from Pico-seconds to Seconds

solid-state battery at a current density of 0.064 mA/cm² applied between 0.4 and 3.5 V vs. In (1.02-4.12 V vs. Li⁺/Li). (d) Capacity upon cycling of the solid-state battery.

Tatsumisago *et al.* used Li₂S as a positive electrode material in combination with 80Li₂S-20P₂S₅, suggesting that reducing the particle size of the Li₂S active material and of the Li₂S-C composite are two important factors to improve the capacity of Li₂S all-solid-state cells⁵. Following a similar strategy, Chen *et al.*³⁵ combined the S cathode with Li₆PS₃Br to construct a solid-state cell, also showing excellent performance with an initial discharge capacity of 1355 mAh/g and reversible capacity of 1080 mAh/g after 50 cycles. In the present work, an all-solid-state battery is assembled combining the Li₆PS₅Cl electrolyte with a nanostructured Li₂S-C composite as a positive electrode material and Indium as a negative electrode material, as described in the experimental section. Cyclic voltammetry was performed applying various voltage windows, resulting in an optimal performance between 0.4 and 3.5 V vs. In (1.0 to 4.1 V vs. Li/Li⁺), see Figure 4.2(a). Galvanostatic cycling was performed applying the optimal voltage cut-offs at a constant current density of 0.064 mA/cm² at 298 K. The (dis)charge curves and the corresponding capacity retention upon cycling are shown in Figure 4.1(c) and 4.1(d) respectively. The cell capacity is reported as the capacity per gram of Li₂S resulting in an initial charge and discharge capacity of approximately 1200 and 634 mAh/g corresponding to a coulombic efficiency of only 52.8%. The low coulombic efficiency during the first few cycles may be the result of the large volume changes associated with the Li₂S positive electrode, where the volume shrink during oxidation may cause loss of contact of the Li_xS phases with the solid electrolyte or/and the carbon electronic conducting phase making subsequent reduction impossible. The initial cycle displays only one charge plateau around 2.4 V and one discharge plateau at 1.5 V vs. In. During subsequent cycling two charge plateaus at 1.8 and 2.4 V vs. In, and one discharge plateau at 1.5 V vs. In are observed. In contrast, using the same electrode combination and applying Li₃PO₄-

4 Unravelling Li-Ion Transport from Pico-seconds to Seconds

$\text{Li}_2\text{S-SiS}_2$ as solid electrolyte resulted in a single charge plateau at 2.0 V and a discharge plateau at 1.5 V vs In. upon cycling.⁵⁹ The present voltage curves appear more like cells applying an organic liquid electrolyte in combination with the $\text{Li}_2\text{S-C}$ positive electrode, also displaying two charge plateaus, at 2.40 and 2.04 V vs. Li/Li^+ ⁶⁰, close to the observed values.

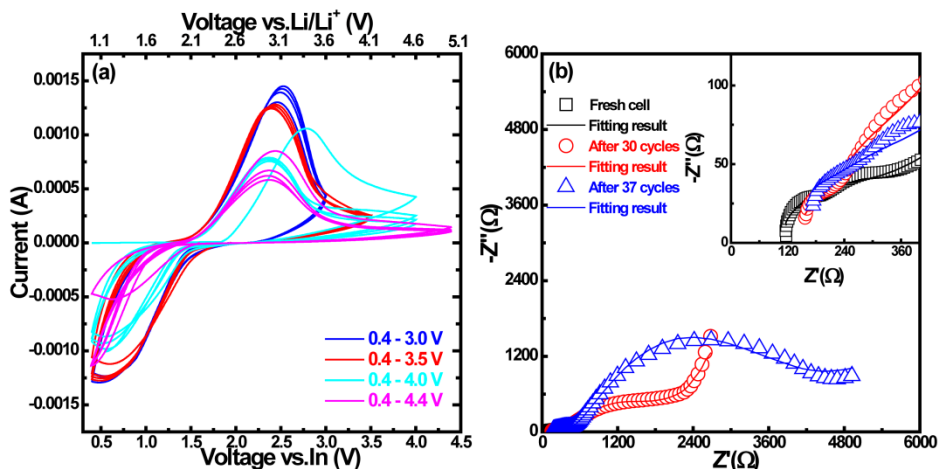


Figure 4.2: (a) Cyclic voltammograms of the all-solid-state batteries $\text{Li}_2\text{S/Li}_6\text{PS}_5\text{Cl/In}$ in different voltage ranges from 0.4 to 3.0, 3.5, 4.0, and 4.4 V (vs. In) at a scanning rate of 0.5 mV/s. Bottom voltage axis shows the values of the voltage versus In, while top voltage axis shows the corresponding values of voltage versus Li/Li^+ . (b) EIS of the assembled solid-state cell after different cycles. Open symbols represent the experimental data, while solid lines represent the data fitting results use equivalent circuits $R_1(R_2Q_2)(R_3Q_3)Q$.

The cycling capacity in Figure 4.1(d) shows that the cell delivers a capacity of 636 mAh/g after 6 cycles, a relatively good capacity retention compared to reported all-solid-state batteries applying Li_2S as positive electrode^{59, 61-63}. Possible explanations for the relatively good electrochemical performance of the present $\text{Li}_2\text{S-C/Li}_6\text{PS}_5\text{Cl/In}$ cell are the optimized voltage window, small particle sizes of electrode and electrolyte, and better performance of the $\text{Li}_6\text{PS}_5\text{Cl}$ solid electrolyte.⁵ To monitor the internal resistance of the battery impedance

spectroscopy was performed on the cell before and after cycling, shown in Figure 4.2(b). For the fresh cell, the impedance spectrum displays a resistance of 135 Ω at high frequencies and an interface resistance of less than 300 Ω . However, after 30 and 37 cycles, both impedance spectra indicate two intersections with the horizontal axis in the high frequencies (left, R_1) and low frequencies (right, R_2). R_1 reflects the resistance of the solid electrolyte, resulting in 157.3 and 175.7 Ω after 30 and 37 cycles respectively, only a slight increase as compared to the fresh cell, indicating that the charge resistance of Li-ion in $\text{Li}_6\text{PS}_5\text{Cl}$ does not increase significantly upon cycling. $(R_2 - R_1)$ is suggested to reflect the interface resistance⁶⁴ of the Li_2S electrode with the $\text{Li}_6\text{PS}_5\text{Cl}$ solid electrolyte, resulting in 1800 and 4000 Ω after 30 and 37 cycles respectively. This may indicate a significant growth of the interfacial resistance upon cycling potentially responsible for the observed capacity fading.

4.3.2 Molecular Dynamics simulations

The Li-density and transitions between Li-sites from the DFT Molecular Dynamics (MD) simulations of $\text{Li}_6\text{PS}_5\text{Cl}$ at three different temperatures are shown in Figure 4.3. At 300 K the Li-density mainly shows local Li-ion mobility over the duration of the MD simulation (10^{-10} seconds), as indicated by the unconnected regions of high Li-ion density in Figure 4.3(a). At this temperature, the Li-ion dynamics is dominated by back and forth transitions between neighboring $48h$ sites (1.68 Å apart), which do not contribute to the macroscopic Li-ion conductivity. At 450 K the Li-density reflects the cage structure of the $48h$ sites, around a central S or Cl atom. At this temperature, the dominant diffusion is within the cages, referred to as intra-cage diffusion, also not contribute to the macroscopic conductivity. Only very occasionally Li-ions make the transition between neighbouring cages (during the 10^{-10} second simulation), which make macroscopic conductivity in $\text{Li}_6\text{PS}_5\text{Cl}$ possible. Thereby three types of transitions can be distinguished from the MD

4 Unravelling Li-Ion Transport from Pico-seconds to Seconds

simulations, short-range $48h$ - $48h$, short-range intra-cage transitions, and long-range inter-cage transitions. Only the latter is responsible for the macroscopic conductivity in $\text{Li}_6\text{PS}_5\text{Cl}$. In Figure 4.3(d-e) for each of these three processes the transition frequency, resulting from the MD simulations, is schematically represented by the thickness of the line connecting the starting and end points of the Li-ion jumps in the unit cell. This gives better insight in the Li-ion kinetics compared to the Li-ion density plots, demonstrating that at 300 K most transitions are due to local $48h$ - $48h$ jumps, occasionally intra-cage jumps occur and only very few inter-cage jumps happen during the MD simulation. This picture changes radically towards high temperatures, where both the intra- and inter-cage jumps increase, at 600 K resulting in a significant amount of inter-cage transitions representing long range macroscopic diffusion. From the transition frequency lines in Figure 4.3(d-e) it is observed that the back and forth $48h$ transitions mainly occur where the cage is centred by a Cl rather than an S atom. This reflects the larger amount of vacancies induced by the charge compensation of the Cl. The present study does not show transitions involving other sites than type 5 tetrahedra sites^{38, 40}, which are localized in the common faces of face sharing double tetrahedra and form the cage like structure (build up by 12 type 5 positions) centred by either a S or Cl atom. The absence of the other type of sites in the diffusion pathway may be the consequence of the relatively short calculation time, however, it does imply that the present DFT based MD simulations predict that the type 5 sites dominate the diffusion mechanism. Also, the suggested transition site connecting the cages, type 2 having common edges of neighbouring tetrahedra, is not specifically included in the inter-cage transition, as illustrated by the various possible inter-cage transitions at 600 K. In Table 4.1 the mean jump frequencies, ν , of each type of transition is given based on $\nu = J/(Nt)$ where J is the number of jumps between neighbouring Li-sites, N the number of Li-ions in the supercell, and

t the total simulation time. Table 4.1 shows that at each simulation temperature the local $48h$ - $48h$ and the intra-cage transitions have a comparable frequency, however, the inter-cage transitions, responsible for macroscopic diffusion, have a frequency at least one order of magnitude smaller. Note that because of the few inter-cage transitions at 300 K no accurate estimation of this transition frequency can be derived from the simulation.

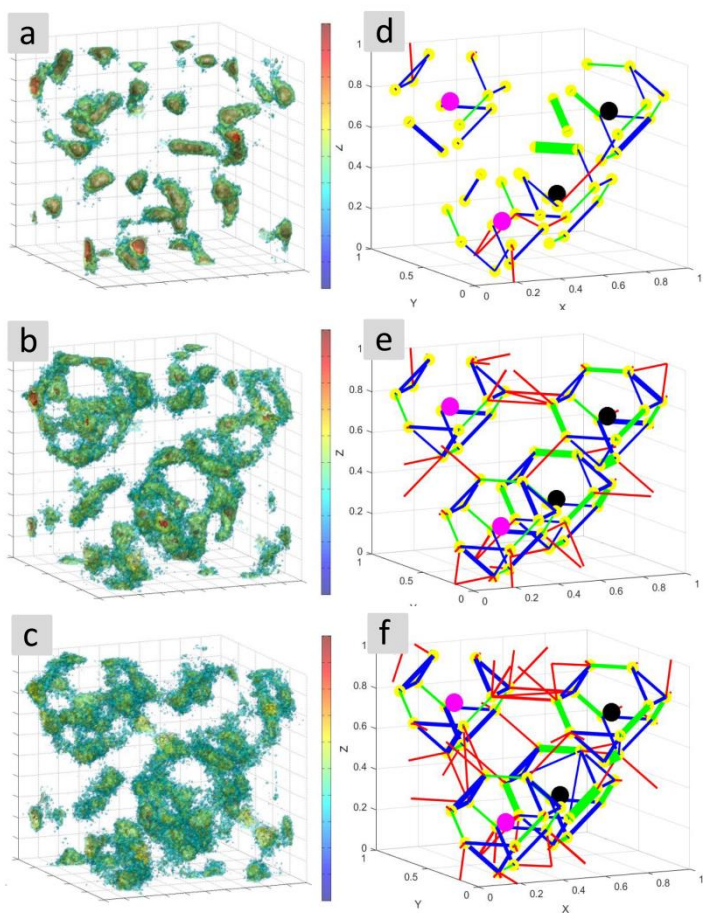


Figure 4.3: (a-c) The integrated Li-density of the Molecular Dynamics Simulations (10^{-10} second duration) in Li_6PS_5Cl at (a) 300 K, (b) 450 K and (c) 600 K. (d-f) Jump statistics derived from the Molecular Dynamics Simulations at (d) 300 K, (e) 450 K and (f) 600 K.

4 Unravelling Li-Ion Transport from Pico-seconds to Seconds

The lines represent three types of Li-ion transitions; Green: Back and forth jumps between 48h-sites Blue: Transitions within the cage consisting of 48h sites, Red: Inter cage jumps responsible for long range diffusion. The thickness of the green, blue and red lines indicates the frequency of the transitions and Yellow spheres indicate Li, Black: S and Purple: Cl.

Transition state theory can be used to calculate the activation energy of the transitions, ΔE_A , from the jump frequencies according to:⁶⁵ $\Delta E_A = -kT \ln(\nu/\nu_0)$ where k is Boltzmann's constant, ν_0 the attempt frequency and T the temperature in Kelvin. Due to the difficulty to determine the attempt frequency it is often assumed to be $\nu_0 = 10^{13}$ Hz⁶⁶ which for the present MD simulations results in activation energies shown in Table 4.1. The similar transition frequency of the local 48h-48h and local intra-cage transitions results in similar activations energies, significantly smaller than the activation energy for the less frequent long range inter-cage transitions. With increasing temperature, the activation energies increase for all three types of transitions, the origin of which may originate from the assumption that the attempt frequency is constant. It is obvious that the attempt frequency will depend on the temperature, but determining accurate temperature dependent attempt frequencies is beyond the scope of this study. However, it is interesting to observe that at 300 K the transition rate of the 48h-48h transitions is larger compared to the intra-cage rate, whereas at 450 and 600 K the intra-cage transition rate is larger, an indication that the potential landscape changes drastically with increasing temperature. From the jump frequencies predicted by the MD-simulations the self-diffusion coefficient, D , can be calculated assuming the Einstein-Smoluchowski relation:

$$D = \frac{l^2 \nu}{3d} \quad (4.1)$$

Where d is the dimensionality of the diffusion path ($d=3$ for the 3D diffusion Li-ion pathway in argyrodite $\text{Li}_6\text{PS}_5\text{Cl}$) and l the jump distance, approximately equal

to 7 Å. By using the Nernst-Einstein equation the diffusivity can be related to the conductivity⁶⁷, σ , assuming no correlation effects⁶⁸:

$$\sigma = \frac{ne^2z^2D}{kT} \quad (4.2)$$

Where n is the Li-ion particle density ($n = 0.0243 \text{ Li}/\text{Å}^3$ for argyrodite $\text{Li}_6\text{PS}_5\text{Cl}$), e the elementary charge, z the ionic charge, k is Boltzmann's constant, and T the temperature in Kelvin. The self-diffusion coefficients and the conductivities in Table 4.1 are determined from the inter-cage transitions because only these contribute to the macroscopic diffusion.

Table 4.1: The MD simulation results of $\text{Li}_6\text{PS}_5\text{Cl}$ calculated at various temperatures.

Temp (K)	Transition Type	Transition rate (s^{-1})	Diff. (cm^2/s)	Cond. (S/cm)	Activation Energy (eV)
300	48h-48h	$2.16 \cdot 10^{11}$			0.10
	Intra-cage	$1.78 \cdot 10^{11}$			0.10
	inter-cage	-	-	-	-
450	48h-48h	$2.61 \cdot 10^{11}$			0.14
	Intra-cage	$3.68 \cdot 10^{11}$			0.13
	inter-cage	$3.12 \cdot 10^{10}$	$2.93 \cdot 10^{-5}$	2.94	0.22
600	48h-48h	$7.35 \cdot 10^{11}$			0.17
	Intra-cage	$5.69 \cdot 10^{11}$			0.15
	inter-cage	$3.75 \cdot 10^{11}$	$3.52 \cdot 10^{-4}$	26.5	0.25

Using Force-Field MD simulations Percher *et al.*³⁸ also distinguished between local and long-range Li-ion transitions in argyrodite $\text{Li}_{6-x}\text{PS}_{5-x}\text{I}_x$, finding significantly different barriers for the local transitions, 0 eV for a transitions similar to the present 48h-48h transitions and a 0.14 eV barrier for transitions throughout the cage structure, and a 0.27 eV barrier from transitions connecting the cages. The predicted³⁸ conductivities for $\text{Li}_{6-x}\text{PS}_{5-x}\text{I}_x$ are around 10^{-4} S/cm, significantly

4 Unravelling Li-Ion Transport from Pico-seconds to Seconds

smaller than those predicted by the present MD simulations for $\text{Li}_6\text{PS}_5\text{Cl}$. Using a bond valence approach in a broad range of argyrodite compositions, Chen *et al.*³⁹ also distinguished the two types of local transitions from the inter-cage transitions, for $\text{Li}_6\text{PS}_5\text{Cl}$ resulting in activation energies of, respectively, 0.15, 0.18 and 0.22 eV, very similar to the present values based on DFT MD simulations.

4.3.3 NMR spin-lattice relaxation experiments

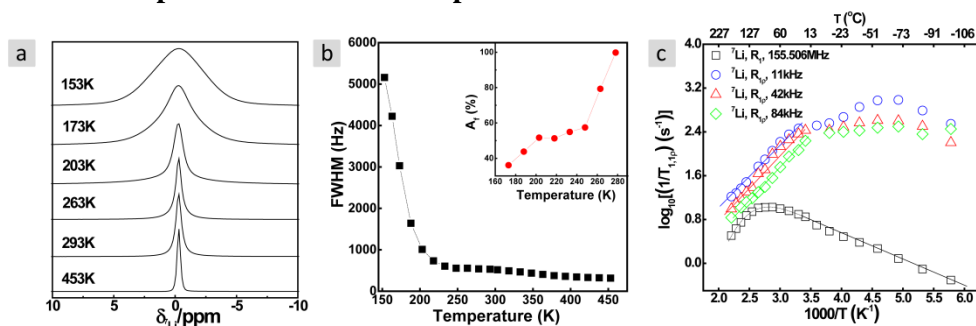


Figure 4.4: (a) Motional narrowing curves of the static ^7Li NMR resonance of $\text{Li}_6\text{PS}_5\text{Cl}$. (b) Evolution of the FWHM of the static ^7Li NMR resonance of $\text{Li}_6\text{PS}_5\text{Cl}$ with temperature. The inset shows the temperature dependence of the fraction of fast lithium ions (A_f) calculated by integrating the area of the fitted Gaussian and Lorentzian line shapes. (c) Arrhenius plots of the ^7Li spin-lattice relaxation (SLR) NMR rates measured in both the laboratory (R_1) and the rotating ($R_{1\rho}$) frame of reference. The Larmor frequency is 155.506 MHz and the locking frequencies are 11, 42 and 84 kHz respectively.

Solid state ^7Li NMR experiments are used as an experimental probe of the bulk mobility of the Li-ions in $\text{Li}_6\text{PS}_5\text{Cl}$, comparison of which with the MD simulations allows developing an understanding of the Li-ion diffusion mechanism. The first indication of mobile Li-ions is observed in Figure 4.4(a) showing the Li-ion motion induced narrowing of the static ^7Li NMR spectra with increasing temperature similar to what was observed by Deiseroth *et al.*¹⁶ At the lowest temperature, 153 K, the spectrum can be fitted by a broad Gaussian where the width is dominated by the dipolar coupling between the spins of the ^7Li nuclei.

4 Unravelling Li-Ion Transport from Pico-seconds to Seconds

Although it appears that at 153 K the so called rigid-lattice regime is not completely achieved, as the FWHM in Figure 4.4(b) does not reach a constant value with decreasing temperature, it does indicate that at 153 K the Li-ion jump frequency is much smaller compared to the line width. Increasing the temperature results in narrowing of the static ^7Li NMR spectra, generally referred to as motional narrowing, indicating that the Li-ion mobility is able to average out the dipolar interactions, which implies that the Li-ion jump frequency is approaching the line width. Consistently, above 153 K it can be fitted with a combination of a Gaussian and a Lorentzian, where the Lorentzian resonance reflects the fraction of mobile Li-ions. At 278 K all Li-ions jump have a jump frequency that exceeds the static line width as reflected by the fact that the resonance can be fitted by a single narrow Lorentzian. Because the rigid-lattice regime is apparently not achieved, Li-ions must already be mobile at 153 K. This is also supported by the fraction of mobile Li-ions (A_f), shown in the inset of Figure 4.4(b) (calculated by integrating the area under the fitted Lorentzian divided by the total integral), resulting in almost 40% of the Li-ions hopping through the lattice at 153 K. Similar motional narrowing behavior was observed for $\text{Li}_6\text{PS}_5\text{Br}$ where the Li-ion mobility was “frozen” only below 67 K. Interestingly, from 200 K up to 250 K A_f marginally increases whereas above 250 K it increases rapidly to reach 100% at 280 K, suggesting that at this temperature all Li-ions in $\text{Li}_6\text{PS}_5\text{Cl}$ are diffusing through the lattice at a time scale exceeding the low-temperature line width, very similar to what has been observed for $\text{Li}_6\text{PS}_5\text{Br}$ using NMR.⁶⁹ For comparison, garnet $\text{Li}_{6.5}\text{La}_3\text{Hf}_{1.5}\text{Ta}_{0.5}\text{O}_{12}$ shows an A_f value of 30% at 280 K and 75% at 360 K,⁷⁰ and high-temperature cubic garnet $\text{Li}_7\text{La}_3\text{Zr}_2\text{O}_{12}$, displays an A_f value of nearly 50% at 263 K⁵⁵ and 100% only at 453 K. Another promising lithium sulfide solid electrolyte is $\text{Li}_7\text{P}_3\text{S}_{11}$ for which ^7Li NMR resulted in an A_f value of 48% at 453 K. Given the comparable low-temperature line width (mainly resulting from dipolar interactions) the much higher A_f values of $\text{Li}_6\text{PS}_5\text{Cl}$ and $\text{Li}_6\text{PS}_5\text{Br}$, suggests very

4 Unravelling Li-Ion Transport from Pico-seconds to Seconds

high Li-ion mobility in these materials. However, to what extent this contributes to the macroscopic conductivity requires more detailed considerations.

To quantitatively determine the Li-ion jump frequencies, temperature-dependent ^7Li static spin-lattice relaxation (SLR) rates in the laboratory frame, $1/T_1$, and in the rotating frame, $1/T_{1\rho}$ are measured, shown in Figure 4.4(c). Provided that the variation of the SLR is only induced by Li-ion mobility, the temperature dependence of the SLR rate in the laboratory frame, $1/T_1$, can be used to quantify the Li-ion jump frequency and the corresponding activation energy^{43-45, 56,50} and the longer range ionic motion taking place at a larger time scales can be probed by SLR NMR measurements in the rotating frame^{43-45, 56}. The present SLR rate $1/T_{1\rho}$ experiments were performed applying lock frequencies of 11, 42, and 84 kHz. When $1/T_{1(\rho)}$ reaches a maximum as a function of temperature the hopping frequency $1/\tau$, where τ is the residence time assumed to be equal to the correlation time between hops, is in the order of the Larmor frequency (ω_0) or lock frequency (ω_1).^{43-45, 56,50} Because the Larmor frequency is 155.506 MHz and the lock frequencies are in the kHz range these SLR experiments are sensitive to Li-ion motion covering many orders of magnitude. Starting with the SLR experiments in the laboratory frame, the condition at the maximum SLR $1/T_1$ rate versus temperature, occurring at 345 K in Figure 3c is $\tau\omega_0 \approx 1$.^{42-45, 71} With a Larmor frequency of $\omega_0/2\pi = 155.506$ MHz, this results in a Li-ion jump frequency of $9.8 \cdot 10^8 \text{ s}^{-1}$ at 345 K. The SLR rates, $1/T_1$ and $1/T_{1\rho}$, are directly related to the spectral density functions of the Li-ion jumping processes.⁴² Assuming a 3D diffusion process, in the high-temperature limit, $\tau\omega_0 \ll 1$, the SLR rates are proportional to the Li-ion residence time τ and in the low-temperature limit, $\tau\omega_0 \gg 1$, the SLR rates are proportional to $\tau^{-1} \cdot \omega_{0(\rho)}^{-\beta}$ (with $1 < \beta \leq 2$). Assuming an Arrhenius behaviour for the Li-ion residence time, $\tau = \tau_0 \exp(-E_a/(k_B T))$ the slope of the high- and low-temperature regimes of the SLR rates in Figure 4.4(c) can be

related to the activation energy for the Li-ion motional processes. The original BPP behaviour⁷¹ predicts symmetric peaks, $\beta = 2$, in the SLR rate as a function of temperature which does not take into account correlation effects and disorder in the diffusion⁴². In particular, the $1/T_1$ rate appears to be asymmetric, similar to what was observed for $\text{Li}_6\text{PS}_5\text{Br}$ ⁶⁹, most likely the result of Li-ion diffusional processes taking place at different length scale, as appears to be the case in $\text{Li}_6\text{PS}_5\text{Cl}$, illustrated by the different types and transition rates predicted by the MD simulations. Both the low and high-temperature flanks of the SLR $1/T_1$ rate follow an Arrhenius behaviour, as observed in Figure 4.4(c), yielding activation energies for the Li-ion mobility of 0.09(4) and 0.29(5) eV respectively. The asymmetry, quantified by $\beta = 1.31$, indicates that the low-temperature flank represents the short-range motional process whereas the high-temperature flank most likely represents a longer-range Li-ion diffusion process⁴². Given the activation energy for the long-range Li-ion diffusion its jump frequency can be quantified to be $1/\tau = 2.0 \cdot 10^{13} \cdot \exp[-0.295/(k_B T)]$. At the onset of the motional narrowing, 153 K, this results in a jump rate of 3.8 kHz which is in the order of the line width (5 kHz) consistently explaining the motional narrowing observed in Figure 4.4(a).

The MD simulations predict both local, short-range motional processes, the $48h$ - $48h$ and intra-cage transitions with similar frequencies and activations energies (between 0.10 and 0.17 eV) and a long-range motional process, the inter-cage transitions with an activation energy between 0.22 and 0.25 eV (Table 4.1). This indicates that the low-temperature flank of the NMR SLR $1/T_1$ rate (characterized by an activation energy of 0.09 eV) represents a combination of the two short-range motional processes ($48h$ - $48h$ and intra-cage) and the high-temperature flank (0.295 eV) represents the long-range inter-cage diffusion, the latter responsible for the macroscopic diffusion. Consistently, the jump frequency based on the NMR SLR $1/T_1$ rate, approximately $1 \cdot 10^{10}$ Hz at 450 K and $7 \cdot 10^{10}$ at 600 K, using the

4 Unravelling Li-Ion Transport from Pico-seconds to Seconds

derived temperature dependent long range transition frequency $1/\tau = 2.0 \cdot 10^{13} \text{ Hz} \cdot \exp[-0.295 \text{ eV}/(k_B T)]$, are in the order of magnitude predicted by the MD simulations for the inter-cage transitions, see Table 4.1.

The ^7Li SLR NMR measurements of the $1/T_{1\rho}$ relaxation rate in the rotating frame, also shown in Figure 4.4(c), probe Li-ion diffusion on a longer time scale compared to the $1/T_1$ relaxation rates. In the rotating frame, the maximum $1/T_{1\rho}$ relaxation rate as a function of temperature satisfies the condition $\tau_{1\rho} \cdot \omega_{\text{lock}} \approx 0.5$.^{42,16-18,29} yielding jump rates of $1.38 \cdot 10^5 \text{ s}^{-1}$ (at 200 K), $5.28 \cdot 10^5 \text{ s}^{-1}$ (at 215 K) and $1.06 \cdot 10^6 \text{ s}^{-1}$ (at 220 K) for the lock frequencies of 11, 42 and 84 kHz respectively. At the high-temperature flank, $1/T_{1\rho}$ relaxation rates in $\text{Li}_6\text{PS}_5\text{Cl}$ for the different lock frequencies yield similar activation energies, albeit slightly smaller compared to the activation energy of the $1/T_1$ relaxation rate, listed in Table 4.2. Taking into account the activation energy, 0.295 eV, the jump frequency based on the $1/T_1$ relaxation, $9.8 \cdot 10^8 \text{ s}^{-1}$ at 345 K results in $7.4 \cdot 10^5 \text{ s}^{-1}$ at 200 K. This value is comparable to the jump frequency derived from the $1/T_{1\rho}$ measurement relaxation rate at the 11 kHz rate lock frequency ($1.38 \cdot 10^5 \text{ s}^{-1}$ at 200 K). This suggests that the $1/T_{1\rho}$ relaxation rate is due to a few inter-cage transitions and apparently this extended diffusion range results in an average lower transition barrier, which will be discussed in the next section.

4 Unravelling Li-Ion Transport from Pico-seconds to Seconds

Table 4.2: Results from the ^7Li NMR SLR experiments for $\text{Li}_6\text{PS}_5\text{Cl}$.

Experiment	Transition Temp. (K)	Transition rate (s^{-1})	Diff. (cm^2/s)	Cond. (S/cm)	Low T E_A (eV)	High T. E_A (eV)
T_1	345	$9.8 \cdot 10^8$	$9.19 \cdot 10^{-7}$	0.12	0.09(4)	0.29(5)
$T_{1\rho}$ 84 kHz	220	$1.06 \cdot 10^6$	$9.94 \cdot 10^{-10}$	$2.04 \cdot 10^{-4}$	-	0.27(1)
$T_{1\rho}$ 42 kHz	215	$5.28 \cdot 10^5$	$4.95 \cdot 10^{-10}$	$1.04 \cdot 10^{-4}$	-	0.25(3)
$T_{1\rho}$ 11 kHz	200	$1.38 \cdot 10^5$	$1.29 \cdot 10^{-10}$	$2.92 \cdot 10^{-5}$	-	0.25(1)

Similar to the jump rates predicted by the MD simulations, the jump rates measured by the NMR SLR can be used to determine the corresponding self-diffusion coefficients and conductivities, assuming no Li-hopping correlation effects⁶⁸, using the Einstein-Smoluchowski relation, Equation (1), and the Nernst-Einstein relation, Equation (2). Using the inter-cage jump distance of 7 \AA and taking into account the Li-ion concentration, $n = 0.0243 \text{ \AA}^{-3}$ this results in the self-diffusion coefficients and conductivities listed in Table 4.2.

Compared to $\text{Li}_6\text{PS}_5\text{Br}$ ⁵⁰, the present $\text{Li}_6\text{PS}_5\text{Cl}$ displays similar activation energy for the local Li-ion transitions, here related to $48h$ - $48h$ back and forth transitions and the intra-cage transitions. However, a significantly larger activation energy for the long range diffusion, the inter-cage transitions, is observed for $\text{Li}_6\text{PS}_5\text{Cl}$. Nevertheless, the long range jump frequencies are comparable at room temperature, indicating a similar high bulk ionic conductivity in $\text{Li}_6\text{PS}_5\text{Cl}$ and $\text{Li}_6\text{PS}_5\text{Br}$.

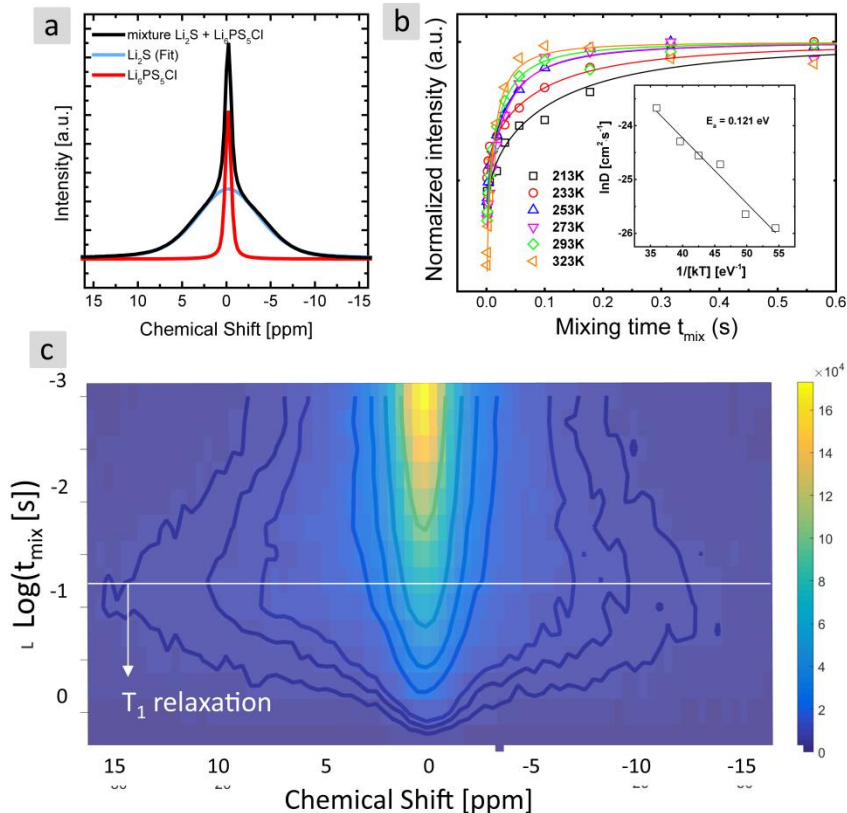
4.3.3 Li ion exchange between Li_2S and $\text{Li}_6\text{PS}_5\text{Cl}$ 

Figure 4.5: (a) The static ^7Li NMR spectrum of the electrode - solid electrolyte Li_2S - $\text{Li}_6\text{PS}_5\text{Cl}$ mixture. (b) Normalized intensity of the static Li_2S ^7Li NMR spectrum, T_1 corrected, as a function of mixing time at different temperatures. The inset shows the temperature dependence of the diffusion parameter D , derived from the fits representing the diffusion model, see text. An Arrhenius law is used to fit the activation energy, E_a , representing the diffusion process over the boundary between the $\text{Li}_6\text{PS}_5\text{Cl}$ solid electrolyte and the Li_2S phases. (c) 1D ^7Li - ^7Li NMR exchange experiment probing the Li-ion transport from the electrolyte $\text{Li}_6\text{PS}_5\text{Cl}$ phase to the electrode Li_2S phase at room temperature.

The ^7Li NMR spin-lattice relaxation (SLR) experiments, shown in Figure 4.4, probe the bulk Li-ion mobility in the $\text{Li}_6\text{PS}_5\text{Cl}$ electrolyte. In addition to bulk conductivity, a critical transport process in solid-state cell is that between the solid

electrolyte and solid electrode phases, the charge transfer reaction, in many cases suggested to be the bottleneck for the power density of all-solid-state batteries.^{6, 10, 72} The difference in line width or in chemical shift allows NMR to probe the exchange of diffusing species between different chemical environments.⁷³ This can be employed to probe the equilibrium Li-ion exchange between different phases, as demonstrated by previous work where ⁷Li exchange NMR was used to probe the spontaneous equilibrium exchange of Li-ions between two different solid electrode phases (Li-rich and Li-poor phases in anatase Li_xTiO₂)⁵⁷, and between the solid electrode phase and a liquid electrolyte phase (anatase Li_{0.5}TiO₂ and LiPF₆ in an EC: DMC solvent)⁵⁸. This extends the timescale in which Li-ion diffusion can be probed from microseconds with spin-relaxation experiments up to seconds, depending on the materials.

In the present work, a similar approach is applied for a mixture of the argyrodite Li₆PS₅Cl electrolyte with the Li₂S positive electrode. The static ⁷Li NMR spectrum of the Li₆PS₅Cl-Li₂S mixture, as shown in Figure 4.5(a), reflects a clear difference in line width. The Li₆PS₅Cl resonance is significantly narrower, a consequence of the Li-ion induced motional narrowing demonstrated in Figure 4.5(a), whereas the broad Li₂S resonance reflects the much smaller mobility in the Li₂S positive electrode. This provides the necessary contrast in the NMR signal allowing the broad ⁷Li component from the Li₂S to be filtered out by an echo experiment as described in the experimental section. The result of the 1D NMR ⁷Li-⁷Li experiment at room temperature is shown in Figure 4.5(c). After filtering out the magnetization of the ⁷Li nuclei in the Li₂S phase, the transfer of the magnetization, carried by the diffusing Li-ions, from the Li₆PS₅Cl solid electrolyte to the Li₂S phase is monitored as a function of mixing time t_{mix} . At $t_{\text{mix}}=0$, the top of the 2D plot, *the* narrow spectrum originates from the Li-ions in the Li₆PS₅Cl solid electrolyte and the broad resonance due to Li-ions in the Li₂S phase is filtered out. With increasing mixing time, going down in Figure 4.5(c), the narrow

4 Unravelling Li-Ion Transport from Pico-seconds to Seconds

$\text{Li}_6\text{PS}_5\text{Cl}$ NMR signal reduces in intensity as a consequence of the reduction in magnetization, carried by the Li-ions that diffuse from the $\text{Li}_6\text{PS}_5\text{Cl}$ phase towards the Li_2S phase. Thereby magnetization is transferred to the Li_2S phase causing the broad resonance, representing Li-ions in Li_2S , to appear with increasing mixing time t_{mix} as shown in Figure 4.5(c) and quantified in Figure 4.5(c) for various temperatures. Thereby this experiment directly probes the spontaneous exchange of Li-ions, i.e. the exchange current between the solid electrolyte and solid electrode phases, a direct measure for the kinetics of the charge transfer process. When the mixing time exceeds approximately 200 ms the T_1 SLR of the $\text{Li}_6\text{PS}_5\text{Cl}$ material causes the total magnetization to disappear, making it impossible to evaluate the exchange beyond this timescale.

To quantify the exchange between the $\text{Li}_6\text{PS}_5\text{Cl}$ and Li_2S phases, the emerging Li_2S signal due to the magnetization transfer carried by the Li-ions, is fitted with a diffusion model. For this a solution to Fick's law for diffusion is determined, $\frac{\partial m(\vec{r}, t)}{\partial t} = \vec{\nabla} \cdot \{D(\vec{r})m(\vec{r}, t)\}$, where $m(\vec{r}, t)$ is the magnetization of Li at position \vec{r} and t , and D is the Li-ion self-diffusion coefficient. Thereby, it is assumed that the spontaneous equilibrium exchange between the electrolyte and electrode phases can be described by an effective diffusion coefficient. According to the mathematical description of the model for spin-diffusion elucidated in detail by Schmidt-Rohr and co-workers⁷⁴, the rate of demagnetization of Li-ions in the solid electrolyte material is determined to be equal to the difference between the initial magnetization and the rate of magnetization in the electrode particles. Assuming a cubic shaped $\text{Li}_6\text{PS}_5\text{Cl}$ solid electrolyte phase embedded in an infinite Li_2S phase this results in the following analytical expression for the rate of demagnetization from in the $\text{Li}_6\text{PS}_5\text{Cl}$ electrolyte into the Li_2S electrode particles as⁵⁷

$$m(t_{\text{mix}}) = \left\{ \frac{m_0}{2} \sqrt{4Dt_{\text{mix}}} \left[\text{ierfc}\left(\frac{d}{\sqrt{4Dt_{\text{mix}}}}\right) + \text{ierfc}\left(\frac{-d}{\sqrt{4Dt_{\text{mix}}}}\right) - \frac{2}{\sqrt{\pi}} \right] \right\}^3 \quad (4.3)$$

Where $\text{ierfc}(x) = \frac{1}{\sqrt{\pi}} \exp(-x^2) - x(1 - \text{erf}(x))$ and d the Li diffusion distance from the $\text{Li}_6\text{PS}_5\text{Cl}$ particle to the Li_2S . For simplicity, it is assumed that diffusion occurs from the center of a $\text{Li}_6\text{PS}_5\text{Cl}$ solid electrolyte particle to the center of the Li_2S electrode particle, which have individual particle sizes of 7 and 32 nm, respectively, determined from the FWHM of these phases in the XRD patterns. Because of the larger Li_2S crystallite size and much smaller conductivity⁷⁵⁻⁷⁶, the assumption of an infinite Li_2S phase appears to be appropriate. Thus, the average diffusion distance is assumed to be the distance between the centers of the $\text{Li}_6\text{PS}_5\text{Cl}$ and Li_2S grains, $d = 20$ nm. The fit results on the normalized intensity of the upcoming Li_2S resonance as a function of mixing time for different temperatures are shown in Figure 4.5(b). The inset of Figure 4.5(b) shows the resulting self-diffusion coefficient (D) as a function of temperature for Li-ion transfer over the electrolyte-electrode interface and the corresponding activation energy. It should be realized that the resulting diffusion coefficient is directly correlated to the lithium diffusion distance d , and the assumption that the Li-diffusion occurs from the center of a $\text{Li}_6\text{PS}_5\text{Cl}$ particle to the center of the Li_2S particle is most likely an overestimation due to the poor conductivity of the Li_2S grains, thereby leading to an overestimation of the diffusion coefficient. The resulting self-diffusion coefficient for the $\text{Li}_6\text{PS}_5\text{Cl}$ - Li_2S exchange is approximately $1 \cdot 10^{-11}$ cm^2/s at room temperature, many orders of magnitude smaller than the bulk diffusion coefficient resulting from the NMR SLR experiments, shown in Table 4.2, and predicted by the MD simulations, shown in Table 4.1. The unique ability of the exchange NMR to distinguish the transport over the $\text{Li}_6\text{PS}_5\text{Cl}$ - Li_2S interface region, gives a direct indication that crossing the $\text{Li}_6\text{PS}_5\text{Cl}$ - Li_2S interface region presents a bottleneck for

4 Unravelling Li-Ion Transport from Pico-seconds to Seconds

Li-ion transport in the all-solid-state battery, as compared to the transport through the $\text{Li}_6\text{PS}_5\text{Cl}$ electrolyte. Surprisingly, the activation energy for the exchange is relatively small, 0.12 eV, compared to that of the bulk diffusion, 0.295 eV by T_1 NMR SLR experiments. This suggests that Li-ion transport over the $\text{Li}_6\text{PS}_5\text{Cl}$ - Li_2S interface is facile, however, the small diffusion coefficient implies a small equilibrium exchange current density. A rationale for that would be that exchange can only occur at a small interface area between the electrolyte and electrode phases, limiting the Li-ion transport over the $\text{Li}_6\text{PS}_5\text{Cl}$ - Li_2S interface. This suggests that establishment of larger electrolyte-electrode interface areas with intimate contact is essential for the all-solid-state battery performance.

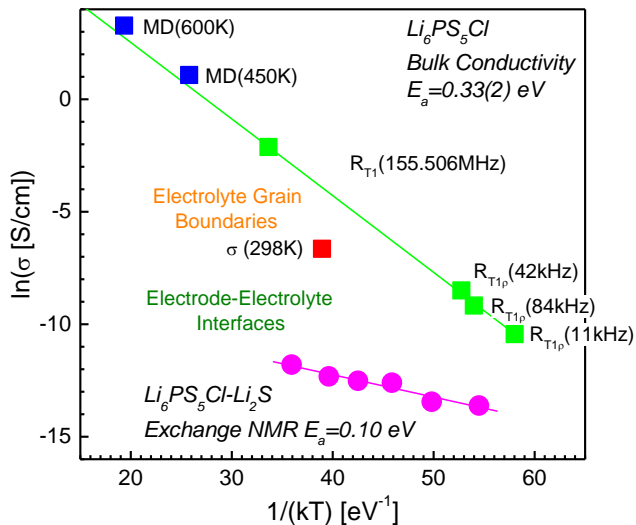


Figure 4.6: Li-ion conductivity in $\text{Li}_6\text{PS}_5\text{Cl}$ deduced from the DFT based MD simulations, ^7Li Solid state NMR SLR experiments, ID exchange experiments between the Li_2S electrode and $\text{Li}_6\text{PS}_5\text{Cl}$ solid electrolyte and the room temperature impedance measurements.

The results from the MD calculations, listed in Table 4.1, the ^7Li NMR SLR experiments, the impedance spectroscopy and the NMR exchange experiments are compared in Figure 4.6 in terms of the resulting conductivity. Thereby the present results compare all relevant Li-ion diffusional processes in the

solid-state battery, from bulk conductivity to $\text{Li}_6\text{PS}_5\text{Cl}$ - $\text{Li}_6\text{PS}_5\text{Cl}$ grain boundaries and the transport over the interface between the $\text{Li}_6\text{PS}_5\text{Cl}$ electrolyte and the Li_2S electrode. This covers Li-ion transport over an extremely wide time-scale, from short time-scale of 10^{-12} s, representing inter-cage transitions, up to approximately 0.1 s, representing the exchange between the $\text{Li}_6\text{PS}_5\text{Cl}$ electrolyte and Li_2S electrode. Fitting the conductivities derived from the ^7Li NMR SLR experiments with an Arrhenius law results in an activation energy of 0.33 eV for the bulk Li-ion conductivity in $\text{Li}_6\text{PS}_5\text{Cl}$, slightly larger compared to the activation energies from the NMR SLR experiments itself. This is most likely because for the multiple inter-cage jump process, probed by the $R_{\text{T1}\rho}$ experiments, a single transition distance was assumed in the calculation of the diffusion coefficients and conductivities. This simplifying assumption is necessary because the diffusion distance during the $R_{\text{T1}\rho}$ experiments cannot be unambiguously be determined. This effectively underestimates the conductivity resulting from the $R_{\text{T1}\rho}$ experiments, explaining the slightly larger activation energy compared to that based on the NMR SLR experiments itself shown in Table 4.2. The bulk conductivity of $\text{Li}_6\text{PS}_5\text{Cl}$ predicted by the MD simulations appears slightly larger compared to those extrapolated from the NMR SLR results, but are nevertheless in very good agreement. Frequently MD simulations are based on simplified force field potentials, allowing larger diffusion times to be simulated in larger super cells, or the kinetic predictions are based on static Nudged Elastic Band calculations disregarding the kinetics of the lattice. However, the present results demonstrate that DFT based MD simulations for these fast ionic conductive materials can be used to predict the Li-ion kinetics, at present in good agreement with the NMR SLR experiments. This makes it an important tool making it possible to gain more insight into the diffusion mechanism at the atomic scale which is valuable for predicting solid electrolyte properties of novel materials.

4 Unravelling Li-Ion Transport from Pico-seconds to Seconds

The room-temperature conductivity determined by impedance spectroscopy, Figure 4.1(b), is significantly smaller than compared to the bulk conductivity measured by the NMR SLR experiments. As discussed, the NMR SLR experiments probe up to a few Li-ion transitions that contribute to the bulk conductivity, the inter-cage transitions, whereas impedance spectroscopy probes transport over a much longer length scale, most likely including $\text{Li}_6\text{PS}_5\text{Cl}$ - $\text{Li}_6\text{PS}_5\text{Cl}$ grain boundaries. Therefore, the smaller conductivity by impedance spectroscopy as compared to the NMR SLR experiments may indicate that grain boundaries lower the conductivity significantly. The present conductivity by impedance spectroscopy is comparable to that reported in literature^{16,52,55-58}, while the activation energy is relatively large compared to that measured with impedance spectroscopy by Rao *et al.* resulting in values as low as 0.11 and 0.16 eV for $\text{Li}_6\text{PS}_5\text{Cl}$.^{37, 41} Given the similar room temperature conductivity it is unlikely that this is the consequence of a difference in the detailed structure and morphology of the presently prepared $\text{Li}_6\text{PS}_5\text{Cl}$ material. This questions whether the activation energy derived from impedance spectroscopy is only determined by the bulk Li-ion mobility in $\text{Li}_6\text{PS}_5\text{Cl}$. A possible explanation would be that the activation energy for grain boundary diffusion influences the activation energy, apparently being lower than the bulk diffusion. The smaller conductivity from impedance spectroscopy compared to the bulk conductivity probed by the NMR experiments would then be explained by a small grain boundary area, similar to what was suggested for the electrolyte-electrode interface.

The NMR exchange experiments make it possible to characterize the equilibrium exchange of Li-ions over the $\text{Li}_6\text{PS}_5\text{Cl}$ - Li_2S interface. Comparing these results with the bulk and impedance conductivity, see Figure 4.6, suggests that the $\text{Li}_6\text{PS}_5\text{Cl}$ grain boundaries limit the conductivity of the electrolyte and that the Li-ion transport over the $\text{Li}_6\text{PS}_5\text{Cl}$ - Li_2S interface is even more limiting the charge transport, thereby being the dominant factor in restricting the power performance

of the all-solid-state battery shown in Figure 4.1. The $\text{Li}_6\text{PS}_5\text{Cl-Li}_6\text{PS}_5\text{Cl}$ and $\text{Li}_6\text{PS}_5\text{Cl-Li}_2\text{S}$ interfaces can be anticipated to have relatively good contact compared to other solid electrolyte-electrode combinations, given the similar structure and low melting temperatures of $\text{Li}_6\text{PS}_5\text{Cl}$ and Li_2S . Thus the present results suggest that also for other solid electrolyte-electrode combinations in the first place the solid-electrolyte interfaces should be considered as the major bottleneck for charge transport in all-solid-state batteries. Interface design therefore should be considered as one of the main directions to improve solid-state battery performance. The impedance spectroscopy results in Figure 4.2(b) show that the degrading cycling performance goes along with an apparent increase in interface resistance. To establish the influence of the transport over the $\text{Li}_6\text{PS}_5\text{Cl-Li}_2\text{S}$ interface, a next challenge will be to use the present NMR exchange experiments to characterize the Li-ion transport as a function of interface preparation procedures and as a function of battery cycling.

4.4 Conclusions

The bulk conductivity in argyrodite $\text{Li}_6\text{PS}_5\text{Cl}$ is investigated by a combination of ^7Li NMR experiments and DFT based Molecular dynamics simulations. This reveals two clearly distinguishable Li-ion motional processes: (1) Local transitions within the cage-like structure formed by Li-ion positions around the S or Cl atom and (2) inter-cage transitions that contribute to the macroscopic diffusion of Li-ions in the crystalline bulk $\text{Li}_6\text{PS}_5\text{Cl}$ structure. Good agreement is established between the bulk conductivity probed by the NMR experiments and predictions by the DFT Molecular Dynamics simulations. Comparison with the macroscopic conductivity measured with impedance spectroscopy suggests a significant influence of $\text{Li}_6\text{PS}_5\text{Cl-Li}_6\text{PS}_5\text{Cl}$ grain boundaries on the conductivity of the electrolyte. However, using exchange NMR, the electrolyte-electrode $\text{Li}_6\text{PS}_5\text{Cl-Li}_2\text{S}$ is found to be the major hurdle for Li-ion transport in all-solid-state batteries, limiting the

power performance. Thereby, exchange NMR is demonstrated to be a valuable tool in all-solid-state battery research making it possible to unravel the different diffusional processes, and to characterize the bottleneck for Li-ion transport, one of the major challenges in all-solid-state batteries.

References

1. Etacheri, V.; Marom, R.; Elazari, R.; Salitra, G.; Aurbach, D., Challenges in the development of advanced Li-ion batteries: a review. *Energ Environ Sci* **2011**, 4 (9), 3243-3262.
2. Minami, T.; Tatsumisago, M.; Wakihara, M.; Iwakura, C.; Kohjiya, S.; Tanaka, I., *Solid state ionics for batteries*. Springer Science & Business Media: 2006.
3. Kim, J. G.; Son, B.; Mukherjee, S.; Schuppert, N.; Bates, A.; Kwon, O.; Choi, M. J.; Chung, H. Y.; Park, S., A review of lithium and non-lithium based solid state batteries. *Journal of Power Sources* **2015**, 282, 299-322.
4. Fergus, J. W., Ceramic and polymeric solid electrolytes for lithium-ion batteries. *J Power Sources* **2010**, 195 (15), 4554-4569.
5. Tatsumisago, M.; Nagao, M.; Hayashi, A., Recent development of sulfide solid electrolytes and interfacial modification for all-solid-state rechargeable lithium batteries. *Journal of Asian Ceramic Societies* **2013**, 1 (1), 17-25.
6. Takada, K., Progress and prospective of solid-state lithium batteries. *Acta Materialia* **2013**, 61 (3), 759-770.
7. Park, M.; Zhang, X.; Chung, M.; Less, G. B.; Sastry, A. M., A review of conduction phenomena in Li-ion batteries. *Journal of Power Sources* **2010**, 195 (24), 7904-7929.
8. Tatsumisago, M.; Hayashi, A., Sulfide Glass-Ceramic Electrolytes for All-Solid-State Lithium and Sodium Batteries. *International Journal of Applied Glass Science* **2014**, 5 (3), 226-235.
9. Knauth, P., Inorganic solid Li ion conductors: An overview. *Solid State Ionics* **2009**, 180 (14-16), 911-916.
10. Cao, C.; Li, Z.-B.; Wang, X.-L.; Zhao, X.-B.; Han, W.-Q., Recent advances in inorganic solid electrolytes for lithium batteries. *Frontiers in Energy Research* **2014**, 2, 25.
11. Takada, K., Interfacial Nanoarchitectonics for Solid-State Lithium Batteries. *Langmuir* **2013**, 29 (24), 7538-7541.
12. Takada, K.; Ohta, N.; Zhang, L.; Xu, X.; Hang, B. T.; Ohnishi, T.; Osada, M.; Sasaki, T., Interfacial phenomena in solid-state lithium battery with sulfide solid electrolyte. *Solid State Ionics* **2012**, 225, 594-597.

13. Mizuno, F.; Hayashi, A.; Tadanaga, K.; Tatsumisago, M., New, Highly Ion-Conductive Crystals Precipitated from $\text{Li}_2\text{S-P}_2\text{S}_5$ Glasses. *Adv Mater* **2005**, *17* (7), 918-921.
14. Murayama, M.; Sonoyama, N.; Yamada, A.; Kanno, R., Material design of new lithium ionic conductor, thio-LISICON, in the $\text{Li}_2\text{S-P}_2\text{S}_5$ system. *Solid State Ionics* **2004**, *170* (3-4), 173-180.
15. Kamaya, N.; Homma, K.; Yamakawa, Y.; Hirayama, M.; Kanno, R.; Yonemura, M.; Kamiyama, T.; Kato, Y.; Hama, S.; Kawamoto, K.; Mitsui, A., A lithium superionic conductor. *Nature Materials* **2011**, *10* (9), 682-686.
16. Deiseroth, H.-J.; Kong, S.-T.; Eckert, H.; Vannahme, J.; Reiner, C.; Zaiß, T.; Schlosser, M., $\text{Li}_6\text{PS}_5\text{X}$: A Class of Crystalline Li-Rich Solids With an Unusually High Li^+ Mobility. *Angewandte Chemie International Edition* **2008**, *47* (4), 755-758.
17. Kennedy, J. H., Ionically conductive glasses based on SiS_2 . *Materials Chemistry and Physics* **1989**, *23* (1), 29-50.
18. Kennedy, J. H.; Zhang, Z.; Eckert, H., XVth International Congress on Glass Ionically conductive sulfide-based lithium glasses. *Journal of Non-Crystalline Solids* **1990**, *123* (1), 328-338.
19. Malugani, J.; Robert, G., Preparation and electrical properties of the $0.37\text{Li}_2\text{S}-0.18\text{P}_2\text{S}_5-0.45\text{LiI}$ glass. *Solid State Ionics* **1980**, *1* (5), 519-523.
20. Souquet, J.; Robinel, E.; Barrau, B.; Ribes, M., Glass formation and ionic conduction in the $\text{M}_2\text{S-GeS}_2$ (M= Li, Na, Ag) systems. *Solid State Ionics* **1981**, *3*, 317-321.
21. Thangadurai, V.; Narayanan, S.; Pinzaru, D., Garnet-type solid-state fast Li ion conductors for Li batteries: critical review. *Chemical Society Reviews* **2014**, *43* (13), 4714-4727.
22. Ihlefeld, J. F.; Clem, P. G.; Doyle, B. L.; Kotula, P. G.; Fenton, K. R.; Apblett, C. A., Fast Lithium-Ion Conducting Thin-Film Electrolytes Integrated Directly on Flexible Substrates for High-Power Solid-State Batteries. *Adv Mater* **2011**, *23* (47), 5663-5667.
23. Fortal'nova, E.; Gavrilencov, O.; Belous, A.; Politova, E., Lithium-ion conducting oxides: Synthesis, structure, and electroconducting properties. *Russ J Gen Chem+* **2009**, *79* (9), 1987-1997.
24. Jacke, S.; Song, J.; Dimesso, L.; Brötz, J.; Becker, D.; Jaegermann, W., Temperature dependent phosphorous oxynitride growth for all-solid-state batteries. *J Power Sources* **2011**, *196* (16), 6911-6914.
25. Mariappan, C. R.; Yada, C.; Rosciano, F.; Roling, B., Correlation between micro-structural properties and ionic conductivity of $\text{Li}_{1.5}\text{Al}_{0.5}\text{Ge}_{1.5}(\text{PO}_4)_3$ ceramics. *J Power Sources* **2011**, *196* (15), 6456-6464.

26. Wang, S.; Ben, L.; Li, H.; Chen, L., Identifying Li⁺ ion transport properties of aluminum doped lithium titanium phosphate solid electrolyte at wide temperature range. *Solid State Ionics* **2014**, *268*, Part A, 110-116.
27. Aono, H.; Sugimoto, E.; Sadaoka, Y.; Imanaka, N.; Adachi, G. y., Ionic Conductivity of the Lithium Titanium Phosphate (Li_{1+x}M_xTi_{2-x}(PO₄)₃, M= Al, Sc, Y, and La) Systems. *Journal of the Electrochemical Society* **1989**, *136* (2), 590-591.
28. Aono, H.; Sugimoto, E.; Sadaoka, Y.; Imanaka, N.; Adachi, G. y., Ionic conductivity of solid electrolytes based on lithium titanium phosphate. *J Electrochem Soc* **1990**, *137* (4), 1023-1027.
29. Bunker, B. C.; Tallant, D. R.; Balfe, C. A.; Kirkpatrick, R. J.; Turner, G. L.; Reidmeyer, M. R., Structure of phosphorus oxynitride glasses. *Journal of the American Ceramic Society* **1987**, *70* (9), 675-681.
30. Seino, Y.; Ota, T.; Takada, K.; Hayashi, A.; Tatsumisago, M., A sulphide lithium super ion conductor is superior to liquid ion conductors for use in rechargeable batteries. *Energ Environ Sci* **2014**, *7* (2), 627-631.
31. Chen, H. M.; Maohua, C.; Adams, S., Stability and ionic mobility in argyrodite-related lithium-ion solid electrolytes. *Physical Chemistry Chemical Physics* **2015**, *17* (25), 16494-16506.
32. Epp, V.; Gün, O. z. I.; Deiseroth, H.-J. r.; Wilkening, M., Highly Mobile Ions: Low-Temperature NMR Directly Probes Extremely Fast Li⁺ Hopping in Argyrodite-Type Li₆PS₅Br. *The Journal of Physical Chemistry Letters* **2013**, *4* (13), 2118-2123.
33. Boulineau, S.; Courty, M.; Tarascon, J.-M.; Viallet, V., Mechanochemical synthesis of Li-argyrodite Li₆PS₅X (X = Cl, Br, I) as sulfur-based solid electrolytes for all-solid-state batteries application. *Solid State Ionics* **2012**, *221*, 1-5.
34. Boulineau, S.; Tarascon, J.-M.; Leriche, J.-B.; Viallet, V., Electrochemical properties of all-solid-state lithium secondary batteries using Li-argyrodite Li₆PS₅Cl as solid electrolyte. *Solid State Ionics* **2013**, *242*, 45-48.
35. Chen, M.; Adams, S., High performance all-solid-state lithium/sulfur batteries using lithium argyrodite electrolyte. *J Solid State Electr* **2015**, *19* (3), 697-702.
36. Rao, R. P.; Adams, S., Studies of lithium argyrodite solid electrolytes for all-solid-state batteries. *physica status solidi (a)* **2011**, *208* (8), 1804-1807.
37. Rao, R. P.; Sharma, N.; Peterson, V. K.; Adams, S., Formation and conductivity studies of lithium argyrodite solid electrolytes using in-situ neutron diffraction. *Solid State Ionics* **2013**, *230*, 72-76.
38. Pecher, O.; Kong, S.-T.; Goebel, T.; Nickel, V.; Weichert, K.; Reiner, C.; Deiseroth, H.-J.; Maier, J.; Haarmann, F.; Zahn, D., Atomistic Characterisation of Li⁺ Mobility and Conductivity in Li_{7-x}PS_{6-x}I_x Argyrodites from Molecular Dynamics Simulations, Solid-State NMR, and Impedance Spectroscopy. *Chemistry-a European Journal* **2010**, *16* (28), 8347-8354.

39. Chen, H. M.; Chen, M.; Adams, S., Stability and ionic mobility in argyrodite-related lithium-ion solid electrolytes. *Physical Chemistry Chemical Physics* **2015**, *17* (25), 16494-16506.
40. Deiseroth, H.-J.; Maier, J.; Weichert, K.; Nickel, V.; Kong, S.-T.; Reiner, C., Li_7PS_6 and $\text{Li}_6\text{PS}_5\text{X}$ (X: Cl, Br, I): Possible Three-dimensional Diffusion Pathways for Lithium Ions and Temperature Dependence of the Ionic Conductivity by Impedance Measurements. *Zeitschrift für anorganische und allgemeine Chemie* **2011**, *637* (10), 1287-1294.
41. Rayavarapu, P.; Sharma, N.; Peterson, V.; Adams, S., Variation in structure and Li^+ -ion migration in argyrodite-type $\text{Li}_6\text{PS}_5\text{X}$ (X = Cl, Br, I) solid electrolytes. *J Solid State Electr* **2012**, *16* (5), 1807-1813.
42. *Diffusion in Condensed Matter - Methods, Materials, Models*. Springer: Berlin, 2005.
43. Epp, V.; Wilkening, M., Li-ion Dynamics in Solids as Seen Via Relaxation NMR. In *Handbook of Solid State Batteries*, 2nd ed.; WORLD SCIENTIFIC: 2015; pp 133-190.
44. Kuhn, A.; Kunze, M.; Sreeraj, P.; Wiemhoefer, H. D.; Thangadurai, V.; Wilkening, M.; Heitjans, P., NMR relaxometry as a versatile tool to study Li ion dynamics in potential battery materials. *Solid State Nuclear Magnetic Resonance* **2012**, *42*, 2-8.
45. Wilkening, M.; Heitjans, P., From Micro to Macro: Access to Long-Range Li^+ Diffusion Parameters in Solids via Microscopic $^{6,7}\text{Li}$ Spin-Alignment Echo NMR Spectroscopy. *Chemphyschem* **2012**, *13* (1), 53-65.
46. Epp, V.; Ma, Q.; Hammer, E.-M.; Tietz, F.; Wilkening, M., Very fast bulk Li ion diffusivity in crystalline $\text{Li}_{1.5}\text{Al}_{0.5}\text{Ti}_{1.5}(\text{PO}_4)_3$ as seen using NMR relaxometry. *Physical Chemistry Chemical Physics* **2015**, *17* (48), 32115-32121.
47. Bottke, P.; Rettenwander, D.; Schmidt, W.; Amthauer, G.; Wilkening, M., Ion Dynamics in Solid Electrolytes: NMR Reveals the Elementary Steps of Li^+ Hopping in the Garnet $\text{Li}_{6.5}\text{La}_3\text{Zr}_{1.75}\text{Mo}_{0.25}\text{O}_{12}$. *Chemistry of Materials* **2015**, *27* (19), 6571-6582.
48. Wohlmuth, D.; Epp, V.; Wilkening, M., Fast Li Ion Dynamics in the Solid Electrolyte $\text{Li}_7\text{P}_3\text{S}_{11}$ as Probed by $^{6,7}\text{Li}$ NMR Spin-Lattice Relaxation. *Chemphyschem* **2015**, *16* (12), 2582-2593.
49. Breuer, S.; Prutsch, D.; Ma, Q.; Epp, V.; Preishuber-Pfluegl, F.; Tietz, F.; Wilkening, M., Separating bulk from grain boundary Li ion conductivity in the sol-gel prepared solid electrolyte $\text{Li}_{1.5}\text{Al}_{0.5}\text{Ti}_{1.5}(\text{PO}_4)_3$. *Journal of Materials Chemistry A* **2015**, *3* (42), 21343-21350.
50. Epp, V.; Gun, O.; Deiseroth, H.-J.; Wilkening, M., Highly Mobile Ions: Low-Temperature NMR Directly Probes Extremely Fast Li^+ Hopping in Argyrodite-Type $\text{Li}_6\text{PS}_5\text{Br}$. *Journal of Physical Chemistry Letters* **2014**, *4*, 2118-2123.

51. Epp, V.; Gun, O.; Deiseroth, H. J.; Wilkening, M., Long-range Li⁺ dynamics in the lithium argyrodite Li₇PSe₆ as probed by rotating-frame spin-lattice relaxation NMR. *Physical Chemistry Chemical Physics* **2013**, *15* (19), 7123-7132.
52. Düvel, A.; Kuhn, A.; Robben, L.; Wilkening, M.; Heitjans, P., Mechano-synthesis of Solid Electrolytes: Preparation, Characterization, and Li Ion Transport Properties of Garnet-Type Al-Doped Li₇La₃Zr₂O₁₂ Crystallizing with Cubic Symmetry. *The Journal of Physical Chemistry C* **2012**, *116* (29), 15192-15202.
53. Narayanan, S.; Epp, V.; Wilkening, M.; Thangadurai, V., Macroscopic and microscopic Li⁺ transport parameters in cubic garnet-type "Li_{6.5}La_{2.5}Ba_{0.5}ZrTaO₁₂" as probed by impedance spectroscopy and NMR. *RSC Advances* **2012**, *2* (6), 2553-2561.
54. Kuhn, A.; Choi, J.-Y.; Robben, L.; Tietz, F.; Wilkening, M.; Heitjans, P., Li Ion Dynamics in Al-Doped Garnet-Type Li₇La₃Zr₂O₁₂ Crystallizing with Cubic Symmetry. In *Zeitschrift für Physikalische Chemie International journal of research in physical chemistry and chemical physics*, 2012; Vol. 226, p 525.
55. Buschmann, H.; Dolle, J.; Berendts, S.; Kuhn, A.; Bottke, P.; Wilkening, M.; Heitjans, P.; Senyshyn, A.; Ehrenberg, H.; Lotnyk, A.; Duppel, V.; Kienle, L.; Janek, J., Structure and dynamics of the fast lithium ion conductor "Li₇La₃Zr₂O₁₂". *Phys Chem Chem Phys* **2011**, *13* (43), 19378-19392.
56. Kuhn, A.; Narayanan, S.; Spencer, L.; Goward, G.; Thangadurai, V.; Wilkening, M., Li self-diffusion in garnet-type Li₇La₃Zr₂O₁₂ as probed directly by diffusion-induced ⁷Li spin-lattice relaxation NMR spectroscopy. *Physical Review B* **2011**, *83* (9), 094302.
57. Wagemaker, M.; Kentgens, A. P. M.; Mulder, F. M., Equilibrium lithium transport between nanocrystalline phases in intercalated TiO₂ anatase. *Nature* **2002**, *418* (6896), 397-399.
58. Ganapathy, S.; van Eck, E. R. H.; Kentgens, A. P. M.; Mulder, F. M.; Wagemaker, M., Equilibrium Lithium-Ion Transport Between Nanocrystalline Lithium-Inserted Anatase TiO₂ and the Electrolyte. *Chemistry-a European Journal* **2011**, *17* (52), 14811-14816.
59. Takeuchi, T.; Kageyama, H.; Nakanishi, K.; Tabuchi, M.; Sakaebe, H.; Ohta, T.; Senoh, H.; Sakai, T.; Tatsumi, K., All-Solid-State Lithium Secondary Battery with Li₂S-C Composite Positive Electrode Prepared by Spark-Plasma-Sintering Process. *J Electrochem Soc* **2010**, *157* (11), A1196-A1201.
60. Takeuchi, T.; Sakaebe, H.; Kageyama, H.; Senoh, H.; Sakai, T.; Tatsumi, K., Preparation of electrochemically active lithium sulfide-carbon composites using spark-plasma-sintering process. *J Power Sources* **2010**, *195* (9), 2928-2934.
61. Hayashi, A.; Ohtsubo, R.; Tatsumisago, M., Electrochemical performance of all-solid-state lithium batteries with mechanochemically activated Li₂S-Cu composite electrodes. *Solid State Ionics* **2008**, *179* (27-32), 1702-1705.

62. Hayashi, A.; Ohtsubo, R.; Ohtomo, T.; Mizuno, F.; Tatsumisago, M., All-solid-state rechargeable lithium batteries with Li_2S as a positive electrode material. *J Power Sources* **2008**, *183* (1), 422-426.
63. Chen, M.; Rao, R. P.; Adams, S., High capacity all-solid-state $\text{Cu-Li}_2\text{S/Li}_6\text{PS}_5\text{Br/In}$ batteries. *Solid State Ionics* **2014**, *262*, 183-187.
64. Huang, B.; Yao, X.; Huang, Z.; Guan, Y.; Jin, Y.; Xu, X., Li_3PO_4 -doped $\text{Li}_7\text{P}_3\text{S}_{11}$ glass-ceramic electrolytes with enhanced lithium ion conductivities and application in all-solid-state batteries. *Journal of Power Sources* **2015**, *284*, 206-211.
65. Vineyard, G. H., Frequency Factors and Isotope Effects in Solid State Rate Processes. *Journal of Physics and Chemistry of Solids* **1957**, *3*, 121-127.
66. Van der Ven, A.; Ceder, G.; Asta, M.; Tepesch, P. D., First-principles theory of ionic diffusion with nondilute carriers. *Physical Review B* **2001**, *64* (18), 17.
67. Friauf, R. J., Correlation Effects for Diffusion in Ionic Crystals. *Journal of Applied Physics* **1962**, *33*, 494-505.
68. Mehrer, H., *Diffusion in Solids: Fundamentals, Methods, Materials, Diffusion-Controlled Processes*. Springer: Berlin, 2007.
69. Epp, V.; Gün, Ö.; Deiseroth, H.-J.; Wilkening, M., Highly Mobile Ions: Low-Temperature NMR Directly Probes Extremely Fast Li^+ Hopping in Argyrodite-Type $\text{Li}_6\text{PS}_5\text{Br}$. *The Journal of Physical Chemistry Letters* **2013**, *4* (13), 2118-2123.
70. Gupta, A.; Murugan, R.; Paranthaman, M. P.; Bi, Z.; Bridges, C. A.; Nakanishi, M.; Sokolov, A. P.; Han, K. S.; Hagaman, E. W.; Xie, H.; Mullins, C. B.; Goodenough, J. B., Optimum lithium-ion conductivity in cubic $\text{Li}_{7-x}\text{La}_3\text{Hf}_{2-x}\text{Ta}_x\text{O}_{12}$. *J Power Sources* **2012**, *209*, 184-188.
71. Bloembergen, N.; Purcell, E. M.; Pound, R. V., Relaxation Effects in Nuclear Magnetic Resonance Absorption. *Physical Review* **1948**, *73* (7), 679-712.
72. Minami, T.; Hayashi, A.; Tatsumisago, M., Recent progress of glass and glass-ceramics as solid electrolytes for lithium secondary batteries. *Solid State Ionics* **2006**, *177* (26-32), 2715-2720.
73. Ernst, R. R. B., G.; Wokaun, A., *Principles of nuclear magnetic resonance in one and two dimensions*. Clarendon Press: Oxford, 1994.
74. Schmidt-Rohr, K. S., H.W., *Multidimensional Solid-State NMR and Polymers*. Academic Press: London, 1994.
75. Mousa, M.; Oei, Y.; Richtering, H., NMR investigations of cation diffusion in some solids with antiferroite structure. *Le Journal de Physique Colloques* **1980**, *41* (C6), C6-223-C6-226.
76. Yang, Y.; Zheng, G.; Misra, S.; Nelson, J.; Toney, M. F.; Cui, Y., High-capacity micrometer-sized Li_2S particles as cathode materials for advanced rechargeable lithium-ion batteries. *J Am Chem Soc* **2012**, *134* (37), 15387-15394.

4 Unravelling Li-Ion Transport from Pico-seconds to Seconds

5

Revealing the Relation between the Structure, Li-ion Conductivity and Solid-State Battery Performance for the Argyrodite $\text{Li}_6\text{PS}_5\text{Br}$ Solid Electrolyte

This chapter is based on the paper: “*Revealing the effects of annealing on Li-ion mobility in the $\text{Li}_6\text{PS}_5\text{Br}$ solid electrolyte synthesized by a mechanical milling route*”, Chuang Yu, Swapna Ganapathy, Ernst R.H. van Eck, Lambert van Eijck, Shibabrata Basak, Henny W. Zandbergen and Marnix Wagemaker*, [Journal of Materials Chemistry A](#), accepted.

5.1 Introduction

Inorganic solid electrolytes for all-solid-state Li-ion batteries are attracting significant attention because of the improved safety they provide in comparison with conventional liquid electrolyte based Li-ion batteries.¹⁻² Other potential advantages include improved chemical and electrochemical stability and more efficient cell packaging, allowing higher practical energy densities, using the same anode and cathode chemistries. One of the crucial parameters for solid electrolytes is that their high room temperature Li-ion conductivity for practical applications should be in the order of 10^{-4} S/cm.³⁻⁴

Intensive research efforts have led to the discovery of several new solid electrolytes with high Li-ion conductivities including the sulphides ($\text{Li}_2\text{S-P}_2\text{S}_5$, $\text{Li}_2\text{S-SiS}_2$, $\text{Li}_2\text{S-GeS}_2$),⁵⁻⁷ oxides ($\text{Li}_7\text{La}_3\text{Zr}_2\text{O}_{12}$ and $\text{Li}_{3x}\text{La}_{2/3-3x}\text{TiO}_3$)⁸ and phosphates (LiPON , $\text{Li}_{1+x}\text{Al}_x\text{Ge}_{2-x}(\text{PO}_4)_3$, $\text{Li}_{1+x}\text{Ti}_{2-x}\text{Al}_x(\text{PO}_4)_3$).^{1-2, 9-10} Among them, the chemically stable oxides and phosphates display relatively low ionic conductivities and high grain boundary resistances.¹ Sulphides generally offer higher conductivities¹¹ and their relatively low annealing temperatures, compared to the oxides and phosphates, apparently leading to a relatively low grain boundary resistance,^{2, 12-13} which makes them promising solid electrolytes for solid-state cells. An important family of sulphide based solid electrolytes is the Li-argyrodites $\text{Li}_6\text{PS}_5\text{X}$ ($\text{X}=\text{Cl}$, Br and I) providing Li-ion conductivities in the range of 10^{-2} - 10^{-3} S/cm at room temperature.⁷ The high conductivity and the low costs of starting materials make the Li-argyrodites attractive for application in all-solid-state batteries. Previous work has demonstrated that the $\text{Li}_6\text{PS}_5\text{Cl}$ argyrodite, with high Li-ion conductivity, can be synthesized by direct ball-milling followed by annealing, resulting in a good solid state Li-S battery performance with both S and Li_2S cathodes.¹⁴⁻¹⁷ Although argyrodite solid electrolytes with large electrochemical stability windows have been reported,¹⁸⁻¹⁹ calculations indicate a

5 Revealing the Relation between the Structure, Li-ion Conductivity

much smaller window for sulphides²⁰ with an upper limit just exceeding the potential of Li_2S , motivating the use of Li_2S as cathode material in combination with sulphide electrolytes.

To improve the all-solid-state battery performance, it is essential to develop an understanding of the influence of synthesis parameters and cycling conditions on the electrochemical performance of argyrodites. For argyrodite solid electrolytes, the annealing temperature appears to be very important for the Li-ion conductivity and electrochemical performance, as illustrated by the role of the halogen dopant position in the lattice,¹⁴ recently studied by DFT.²¹ The energy barriers for short range jumps and long range jumps were investigated by MD simulations and valence calculations indicating the detailed influence of the halogen on the diffusion mechanism.^{15, 21} However, little is known about how annealing and ball milling strategies influence the bulk mobility as well as the macroscopic Li-ion conductivity, including grain boundaries, and how this affects the solid state battery performance. Additionally, little is known about the impact of the electrochemical (dis)charge window on the cycle life, which is in particular relevant in the context of the predicted limited electrochemical stability window for these sulfide electrolytes.

In the present work, a detailed study on the effect of annealing on the Li-ion dynamics in the argyrodite $\text{Li}_6\text{PS}_5\text{Br}$ solid electrolyte has been performed. By employing both impedance spectroscopy and spin-lattice relaxation (SLR) NMR measurements, differences in the local Li-ion mobility and bulk diffusion as well as the impact of grain boundaries are revealed between differently prepared $\text{Li}_6\text{PS}_5\text{Br}$ solid electrolyte materials. Combined Rietveld refinement of Neutron and X-ray powder diffraction data were performed to probe structural differences between the prepared $\text{Li}_6\text{PS}_5\text{Br}$ materials. Transmission electron microscopy (TEM) measurements were performed to investigate the crystallinity and the distribution

5 Revealing the Relation between the Structure, Li-ion Conductivity

of Br dopant. Finally, cyclic voltammetry (CV) was performed to determine the optimum (dis)charge voltage window for the nano-Li₂S/Li₆PS₅Br/In solid-state cells. By employing the optimized electrochemical window for (dis)charging, a significant difference in the performance is observed for the differently prepared solid electrolytes where only the solid-state cell using annealed nano-sized Li₆PS₅Br as the solid electrolyte maintained capacities above 500 mAh/g (per gram of active material) for 25 cycles.

5.2 Experimental

Reagent-grade Li₂S (99.98%, Sigma-Aldrich), P₂S₅ (99%, Sigma-Aldrich), and LiBr (99.0%, Sigma-Aldrich) crystalline powders were used as starting materials. The required amount of the starting materials was ball milled together in a tungsten carbide (WC) coated (inner) stainless steel jar with 10 WC balls (8 g/ball) in an Argon filled glovebox (H₂O, O₂ < 0.3 ppm) because of the reactivity of the sample with oxygen and moisture. The total weight of the mixture was almost 2.0 grams, and the ball milling speed was fixed at 500 rpm. The milling duration was varied to find the optimal milling time. After subsequent milling times, a small amount of powder was collected to perform powder XRD measurements. After the ball milling process, half of the sample was set aside as the ball-milled only Li₆PS₅Br (Li₆PS₅Br), and the remaining material was sealed in a quartz tube and annealed at 300 °C for 5 hours to obtain the annealed Li₆PS₅Br (AN-Li₆PS₅Br) solid electrolyte. The AN-Li₆PS₅Br was further milled with a rotation speed of 450 rpm for 4 h to obtain the AN-BM-Li₆PS₅Br sample.

Powder XRD patterns were collected over a 2θ range of 10-80° to identify the crystalline phases of the different samples using Cu_{Kα} X-rays (1.5406 Å at 45 kV and 40 mA) on an X'Pert Pro X-ray diffractometer (PANalytical). To prevent reaction with moisture and oxygen, the powders were sealed in an airtight XRD sample holder in an Argon filled glove box. Neutron diffraction data was collected

5 Revealing the Relation between the Structure, Li-ion Conductivity

on the new neutron powder diffractometer PEARL of the TU Delft.²² Data were collected at room temperature using the (533) reflection of the germanium monochromator ($\lambda = 1.665 \text{ \AA}$). The sample was loaded under Argon in a 6 mm diameter air-tight vanadium sample can. The sample was measured for 18 hours from 10.4-160 2θ degrees. The sample can is under vacuum during the data collection. The data treatment consisted of a relative correction for detection efficiency of (each of) the 1408 detector pixels and a subtraction of the background, caused by the instrument and the sample can. The X-ray and neutron diffraction data were refined simultaneously using the Rietveld method implemented in GSAS.²³ Besides the atomic and lattice parameters, the absorption and line-broadening parameters, the crystal phase fractions, and the background were fitted, respectively. The S and Br occupancies on both the $4a$ and $4c$ crystallographic sites were restricted by setting the sum to 1 on each site.

For the TEM investigations, a suspension in hexane was prepared which was drop casted onto a standard gold grid with a holey carbon film, inside an argon filled glove box. To prevent any contact with air TEM grids with the sample were loaded into a custom made vacuum transfer TEM holder. TEM measurements were carried out in a FEI-Tecnai operating at 200 kV.

Ionic conductivities of the $\text{Li}_6\text{PS}_5\text{Br}$ electrolyte materials were determined by AC impedance. Stainless-steel disks were attached on both faces of the 10 mm diameter powder pellets.¹⁶⁻¹⁷ AC impedance measurements were performed using an Autolab (PGSTAT302N) in the frequency range of 0.1 Hz to 1 MHz with an applied voltage of 0.05 V.

Solid-state NMR measurements were performed on a Chemagnetics 400 Infinity spectrometer ($B_0=9.4 \text{ T}$), operating at the 155.506 MHz ^7Li resonance frequency. The $\pi/2$ pulse length was determined to be 3.1 μs with an RF field strength of 85 kHz. Chemical shifts were referenced with respect to a 0.1 M LiCl

5 Revealing the Relation between the Structure, Li-ion Conductivity

solution. The air sensitive $\text{Li}_6\text{PS}_5\text{Br}$ materials were sealed in custom-made Teflon tubes in an Argon filled glove box (H_2O , $\text{O}_2 < 0.3$ ppm). Variable temperature measurements were performed using a 5 mm static goniometer probe. For all three $\text{Li}_6\text{PS}_5\text{Br}$ samples, spectra were acquired in the temperature range of -100 °C to $+180$ °C. T_1 relaxation times were determined at various temperatures using a saturation recovery experiment. Corresponding $T_{1\rho}$ measurements were performed using the spin-lock method at a lock frequency of 20 kHz. Additional single pulse experiments were performed at different temperatures to determine the evolution of the linewidth as a function of temperature employing a line width of 250 kHz. In each case, a recycle delay of $3T_1$ was used.

Laboratory-scale solid-state $\text{Li}_2\text{S}/\text{Li}_6\text{PS}_5\text{Br}/\text{In}$ batteries were prepared. Commercial Li_2S was first milled with a rotation speed of 500 rpm for 4 h, and then milled with $\text{Li}_6\text{PS}_5\text{Br}$, AN- $\text{Li}_6\text{PS}_5\text{Br}$ and AN-BM- $\text{Li}_6\text{PS}_5\text{Br}$ separately and super P (TIMCAL) with a weight ratio of 4:4:2 using a rotation speed of 450 rpm for 2 h to obtain the final cathode mixture. A two-layer pellet, 10 mm in diameter, consisting of 12 mg of the described cathode mixture and 88 mg $\text{Li}_6\text{PS}_5\text{Br}$, AN- $\text{Li}_6\text{PS}_5\text{Br}$, or AN-BM- $\text{Li}_6\text{PS}_5\text{Br}$ solid electrolyte, was obtained by pressing the electrode and electrolyte powders by applying 6 tons of pressure. A piece of In foil was subsequently attached to the other side. Finally, the full solid-state battery pellet was pressed with 2 tons of pressure for 30 s. Cyclic voltammetry (CV) measurements of the solid-state battery with the AN- $\text{Li}_6\text{PS}_5\text{Br}$ solid electrolyte were performed at different voltage windows applying a sweep rate of 0.5 mV/s to determine the optimum (dis)charge voltage window. The assembled cells, either with $\text{Li}_6\text{PS}_5\text{Br}$, AN- $\text{Li}_6\text{PS}_5\text{Br}$ or AN-BM- $\text{Li}_6\text{PS}_5\text{Br}$, were charged and discharged applying a current density of 0.064 mA/cm² between 0 and 3.5 V vs. In in order to evaluate the electrochemical performance. The obtained capacity was normalized by the weight of Li_2S in the cathode.

5.3 Results and discussion

5.3.1 Impedance, diffraction and TEM characterization of $\text{Li}_6\text{PS}_5\text{Br}$

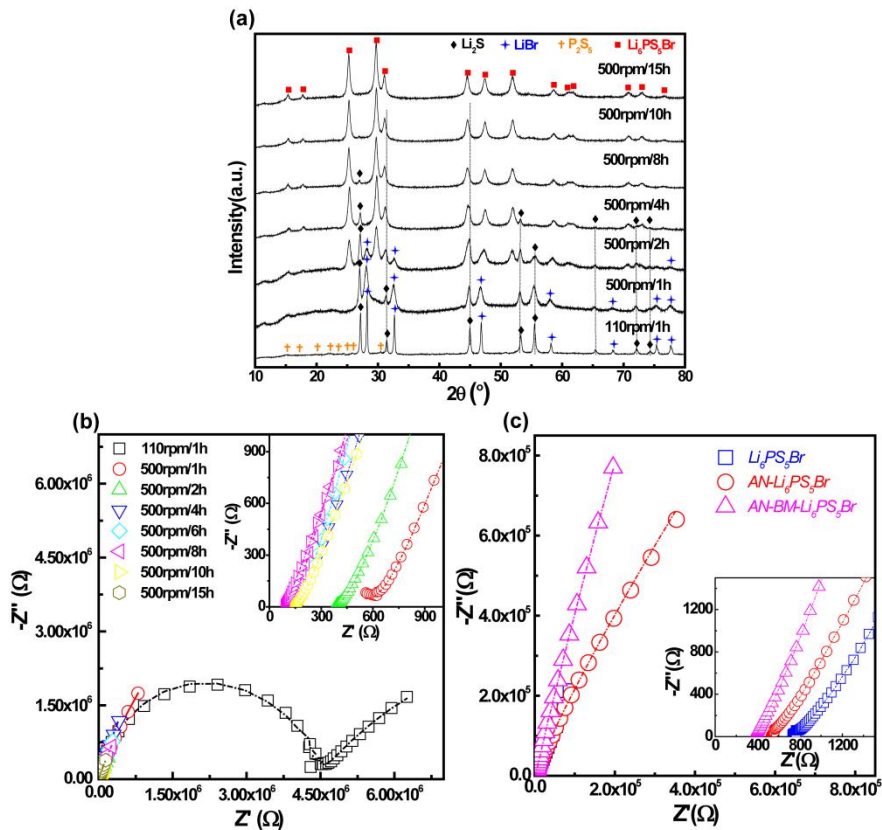


Figure 5.1: (a) XRD patterns of the Li_2S , P_2S_5 and LiBr mixtures ball-milled for different milling durations. (b) Complex impedance plots for the samples ball-milled for different durations. The dotted lines represent fits using an equivalent circuit $(R_{\text{bulk}}Q_{\text{bulk}})(R_{\text{gb}}Q_{\text{gb}})Q$. (c) The AC impedance results of $\text{Li}_6\text{PS}_5\text{Br}$ (ball milled for 8 hours at 500 rpm) (blue), AN- $\text{Li}_6\text{PS}_5\text{Br}$ ($\text{Li}_6\text{PS}_5\text{Br}$ subsequently annealed for at 300°C for 5 hours) (red) and AN-BM- $\text{Li}_6\text{PS}_5\text{Br}$ (AN- $\text{Li}_6\text{PS}_5\text{Br}$ subsequently ball milled for 4 hours at 450 rpm) (pink). The dotted lines represent fits using an equivalent circuit $(R_{\text{bulk}}Q_{\text{bulk}})(R_{\text{gb}}Q_{\text{gb}})Q$.

5 Revealing the Relation between the Structure, Li-ion Conductivity

XRD patterns of the $\text{Li}_6\text{PS}_5\text{Br}$ samples synthesized by mechanical milling at 500 rpm for different durations are shown in Figure 5.1a. As illustrated, the diffraction peaks of the sample milled at 110 rpm for 1 hour could be indexed to the starting materials Li_2S , LiBr and P_2S_5 . This step appears to be necessary in order to mix the raw materials homogeneously. After that, the milling speed was increased to 500 rpm to provide the mechanical energy necessary to obtain the $\text{Li}_6\text{PS}_5\text{Br}$ phase. After 1 h of milling, the initially sharp diffraction peaks originating from the Li_2S phase broadened, indicating a decrease in particle size. Moreover, a halo pattern located in the low 2θ region appeared, indicating the formation of an amorphous phase.²⁴ As the milling duration increases, diffraction peaks at 25.2 , 29.7 , 31.1 and 51.9° appear which can be attributed to the $\text{Li}_6\text{PS}_5\text{Br}$ phase. Compared to the pattern measured after 1 h milling, the intensity of the Li_2S diffraction peaks decreases and after a milling time of 10 h, the diffraction peak due to Li_2S located at 53.3° disappears completely.

The influence of the milling time on the Li-ion conductivity is investigated by AC Impedance spectroscopy. The resistance of the mixture decreases sharply with increasing milling duration until a constant value is obtained after 8 h of milling, as shown in Figure 5.1b. The increase in Li^+ conductivity during the milling process is associated with the concurrent decrease of the poorly conducting Li_2S phase and the increase of Li-ion conducting $\text{Li}_6\text{PS}_5\text{Br}$ phase in the mixture. Because the material obtained after 8 hours reaches the maximum conductivity, this material is used for further investigations and referred to as $\text{Li}_6\text{PS}_5\text{Br}$. Subsequently, this material is annealed at 300°C for 5 h and the resulting material is referred to AN- $\text{Li}_6\text{PS}_5\text{Br}$. Finally, the AN- $\text{Li}_6\text{PS}_5\text{Br}$ is ball-milled at a rotation speed of 450 rpm for 4 hours, the resulting material of which is referred to as AN-BM- $\text{Li}_6\text{PS}_5\text{Br}$. The AC impedance and fitting results for the $\text{Li}_6\text{PS}_5\text{Br}$, AN- $\text{Li}_6\text{PS}_5\text{Br}$ and AN-BM- $\text{Li}_6\text{PS}_5\text{Br}$ samples are shown in Figure 5.1c. The bulk and grain boundary resistances respectively result in (924.8 ± 16.58) and $(3.02 \pm$

5 Revealing the Relation between the Structure, Li-ion Conductivity

$0.64 \cdot 10^6 \Omega$ for $\text{Li}_6\text{PS}_5\text{Br}$, (516.8 ± 32.28) and $(619.9 \pm 22.26) \Omega$ for $\text{AN-Li}_6\text{PS}_5\text{Br}$ and (381.7 ± 10.81) and $(686.8 \pm 35.88) \Omega$ and for $\text{AN-BM-Li}_6\text{PS}_5\text{Br}$. The corresponding room temperature bulk conductivities are $6.20 \cdot 10^{-4}$, $1.11 \cdot 10^{-3}$ and $1.38 \cdot 10^{-3} \text{ S/cm}$ for $\text{Li}_6\text{PS}_5\text{Br}$, $\text{AN-Li}_6\text{PS}_5\text{Br}$ and $\text{AN-BM-Li}_6\text{PS}_5\text{Br}$, respectively. The annealing process increases the conductivity significantly and the subsequent ball milling step appears to further increase the bulk conductivity. Annealing dramatically lowers the grain boundary resistance as observed by impedance spectroscopy, whereas the subsequent ball milling process results in a small increase of the grain boundary resistance. Perhaps the most surprising result is that the bulk conductivity of $\text{AN-BM-Li}_6\text{PS}_5\text{Br}$ is larger than that of the $\text{AN-Li}_6\text{PS}_5\text{Br}$, suggesting that decreasing the particle size of $\text{AN-Li}_6\text{PS}_5\text{Br}$ enhances the Li-ion bulk conductivity. However, it should be realized that in this geometrically complex systems, it is difficult to distinguish the bulk conductivity from the grain boundary resistance using impedance spectroscopy.

5 Revealing the Relation between the Structure, Li-ion Conductivity

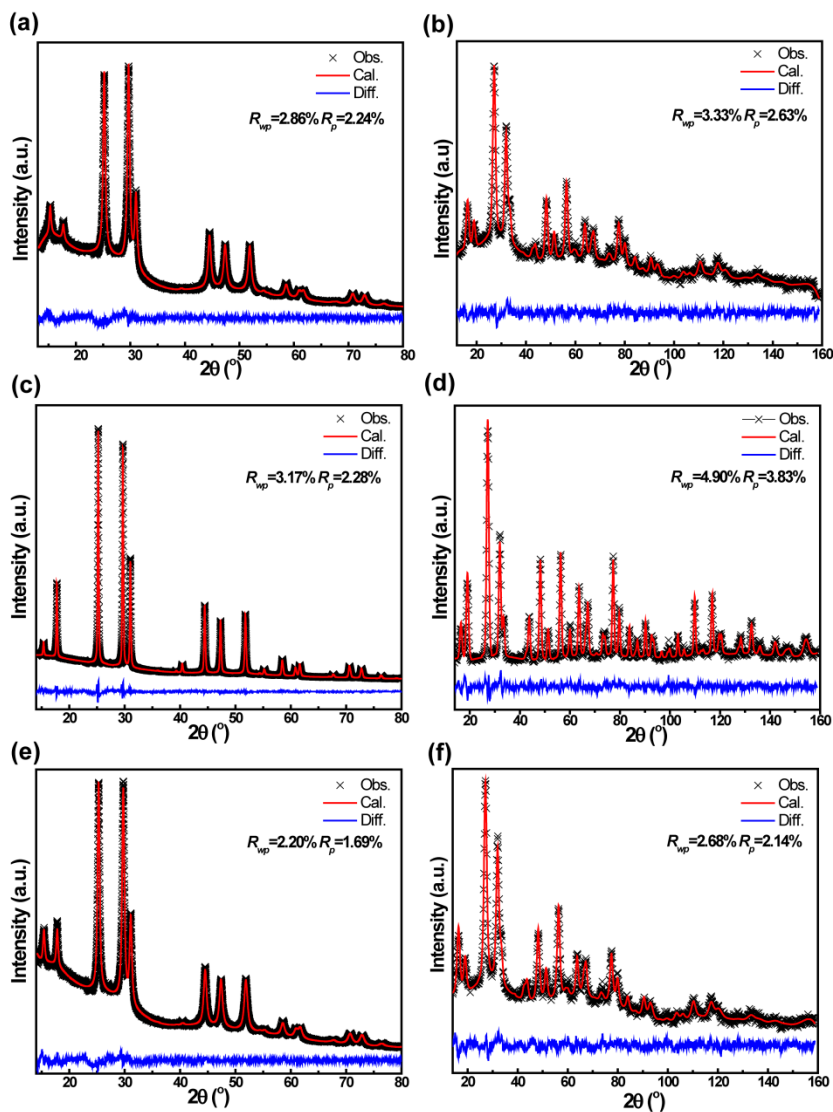


Figure 5.2: Room temperature X-ray and neutron diffraction patterns including Rietveld refinement of the (a-b) $\text{Li}_6\text{PS}_5\text{Br}$, (c-d) $\text{AN-Li}_6\text{PS}_5\text{Br}$, and (e-f) $\text{AN-BM-Li}_6\text{PS}_5\text{Br}$, respectively.

Both powder neutron diffraction and X-ray diffraction were performed, which were simultaneously refined in the cubic $F-43m$ space group using the

Rietveld method as implemented in GSAS²³. The neutron powder patterns and the X-ray patterns of the three $\text{Li}_6\text{PS}_5\text{Br}$ materials are shown in Figure 5.2 and the crystallographic parameters resulting from the refinements are provided in Table 5.1, respectively. The smaller linewidth of the reflections of the AN- $\text{Li}_6\text{PS}_5\text{Br}$ material in Figure 5.2(c-d) compared to that of $\text{Li}_6\text{PS}_5\text{Br}$ in Figure 5.2(a-b) indicates an increase in crystallinity and crystallite size upon annealing. From the refinement of the patterns, assuming only size broadening, the average crystallite size of the $\text{Li}_6\text{PS}_5\text{Br}$ material is 15 nm and 74 nm for the AN- $\text{Li}_6\text{PS}_5\text{Br}$ material. As shown in Figure 5.2(e-f), subsequent ball milling of AN- $\text{Li}_6\text{PS}_5\text{Br}$ resulting in the AN-BM- $\text{Li}_6\text{PS}_5\text{Br}$ material increases the width of the reflections again, leading to an average crystallite size of 22 nm from the refinements. The substantial background observed in the diffraction pattern of $\text{Li}_6\text{PS}_5\text{Br}$, especially visible at low angles in Figure 5.2a, indicates the presence of a significant amorphous fraction. The much lower background in Figure 5.2c indicates that, as expected based on the glass temperature of 265 °C, annealing the sample at 300 °C converts most of the amorphous fraction to the crystalline $\text{Li}_6\text{PS}_5\text{Br}$ phase. For the AN-BM- $\text{Li}_6\text{PS}_5\text{Br}$ material, the background increases again, suggesting that the final ball milling procedure increases the amorphous fraction again. However, the larger lattice parameters of the AN-BM- $\text{Li}_6\text{PS}_5\text{Br}$ material compared to that of the $\text{Li}_6\text{PS}_5\text{Br}$ material and the smaller background suggest that the crystalline fraction of the AN-BM- $\text{Li}_6\text{PS}_5\text{Br}$ material is larger than that of the $\text{Li}_6\text{PS}_5\text{Br}$ material, which is also confirmed by the TEM experiments discussed in the next paragraph.

The simultaneous refinement of the X-ray and neutron diffraction data allows us to determine the average amount of Br and S on the 4a (0,0,0) and 4c (0.25,0.25,0.25) crystallographic sites. Similar to what was found for $\text{Li}_6\text{PS}_5\text{Cl}$ argyrodite,¹⁴ there is a slight preference for Br to occupy the 4c site as shown in Table 5.1. Interestingly, upon annealing, the Br occupancy on the 4c site increases significantly, while decreasing on the 4a site, keeping the total Br content close to

5 Revealing the Relation between the Structure, Li-ion Conductivity

the intended $\text{Li}_6\text{PS}_5\text{Br}$ composition. Note that during the fitting, the total occupancy of the $4a$ site and of the $4c$ site by Br and S is restricted to unity. The increase of the average Br_{4c} occupancy in the AN- $\text{Li}_6\text{PS}_5\text{Br}$ sample indicates that the Br_{4c} occupancy in the amorphous phase of the $\text{Li}_6\text{PS}_5\text{Br}$ sample, which turns crystalline upon annealing, has a larger Br_{4c} occupancy compared to the crystalline fraction of the $\text{Li}_6\text{PS}_5\text{Br}$ sample. Vice versa the Br_{4a} occupancy decreases upon annealing, keeping the total Br occupancy, and hence the Br concentration approximately constant and close to the intended composition as shown in Table 5.1.

Table 5.1: Room temperature X-ray diffraction patterns including Rietveld refinement of the (a) $\text{Li}_6\text{PS}_5\text{Br}$, (b) AN- $\text{Li}_6\text{PS}_5\text{Br}$, (c) and AN-BM- $\text{Li}_6\text{PS}_5\text{Br}$ materials.

	Atom	Fractional coordinates			Wyckoff	Occupancy	U_{iso} (\AA^2)
		X	Y	z			
	Li	0.174(5)	0.174(5)	0.029(0)	48h	0.47(3)	0.172(7)
BM- $\text{Li}_6\text{PS}_5\text{Br}$	P	0.5	0.5	0.5	4b	1.0	0.080(5)
	S(0)	0.617(3)	0.617(3)	0.617(3)	16e	1.0	0.074(3)
F-43m a=9.941(7) \AA	S(1)	0.0	0.0	0.0	4c	0.52(5)	0.080(6)
	Br(1)	0.0	0.0	0.0	4c	0.47(5)	0.025(3)
	S(2)	0.25	0.25	0.25	4a	0.56(3)	0.065(6)
	Br(2)	0.25	0.25	0.25	4a	0.43(7)	0.055(8)
$\text{Li}_{5.67}\text{PS}_{5.09}\text{Br}_{0.91}$, Average crystallite size: 15 nm							

5 Revealing the Relation between the Structure, Li-ion Conductivity

	Atom	Fractional coordinates			Wyckoff	Occupancy	U _{iso}
		X	Y	z			(Å ²)
AN-BM- Li ₆ PS ₅ Br F-43m a=9.974(4) Å	Li	0.196(3)	0.196(3)	0.021(8)	48h	0.48(2)	0.141(4)
	P	0.5	0.5	0.5	4b	1.0	0.054(7)
	S(0)	0.618(6)	0.618(6)	0.618(6)	16e	1.0	0.064(8)
	S(1)	0.0	0.0	0.0	4c	0.24(6)	0.070(6)
	Br(1)	0.0	0.0	0.0	4c	0.75(4)	0.075(8)
	S(2)	0.25	0.25	0.25	4a	0.85(3)	0.061(5)
	Br(2)	0.25	0.25	0.25	4a	0.14(7)	0.050(7)
	Li _{5.78} PS _{5.1} Br _{0.90} , Average crystallite size: 74 nm						
	Atom	Fractional coordinates			Wyckoff	Occupancy	U _{iso}
		X	Y	z			(Å ²)
BM-AN- BM- Li ₆ PS ₅ Br F-43m a=9.971(4) Å	Li	0.173(1)	0.173(1)	0.037(5)	48h	0.46(7)	0.169(1)
	P	0.5	0.5	0.5	4b	1.0	0.067(8)
	S(0)	0.617(2)	0.617(2)	0.617(2)	16e	1.0	0.055(4)
	S(1)	0.0	0.0	0.0	4c	0.53(3)	0.076(2)
	Br(1)	0.0	0.0	0.0	4c	0.47(5)	0.032(1)
	S(2)	0.25	0.25	0.25	4a	0.64(5)	0.088(5)
	Br(2)	0.25	0.25	0.25	4a	0.35(5)	0.031(4)
	Li _{5.60} PS _{5.18} Br _{0.82} , Average crystallite size: 22 nm						

5 Revealing the Relation between the Structure, Li-ion Conductivity

Subsequent ball milling, going from the AN-Li₆PS₅Br to the AN-BM-Li₆PS₅Br sample, decreases the Br_{4c} occupancy (and increases the Br_{4a} occupancy) again to a value still larger (smaller) compared to the Li₆PS₅Br sample. Assuming that upon annealing the amorphous material crystallizes around the crystalline core of the Li₆PS₅Br sample, this indicates that the 4c (4a) occupancy in the center of the particles is larger (smaller) compared to that at the surface of the particles. Hence these results indicate that, although the Br appears homogeneously distributed through the particles, the relative 4a/4c site occupancy is inhomogeneous throughout the particles.

Recently, modeling has shown that the distribution of the halogen dopant over the 4a and 4c sites strongly influences the Li-ion conductivity.²¹ Therefore, the suggested inhomogeneous site distribution of the Br dopant in the present argyrodite materials is likely to result in an inhomogeneous Li-ion conductivity, control of which may be an important parameter for the design of optimal solid electrolytes.

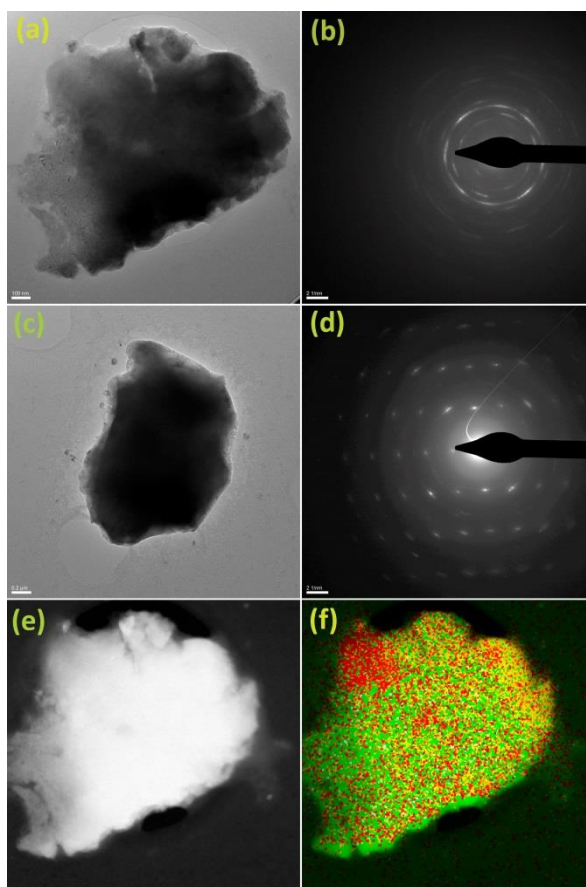


Figure 5.3: High-magnification bright-field TEM images and the corresponding electron diffraction patterns for $\text{Li}_6\text{PS}_5\text{Br}$ (a and b) and AN-BM- $\text{Li}_6\text{PS}_5\text{Br}$ (c and d). EDX mapping for the $\text{Li}_6\text{PS}_5\text{Br}$ sample (e and f). The yellow, green and red dots represent the distribution of S, Br, and P.

Figures 5.3a and 5.3c show the bright-field TEM (BF-TEM) images of the $\text{Li}_6\text{PS}_5\text{Br}$ and AN-BM- $\text{Li}_6\text{PS}_5\text{Br}$ samples, respectively, and Figures 5.3b and 5.3d show the electron diffraction patterns for $\text{Li}_6\text{PS}_5\text{Br}$ and AN-BM- $\text{Li}_6\text{PS}_5\text{Br}$ samples, acquired from the particles shown in 5.3a and 5.3c, respectively. The presence of a ring like diffraction pattern for the $\text{Li}_6\text{PS}_5\text{Br}$ sample, without distinct diffraction

5 Revealing the Relation between the Structure, Li-ion Conductivity

spots, indicates the presence of a significant fraction of the amorphous material. After subsequent annealing and ball milling, the diffraction spots for AN-BM- $\text{Li}_6\text{PS}_5\text{Br}$ become more distinct, indicating that the material becomes more crystalline, as shown in Figure 5.3d. The Scanning Tunneling Microscope-Energy Dispersive X-ray (STEM-EDX) mapping of the $\text{Li}_6\text{PS}_5\text{Br}$ sample (Figure 5.3f) shows a homogenous distribution of S, P and Br, indicating that this mechanical milling route is an effective synthesis method to prepare $\text{Li}_6\text{PS}_5\text{Br}$. Since the AN- $\text{Li}_6\text{PS}_5\text{Br}$ and AN-BM- $\text{Li}_6\text{PS}_5\text{Br}$ are prepared starting from the $\text{Li}_6\text{PS}_5\text{Br}$ sample with subsequent annealing and ball-milling processes, the S, P and Br in those samples are also expected to remain homogeneously distributed.

5.3.2 Solid-state NMR relaxation experiments.

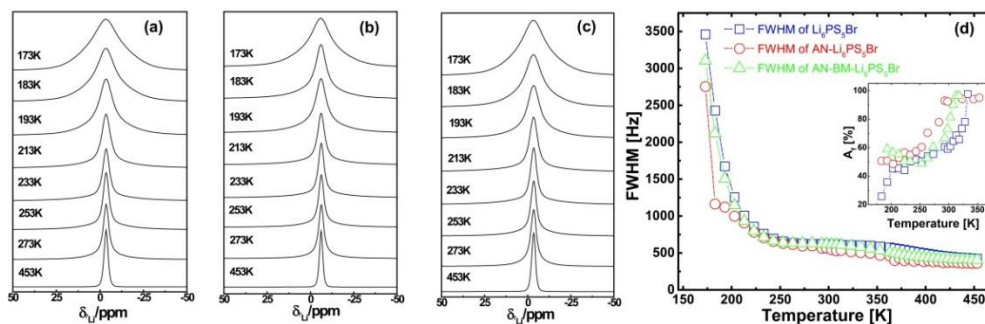


Figure 5.4: ${}^7\text{Li}$ NMR motional narrowing spectra for (a) $\text{Li}_6\text{PS}_5\text{Br}$, (b) AN- $\text{Li}_6\text{PS}_5\text{Br}$ and (c) AN-BM- $\text{Li}_6\text{PS}_5\text{Br}$. (d) Evolution of the FWHM of the static ${}^7\text{Li}$ NMR resonance with temperature for $\text{Li}_6\text{PS}_5\text{Br}$, AN- $\text{Li}_6\text{PS}_5\text{Br}$ and AN-BM- $\text{Li}_6\text{PS}_5\text{Br}$. The inset shows the fraction of the mobile Li-ions in the three materials versus temperature.

Measurement of the ${}^7\text{Li}$ spin-spin (T_2) and spin-lattice (T_1) relaxation time as a function of temperature provides insight into the mobility of Li-ions.²⁵⁻²⁷ The decreasing FWHM of the static ${}^7\text{Li}$ NMR resonances with increasing temperature observed in Figures 5.4(a-c) for the three $\text{Li}_6\text{PS}_5\text{Br}$ samples indicates increased Li-ion mobility, an effect that is referred to as motional narrowing. At lower

temperatures *i.e.* 173 K the ${}^7\text{Li}$ - ${}^7\text{Li}$ dipolar interactions are responsible for the broad resonances observed, which is averaged out when the temperature is increased because the Li-ion hopping frequency exceeds the dipolar interaction strength.²⁸ The low temperature static spectrum can be consistently fitted with a Gaussian line shape. The ${}^7\text{Li}$ resonance of the AN- $\text{Li}_6\text{PS}_5\text{Br}$ shows a much narrower line width than that of $\text{Li}_6\text{PS}_5\text{Br}$, at 173 K, suggesting that a larger fraction of mobile Li-ions is present in the AN- $\text{Li}_6\text{PS}_5\text{B}$ material. The AN-BM- $\text{Li}_6\text{PS}_5\text{Br}$ material has a larger line width than that of AN- $\text{Li}_6\text{PS}_5\text{Br}$ and narrower line width than $\text{Li}_6\text{PS}_5\text{Br}$. A contributing factor towards the broader lines observed for both the ball-milled samples may also be the decreased crystallinity of both the $\text{Li}_6\text{PS}_5\text{Br}$ and AN-BM- $\text{Li}_6\text{PS}_5\text{Br}$ samples. This potentially results in a distribution of chemical shifts, induced by the high energy ball-milling. Interestingly, comparing AN- $\text{Li}_6\text{PS}_5\text{Br}$ to previously studied $\text{Li}_6\text{PS}_5\text{Cl}$ ¹⁷, the $\text{Li}_6\text{PS}_5\text{Br}$ ${}^7\text{Li}$ NMR resonance is shifted up-field to approximately -3 ppm, which is most likely caused by the increased shielding of the Li-ions by the neighboring Br dopants. The motional narrowing curve of $\text{Li}_6\text{PS}_5\text{Br}$, AN-, and AN-BM- $\text{Li}_6\text{PS}_5\text{Br}$ measured versus temperature (See Figure 5.4d) is in good agreement with that published by Epp and co-workers for the $\text{Li}_6\text{PS}_5\text{Br}$ material.²⁹ Epp *et al.* measured NMR spectra at 13 K and obtained an onset temperature for the Li-ion mobility of 87 K. Because of the temperature limitations of the instrument utilized for the present investigation, the measurements do not reach the so called rigid-lattice regime where Li-ion hopping is frozen. Above room temperature, the line shape can be deconvoluted into a narrow Lorentzian and a broad Gaussian which are assigned to mobile and static Li-ion populations, respectively.³⁰ This allows us to evaluate the fraction of mobile Li-ions (A_f) in $\text{Li}_6\text{PS}_5\text{Br}$, AN- and AN-BM- $\text{Li}_6\text{PS}_5\text{Br}$ as a function of temperature, shown in the inset of Figure 5.4d. At 183 K, an A_f value of 25% was determined for $\text{Li}_6\text{PS}_5\text{Br}$, while that for AN- and AN-BM- $\text{Li}_6\text{PS}_5\text{Br}$ is

5 Revealing the Relation between the Structure, Li-ion Conductivity

approximately 50%, indicating that annealing increases the amount of mobile Li-ions significantly.

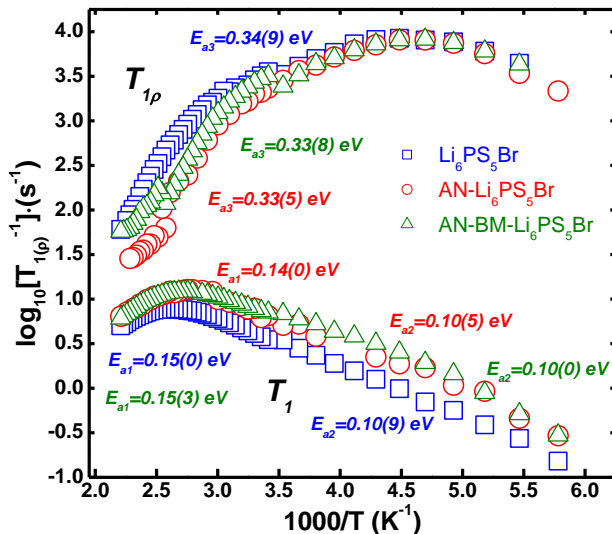


Figure 5.5: Temperature dependence of the ${}^7\text{Li}$ spin-lattice relaxation NMR rates $T_{1(p)}^{-1}$ measured in both the laboratory and the rotating frame of reference for the $\text{Li}_6\text{PS}_5\text{Br}$, $\text{AN-Li}_6\text{PS}_5\text{Br}$ and $\text{AN-BM-Li}_6\text{PS}_5\text{Br}$ materials. The Larmor frequency is 155.506 MHz (T_1^{-1}) and the spin lock frequency is 20 kHz (T_{1p}^{-1}).

To quantitatively determine the local Li-ion temperature-dependent mobility, ${}^7\text{Li}$ static spin-lattice relaxation (SLR) rates in the laboratory frame, $1/T_1$, and in the rotating frame, $1/T_{1p}$ are measured, the results of which are shown in Figure 5.5. Provided that the variation of the SLR is only induced by Li-ion mobility, the temperature dependence of the SLR rate in the laboratory frame, $1/T_1$, can be used to quantify the Li-ion jump frequency and the corresponding activation energy.^{27, 31-33} The longer range ionic motion taking place at a larger time scales can be probed by SLR NMR measurements in the rotating frame.^{27, 31-33} The hopping frequency $1/\tau$, where τ is the residence time, is assumed to be equal to the

5 Revealing the Relation between the Structure, Li-ion Conductivity

correlation time between hops. When $1/T_{1(\rho)}$ reaches a maximum as a function of temperature, the hopping frequency $1/\tau$ is in the order of the Larmor frequency (ω_0) or spin lock frequency (ω_1).^{27, 31-33} In the laboratory frame, the longitudinal relaxation rate $1/T_1$ reaches a maximum near $\omega_0^2 \cdot \tau_c^2 \approx 1$, a consequence of the effective energy transfer between the system with the diffusing atoms. The maximum relaxation rate $1/T_1$ is reached at 383 for $\text{Li}_6\text{PS}_5\text{Br}$ and 358 K for both AN- $\text{Li}_6\text{PS}_5\text{Br}$ and AN-BM- $\text{Li}_6\text{PS}_5\text{Br}$. With a Larmor frequency of $\omega_0/2\pi=155.506$ MHz, the Li-ion jump frequency $1/\tau_c$ for the $\text{Li}_6\text{PS}_5\text{Br}$ (at 383 K) and for AN- $\text{Li}_6\text{PS}_5\text{Br}$ and AN-BM- $\text{Li}_6\text{PS}_5\text{Br}$ (at 358 K) can be determined to be approximately $9.8 \cdot 10^8 \text{ s}^{-1}$, similar to what was reported previously for $\text{Li}_6\text{PS}_5\text{Br}$.²⁹ Because this jump rate is achieved at a lower temperature for both AN- $\text{Li}_6\text{PS}_5\text{Br}$ and AN-BM- $\text{Li}_6\text{PS}_5\text{Br}$, this indicates that these materials have a higher local Li-ion mobility compared to the $\text{Li}_6\text{PS}_5\text{Br}$ material. Taking into account the diffraction results, the origin of the higher Li-ion mobility may originate from the larger crystallinity and/or the Br distribution over the $4a$ and $4c$ sites. The SLR rates, $1/T_1$ and $1/T_{1\rho}$, are directly related to the spectral density functions of the Li-ion jumping processes.³⁴ Assuming a 3D diffusion process, in the high temperature limit, $\tau \cdot \omega_0 \ll 1$, the SLR rates are proportional to the Li-ion residence time τ and in the low temperature limit, $\tau \cdot \omega_0 \gg 1$, the SLR rates are proportional to $\tau^{-1} \cdot \omega_{b(\rho)}^{-\beta}$ (with $1 < \beta \leq 2$). Assuming an Arrhenius behavior for the Li-ion residence time, $\tau = \tau_0 \cdot \exp(-E_a/(k_B T))$, the slope of the high and low temperature regimes of the SLR rates in Figure 5.5 can be related to the activation energy for the Li-ion motional processes. The original BPP behaviour²⁸ predicts symmetric peaks, $\beta = 2$, in the SLR rate as a function of temperature which does not take into account correlation effects and disorder in diffusion.³⁴ In particular the $1/T_1$ rate appears to be asymmetric, most likely the result of Li-ion diffusional processes taking place at different length scales, illustrated by the different transitions predicted by MD

5 Revealing the Relation between the Structure, Li-ion Conductivity

simulations.²¹ In both the low-temperature and high-temperature flanks, the jump rates exhibit Arrhenius behavior, yielding activation energies of 0.10(9) and 0.15(0) eV for $\text{Li}_6\text{PS}_5\text{Br}$, 0.10(5) and 0.14(0) eV for AN- $\text{Li}_6\text{PS}_5\text{Br}$, and 0.10(0) and 0.15(3) eV for AN-BM- $\text{Li}_6\text{PS}_5\text{Br}$, respectively. The asymmetry, quantified by $\beta = 1.73, 1.78$ and 1.67 for $\text{Li}_6\text{PS}_5\text{Br}$, AN- and AN-BM- $\text{Li}_6\text{PS}_5\text{Br}$, is slightly higher than the previous results reported for annealed $\text{Li}_6\text{PS}_5\text{Br}$ probed by temperature dependent SLR NMR ($1/T_1$ and $1/T_{1\rho}$).²⁹ The low temperature flank represents a short range motional process whereas the high temperature flank most likely represents longer range Li-ion resulting in actual diffusion.³⁴ The activation energy for all three $\text{Li}_6\text{PS}_5\text{Br}$ in the high temperature flank are close to that deduced by temperature-dependent ionic conductivity measurements reported by Rao *et al.*¹⁵ *i.e.* 0.17 eV from 300 to 600 K, and are slightly smaller in comparison with the 0.2 eV reported by Epp *et al.*²⁹ The activation energy for three $\text{Li}_6\text{PS}_5\text{Br}$ samples in the low temperature flank, representing local motional processes, is approximately 0.1 eV, which is comparable to the values for the 48h-48h and intra-cage local Li-ion motional processes predicted by MD simulations for $\text{Li}_6\text{PS}_5\text{Br}$.²¹ This suggests that the $1/T_1$ rates in the low temperature flank reflect local Li-ion movement inside $\text{Li}_6\text{PS}_5\text{Br}$ similar to what was found for $\text{Li}_6\text{PS}_5\text{Cl}$.¹⁷

The ^7Li SLR measurements in the rotating frame ($1/T_{1\rho}$), also shown in Figure 5.5, were performed to probe Li-ion mobility on a larger length and time scale in all three $\text{Li}_6\text{PS}_5\text{Br}$ materials to complement the local hopping probed by $1/T_1$ relaxation. In the rotating frame at a lock frequency ω_{lock} , the maximum condition for lithium jump rate is $\omega_{\text{lock}} \cdot \tau \approx 0.5$.³⁵ The corresponding jump rates in this rotating frame (locking frequency 20 kHz) are the same, $2.512 \cdot 10^5 \text{ s}^{-1}$ at 228 K for these three $\text{Li}_6\text{PS}_5\text{Br}$ materials. This indicates that the time scale of Li-ion diffusion on a longer length scale (several hops) is comparable for all three materials. However, the activation energies for the high temperature flank of the

5 Revealing the Relation between the Structure, Li-ion Conductivity

$1/T_{1\rho}$ rates, observed in Figure 5.5, are considerably higher at 0.33-0.34 eV, in comparison with the 0.14-0.15 eV of the high temperature flank of the $1/T_1$ relaxation rates. The larger diffusion time probed by the measurement in the rotating frame suggests that not only the local bulk kinetics are probed, but also that Li-ion diffusion through grain boundaries are observed. The slightly smaller activation energies of the AN-Li₆PS₅Br and AN-BM-Li₆PS₅Br materials deduced from the $1/T_{1\rho}$ rates in the high temperature flank suggests that the annealing process promotes Li-motion in Li₆PS₅Br over longer length scales. This could suggest better mobility over grain boundaries, consistent with the lower grain boundary resistances observed for these materials with room temperature impedance spectroscopy, Figure 5.1c. In summary, the ⁷Li NMR relaxation experiments indicate slightly improved Li-ion mobility for the annealed materials both for local Li-ion hopping, and longer range diffusion, although the activation energies are very similar. The much higher activation energy for the long range diffusion, as observed from the spin locked SRL experiments, suggests that these experiments probe the Li-ion diffusion over grain boundaries.

5.3.3 Electrochemical performance

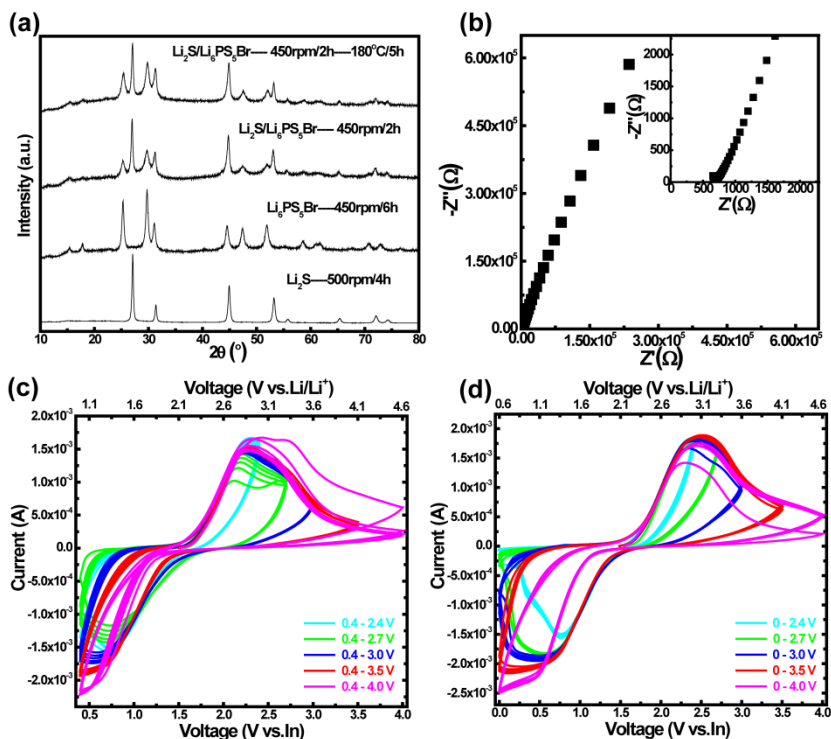


Figure 5.6: (a) XRD patterns of Li_2S cathode, $\text{Li}_6\text{PS}_5\text{Br}$ electrolyte and the mixture of those two. (b) The complex impedance plot for the mixture of Li_2S and $\text{Li}_6\text{PS}_5\text{Br}$ ball milled with 450 rpm for 2 h. Cyclic voltammograms of the nano- $\text{Li}_2\text{S}/\text{AN-Li}_6\text{PS}_5\text{Br}/\text{In}$ all-solid-state batteries for different voltage cut-off windows (c) 0.4 - 2.4, 0.4 - 2.7, 0.4 - 3.0, 0.4 - 3.5, and 0.4 to 4.0 V and (d) 0 - 2.4, 0 - 2.7, 0 - 3.0, 0 - 3.5, and 0 - 4.0 V; all vs. In, at a scanning rate of 0.5 mV/s. The bottom X-axis shows the values of the voltage versus In, the top X-axis shows the corresponding values of voltage versus Li/Li^+ .

When combining a cathode material with a solid electrolyte, it is essential to investigate the chemical and electrochemical stability. Nano- Li_2S was selected as the cathode material for this study and the stability and conductivity of the cathode mixture with the AN- $\text{Li}_6\text{PS}_5\text{Br}$ solid electrolyte was investigated by Cyclic

5 Revealing the Relation between the Structure, Li-ion Conductivity

Voltammetry (CV), powder XRD and AC impedance spectroscopy, the results of which are shown in Figure 5.6. In the diffraction patterns of the Li_2S and AN- $\text{Li}_6\text{PS}_5\text{Br}$ mixture before and after milling and annealing, no additional diffraction peaks are detected, suggesting that nano- Li_2S is stable with the annealed $\text{Li}_6\text{PS}_5\text{Br}$ solid electrolyte up to 180 °C. Another important factor to consider is the overall conductivity of the cathode-electrolyte mixture,³⁶⁻³⁷ which for the present mixture resulted in a resistance of 750 Ω yielding a Li^+ conductivity of $\sim 10^{-4}$ S/cm, indicating that this nano- Li_2S - $\text{Li}_6\text{PS}_5\text{Br}$ cathode mixture is a viable solid-state electrode. Initially, it has been suggested that sulfide solid electrolytes, including the presently investigated argyrodite $\text{Li}_6\text{PS}_5\text{Br}$, have a very wide electrochemical stability window. However, recent calculations³⁸⁻³⁹ and experimental observations indicate otherwise.⁴⁰⁻⁴² The performance of the all-solid-state batteries will depend on the formation of oxidation and/or reduction products at the interfaces between the electrode material and the solid electrolyte, and to what extent this hinders Li-ion transport. Previous results¹⁶⁻¹⁷ on the chloride doped argyrodite $\text{Li}_6\text{PS}_5\text{Cl}$ solid electrolyte have shown that the (dis)charge voltage window has a significant influence on the electrochemical performances of these solid-state batteries. At present, the optimal (dis)charge voltage window was determined for the nano- Li_2S /AN- $\text{Li}_6\text{PS}_5\text{Br}$ /In solid-state batteries by systematic variation of the voltage window for cyclic voltammetry (CV) measurements, shown in Figure 5.6. This indicates that the highest apparent coulombic efficiency, and hence the optimum charge/discharge window for this assembled nano- Li_2S /AN- $\text{Li}_6\text{PS}_5\text{Br}$ /In solid-state cell is between 0 and 3.5 V vs. In (from 0.6 to 4.1 V vs. Li/Li^+).

5 Revealing the Relation between the Structure, Li-ion Conductivity

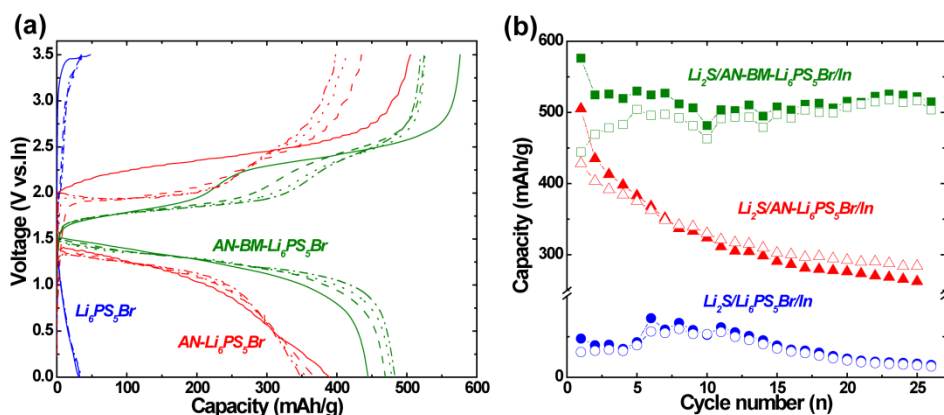


Figure 5.7: (a) Galvanostatic voltage curves for the first 4 cycles of the assembled nano- $\text{Li}_2\text{S}/\text{Li}_6\text{PS}_5\text{Br}$ ($\text{Li}_6\text{PS}_5\text{Br}$ or $\text{AN-Li}_6\text{PS}_5\text{Br}$ or $\text{AN-BM-Li}_6\text{PS}_5\text{Br}$)/In solid-state batteries at a current density of $0.064 \text{ mA}/\text{cm}^2$ applied between 0 and 3.5 V vs. In (0.62 - 4.12 V vs. Li^+/Li). The solid, dashed, dotted and dashed dotted lines represent cycles 1-4 respectively. (b) Capacity retention cycling of the solid-state batteries at a current density of $0.064 \text{ mA}/\text{cm}^2$ applied between 0 and 3.5 V vs. In (0.62 - 4.12 V vs. Li^+/Li).

To investigate the impact of annealing and subsequent ball milling treatment on the solid-state battery performance, cathodic mixtures of the nano- Li_2S cathode were prepared with the $\text{Li}_6\text{PS}_5\text{Br}$, $\text{AN-Li}_6\text{PS}_5\text{Br}$ and $\text{AN-BM-Li}_6\text{PS}_5\text{Br}$ solid electrolyte materials. In Figure 5.7a, the first 4 charge/discharge curves are compared at the same current density of $0.064 \text{ mA}/\text{cm}^2$ in the earlier determined optimal voltage window of 0 - 3.5 V vs. In (0.62 - 4.12 V vs. Li^+/Li). The differences in capacity retention are striking, where the solid-state cell using $\text{AN-BM-Li}_6\text{PS}_5\text{Br}$ shows a significantly better electrochemical performance when compared to that for both the $\text{AN-Li}_6\text{PS}_5\text{Br}$ and $\text{Li}_6\text{PS}_5\text{Br}$ solid electrolyte materials. For the solid-state cell using $\text{Li}_6\text{PS}_5\text{Br}$ as electrolyte, the (dis)charge curves during the first four cycles show no obvious (dis)charge plateau and a very low discharge capacity, less than 50 mAh/g. In contrast, the charge curve of the solid-state cells with the $\text{AN-Li}_6\text{PS}_5\text{Br}$ and $\text{AN-BM-Li}_6\text{PS}_5\text{Br}$ solid electrolytes

5 Revealing the Relation between the Structure, Li-ion Conductivity

deliver two distinct charge plateaus, located at 1.8 and 2.3 V vs. In, respectively and a discharge plateau located at approximately 1.4 V vs. In. Although the AN-Li₆PS₅Br solid-state cell results in a promising initial discharge capacity, it degrades to below 400 mAh/g within a few cycles. The best capacity retention is achieved with the AN-BM-Li₆PS₅Br solid electrolyte, resulting in a capacity of approximately 500 mAh/g retained over 25 cycles. The initial discharge capacity is comparable to that demonstrated by Li₂S cathodes in combination with organic liquid electrolytes, which is reported to be 785 mAh/g at a higher rate i.e. 0.2 C.⁴³ The present mixture III provides a higher discharge capacity and better cyclability compared to most reported comparable solid-state cells employing composite Li₂S electrodes in combination with argyrodite and 80Li₂S-20P₂S₅ solid electrolytes.^{19,27,53-55} However, the electrochemical performance reported in this work is not as good as that for the solid-state cell in combination with a mixed-conductive Li₂S nanocomposite cathode and Li₆PS₅Cl electrolyte⁴⁴ which is most likely due to the better distribution of Li₂S, Li₆PS₅Cl and carbon in the cathode mixture.

During the first 5 cycles, the discharge capacity increases per cycle, this is attributed to the activation process of the Li₂S cathode mixture. However, a higher charge capacity than discharge capacity is observed over many cycles. This may indicate that not only the Li₂S cathode is oxidized but also the Li₆PS₅Br electrolyte at the interface with the Li₂S may be oxidized. Calculations indicate that a very narrow stability window for argyrodite Li₆PS₅Cl,³⁸⁻³⁹ resulting in S, P₂S₅ and LiCl oxidation products above 2.3 V vs. Li/Li⁺. For Li₆PS₅Br at the Li₂S interface, this suggests that cycling up to 4.12 V vs. Li⁺/Li during charge leads to the formation of S, P₂S₅ and LiBr in the present cells, potentially explaining the larger charge capacity observed during cycling. It should be noted that this potentially increases the amount of S in the cell, acting as a positive electrode material that may participate in subsequent (dis)charge cycles. This demonstrates a compromise

5 Revealing the Relation between the Structure, Li-ion Conductivity

made in using a large cut-off potential during charge. The large cut-off potential is necessary to overcome the large internal resistance, most likely dominated by the $\text{Li}_6\text{PS}_5\text{Br-Li}_2\text{S}$ interface, and utilize the Li_2S capacity. At the same time, this initiates the oxidation of the $\text{Li}_6\text{PS}_5\text{Br}$ solid electrolyte. This suggests that the poor capacity retention of the AN- $\text{Li}_6\text{PS}_5\text{Br}$ material, shown in Figure 5.7b, is related to the larger overpotentials during charge and discharge, observed in Figure 5.7a, causing more severe electrolyte decomposition. As the bulk and grain boundary conductivity of the AN- $\text{Li}_6\text{PS}_5\text{Br}$ and AN-BM- $\text{Li}_6\text{PS}_5\text{Br}$ does not differ very much, which is concluded from impedance spectroscopy and the solid state NMR relaxation experiments, the larger overpotentials of the AN- $\text{Li}_6\text{PS}_5\text{Br}$ material must be the consequence of the larger crystallite size providing less interfacial area with the Li_2S cathode and hence posing a larger interfacial resistance.

In contrast, the larger interfacial area provided by the AN-BM- $\text{Li}_6\text{PS}_5\text{Br}$ material, results in lower overpotentials. This appears to cause the stabilization of the $\text{Li}_6\text{PS}_5\text{Br}$, as the differences of (dis)charge capacity becomes smaller upon cycling in Figure 5.7. Hence, despite of the suggested formation of an oxidation layer at the $\text{Li}_6\text{PS}_5\text{Br-Li}_2\text{S}$ interface, as well as the large volumetric changes that occur upon Li_2S oxidation, these solid-state cells provide a relatively constant capacity retention, at least up to 25 cycles.

5.4 Conclusions

The impedance spectra in Figure 5.1c indicate a significant increase in the bulk conductivity upon annealing the $\text{Li}_6\text{PS}_5\text{Br}$ material (AN- $\text{Li}_6\text{PS}_5\text{Br}$) prepared by ball milling. The NMR relaxation experiments in Figures 5.4 and 5.5 show that the bulk Li-ion mobility is only marginally improved, and that the increase in conductivity should be mainly attributed to the larger fraction of mobile Li-ions. This increase is most likely due to the increased crystalline fraction present shown by XRD and TEM in Figures 5.2 and 5.3, which is known to display a better mobility⁴⁵.

Additionally, the simultaneous refinements of the neutron and X-ray diffraction data suggest that the conductivity may be inhomogeneous due to differences of the Br dopant distribution throughout the $\text{Li}_6\text{PS}_5\text{Br}$ particles. Although the Br dopant appears to be homogeneously distributed over the material, it is not homogeneously distributed over two crystallographic sites. For the annealed materials, AN- $\text{Li}_6\text{PS}_5\text{Br}$ and AN-BM- $\text{Li}_6\text{PS}_5\text{Br}$, the site distribution appears to be more favorable for a high conductivity in the crystalline fraction that forms due to the annealing process. An interesting future research direction may be to investigate the role of these distributions in solid-state battery performances, and synthesis routes to control the site distribution of the halogen dopant.

Annealing lowers the grain boundary resistance dramatically, whereas subsequent ball milling results in a slight increase in grain boundary resistance. Compared to the T_1 NMR relaxation experiments, the $T_{1\rho}$ experiments probe a longer diffusion length scale. The much larger activation energy deduced from the $T_{1\rho}$ experiments suggests this includes diffusion across grain boundaries processes. However, these larger activation energies observed change only marginally with annealing and ball milling treatment, suggesting that this does not change the Li-ion dynamics across the grain boundary regions. This also suggests that at the $\text{Li}_6\text{PS}_5\text{Br}$ - $\text{Li}_6\text{PS}_5\text{Br}$ interfaces, a larger crystalline fraction is beneficial for the conductivity, most likely increasing the fraction of mobile ions at the interfaces, rather than the mobility itself. Additionally, we anticipate that the inhomogeneous distribution of Br over the two crystallographic sites may be at least partially responsible for the larger Li-ion mobility at the interfaces.

Both impedance spectroscopy and NMR experiments indicate a very similar bulk and grain boundary Li-ion mobility for the annealed (AN- $\text{Li}_6\text{PS}_5\text{Br}$ average crystallite size 74 nm) and additionally ball milled (AN-BM- $\text{Li}_6\text{PS}_5\text{Br}$ average

5 Revealing the Relation between the Structure, Li-ion Conductivity

crystallite size 22 nm) materials. However, solid-state battery with AN-BM- $\text{Li}_6\text{PS}_5\text{Br}$ electrolyte provides much better capacity retention upon cycling. The smaller particles of the annealed and ball milled material, AN-BM- $\text{Li}_6\text{PS}_5\text{Br}$, appear essential for stable capacity retention, most likely through the establishment of more abundant interfacial contacts with the Li_2S cathode resulting from the higher surface area of the small solid electrolyte particles, lowering the interfacial resistance. These results indicate a difference in demands for the solid electrolyte in the solid electrolyte region of the cell compared to the solid electrolyte in the cathode mixture. In the solid electrolyte region, the lowest overall resistance dominated by the grain boundary resistance is achieved for the annealed material (AN- $\text{Li}_6\text{PS}_5\text{Br}$), whereas smaller solid electrolyte particle sizes are required to provide sufficient solid electrolyte-cathode interfaces, to minimize the resistance of this rate limiting Li-ion transport step.

In conclusion, the internal resistance of the solid electrolyte is dominated by the solid electrolyte-solid electrolyte $\text{Li}_6\text{PS}_5\text{Br}$ interfaces, lowering of which can be achieved by annealing treatment. The results indicate that an inhomogeneous distribution of the Br dopant over the crystallite sites may play an important role in the conductivity at the interfaces. The largest contributor to the internal resistance of the $\text{Li}_2\text{S}/\text{Li}_6\text{PS}_5\text{Br}/\text{In}$ solid-state battery appears to exist at the $\text{Li}_6\text{PS}_5\text{Br}/\text{Li}_2\text{S}$ interface. To utilize a majority of the Li_2S capacity, a large overpotential is required, even at the low currents. This compromises the electrochemical stability of the $\text{Li}_6\text{PS}_5\text{Br}$ solid electrolyte, most likely leading to oxidation products. Despite the electrochemical instability at the $\text{Li}_6\text{PS}_5\text{Br}/\text{Li}_2\text{S}$ interface and the large volumetric changes upon charging Li_2S , the capacity retention of this all-solid-state battery is promising, most likely because of the abundant $\text{Li}_6\text{PS}_5\text{Br}/\text{Li}_2\text{S}$ interfaces that provide sufficient Li-ion conductivity and the large fraction of $\text{Li}_6\text{PS}_5\text{Br}$ in the positive electrode mixture. Evidently, the improvement of these solid-state battery

systems requires focusing on the stabilization of the solid electrolyte-electrode interfaces, both towards electrochemical instabilities and volumetric changes. Additionally, the present results indicate the importance of inhomogenizing in the conductivity and the importance of distinguishing between the electrolyte properties only in the electrolyte region and the electrolyte in the cathode mixture.

References

1. Fergus, J. W., Ceramic and polymeric solid electrolytes for lithium-ion batteries. *J Power Sources* **2010**, *195* (15), 4554-4569.
2. Knauth, P., Inorganic solid Li ion conductors: An overview. *Solid State Ionics* **2009**, *180* (14-16), 911-916.
3. Jung, Y. S.; Oh, D. Y.; Nam, Y. J.; Park, K. H., Issues and Challenges for Bulk-Type All-Solid-State Rechargeable Lithium Batteries using Sulfide Solid Electrolytes. *Israel J Chem* **2015**, *55* (5), 472-485.
4. Bachman, J. C.; Muy, S.; Grimaud, A.; Chang, H.-H.; Pour, N.; Lux, S. F.; Paschos, O.; Maglia, F.; Lupart, S.; Lamp, P., Inorganic Solid-State Electrolytes for Lithium Batteries: Mechanisms and Properties Governing Ion Conduction. *Chemical reviews* **2015**, *116* (1), 140-162.
5. Mizuno, F.; Hayashi, A.; Tadanaga, K.; Tatsumisago, M., New, Highly Ion-Conductive Crystals Precipitated from $\text{Li}_2\text{S-P}_2\text{S}_5$ Glasses. *Adv Mater* **2005**, *17* (7), 918-921.
6. Kamaya, N.; Homma, K.; Yamakawa, Y.; Hirayama, M.; Kanno, R.; Yonemura, M.; Kamiyama, T.; Kato, Y.; Hama, S.; Kawamoto, K.; Mitsui, A., A lithium superionic conductor. *Nature Materials* **2011**, *10* (9), 682-686.
7. Deiseroth, H.-J.; Kong, S.-T.; Eckert, H.; Vannahme, J.; Reiner, C.; Zaiß, T.; Schlosser, M., $\text{Li}_6\text{PS}_5\text{X}$: A Class of Crystalline Li-Rich Solids With an Unusually High Li^+ Mobility. *Angewandte Chemie International Edition* **2008**, *47* (4), 755-758.
8. Thangadurai, V.; Narayanan, S.; Pinzaru, D., Garnet-type solid-state fast Li ion conductors for Li batteries: critical review. *Chem. Soc. Rev.* **2014**, *43* (13), 4714-4727.
9. Aono, H.; Sugimoto, E.; Sadaoka, Y.; Imanaka, N.; Adachi, G. y., Ionic conductivity of solid electrolytes based on lithium titanium phosphate. *J Electrochem Soc* **1990**, *137* (4), 1023-1027.
10. Kim, J. G.; Son, B.; Mukherjee, S.; Schuppert, N.; Bates, A.; Kwon, O.; Choi, M. J.; Chung, H. Y.; Park, S., A review of lithium and non-lithium based solid state batteries. *Journal of Power Sources* **2015**, *282*, 299-322.

5 Revealing the Relation between the Structure, Li-ion Conductivity

11. Cao, C.; Li, Z.-B.; Wang, X.-L.; Zhao, X.-B.; Han, W.-Q., Recent advances in inorganic solid electrolytes for lithium batteries. *Frontiers in Energy Research* **2014**, *2*, 25.
12. Takada, K., Progress and prospective of solid-state lithium batteries. *Acta Materialia* **2013**, *61* (3), 759-770.
13. Seino, Y.; Ota, T.; Takada, K.; Hayashi, A.; Tatsumisago, M., A sulphide lithium super ion conductor is superior to liquid ion conductors for use in rechargeable batteries. *Energ Environ Sci* **2014**, *7* (2), 627-631.
14. Rao, R. P.; Sharma, N.; Peterson, V. K.; Adams, S., Formation and conductivity studies of lithium argyrodite solid electrolytes using in-situ neutron diffraction. *Solid State Ionics* **2013**, *230*, 72-76.
15. Rayavarapu, P.; Sharma, N.; Peterson, V.; Adams, S., Variation in structure and Li⁺-ion migration in argyrodite-type Li₆PS₅X (X = Cl, Br, I) solid electrolytes. *J Solid State Electr* **2012**, *16* (5), 1807-1813.
16. Chuang Yu, L. v. E., Swapna Ganapathy, Marnix Wagemaker, Synthesis, structure and electrochemical performance of the argyrodite Li₆PS₅Cl solid electrolyte for Li-ion solid state batteries. *Electrochim Acta* **2016**, *215*, 93-99.
17. Yu, C.; Ganapathy, S.; de Klerk, N. J.; Roslon, I.; Van Eck, E. R.; Kentgens, A. P.; Wagemaker, M., Unravelling Li-ion transport from pico-seconds to seconds: Bulk versus interfaces in an argyrodite Li₆PS₅Cl-Li₂S all solid state Li-ion battery. *J Am Chem Soc* **2016**.
18. Boulineau, S.; Courty, M.; Tarascon, J.-M.; Viallet, V., Mechanochemical synthesis of Li-argyrodite Li₆PS₅X (X = Cl, Br, I) as sulfur-based solid electrolytes for all solid state batteries application. *Solid State Ionics* **2012**, *221*, 1-5.
19. Chen, M.; Rao, R. P.; Adams, S., High capacity all-solid-state Cu-Li₂S/Li₆PS₅Br/In batteries. *Solid State Ionics* **2014**, *262*, 183-187.
20. Richards, W. D.; Miara, L. J.; Wang, Y.; Kim, J. C.; Ceder, G., Interface stability in solid-state batteries. *Chem Mater* **2015**, *28* (1), 266-273.
21. de Klerk, N. J.; Roslon, I.; Wagemaker, M., Diffusion mechanism of Li-argyrodite solid electrolytes for Li-ion batteries and prediction of optimised halogen doping: the effect of Li-vacancies, halogens, and halogen disorder. *Chem Mater* **2016**.
22. van Eijck, L.; Cussen, L. D.; Sykora, G. J.; Schooneveld, E. M.; Rhodes, N. J.; van Well, A. A.; Pappas, C., Design and performance of a novel neutron powder diffractometer: PEARL at TU Delft. *Journal of Applied Crystallography* **2016**, *49* (5), 1398-1401.
23. Toby, B. H., EXPGUI, a graphical user interface for GSAS. *Journal of applied crystallography* **2001**, *34* (2), 210-213.
24. Ujiie, S.; Hayashi, A.; Tatsumisago, M., Structure, ionic conductivity and electrochemical stability of Li₂S-P₂S₅-LiI glass and glass-ceramic electrolytes. *Solid State Ionics* **2012**, *211*, 42-45.

25. Wagemaker, M., *Structure and Dynamics of Lithium in Anastase TiO₂*. TU Delft, Delft University of Technology: 2003.
26. Wagemaker, M.; van de Krol, R.; Kentgens, A. P. M.; van Well, A. A.; Mulder, F. M., Two Phase Morphology Limits Lithium Diffusion in TiO₂ (Anatase): A ⁷Li MAS NMR Study. *J Am Chem Soc* **2001**, *123* (46), 11454-11461.
27. Wilkening, M.; Heitjans, P., From Micro to Macro: Access to Long-Range Li⁺ Diffusion Parameters in Solids via Microscopic ^{6,7}Li Spin-Alignment Echo NMR Spectroscopy. *Chemphyschem* **2012**, *13* (1), 53-65.
28. Bloembergen, N.; Purcell, E. M.; Pound, R. V., Relaxation Effects in Nuclear Magnetic Resonance Absorption. *Physical Review* **1948**, *73* (7), 679-712.
29. Epp, V.; Gün, Ö.; Deiseroth, H.-J.; Wilkening, M., Highly Mobile Ions: Low-Temperature NMR Directly Probes Extremely Fast Li⁺ Hopping in Argyrodite-Type Li₆PS₅Br. *The Journal of Physical Chemistry Letters* **2013**, *4* (13), 2118-2123.
30. Gupta, A.; Murugan, R.; Paranthaman, M. P.; Bi, Z.; Bridges, C. A.; Nakanishi, M.; Sokolov, A. P.; Han, K. S.; Hagaman, E. W.; Xie, H.; Mullins, C. B.; Goodenough, J. B., Optimum lithium-ion conductivity in cubic Li_{7-x}La₃Hf_{2-x}Ta_xO₁₂. *J Power Sources* **2012**, *209*, 184-188.
31. Epp, V.; Wilkening, M., Li-ion Dynamics in Solids as Seen Via Relaxation NMR. In *Handbook of Solid State Batteries*, 2nd ed.; WORLD SCIENTIFIC: 2015; pp 133-190.
32. Kuhn, A.; Kunze, M.; Sreeraj, P.; Wiemhoefer, H. D.; Thangadurai, V.; Wilkening, M.; Heitjans, P., NMR relaxometry as a versatile tool to study Li ion dynamics in potential battery materials. *Solid State Nuclear Magnetic Resonance* **2012**, *42*, 2-8.
33. Kuhn, A.; Narayanan, S.; Spencer, L.; Goward, G.; Thangadurai, V.; Wilkening, M., Li self-diffusion in garnet-type Li₇La₃Zr₂O₁₂ as probed directly by diffusion-induced ⁷Li spin-lattice relaxation NMR spectroscopy. *Physical Review B* **2011**, *83* (9), 094302.
34. *Diffusion in Condensed Matter - Methods, Materials, Models*. Springer: Berlin, 2005.
35. Kuhn, A.; Choi, J.-Y.; Robben, L.; Tietz, F.; Wilkening, M.; Heitjans, P., Li Ion Dynamics in Al-Doped Garnet-Type Li₇La₃Zr₂O₁₂ Crystallizing with Cubic Symmetry. *Zeitschrift für Physikalische Chemie International journal of research in physical chemistry and chemical physics* **2012**, *226* (5-6), 525-537.
36. Yu, C.; Wang, H.; Guan, X.; Zheng, J.; Li, L., Conductivity and electrochemical performance of cathode xLi₂MnO₃·(1-x)LiMn_{1/3}Ni_{1/3}Co_{1/3}O₂ (x = 0.1, 0.2, 0.3, 0.4) at different temperatures. *Journal of Alloys and Compounds* **2013**, *546*, 239-245.

5 Revealing the Relation between the Structure, Li-ion Conductivity

37. Park, M.; Zhang, X.; Chung, M.; Less, G. B.; Sastry, A. M., A review of conduction phenomena in Li-ion batteries. *J Power Sources* **2010**, *195* (24), 7904-7929.
38. Richards, W. D.; Miara, L. J.; Wang, Y.; Kim, J. C.; Ceder, G., Interface Stability in Solid-State Batteries. *Chem Mater* **2016**, *28* (1), 266-273.
39. Zhu, Y.; He, X.; Mo, Y., Origin of outstanding stability in the lithium solid electrolyte materials: insights from thermodynamic analyses based on first-principles calculations. *Acs Appl Mater Inter* **2015**, *7* (42), 23685-23693.
40. Sakuda, A.; Hayashi, A.; Tatsumisago, M., Interfacial Observation between LiCoO₂ Electrode and Li₂S-P₂S₅ Solid Electrolytes of All-Solid-State Lithium Secondary Batteries Using Transmission Electron Microscopy. *Chem Mater* **2010**, *22* (3), 949-956.
41. Sakuda, A.; Hayashi, A.; Ohtomo, T.; Hama, S.; Tatsumisago, M., All-solid-state lithium secondary batteries using LiCoO₂ particles with pulsed laser deposition coatings of Li₂S-P₂S₅ solid electrolytes. *Journal of Power Sources* **2011**, *196* (16), 6735-6741.
42. Visbal, H.; Aihara, Y.; Ito, S.; Watanabe, T.; Park, Y.; Doo, S., The effect of diamond-like carbon coating on LiNi_{0.8}Co_{0.15}Al_{0.05}O₂ particles for all-solid-state lithium-ion batteries based on Li₂S-P₂S₅ glass-ceramics. *Journal of Power Sources* **2016**, *314*, 85-92.
43. Seh, Z. W.; Wang, H.; Hsu, P.-C.; Zhang, Q.; Li, W.; Zheng, G.; Yao, H.; Cui, Y., Facile synthesis of Li₂S-polypyrrole composite structures for high-performance Li₂S cathodes. *Energ Environ Sci* **2014**, *7* (2), 672-676.
44. Han, F.; Yue, J.; Fan, X.; Gao, T.; Luo, C.; Ma, Z.; Suo, L.; Wang, C., High-Performance All-Solid-State Lithium-Sulfur Battery Enabled by a Mixed-Conductive Li₂S Nanocomposite. *Nano Lett* **2016**, *16* (7), 4521-7.
45. Hayashi, A.; Noi, K.; Tanibata, N.; Nagao, M.; Tatsumisago, M., High sodium ion conductivity of glass-ceramic electrolytes with cubic Na₃PS₄. *J Power Sources* **2014**, *258*, 420-423.

6

Accessing the Bottleneck in All-Solid-State Batteries, Li-ion Transport over the Interface between the Solid-Electrolyte and Electrode

This chapter is based on the paper: “*Accessing the bottleneck in all-solid state batteries, Li-ion transport over the interface between the solid-electrolyte and electrode*”, Chuang Yu[#], Swapna Ganapathy[#], Ernst R.H. van Eck, Heng Wang, Shibabrata Basak, Zhaolong Li and Marnix Wagemaker*, [Nature Communications](#), accepted.

6.1 Introduction

The high energy density and long cycle life of Li-ion batteries has enabled the development of mobile electronic equipment, and recently of electrical vehicles (EV's) and static energy storage to stabilize the grid and balance renewable energy supply and demand. However, the use of liquid organic electrolytes in Li-ion batteries raises safety issues, in particular for relatively large systems as employed in electrical cars and grid storage. The origin of the safety risk is the gas production and leakage of the flammable liquid organic electrolytes when operating at high voltages and/or elevated temperatures. A potential solution is the use of solid-state electrolytes, a goal which has been pursued for many decades.¹⁻¹¹ Recently, solid-state Li-ion battery research has intensified dramatically,^{4-9, 12-15} propelled by the development of several structural families of highly conductive solid electrolytes including LISICON like compounds,^{14, 16-18} Argyrodites,¹⁹ Garnets,²⁰⁻²¹ and NASICON type structures²².

In addition to the improved battery safety, solid electrolytes potentially offer additional advantages. These include freedom in design of the battery geometry and improvement of the packing efficiency of the cells, which will enable increased practical battery energy densities. Additionally, a number of solid-state electrolytes may offer a larger electrochemical stability window compared to liquid electrolytes or lead to a narrow stable interfacial passivation layer, which facilitates a long cycle life and offers the possibility of employing high-voltage cathodes, which in turn further increase the battery energy density. On the anode side, solid-state batteries open the door to safe application of Li-metal by suppressing dendrite formation, also increasing the energy density.

Despite the great progress in synthesizing excellent Li-ion conducting solid electrolytes, the rate capability of almost all-solid-state cells is poor, in particular those employing cathodes undergoing a high volume change such as sulphide

based electrodes²³⁻³¹ and those utilizing high-voltage cathodes.³²⁻³³ Despite providing a high bulk Li-ion conductivity, the poor rate and cycle performance of solid-state batteries is ascribed to a high internal resistance for Li-ion transfer over the solid-solid electrode-electrolyte interfaces.^{4-9, 33-39} Although difficult to ascertain experimentally, the origin of the interfacial resistance will depend on the electrode-electrolyte combination and its preparation route. Both chemical incompatibility and a narrow solid electrolyte electrochemical window^{4, 11, 40} may result in an interface layer that poses high resistance towards Li-ion transport.³³⁻⁴² Driven by the potential difference between the positive electrode and electrolyte, the interfaces will induce space charges, potentially leading to local Li-ion depletion of the electrolyte. This poses an additional hurdle for Li-ion transport over the solid-solid electrode-electrolyte interface.^{36, 43} Finally, perhaps one of the biggest challenges is the mechanical stability, where the volume changes of electrode materials during (dis)charge may cause loss of contact between the electrode and the electrolyte particles, blocking Li-ion transport across the interface. These challenges indicate that whether or not solid-state batteries will be able to deliver the performance necessary for EV's will depend on the development of stable interfaces that allow facile ionic charge transfer. Several strategies have been developed to improve the interface resistances; an example of which includes coating the electrodes with an oxide barrier layer enabling high-rate cycling.^{38, 43} To guide the interfacial design, it is paramount to investigate interface reactions and charge transport over the solid-solid electrode-electrolyte interfaces. The charge transfer resistance is most often estimated by impedance spectroscopy, which appears accurate in well-defined thin film solid-state batteries, but difficult if not impossible in the complex morphologies of bulk solid-state batteries.⁴⁴ Using impedance spectroscopy, it is not trivial to distinguish the interface from the bulk Li-ion conductivity as it probes the charge kinetics over tens of nanometers,

including the influence of porosity, grain boundaries and effects introduced by the contact of the solid electrolyte under investigation with the electrodes.

Nuclear magnetic resonance (NMR) spectroscopy, a non-destructive contactless probe, has been shown to offer unique complementary information to impedance spectroscopy, by its high sensitivity towards the Li-ion mobility in bulk battery materials.⁴⁵⁻⁴⁸ An additional opportunity provided by solid-state NMR in multi-phase battery materials, either consisting of multiple electrode phases or a mixture of electrode and electrolyte phases, is the possibility to measure the spontaneous Li-ion exchange between different lithium containing phases. This provides unique selectivity for charge transfer over phase boundaries,^{24, 47, 49} as recently shown to be feasible for the $\text{Li}_6\text{PS}_5\text{Cl-Li}_2\text{S}$ solid electrolyte-electrode combination.²⁴

Here we employ for the first time two-dimensional exchange NMR spectroscopy (2D-EXSY) providing unique quantitative insight in the spontaneous exchange between a solid electrolyte and an electrode. Enabled by the difference in NMR chemical shift, the Li-ion transport was determined over the interface of the $\text{Li}_6\text{PS}_5\text{Br-Li}_2\text{S}$ cathode mixture at different stages in the preparation and before and after cycling, giving unprecedented insight into the evolution of the resistance between the solid electrolyte and cathode. Nano-sizing Li_2S and establishing intimate contact with the argyrodite $\text{Li}_6\text{PS}_5\text{Br}$ electrolyte is shown to be necessary to provide measurable charge transfer over the interfaces. Although charge transport over the $\text{Li}_6\text{PS}_5\text{Br-Li}_2\text{S}$ interfaces is facile, the small amount of contact area in pristine, uncycled, cathodic mixtures, results in an interfacial conductivity that is orders of magnitude smaller than the bulk conductivity. After cycling, the Li-ion kinetics over the interface dramatically decrease, most likely due to both the large volumetric changes that compromise the interfacial contact and by increased barriers for diffusion due to the formation of side products. Both these factors are

responsible for the decrease in capacity during repeated cycling. These observations demonstrate the crucial importance of developing strategies that preserve the interfacial integrity during cycling, and introduce the unique ability of exchange NMR to investigate the interfacial charge transport allowing direct and non-invasive quantification.

6.2 Experimental

Reagent-grade Li_2S (99.98%, Sigma-Aldrich), P_2S_5 (99%, Sigma-Aldrich), and LiBr (99.0%, Sigma-Aldrich) crystalline powders were used as raw materials. The required amount of starting materials according to the molar ratios were ball milled in a WC coated (inner) stainless steel jar with 10 WC balls (8 g/ball) filled in an Argon filled glovebox (H_2O , $\text{O}_2 < 0.3$ ppm) because of the reactivity with oxygen and moisture. The total weight of the mixture was almost 2.0 g in the jar and the ball milling rotation speed was fixed at 600 rpm for 15 h. After the ball milling process the mixture was sealed in a quartz tube and annealed at 300 °C for 5 h to obtain the final $\text{Li}_6\text{PS}_5\text{Br}$ powder. The pristine Li_2S - $\text{Li}_6\text{PS}_5\text{Br}$ mixtures I-IV used in this work were prepared as follows; For mixture I, commercial Li_2S (99.98%, Sigma-Aldrich) and ball-milled $\text{Li}_6\text{PS}_5\text{Br}$ (450 rpm/4 h) were mixed and milled with a rotation speed of 110 rpm for 1 h. For mixture II, nano- Li_2S (obtained by milling the commercial Li_2S with rotation speed of 500 rpm for 4 h) was mixed with the same $\text{Li}_6\text{PS}_5\text{Br}$ using a speed of 110 rpm for 1 h. For mixture III, the above nano- Li_2S was milled with $\text{Li}_6\text{PS}_5\text{Br}$ with a rotation speed of 500 rpm for 1 h. All of those mixtures were pressed into pellets with a diameter of 10 mm and then crushed into small pieces for the final ion exchange NMR experiments. Mixture IV was prepared by annealing a pellet pressed from mixture III at 150 °C for 3 h. The weight ratio of Li_2S and $\text{Li}_6\text{PS}_5\text{Br}$ in all four mixtures was fixed to 1:1.

Powder X-ray diffraction (XRD) patterns were collected over a two-theta range of 10-80° to identify the crystalline phases of the prepared materials using

6 Accessing the Bottleneck in All-Solid-State Batteries

$\text{Cu}_{K\alpha}$ X-rays (1.5406 \AA at 45 kV and 40 mA) on a X'Pert Pro X-ray diffractometer (PANalytical). To prevent reaction with moisture and oxygen, the powder materials were sealed in an airtight XRD sample holder in an Argon filled glove box.

For the TEM and Energy Dispersive X-ray (STEM-EDX) investigations, a suspension in hexane was prepared which was drop casted onto a standard gold grid with a holey carbon film, inside an argon filled glove box. To prevent any contact with air TEM grids with the sample were loaded into a custom made vacuum transfer TEM holder. TEM measurements were carried out in a FEI – Tecnai operating at 200 kV.

Ionic conductivities of the annealed $\text{Li}_6\text{PS}_5\text{Br}$ solid electrolyte were measured by pelletizing the powder to a 10 mm diameter. Stainless-steel disks were attached to both faces of the pellets. AC impedance measurements were performed for the cell by an Autolab (PGSTAT302N) in the frequency range of 0.1 Hz to 1 MHz with an applied voltage of 0.05 V.

Laboratory-scale solid-state Li-S batteries were fabricated in the following manner. Each of the pristine mixtures (I-IV) was milled with super P with a weight ratio of 4:1 using a rotation speed of 110 rpm for 1 h to obtain the final cathode mixture. Then, a two-layer pellet ($d=10 \text{ mm}$), consisting of 12 mg the described cathode mixture and 88 mg of the $\text{Li}_6\text{PS}_5\text{Br}$ electrolyte, was prepared by pressing them together under 6 tons/cm^2 . After that a piece of In foil was attached to the other side. Then, the whole triple-pellet was pressed under 2 tons/cm^2 of pressure for 30 s. The assembled cells were charged and discharged under a current density of 0.064 mA/cm^2 between 0 and 3.5 V vs. In to evaluate their electrochemical performances. In addition, the cycled mixture III was obtained by collecting the cathode mixture III after two full charge-discharge cycles in the solid-state cell. The capacities obtained were normalized by the weight of Li_2S in the cathode mixture. Electrochemical Impedance Spectrometry (EIS) measurements were performed with an Autolab PGSTAT302N before and after several charge-

discharge cycles in the frequency range of 0.1 Hz and 1 MHz with an applied voltage of 0.05 V.

^7Li static and MAS solid-state NMR measurements were performed on a Chemagnetics 400 Infinity spectrometer ($B_0=9.4$ T, 155.506 MHz for ^7Li). The $\pi/2$ pulse length was determined to be $3.2 \mu\text{s}$ with an RF field strength of 84 kHz for the static and $2.3 \mu\text{s}$ with an RF field strength of 120 kHz for the MAS measurements. Chemical shifts were referenced with respect to a 0.1 M LiCl solution. For the static NMR measurements, the air sensitive $\text{Li}_6\text{PS}_5\text{Br}$ solid electrolyte sample and the Li_2S electrode- $\text{Li}_6\text{PS}_5\text{Br}$ solid electrolyte mixtures were sealed in custom-made Teflon tubes in an Argon filled glove box (H_2O , $\text{O}_2 < 0.3$ ppm). Variable temperature one-dimensional (1D) exchange measurements were performed using a 5 mm static goniometer probe from 213 K to 433 K. T_1 relaxation times were additionally determined at various temperatures using a saturation recovery experiment. The pulse sequence used has been described in detail elsewhere with the appropriate phase cycle for cancellation of direct magnetization that may occur after T_1 relaxation.^{47, 49} Briefly, the sequence consists of $\pi/2$, τ , π , τ , $-\pi/2$, t_{mix} , $+\pi/2$, acquisition. An echo time τ ranging from 200-800 μs was utilized to preserve the intensity of the narrow $\text{Li}_6\text{PS}_5\text{Br}$ resonance and filter out the broad Li_2S resonance, effectively functioning as a T_2 filter. These 1D exchange experiments were performed for a range of mixing times, t_{mix} , to follow the spontaneous equilibrium exchange of Li between the $\text{Li}_6\text{PS}_5\text{Br}$ and Li_2S phases. Li-ion exchange between the $\text{Li}_6\text{PS}_5\text{Br}$ and Li_2S phases for mixtures I-IV was also measured under magic angle spinning (MAS) with a 3.2 mm T3 MAS probe at a spinning speed of 20 kHz with two-dimensional rotor synchronized exchange spectroscopy (2D-EXSY) experiments performed at 348, 298 and 248 K at various mixing times.⁵⁰⁻⁵¹ 2D-Exchange experiments for cycled mixture III were performed on a Varian VNMRs 850 MHz spectrometer ($B_0=20$ T, 330.2 MHz for ^7Li) using a

triple resonance 1.6 mm Varian T3 MAS probe at 30 kHz MAS at 298K. The $\pi/2$ pulse length was determined to be 2.2 μs with an RF field strength of 130 kHz. All 2D spectra consist of 16 scans for each of the 200 transients, each transient incremented by 200 μs with a recycle delay of up to 5 s.

6.3 Results and discussions

The argyrodite $\text{Li}_6\text{PS}_5\text{Br}$ solid electrolyte material was prepared by ball milling at 600 rpm for different milling times followed by annealing at 300 °C for 5 hours. Impedance spectroscopy of the annealed $\text{Li}_6\text{PS}_5\text{Br}$ shows a room temperature conductivity of 0.011(1) S/cm, comparable to literature values.⁵² Relaxation NMR (Figure 6.7), which probes the Li-ion hopping through the bulk lattice, resulted in a conductivity of 0.013(1) S/cm at 78 °C with an activation energy of 0.10(5) eV, indicating mobility comparable with recently reported NMR results,⁵³ and a larger bulk conductivity than that resulting from impedance spectroscopy. This may indicate that, like for the analogous $\text{Li}_6\text{PS}_5\text{Cl}$, grain boundaries may be responsible for the lower bulk conductivity measured by impedance spectroscopy.²⁴

To gain insight into how the preparation of the cathode mixtures of the Li_2S cathode and $\text{Li}_6\text{PS}_5\text{Br}$ solid electrolyte affect the Li-ion transport over the electrode-electrolyte interface, the preparation steps, shown in Figure 6.1a, were investigated by both electrochemical impedance spectroscopy (EIS) and ^7Li exchange NMR. In addition, the capacity retention was determined by galvanostatic charging where all the mixtures have a 1:1 mass ratio of the $\text{Li}_6\text{PS}_5\text{Br}$ solid electrolyte to the Li_2S cathode material.

Recent research has shown that both nanosizing Li_2S and intimate mixing with $\text{Li}_6\text{PS}_5\text{Br}$ (mixture III in Figure 6.1a) is crucial to obtain high capacities over multiple cycles.²⁷ This is confirmed in Figure 6.1b by comparing the capacity retention of cathode mixture I (120 nm sized Li_2S) with cathode mixture III (38 nm sized Li_2S according to XRD, see Figure 6.8) cycled versus an In foil anode at a

current density of 0.064 mA/cm^2 in the voltage window of 0-3.5 V vs. In (0.62-4.12 V vs. Li^+/Li). The crystallite sizes are determined from XRD line broadening shown in Figure 6.8, which are consistent with TEM observations in Figure 6.9. The comparison of the first 4 charge/discharge voltage curves in Figure 6.1(c-f) shows that for the large Li_2S particle size in mixture I, no obvious charge plateau is observed, whereas the nano- Li_2S (mixture III) delivers two distinct charge plateaus, located at 1.8 and 2.5 V vs. In, respectively. On discharge, both cathode mixtures show a discharge plateau at 1.4 V vs. In. and the nano-size Li_2S mixture displays an additional, albeit ill-defined, plateau between 0.5 and 1.0 V vs. In. Interestingly, nano-sized Li_2S shows a slight increase in discharge capacity with increasing cycle number during the first 5 cycles, while the charge and discharge capacity of commercial Li_2S dramatically decrease with increasing cycle numbers, as shown in Figure 6.1b, both also observed by Nagao *et al.*⁵⁴ The increase in discharge capacity of the nano- Li_2S cathode is attributed to the activation process of Li_2S occurring during the first few charge/discharge cycles of the solid-state cell. The difference in (dis)charge capacity upon cycling, shown in Figure 6.1b is striking. Nano-size Li_2S delivers 628 mAh/g versus 56 mAh/g for large-sized Li_2S .

The present mixture III provides a higher discharge capacity and better cyclability compared to most reported comparable solid-state cells employing composite Li_2S electrodes in combination with argyrodite and $80\text{Li}_2\text{S}-20\text{P}_2\text{S}_5$ solid electrolytes.^{27, 54-56} However, capacity retention in this work is not as good as that for the solid-state cell in combination of a mixed-conductive Li_2S nanocomposite cathode and $\text{Li}_6\text{PS}_5\text{Cl}$ electrolyte most likely due to the better distribution of Li_2S , $\text{Li}_6\text{PS}_5\text{Cl}$ and carbon in the cathode mixture.⁵⁷

6 Accessing the Bottleneck in All-Solid-State Batteries

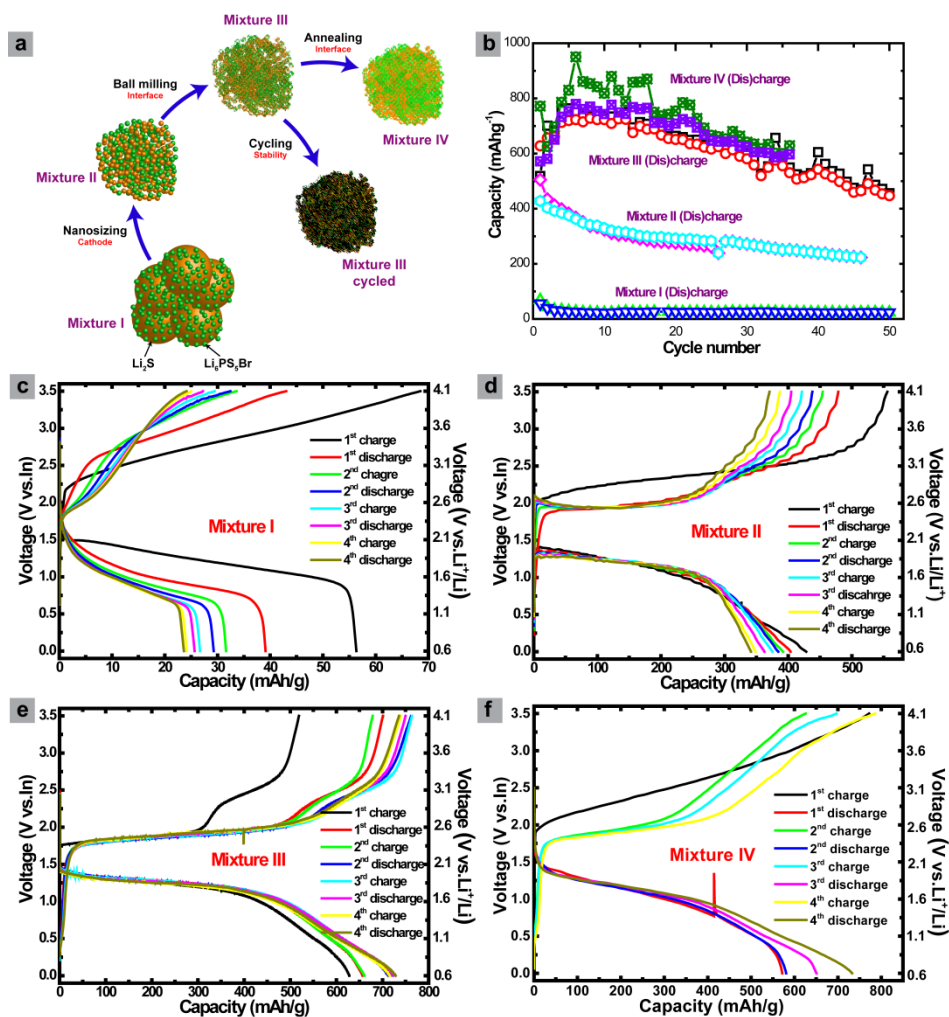


Figure 6.1: Schematic representation of the different stages in solid-state battery cathode preparation and the solid-state battery capacity retention. (a) The different stages in cathode preparation and cycling for which the Li-ion transport over the Li₂S-Li₆PS₅Br interfaces, the charge transfer reaction is measured by ⁷Li exchange NMR and electrochemical impedance spectroscopy (EIS). (b) The charge/discharge capacity upon cycling of the solid-state Li-S cell using micro-sized Li₂S (mixture I in (a)), nano-Li₂S (mixture II in (a)), mixed nano-Li₂S (mixture III in (a)), and heated mixture III (mixture IV in (a)) as the active material. (c-f) Charge and discharge curves of solid-state batteries

using four kinds of mixture as cathode materials. The charge/discharge current density was set at 0.064 mA/cm^2 ($5.03 \cdot 10^{-5} \text{ A}$), and the lower and upper voltage cut-off were set to 0 and 3.5 V vs. In.

The large impact of the Li_2S particle size *i.e.* 120 nm for mixture I and 38 nm for mixture III on the (dis)charge capacity, can be attributed to the poor ionic and electronic conductivity of Li_2S in the first place. Smaller Li_2S particle sizes will reduce charge transport distances, reducing the kinetic restrictions of Li_2S . Additionally, thorough mixing of the nano-sized Li_2S with the $\text{Li}_6\text{PS}_5\text{Br}$ solid electrolyte will lead to more Li_2S - $\text{Li}_6\text{PS}_5\text{Br}$ interfaces. However, to what extent these interfaces allow facile Li-ion transport depending on the preparation and cycling conditions is too difficult to assess. Electrochemical impedance spectroscopy (EIS) is employed for all mixtures I-IV before and after cycling, as shown in Figure 6.10. Assuming simple equivalent circuits, $R_1(R_2Q_2)Q^{58}$, $R_1(R_2Q_2)(R_3Q_3)Q_4$ and $R_1(R_2Q_2)(Q_3(R_3W))$ the EIS data was fitted, in each case not resulting in very good fits, see Figure 6.10 and Table 6.2. Given the small number of parameters, and aiming at an accurate determination of R_1 , the bulk solid electrolyte resistance, and R_2 , the grain boundary resistance between the solid electrolyte and the Li_2S cathode, the best choice appears to be the most simple circuit, $R_1(R_2Q_2)Q^{58}$ for the pristine mixtures. For the cycled mixtures an additional semi-circle indicates the establishment of an another interface, possible at the In anode, which was most accurately fit by the $R_1(R_2Q_2)(R_3Q_3)Q_4$ equivalent circuit. The resulting values for the R_1 and R_2 resistances are listed in Table 6.2.

The results R_1 and R_2 from EIS in Table 6.2 show that, for all mixtures, cycling leads to an increase of both the bulk and interface impedance. The increase in interface impedance is most likely the consequence of a combination of electrochemical reactions at the $\text{Li}_6\text{PS}_5\text{Br}$ - Li_2S interface and loss of interfacial contact due to the volumetric changes of the Li_2S cathode upon cycling as will be discussed in more detail below. The results in Table 6.2, indicate that nanosizing,

going from mixture I to II, and mixing, going from mixture II to III, has only minor influences on the interfacial resistance. This is difficult to explain because the amount of $\text{Li}_6\text{PS}_5\text{Br-Li}_2\text{S}$ interface area is expected to change significantly upon nanosizing and mixing. Moreover, the similar interface and bulk resistances of mixtures I and III do not appear to be consistent with the much better capacities observed for mixture III compared to mixture I during galvanostatic charge/discharge cycling shown in Figure 6.1b. Additionally, it appears unlikely that the bulk $\text{Li}_6\text{PS}_5\text{Br}$ conductivity is affected by cycling, and that annealing, going from mixture III to IV, increases both bulk and interfacial resistance. These inconsistent observations illustrate the difficulty in assessing the interface resistance in the complex bulk morphologies of this all-solid-state batteries.⁴⁴

Aiming at unambiguous quantification of the charge transfer kinetics over the $\text{Li}_6\text{PS}_5\text{Br-Li}_2\text{S}$ interface, and how this is affected by the battery preparation and cycling conditions, $^7\text{Li-}^7\text{Li}$ 2D NMR exchange experiments are conducted for the mixtures I - IV, shown in Figure 6.1a. 2D exchange NMR enables the measurement of spontaneous Li-ion exchange between different Li-ion environments,^{47, 49, 59} at present for the first time realized between a solid electrolyte and electrode material. These experiments provide selective and non-invasive quantification of the Li-ion transport over the solid-solid electrolyte-electrode interface in realistic solid-state cathode mixtures. ^7Li Magic Angle Spinning (MAS) NMR spectra of the $\text{Li}_2\text{S-Li}_6\text{PS}_5\text{Br}$ mixtures I, II and III are shown in Figures 6.2a, 6.2e, and 6.2i. MAS can average out anisotropic interactions that are described by rank-2 tensors, such as dipolar, first order quadrupolar and chemical shift anisotropy, provided that the MAS frequency is larger than the interaction width. Compared to $\text{Li}_6\text{PS}_5\text{Cl}$, the ^7Li NMR resonance for $\text{Li}_6\text{PS}_5\text{Br}$ is shifted upfield caused by increased shielding of the Li-ions by the neighbouring Br dopants. This results in a difference in chemical shift between Li in Li_2S and in $\text{Li}_6\text{PS}_5\text{Br}$, which allows us to distinguish between Li-ions in $\text{Li}_6\text{PS}_5\text{Br}$ and Li_2S phases, making it possible to conduct the 2D

exchange NMR experiments. The 2D NMR spectra shown in Figure 6.2 show that ^7Li in Li_2S is represented by a broad homogeneous resonance whereas ^7Li in $\text{Li}_6\text{PS}_5\text{Br}$ is represented by a star shaped resonance. The latter is the consequence of the large Li-ion mobility in the $\text{Li}_6\text{PS}_5\text{Br}$ solid electrolyte which results in a Lorentzian line shape that upon 2D Fourier transformation results in the star-shaped NMR resonance observed.

2D exchange NMR effectively measures the spectrum of the ^7Li atoms at $t=0$ s, then waits a ‘mixing time’ t_{mix} , and subsequently measures the spectrum of the same ^7Li atoms again at $t=t_{\text{mix}}$. The results of such measurements are shown in Figure 6.2. The signal occurring on the diagonal reflects the 1D NMR signal shown in Figure 6.2a, 6.2e and 6.2i, which represents ^7Li atoms that have the same spectrum before and after t_{mix} . During t_{mix} these Li-ions remained within the same material, either within $\text{Li}_6\text{PS}_5\text{Br}$ or within Li_2S . Off-diagonal intensity, clearly visible for mixture III at $t_{\text{mix}}=10$ ms in Figure 6.2k and strongly present at $t_{\text{mix}}=100$ ms in Figure 6.2l, represents Li-ions that at $t=0$ were located in $\text{Li}_6\text{PS}_5\text{Br}$ and during $t=t_{\text{mix}}$ diffused to Li_2S and vice versa. This off-diagonal intensity quantifies the amount of Li-ions that spontaneously moved between the electrode and the electrolyte during t_{mix} . Hence, by integrating the amount of off-diagonal intensity and dividing this by the intensity on the diagonal at $t_{\text{mix}}=0$ and t_{mix} we obtain the exchange current density, the amount of Li-ions that undergoes the charge transfer reaction between the $\text{Li}_6\text{PS}_5\text{Br}$ solid electrolyte and Li_2S cathode. For the 2D spectrum in Figure 6.2l, this results in that approximately 20% of the Li-ions moved from the $\text{Li}_6\text{PS}_5\text{Br}$ to the Li_2S material in mixture III and vice versa within the mixing time $t_{\text{mix}}=100$ ms. At $t_{\text{mix}}=100$ μs , Figure 6.2j, no off-diagonal signal is detected because this mixing time is too short for Li-ions to diffuse from $\text{Li}_6\text{PS}_5\text{Br}$ to Li_2S material or vice versa. If the temperature is lowered to 248 K the off-diagonal signal observed at large mixing times, shown in Figure 6.3, is much weaker compared to $t_{\text{mix}}=100$ ms in Figure 6.2l, because the Li-ion motion between

6 Accessing the Bottleneck in All-Solid-State Batteries

$\text{Li}_6\text{PS}_5\text{Br}$ and Li_2S is frozen. In contrast, the off-diagonal signal at 348 K is stronger as shown in Figure 6.3 because of thermal activation of the Li-ion diffusion between $\text{Li}_6\text{PS}_5\text{Br}$ and Li_2S . This indicates that the cross-peak intensities observed in Figure 6.2 must be due to Li-ion diffusion, and cannot arise from spin diffusion due to the presence of dipolar couplings (which are suppressed by MAS and also unlikely to cross the grain boundaries).

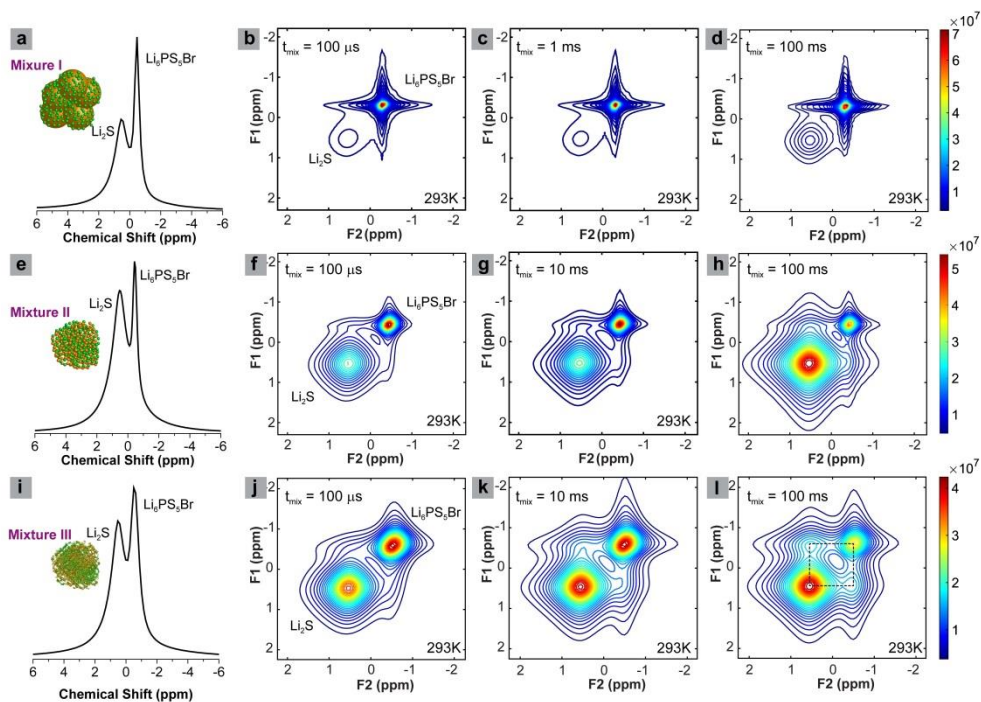


Figure 6.2: NMR measuring the spontaneous Li-ion transport between the $\text{Li}_6\text{PS}_5\text{Br}$ solid electrolyte and the Li_2S cathode. (a,e,i) One-dimensional (1D) ^7Li magic angle spinning (MAS) spectra corresponding to the $\text{Li}_6\text{PS}_5\text{Br}$ - Li_2S cathode mixtures (a) mixture I, where Li_2S is micron sized (e) mixture II, where Li_2S is nano sized (i) mixture III, where nano sized Li_2S is thoroughly mixed with $\text{Li}_6\text{PS}_5\text{Br}$. Two-dimensional (2D) ^7Li - ^7Li exchange spectra (2D-EXSY) recorded at a ^7Li resonance frequency of 155.506 MHz and a spinning speed of 20 kHz at room temperature for short (100 μs) to long mixing times t_{mix} (100 ms) for (b,c,d) mixture I, (f,g,h) for mixture II and (j,k,l) for mixture III. For both

*mixtures I and II no obvious off-diagonal cross-peak intensity is observed, indicating that the exchange over the solid-solid $\text{Li}_6\text{PS}_5\text{Br-Li}_2\text{S}$ is very small (based on whether an upper limit for the conductivity can be determined as shown in **Figure 4**). For mixture III the off-diagonal cross-peaks appear at $t_{\text{mix}}=10$ ms, and are most pronounced at $t_{\text{mix}}=100$ ms, and they correspond to Li-ion exchange from Li_2S to $\text{Li}_6\text{PS}_5\text{Br}$ and vice versa. Note that the star shape of the ^7Li resonance in $\text{Li}_6\text{PS}_5\text{Br}$ is the consequence of the 2D Fourier transform of its Lorentzian shape, a result of the high mobility of Li-ions within the $\text{Li}_6\text{PS}_5\text{Br}$ phase.*

Comparing the 2D spectra at $t_{\text{mix}}=100$ ms of mixtures I, II and III in Figure 6.2d, 6.2h, and 6.2l only mixture III displays evident off-diagonal intensity, which implies that only for mixture III there is significant Li-ion transport between $\text{Li}_6\text{PS}_5\text{Br}$ and Li_2S during 100 ms. From the exchanged amount of Li-ions, and taking into account the average crystallite sizes (23 nm for $\text{Li}_6\text{PS}_5\text{Br}$ and 38 nm for Li_2S from XRD refinement and TEM which appear to be close to the particle sizes from EDX, see Figure 6.8 and Figure 6.9) the approximate exchange current density at room temperature can be calculated, amounting approximately to 1.0 mA/cm^2 for mixture III and less than 0.05 mA/cm^2 for mixtures I and II which is small compared to the one in the liquid electrolyte Li-ion batteries.^{49, 60} The large increase in spontaneous Li-ion transport between mixtures II and III indicates that reducing the Li_2S particle size alone is not enough to provide significant Li-ion transport over the $\text{Li}_6\text{PS}_5\text{Br-Li}_2\text{S}$ interface. Additionally, intimate mixing, here realized by high-speed ball-milling as shown in Figure 6.1a, appears essential, most likely because it creates more interfacial area. The improved Li-ion transport over the interfaces going from mixture I and II towards III comes along with substantially better solid-state battery performance shown in Figure 6.1b, indicating that facile Li-ion transport is paramount for solid-state battery performance. Annealing mixture III at 150 °C, resulting in mixture IV, did not lead to a significantly different Li-ion exchange compared to mixture III; hence these

6 Accessing the Bottleneck in All-Solid-State Batteries

mild annealing temperatures do not improve the interfaces with respect to the Li-ion transport.

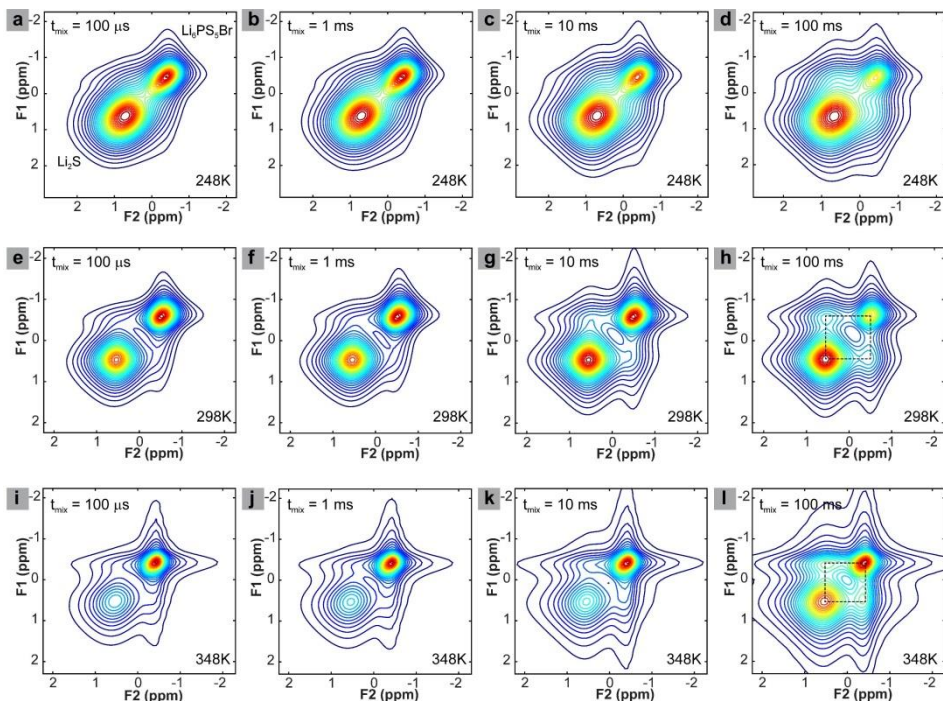


Figure 6.3: Two-dimensional ${}^7\text{Li}$ - ${}^7\text{Li}$ exchange spectra (2D-EXSY) measured under magic angle spinning (MAS) at ${}^7\text{Li}$ resonance frequency of 155.506 MHz and spinning speed of 20 kHz for the $\text{Li}_6\text{PS}_5\text{Br}$ - Li_2S electrolyte-electrode mixture III at (a)-(d) 248 K, (e)-(h) 298 K, and (i)-(l) 348 K at mixing times of (a)/(e)/(i) 100 μs , (b)/(f)/(j) 1 ms, (c)/(g)/(k) 10 ms, and (d)/(h)/(l) 100 ms respectively. The diagonal signal corresponds to Li_2S and $\text{Li}_6\text{PS}_5\text{Br}$ and the off-diagonal cross-peaks correspond to exchange Li.

Figure 6.4 shows the impact of cycling on the spontaneous Li-ion exchange between $\text{Li}_6\text{PS}_5\text{Br}$ and Li_2S mixture III. At $t_{\text{mix}}=100$ ms (Figure 6.4c) no off-diagonal signal is observed, as opposed to the uncycled pristine mixture III that shows considerable Li-ion exchange as shown in Figure 6.2l. Only at $t_{\text{mix}}=500$ ms in Figure 6.4d a weak signature of Li-ion exchange between $\text{Li}_6\text{PS}_5\text{Br}$ and Li_2S is

observed. This proves that cycling changes the charge transfer over the interface considerably; leading to less facile Li-ion transport over the solid-solid $\text{Li}_6\text{PS}_5\text{Br}$ - Li_2S interface.

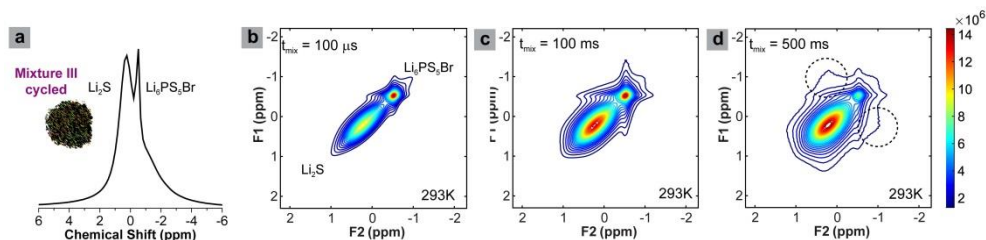


Figure 6.4: NMR measuring the spontaneous Li-ion transport between the $\text{Li}_6\text{PS}_5\text{Br}$ solid electrolyte and the Li_2S cathode after cycling. (a) One-dimensional (1D) ^7Li magic angle spinning (MAS) spectrum of the cycled $\text{Li}_6\text{PS}_5\text{Br}$ - Li_2S cathode mixture III. (b)-(d) Two-dimensional ^7Li - ^7Li exchange spectra (2D-EXSY) measured under MAS at a resonance frequency of 330.39 MHz and spinning speed of 30 kHz at 298 K for the cycled mixture III at (b) $t_{\text{mix}}=100 \mu\text{s}$, (c) $t_{\text{mix}}=100 \text{ ms}$, and (d) $t_{\text{mix}}=500 \text{ ms}$. Only after $t_{\text{mix}}=500 \text{ ms}$, off-diagonal exchange intensity is observed reflecting the Li-ion exchange from Li_2S to $\text{Li}_6\text{PS}_5\text{Br}$ and vice versa in the cycled cathode mixture III.

In addition to the 2D-Exchange measurements, faster 1D ^7Li - ^7Li exchange experiments under static conditions were performed to quantify the exchange as a function of t_{mix} and temperature.^{24, 47, 49} The much larger static line width of ^7Li in Li_2S compared to that of $\text{Li}_6\text{PS}_5\text{Br}$, see Figure 6.5a, is a consequence of the poor Li-ion mobility in Li_2S that is unable to average out the dipolar and first order quadrupolar interactions. This makes it possible to selectively filter out the broad Li_2S component using a T_2 filter. As a result, the repopulation of the Li_2S , through the transfer of magnetization carried by the ^7Li species diffusing from the $\text{Li}_6\text{PS}_5\text{Br}$ electrolyte back into Li_2S is monitored as a function of the exchange time t_{mix} at different temperatures, shown in Figure 6.5(c-d). When t_{mix} exceeds 500 ms, the T_1 relaxation process dominates the decay of the total magnetization, which limits the evaluation of exchange to this timescale. In the present case, the Li_2S - $\text{Li}_6\text{PS}_5\text{Br}$

6 Accessing the Bottleneck in All-Solid-State Batteries

mixture, offers both a difference in chemical shift and a difference in line broadening, allowing quantification of Li-ion exchange between these materials both by 2D exchange and by 1D exchange (T_2 filter) experiments, which are shown to be in excellent agreement in Figure 6.5b. These two possibilities illustrate the versatility of NMR exchange for these systems. In general, the range of ^7Li chemical shifts in compounds is quite narrow, which in many cases may not provide enough contrast in chemical shift between the electrode and the solid electrolyte. However, typically solid electrolytes have larger conductivities compared to electrode materials, which in practice will provide for most combinations a difference in line broadening enabling the quantification of the exchange with 1D exchange (T_2 filter) experiments. Perhaps the largest practical restriction is the T_1 spin-lattice relaxation time of the materials, which determines the maximum exchange time that can be accessed. This is for instance a challenge for cathode materials having paramagnetic moments present. A potential strategy is to move towards ^6Li , in general having larger values for T_1 because of the weaker spin-lattice coupling. However, the compromise is the lower abundance and sensitivity of ^6Li , which increases measurement times. Therefore, we foresee that for most electrode-solid electrolyte combinations NMR exchange experiments will be able to quantify the Li-ion transport over the interfaces, making this versatile, albeit, not straightforward approach to quantify the Li-ion transport over the interfaces in all-solid state batteries.

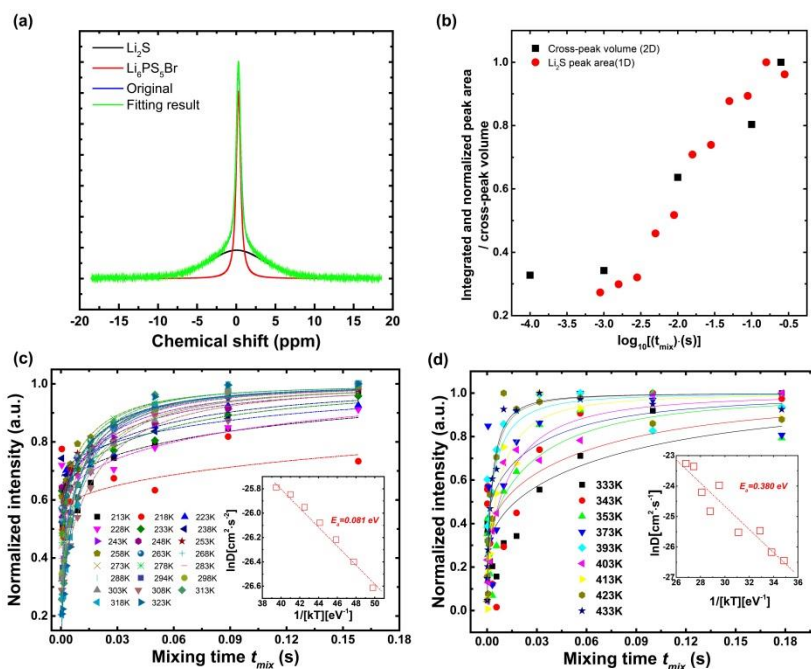


Figure 6.5: (a) Static ${}^7\text{Li}$ spectrum of mixture III measured at 298K and a resonance frequency of 155.506 MHz. (b) Evolution of cross peak volume from the 2D exchange spectra for the pristine mixture III, and the area of the remerging Li_2S signal from the 1D exchange spectra, both as a function of mixing time, at 298K. Normalized intensity of the static Li_2S ${}^7\text{Li}$ NMR spectrum of (c) pristine and (d) cycled mixture III, T_1 corrected, as a function of mixing time at different temperatures. The inset shows the temperature dependence of the diffusion parameter D , derived from the fits representing the diffusion model (subsequent text). An Arrhenius law is used to fit the activation energy, E_a , representing the diffusion process over the boundary between the $\text{Li}_6\text{PS}_5\text{Br}$ solid electrolyte and the Li_2S phases.

Quantification of exchange between the Li_2S and $\text{Li}_6\text{PS}_5\text{Br}$ species was performed by fitting the growing Li_2S signal (See in Figure 6.5c and 6.5d) to a diffusion model, derived from Fick's law for diffusion as explained in detail in the Appendix. From this, an average self-diffusion coefficient (D) as a function of temperature for the Li-ion transfer over the electrolyte-electrode interface and the

corresponding activation energy are determined shown in Figure 6.5c and 6.5d. Here, it is assumed that diffusion occurs from the center of a $\text{Li}_6\text{PS}_5\text{Br}$ solid electrolyte crystallite (with an average size of 23 nm) to the center of the Li_2S particle (with an average size of 38 nm), where the average crystallite sizes are determined from XRD broadening. This assumes intimate mixing of $\text{Li}_6\text{PS}_5\text{Br}$ and Li_2S on the length scale of these crystallite sizes, which is confirmed by the distribution of Br and P determined by EDX mapping shown in Figure 6.9. This results in a self-diffusion coefficient for the $\text{Li}_6\text{PS}_5\text{Br}$ - Li_2S mixture III of approximately $1 \cdot 10^{-11} \text{ cm}^2/\text{s}$ at room temperature, both obtained from the 2D and 1D exchange measurements. This is two orders of magnitude smaller than the self-diffusion coefficient for bulk diffusion, as determined from relaxation NMR ($10^{-9} \text{ cm}^2/\text{s}$) both determined by Epp *et al*⁵³ and at present (see Figure 6.7).

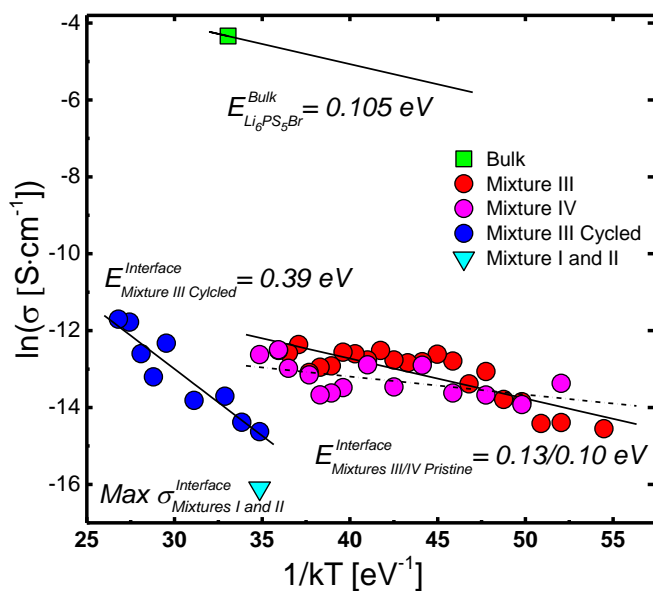


Figure 6.6: Comparison of the Li-ion bulk and interface conductivities. Li-ion conductivity for bulk $\text{Li}_6\text{PS}_5\text{Br}$ determined by ^7Li Solid-state NMR spin lattice relaxation (SLR) experiments and the conductivity over the $\text{Li}_6\text{PS}_5\text{Br}$ - Li_2S interface from 2D/1D NMR

exchange experiments for different cathode mixtures, I: micro Li₂S-Li₆PS₅Br, II: nano-Li₂S-Li₆PS₅Br, III: mixed nano-Li₂S-Li₆PS₅Br, IV: annealed mixed nano-Li₂S-Li₆PS₅Br and V: mixture III cycled (see Figure 6.1a).

Using the Nernst-Einstein equation⁶¹ and assuming no correlation effects⁶² the conductivity can be calculated from both the bulk and interface self-diffusion coefficients. The resulting bulk conductivity, determined by the NMR relaxation experiments (see Figure 6.7), and the interface conductivities from the exchange experiments for mixtures I, II, III and IV are shown as a function of temperature in Figure 6.6. The activation energy of the bulk conductivity is obtained by fitting the high temperature slope of the T_1 relaxation, as shown in Figure 6.7. For mixtures I and II, no exchange was observed, but based on the maximum exchange time probed (250 ms), an upper limit of the conductivity is determined shown in Figure 6.6. This illustrates that nanosizing Li₂S, and intimate mixing of nano-Li₂S with Li₆PS₅Br is essential to provide significant Li-ion conductivity over the Li₂S-Li₆PS₅Br interface. However, the conductivity over the interface appears several orders of magnitude smaller compared to the bulk Li₆PS₅Br conductivity. The activation energy for Li-ion transport over the Li₂S-Li₆PS₅Br interface is slightly larger compared to that of the bulk Li₆PS₅Br conductivity, indicating that in the pristine, uncycled mixture III the barrier for Li-ion transport over the interface is small. However, the much smaller interface conductivity compared to the bulk conductivity suggests that there is poor wetting between Li₂S and Li₆PS₅Br. Hence, there is little electrode-electrolyte contact area where the Li-ion transport can take place.

Based on DFT calculations it is expected that the argyrodite solid electrolytes are stable at the Li₂S potential (~2.3 V),⁴⁰ and consequentially no redox instability should be expected in the pristine cathode mixture, which potentially could increase the interface impedance. This is consistent with the relatively small

activation energy for Li-ion transport over the interface for the uncycled mixture III, similar to that for the $\text{Li}_6\text{PS}_5\text{Br}$ bulk Li-ion diffusion.

After two full charge-discharge cycles, between 0.62-4.12 V vs. Li^+/Li , the Li-ion exchange is significantly lowered, as observed by comparing Figure 6.2l and Figure 6.4c. In Figure 6.6, this results in a drop in conductivity of almost one order of magnitude (near room temperature). Additionally, the cycling raises the activation energy for Li-ion transport over the Li_2S - $\text{Li}_6\text{PS}_5\text{Br}$ interface by a factor of three from 0.13 to 0.39 eV. This may be due to (1) large volumetric changes of Li_2S upon charge and discharge causing contact loss between Li_2S and $\text{Li}_6\text{PS}_5\text{Br}$ and (2) redox instabilities at the Li_2S - $\text{Li}_6\text{PS}_5\text{Br}$ interfaces leading to an interfacial layer that poses a higher barrier for Li-ion transport. We anticipate that both play a role at the Li_2S - $\text{Li}_6\text{PS}_5\text{Br}$ interface where (1) is responsible for the drop in interface conductivity because of loss of interfacial contact and (2) for the increase in activation energy due to an interfacial layer increasing the diffusion barrier. During cycling the voltage was varied between 0.62-4.12 V vs. Li^+/Li , far outside the narrow electrochemical stability window predicted for these sulphide electrolytes.⁴⁰⁻⁴¹ Recently, it was demonstrated that charging up to similar potentials results in oxidation of argyrodite $\text{Li}_6\text{PS}_5\text{Cl}$ towards elemental sulfur, lithium polysulfides, $\text{P}_2\text{S}_{x \leq 5}$ and LiCl .⁶³ Based on this we suggest that the increase in activation energy is a result of the formation of an interfacial layer of similar oxidation products from the $\text{Li}_6\text{PS}_5\text{Br}$ solid electrolyte that develop during the first cycles. Additionally, sulphide electrolytes have been reported to act as active material during charging.⁶⁴ Oxidation of $\text{Li}_6\text{PS}_5\text{Br}$ may be responsible for the change in the T_1 in the cycled mixture III compared to the pristine material, both shown in Figure 6.7. However, it appeared difficult to obtain accurate fits for the T_1 of $\text{Li}_6\text{PS}_5\text{Br}$ due to the presence of Li_2S in the cycled mixtures. To investigate the influence of oxidation of $\text{Li}_6\text{PS}_5\text{Br}$ on the T_1 further in the absence of Li_2S , $\text{Li}_6\text{PS}_5\text{Br}$ was charged by using it as cathode (by mixing with carbon). The result

shown in Figure 6.7 shows that T_1 is hardly affected by charging, indicating that the bulk of the $\text{Li}_6\text{PS}_5\text{Br}$ material remains intact not excluding that the surface may be oxidized.

To assess the role of the conductivity over the $\text{Li}_2\text{S-Li}_6\text{PS}_5\text{Br}$ interface in the all-solid-state batteries, the resistance due to both the $\text{Li}_6\text{PS}_5\text{Br}$ solid electrolyte and the $\text{Li}_2\text{S-Li}_6\text{PS}_5\text{Br}$ interface is approximated from the NMR results. The $\text{Li}_6\text{PS}_5\text{Br}$ bulk conductivity is determined from the T_1 relaxation experiments (Figure 6.7). In combination with the solid electrolyte pellet thickness, l , and surface area, A , as used for the electrochemical impedance spectroscopy (see Figure 6.7 and 6.10) and the cycling performance shown in Figure 6.1b, the bulk solid electrolyte resistance R is calculated with $R=l/(A\sigma)$ and reported in Table 6.2. To calculate the $\text{Li}_2\text{S-Li}_6\text{PS}_5\text{Br}$ interface resistance, it is assumed that interface thickness, l , equals the average distance between the solid electrolyte and the electrode, which was also used to calculate the diffusion coefficient from the NMR exchange experiments. The interface area, A , between Li_2S and $\text{Li}_6\text{PS}_5\text{Br}$ in the cathode mixtures is difficult to estimate, and therefore for simplicity we assume the interface area to be equal to the area of the solid electrolyte pellet, to make at least a qualitative comparison possible, which results in the interface resistance determined from the NMR exchange experiments in Table 6.1.

6 Accessing the Bottleneck in All-Solid-State Batteries

Table 6.1: Bulk and interface resistances of the mixtures derived from the conductivity in Figure 6.6 determined from the NMR exchange experiments.

		NMR ⁽¹⁾
Mixture I	Bulk	37 Ω
	Interface	> 82 Ω
Mixture II	Bulk	37 Ω
	Interface	> 82 Ω
Mixture III	Bulk	37 Ω
	Interface	1.5 Ω
Mixture IV	Bulk	-
	Interface	2.4 Ω
Mixture III Cycled	Bulk	35 Ω
	Interface	68 Ω

⁽¹⁾ Assuming for the bulk resistance an electrolyte thickness of 1600 μm (the thickness of the pellets tested by EIS) and a surface area of 0.78 cm^2 based on the diameter. And assuming an electrode - electrolyte interface area of 0.78 cm^2 (see text).

The resistances in Table 6.1, estimated from the exchange NMR, provide a consistent picture of the role of the electrode-electrolyte interface on the solid-state battery performance of the different mixtures shown in Figure 6.1b. The results for the bulk and interface resistance obtained by electrochemical impedance spectroscopy (EIS) reported in Table 6.2 suggest that the battery performance of mixtures I, II and III should be similar. In contrast the NMR exchange results in Table 6.1 indicate that the high interfacial resistances for mixtures I and II are responsible for the poor capacities during galvanostatic cycling observed in Figure 6.1b. This can be explained by a combination of both Li_2S nanosizing and mixing with the $\text{Li}_6\text{PS}_5\text{Br}$, resulting in much more interfacial area between the Li_2S electrode and the $\text{Li}_6\text{PS}_5\text{Br}$ solid electrolyte. Table 6.1 indicates that in the pristine cathode mixture III the interfacial resistance is relatively small compared to the

bulk resistance of a 1600 μm thick electrolyte. In practice, a solid electrolyte thickness of 100 μm is more realistic to achieve high energy density and power density, which would result in a bulk resistance of just 1.9 Ω for the pristine cathode mixture III, comparable to the interface resistance of 1.5 Ω . Just two galvanostatic charge/discharge cycles increase the interface resistance to 68 Ω , illustrating that the overpotential during galvanostatic cycling will be dominated by the Li-ion transport over interface between the Li_2S cathode and the $\text{Li}_6\text{PS}_5\text{Br}$ solid electrolyte. As discussed above, this is most likely a consequence of both contact loss due to the large volumetric changes of the cathode and an interfacial barrier arising from the solid electrolyte oxidation and/or reduction.

6.4 Conclusions

Using the Li_2S - $\text{Li}_6\text{PS}_5\text{Br}$ solid-state battery as an example, the present experimental results demonstrate that Li-ion interfacial transport over the electrode-electrolyte interfaces is the major bottleneck to Li-ion transport through all-solid-state batteries. Both the preparation conditions and battery cycling affect interfacial transport considerably. Therefore, realizing high energy density all-solid-state batteries will require interface design to prevent the large increase in impedance during cycling, where in particular volumetric changes and redox instabilities appear responsible. This work demonstrates the ability of exchange NMR between distinguishable Li-ion sites in the electrode and the solid electrolyte to quantify unambiguously the amount and timescale of Li-ion transport over the solid electrolyte-electrode interface in bulk solid state batteries. Thereby this approach may be a valuable support to the development of interface design strategies necessary for future high performance all-solid-state batteries.

6.5 Supplement

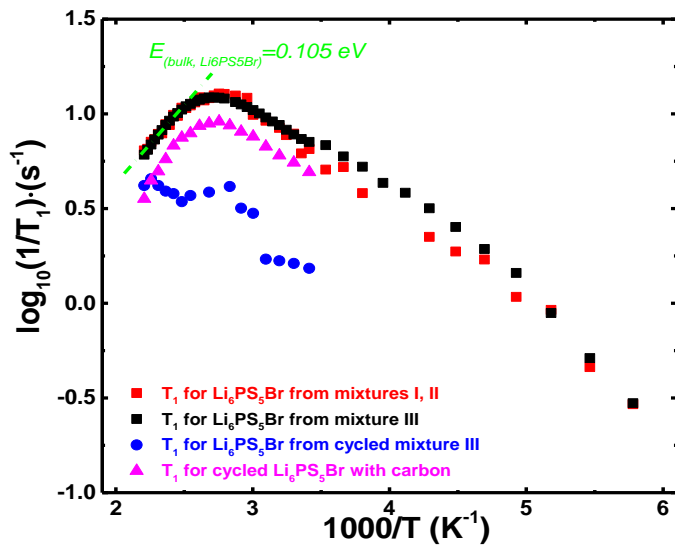


Figure 6.7: Temperature dependence of the ${}^7\text{Li}$ spin-lattice relaxation NMR rates T_1^{-1} measured for $\text{Li}_6\text{PS}_5\text{Br}$ in mixtures I-III and in the cycled mixture III.

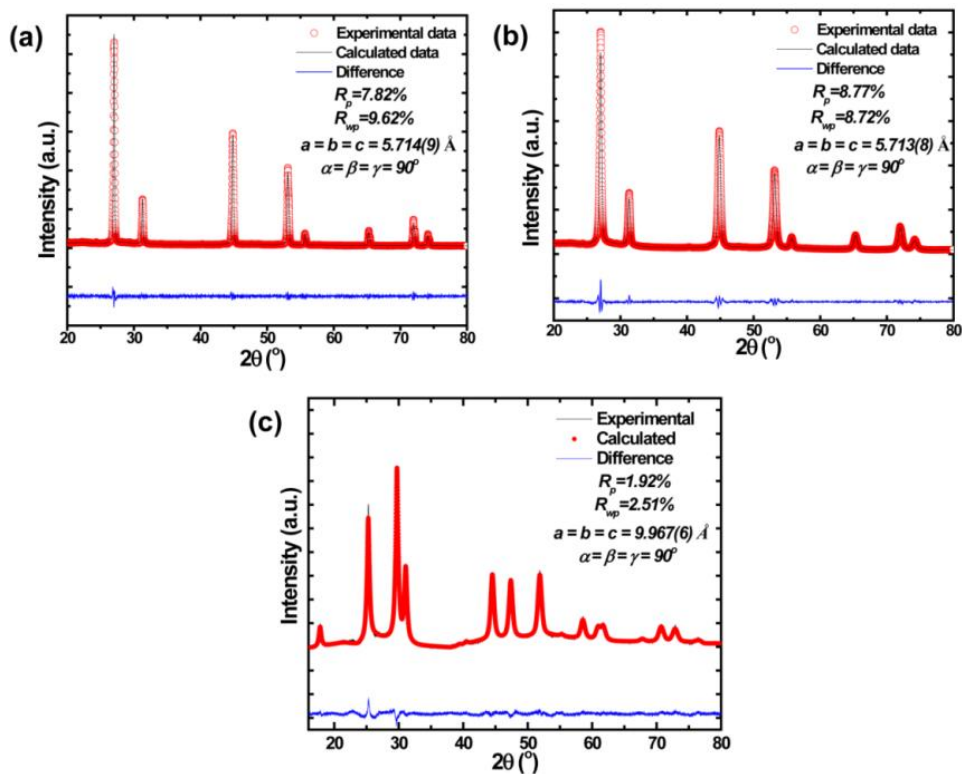


Figure 6.8: XRD and Rietveld refinement of commercial Li_2S (a), nano Li_2S (b), and the $\text{Li}_6\text{PS}_5\text{Br}$ solid electrolyte (c). The average crystallite sizes are 120, 38, and 23 nm respectively, all of which are obtained based on the above refinement results.

6 Accessing the Bottleneck in All-Solid-State Batteries

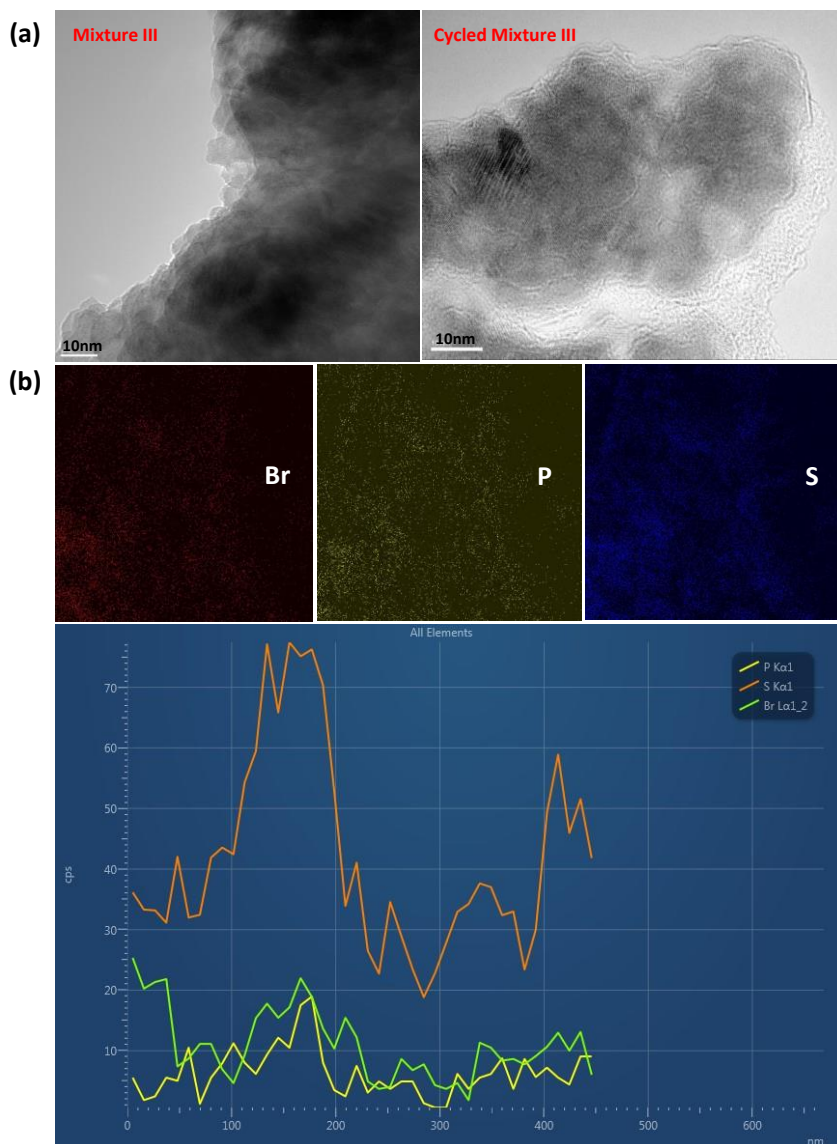


Figure 6.9: (a) TEM images of pristine and cycled mixture III. (b) EDX mapping of Br, P, S and a line map for mixture III. The EDX mapping, and line scan indicate that the mixing of the Li_2S and the $\text{Li}_6\text{PS}_5\text{Br}$ is on a length scale smaller than 100 nm.

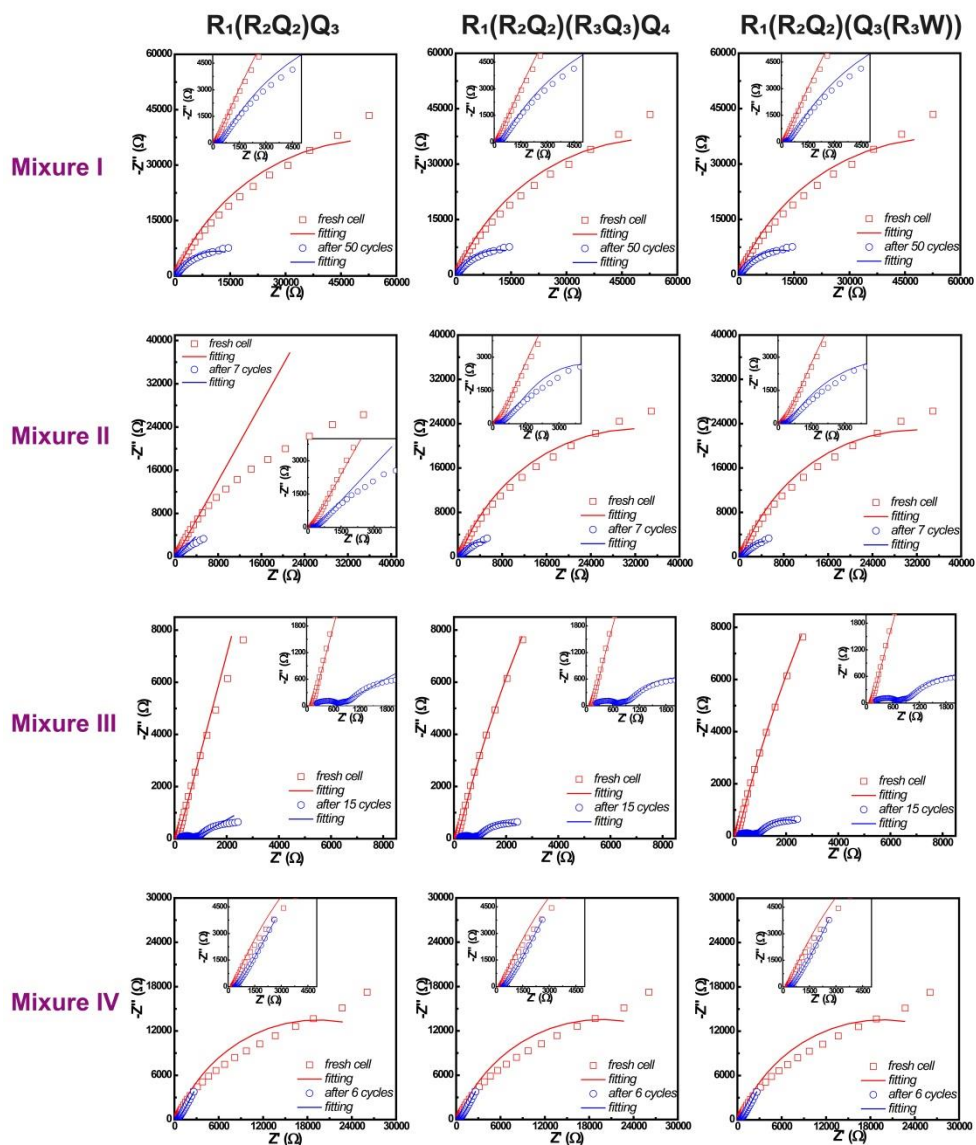


Figure 6.10: Part I. EIS curves and fits of the fresh and cycled solid-state batteries using different $\text{Li}_2\text{S-Li}_6\text{PS}_5\text{Br}$ mixtures (I-IV) mixed with carbon with a weight ratio of 2:2:1 as cathode combined with $\text{Li}_6\text{PS}_5\text{Br}$ electrolyte and In foil anode. The results are fitted by $R_1(R_2Q_2)Q_3$, $R_1(R_2Q_2)(R_3Q_3)Q_4$ and $R_1(R_2Q_2)(Q_3(R_3W))$ equivalent circuits. For the

6 Accessing the Bottleneck in All-Solid-State Batteries

equivalent circuit $R_1(R_2Q_2)Q_3$, R_1 reflects the resistance of the solid electrolyte, and R_2 reflects the Li_2S cathode electrode- $\text{Li}_6\text{PS}_5\text{Br}$ solid electrolyte interface. The application of the two other equivalent circuits $R_1(R_2Q_2)(R_3Q_3)Q_4$ is motivated by the appearance of a new semicircle in the cycled data, indicating the formation of an additional interface upon cycling, possibly at the In anode.

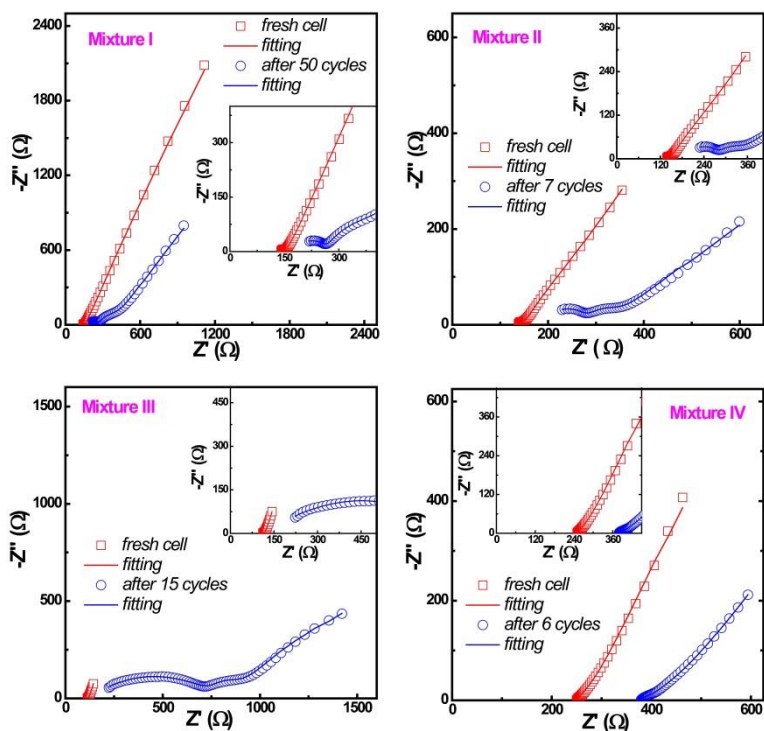


Figure 6.10: Part II. EIS curves of the fresh and cycled solid-state batteries using different Li_2S - $\text{Li}_6\text{PS}_5\text{Br}$ mixtures (I-IV) mixed with carbon with a weight ratio of 2:2:1 as cathode combined with $\text{Li}_6\text{PS}_5\text{Br}$ electrolyte and In foil anode. The EIS data of fresh cells are fitted by the equivalent circuit $R_1(R_2Q_2)Q_3$, while the data for cycled cells are fitted by the equivalent circuit $R_1(R_2Q_2)(R_3Q_3)Q_4$, the latter motivated by the appearance of an additional semicircle which indicate the formation of an additional interface upon cycling, possibly at the In anode. Because the aim is to get an accurate estimation of R_1 (the bulk solid electrolyte resistance) and R_2 (the resistance of the Li_2S - $\text{Li}_6\text{PS}_5\text{Br}$ interface) for

comparison with the NMR experiments only the high frequency part of the EIS data was included in the fit.

Table 6.2: EIS fitting results based on various equivalent circuits

Resistances resulting from the EIS fits in Figure 6.10, using three equivalent circuit models for mixtures I-IV. The R_1 reflects the resistance of the solid electrolyte, and R_2 reflects the Li_2S cathode electrode- $\text{Li}_6\text{PS}_5\text{Br}$ solid electrolyte interface. The application of the two other equivalent circuits $R_1(R_2Q_2)(R_3Q_3)Q_4$ is motivated by the appearance of a new semicircle in the cycled data, indicating the formation of an additional interface upon cycling, possibly at the In anode. The values of R_1 and R_2 marked in blue are the most accurate fits, resulting from the fit shown in Figure 6.10 Part II. When values are absent the error in the resistance is more than 100%.

		$R(RQ)Q$					
		R_1/Ω	Error/%	R_2/Ω	Error/%		
Mixture I	fresh	137.2	2.728	23	23.08		
	cycled	170.0	10.81	-	-		
Mixture II	fresh	137.8	0.6	7.6	14		
	cycled	122.8	148.1	244.2	90.4		
Mixture III	fresh	111.1	0.3	9.2	9		
	cycled	139.5	9.54	560.8	4.85		
Mixture IV	fresh	250.5	0.7	24.4	46		
	cycled	370.1	0.9	130	78		
		$R(RQ)(RQ)Q$					
		R_1/Ω	Error/%	R_2/Ω	Error/%	R_3/Ω	Error/%
Mixture I	fresh	-	-	-	-	-	-
	cycled	177.1	7.11	89.65	17	110	10.3
Mixture II	fresh	141.3	1.31	540.8	166.1	-	-
	cycled	190.4	5.4	87.2	18	44.1	22
Mixture III	fresh	111.0	1.47	-	-	-	-
	cycled	129.2	3.6	633.5	1.6	62.8	20
Mixture IV	fresh	251.4	2.92	40.08	72.84	-	-
	cycled	373.7	0.71	127.6	33.3	-	-

		$R(RQ)(Q(RW))$					
		R_1/Ω	Error/%	R_2/Ω	Error/%	R_3/Ω	Error/%
Mixture I	fresh	-	-	-	-	-	-
	cycled	-	-	-	-	-	-
Mixture II	fresh	141.3	1.31	-	-	-	-
	cycled	59.96	-	9341	-	-	-
Mixture III	fresh	111	1.468	-	-	-	-
	cycled	-	-	212.1	-	1824	5.157
Mixture IV	fresh	251.4	2.918	40.08	72.84	-	-
	cycled	373.7	0.7146	127.6	33.3	-	-

References

1. Kulkarni, A.; Maiti, H.; Paul, A., Fast ion conducting lithium glasses-review. *B Mater Sci* **1984**, *6* (2), 201-221.
2. Goodenough, J. B., Ceramic solid electrolytes. *Solid State Ionics* **1997**, *94* (1-4), 17-25.
3. Thangadurai, V.; Weppner, W., Recent progress in solid oxide and lithium ion conducting electrolytes research. *Ionics* **2006**, *12* (1), 81-92.
4. Li, J.; Ma, C.; Chi, M.; Liang, C.; Dudney, N. J., Solid Electrolyte: the Key for High-Voltage Lithium Batteries. *Advanced Energy Materials* **2015**, *5* (4).
5. Kim, J. G.; Son, B.; Mukherjee, S.; Schuppert, N.; Bates, A.; Kwon, O.; Choi, M. J.; Chung, H. Y.; Park, S., A review of lithium and non-lithium based solid state batteries. *J Power Sources* **2015**, *282*, 299-322.
6. Bachman, J. C.; Mui, S.; Grimaud, A.; Chang, H.-H.; Pour, N.; Lux, S. F.; Paschos, O.; Maglia, F.; Lupart, S.; Lamp, P., Inorganic solid-state electrolytes for lithium batteries: mechanisms and properties governing ion conduction. *Chemical reviews* **2015**, *116* (1), 140-162.
7. Xiayin, Y.; Bingxin, H.; Jingyun, Y.; Gang, P.; Zhen, H.; Chao, G.; Deng, L.; Xiaoxiong, X., All-solid-state lithium batteries with inorganic solid electrolytes: Review of fundamental science. *Chinese Physics B* **2016**, *25* (1), 018802.
8. Goodenough, J. B.; Singh, P., Review-Solid Electrolytes in Rechargeable Electrochemical Cells. *J Electrochem Soc* **2015**, *162* (14), A2387-A2392.
9. Janek, J.; Zeier, W. G., A solid future for battery development. *Nature Energy* **2016**, *1*, 16141.
10. Fergus, J. W., Ceramic and polymeric solid electrolytes for lithium-ion batteries. *J Power Sources* **2010**, *195* (15), 4554-4569.
11. Knauth, P., Inorganic solid Li ion conductors: An overview. *Solid State Ionics* **2009**, *180* (14), 911-916.

12. Li, F.; Kitaura, H.; Zhou, H., The pursuit of rechargeable solid-state Li-air batteries. *Energ Environ Sci* **2013**, *6* (8), 2302-2311.
13. Yao, X.; Liu, D.; Wang, C.; Long, P.; Peng, G.; Hu, Y.-S.; Li, H.; Chen, L.; Xu, X., High-Energy All-Solid-State Lithium Batteries with Ultralong Cycle Life. *Nano Letters* **2016**, *16* (11), 7148-7154.
14. Kato, Y.; Hori, S.; Saito, T.; Suzuki, K.; Hirayama, M.; Mitsui, A.; Yonemura, M.; Iba, H.; Kanno, R., High-power all-solid-state batteries using sulfide superionic conductors. *Nature Energy* **2016**, *1*, 16030.
15. Cao, C.; Li, Z.-B.; Wang, X.-L.; Zhao, X.-B.; Han, W.-Q., Recent advances in inorganic solid electrolytes for lithium batteries. *Frontiers in Energy Research* **2014**, *2*, 25.
16. Mizuno, F.; Hayashi, A.; Tadanaga, K.; Tatsumisago, M., New, Highly Ion-Conductive Crystals Precipitated from $\text{Li}_2\text{S-P}_2\text{S}_5$ Glasses. *Adv Mater* **2005**, *17* (7), 918-921.
17. Kamaya, N.; Homma, K.; Yamakawa, Y.; Hirayama, M.; Kanno, R.; Yonemura, M.; Kamiyama, T.; Kato, Y.; Hama, S.; Kawamoto, K., A lithium superionic conductor. *Nature materials* **2011**, *10* (9), 682-686.
18. Seino, Y.; Ota, T.; Takada, K.; Hayashi, A.; Tatsumisago, M., A sulphide lithium super ion conductor is superior to liquid ion conductors for use in rechargeable batteries. *Energ Environ Sci* **2014**, *7* (2), 627-631.
19. Deiseroth, H. J.; Kong, S. T.; Eckert, H.; Vannahme, J.; Reiner, C.; Zaiß, T.; Schlosser, M., $\text{Li}_6\text{PS}_5\text{X}$: A Class of Crystalline Li-Rich Solids With an Unusually High Li^+ Mobility. *Angewandte Chemie International Edition* **2008**, *47* (4), 755-758.
20. Murugan, R.; Thangadurai, V.; Weppner, W., Fast lithium ion conduction in garnet-type $\text{Li}_7\text{La}_3\text{Zr}_2\text{O}_{12}$. *Angewandte Chemie International Edition* **2007**, *46* (41), 7778-7781.
21. Thangadurai, V.; Narayanan, S.; Pinzaru, D., Garnet-type solid-state fast Li ion conductors for Li batteries: critical review. *Chemical Society Reviews* **2014**, *43* (13), 4714-4727.
22. Aono, H.; Sugimoto, E.; Sadaoka, Y.; Imanaka, N.; Adachi, G. y., Ionic conductivity of solid electrolytes based on lithium titanium phosphate. *J Electrochem Soc* **1990**, *137* (4), 1023-1027.
23. Chen, M.; Adams, S., High performance all-solid-state lithium/sulfur batteries using lithium argyrodite electrolyte. *J Solid State Electr* **2015**, *19* (3), 697-702.
24. Yu, C.; Ganapathy, S.; de Klerk, N. J.; Roslon, I.; Van Eck, E. R.; Kentgens, A. P.; Wagemaker, M., Unravelling Li-Ion Transport from Picoseconds to Seconds: Bulk versus Interfaces in an Argyrodite $\text{Li}_6\text{PS}_5\text{Cl-Li}_2\text{S}$ All-Solid-State Li-Ion Battery. *J Am Chem Soc* **2016**, *138* (35), 11192-11201.

25. Yu, C.; van Eijck, L.; Ganapathy, S.; Wagemaker, M., Synthesis, structure and electrochemical performance of the argyrodite $\text{Li}_6\text{PS}_5\text{Cl}$ solid electrolyte for Li-ion solid state batteries. *Electrochim Acta* **2016**, *215*, 93-99.
26. Chen, M.; Prasada Rao, R.; Adams, S., The unusual role of $\text{Li}_6\text{PS}_5\text{Br}$ in all-solid-state $\text{CuS}/\text{Li}_6\text{PS}_5\text{Br}/\text{In-Li}$ batteries. *Solid State Ionics* **2014**, *268*, 300-304.
27. Chen, M.; Rao, R. P.; Adams, S., High capacity all-solid-state $\text{Cu-Li}_2\text{S}/\text{Li}_6\text{PS}_5\text{Br}/\text{In}$ batteries. *Solid State Ionics* **2014**, *262*, 183-187.
28. Chen, M.; Yin, X.; Reddy, M. V.; Adams, S., All-solid-state $\text{MoS}_2/\text{Li}_6\text{PS}_5\text{Br}/\text{In-Li}$ batteries as a novel type of Li/S battery. *J Mater Chem A* **2015**, *3* (20), 10698-10702.
29. Takada, K.; Kitami, Y.; Inada, T.; Kajiyama, A.; Kouguchi, M.; Kondo, S.; Watanabe, M.; Tabuchi, M., Electrochemical reduction of Li_2FeS_2 in solid electrolyte. *J Electrochem Soc* **2001**, *148* (10), A1085-A1090.
30. Kim, B.-C.; Takada, K.; Ohta, N.; Seino, Y.; Zhang, L.; Wada, H.; Sasaki, T., All-solid-state Li-ion secondary battery with FeS anode. *Solid State Ionics* **2005**, *176* (31), 2383-2387.
31. Hang, B. T.; Ohnishi, T.; Osada, M.; Xu, X.; Takada, K.; Sasaki, T., Lithium silicon sulfide as an anode material in all-solid-state lithium batteries. *J Power Sources* **2010**, *195* (10), 3323-3327.
32. Takada, K., Progress and prospective of solid-state lithium batteries. *Acta Materialia* **2013**, *61* (3), 759-770.
33. Kitaura, H.; Hayashi, A.; Tadanaga, K.; Tatsumisago, M., Improvement of electrochemical performance of all-solid-state lithium secondary batteries by surface modification of LiMn_2O_4 positive electrode. *Solid State Ionics* **2011**, *192* (1), 304-307.
34. Ohta, N.; Takada, K.; Zhang, L.; Ma, R.; Osada, M.; Sasaki, T., Enhancement of the High-Rate Capability of Solid-State Lithium Batteries by Nanoscale Interfacial Modification. *Adv Mater* **2006**, *18* (17), 2226-2229.
35. Takada, K., Interfacial nanoarchitectonics for solid-state lithium batteries. *Langmuir* **2013**, *29* (24), 7538-7541.
36. Luntz, A. C.; Voss, J.; Reuter, K., Interfacial Challenges in Solid-State Li-Ion Batteries. *The Journal of Physical Chemistry Letters* **2015**, *6* (22), 4599-4604.
37. Li, Y.; Zhou, W.; Chen, X.; Lü, X.; Cui, Z.; Xin, S.; Xue, L.; Jia, Q.; Goodenough, J. B., Mastering the interface for advanced all-solid-state lithium rechargeable batteries. *Proceedings of the National Academy of Sciences* **2016**, *113* (47), 13313-13317.
38. Tatsumisago, M.; Nagao, M.; Hayashi, A., Recent development of sulfide solid electrolytes and interfacial modification for all-solid-state rechargeable lithium batteries. *Journal of Asian Ceramic Societies* **2013**, *1* (1), 17-25.

39. Jung, Y. S.; Oh, D. Y.; Nam, Y. J.; Park, K. H., Issues and Challenges for Bulk-Type All-Solid-State Rechargeable Lithium Batteries using Sulfide Solid Electrolytes. *Israel J Chem* **2015**, *55* (5), 472-485.
40. Richards, W. D.; Miara, L. J.; Wang, Y.; Kim, J. C.; Ceder, G., Interface Stability in Solid-State Batteries. *Chem Mater* **2016**, *28* (1), 266-273.
41. Zhu, Y.; He, X.; Mo, Y., Origin of outstanding stability in the lithium solid electrolyte materials: insights from thermodynamic analyses based on first-principles calculations. *Acs Appl Mater Inter* **2015**, *7* (42), 23685-23693.
42. Sakuda, A.; Hayashi, A.; Tatsumisago, M., Interfacial observation between LiCoO₂ electrode and Li₂S-P₂S₅ solid electrolytes of all-solid-state lithium secondary batteries using transmission electron microscopy. *Chem Mater* **2009**, *22* (3), 949-956.
43. Takada, K.; Ohta, N.; Tateyama, Y., Recent Progress in Interfacial Nanoarchitectonics in Solid-State Batteries. *J Inorg Organomet P* **2015**, *25* (2), 205-213.
44. Dudney, N. J.; West, W. C.; Nanda, J., *Handbook of Solid State Batteries*. World Scientific: 2015; Vol. 6.
45. Kuhn, A.; Kunze, M.; Sreeraj, P.; Wiemhöfer, H.-D.; Thangadurai, V.; Wilkening, M.; Heitjans, P., NMR relaxometry as a versatile tool to study Li-ion dynamics in potential battery materials. *Solid state nuclear magnetic resonance* **2012**, *42*, 2-8.
46. Wilkening, M.; Heitjans, P., From Micro to Macro: Access to Long-Range Li⁺ Diffusion Parameters in Solids via Microscopic ^{6,7}Li Spin-Alignment Echo NMR Spectroscopy. *Chemphyschem* **2012**, *13* (1), 53-65.
47. Wagemaker, M.; Kentgens, A.; Mulder, F., Equilibrium lithium transport between nanocrystalline phases in intercalated TiO₂ anatase. *Nature* **2002**, *418* (6896), 397-399.
48. Wagemaker, M.; van de Krol, R.; Kentgens, A. P.; Van Well, A. A.; Mulder, F. M., Two phase morphology limits lithium diffusion in TiO₂ (anatase): A ⁷Li MAS NMR study. *J Am Chem Soc* **2001**, *123* (46), 11454-11461.
49. Ganapathy, S.; van Eck, E. R.; Kentgens, A. P.; Mulder, F. M.; Wagemaker, M., Equilibrium Lithium-Ion Transport Between Nanocrystalline Lithium-Inserted Anatase TiO₂ and the Electrolyte. *Chemistry-A European Journal* **2011**, *17* (52), 14811-14816.
50. Ernst, R. R.; Bodenhausen, G.; Wokaun, A., *Principles of nuclear magnetic resonance in one and two dimensions*. Clarendon Press Oxford: 1987; Vol. 14.
51. Ernst, M.; Kentgens, A. P.; Meier, B. H., 2D exchange NMR spectra under slow MAS: A simplified scheme to obtain pure-phase spectra without unwanted cross peaks. *Journal of Magnetic Resonance* **1999**, *138* (1), 66-73.

52. Boulineau, S.; Courty, M.; Tarascon, J.-M.; Viallet, V., Mechanochemical synthesis of Li-argyrodite $\text{Li}_6\text{PS}_5\text{X}$ (X=Cl, Br, I) as sulfur-based solid electrolytes for all-solid-state batteries application. *Solid State Ionics* **2012**, *221*, 1-5.
53. Epp, V.; Gün, O. z. I.; Deiseroth, H.-J. r.; Wilkening, M., Highly mobile ions: low-temperature NMR directly probes extremely fast Li^+ hopping in argyrodite-type $\text{Li}_6\text{PS}_5\text{Br}$. *The Journal of Physical Chemistry Letters* **2013**, *4* (13), 2118-2123.
54. Nagao, M.; Hayashi, A.; Tatsumisago, M., High-capacity Li_2S -nanocarbon composite electrode for all-solid-state rechargeable lithium batteries. *J Mater Chem* **2012**, *22* (19), 10015-10020.
55. Hayashi, A.; Ohtsubo, R.; Ohtomo, T.; Mizuno, F.; Tatsumisago, M., All-solid-state rechargeable lithium batteries with Li_2S as a positive electrode material. *J Power Sources* **2008**, *183* (1), 422-426.
56. Hayashi, A.; Ohtsubo, R.; Tatsumisago, M., Electrochemical performance of all-solid-state lithium batteries with mechanochemically activated Li_2S -Cu composite electrodes. *Solid State Ionics* **2008**, *179* (27), 1702-1705.
57. Han, F.; Yue, J.; Fan, X.; Gao, T.; Luo, C.; Ma, Z.; Suo, L.; Wang, C., High-Performance All-Solid-State Lithium-Sulfur Battery Enabled by a Mixed-Conductive Li_2S Nanocomposite. *Nano letters* **2016**, *16* (7), 4521-4527.
58. Huang, B.; Yao, X.; Huang, Z.; Guan, Y.; Jin, Y.; Xu, X., Li_3PO_4 -doped $\text{Li}_7\text{P}_3\text{S}_{11}$ glass-ceramic electrolytes with enhanced lithium ion conductivities and application in all-solid-state batteries. *J Power Sources* **2015**, *284*, 206-211.
59. Schmidt-Rohr, K.; Spiess, H. W., *Multidimensional solid-state NMR and polymers*. Academic Press: 1994.
60. Doyle, M.; Newman, J., Analysis of capacity-rate data for lithium batteries using simplified models of the discharge process. *J Appl Electrochem* **1997**, *27* (7), 846-856.
61. Friauf, R. J., Correlation effects for diffusion in ionic crystals. *J Appl Phys* **1962**, *33* (1), 494-505.
62. Mehrer, H., *Diffusion in solids: fundamentals, methods, materials, diffusion-controlled processes*. Springer Science & Business Media: 2007; Vol. 155.
63. Auvergniot, J.; Cassel, A.; Ledeuil, J.-B.; Viallet, V.; Seznec, V.; Dedryvère, R., Interface Stability of Argyrodite $\text{Li}_6\text{PS}_5\text{Cl}$ toward LiCoO_2 , $\text{LiNi}_{1/3}\text{Co}_{1/3}\text{Mn}_{1/3}\text{O}_2$, and LiMn_2O_4 in Bulk All-Solid-State Batteries. *Chem Mater* **2017**, *29* (9), 3883-3890.
64. Hakari, T.; Nagao, M.; Hayashi, A.; Tatsumisago, M., All-solid-state lithium batteries with Li_3PS_4 glass as active material. *J Power Sources* **2015**, *293*, 721-725.

Appendix

Quantification of interfacial exchange

Quantification of exchange between the Li_2S and $\text{Li}_6\text{PS}_5\text{Br}$ species was performed by fitting the growing Li_2S signal to a diffusion model wherein a solution to Fick's law for diffusion is determined

It is given by $\frac{\partial m(\vec{r}, t)}{\partial t} = \vec{\nabla}^2 \cdot \{D(\vec{r})m(\vec{r}, t)\}$, where $m(\vec{r}, t)$ is the magnetization of

Li at position \vec{r} and t , and D is the Li-ion self-diffusion coefficient. We assume that the equilibrium exchange between the electrode and electrolyte can be described by an effective diffusion coefficient. Using the mathematical model for spin-diffusion described by Schmidt-Rohr *et al.*¹ the rate of magnetization of the electrode particles is described by the difference between the initial magnetization and the rate of demagnetization of the electrolyte particles. Making the assumption that the $\text{Li}_6\text{PS}_5\text{Br}$ solid electrolyte particles are cube shaped and are embedded in an infinite Li_2S matrix, the analytical expression for the rate of magnetization of the Li_2S phase from the $\text{Li}_6\text{PS}_5\text{Br}$ phase can be given as²

$$m(t_{\text{mix}}) = 1 - \left\{ \frac{m_0}{2} \sqrt{4Dt_{\text{mix}}} \left[\text{ierfc}\left(\frac{d}{\sqrt{4Dt_{\text{mix}}}}\right) + \text{ierfc}\left(\frac{-d}{\sqrt{4Dt_{\text{mix}}}}\right) - \frac{2}{\sqrt{\pi}} \right] \right\}^3$$

Where $\text{ierfc}(x) = \frac{1}{\sqrt{\pi}} \exp(-x^2) - x(1 - \text{erf}(x))$ and d the Li diffusion distance from

the $\text{Li}_6\text{PS}_5\text{Br}$ particle to Li_2S . We assume that diffusion occurs from the center of a $\text{Li}_6\text{PS}_5\text{Br}$ solid electrolyte particle to the center of a Li_2S particle for the sake of simplicity. The average particle sizes are determined from the FWHM of their XRD patterns to be 23 nm and 38 nm for the $\text{Li}_6\text{PS}_5\text{Br}$ and Li_2S phases respectively from mixture III, and due to the larger Li_2S crystallite size and much lower conductivity^{3,4} our assumption of an infinite Li_2S is reasonable. The average diffusion distance from the center of a $\text{Li}_6\text{PS}_5\text{Br}$ particle to a Li_2S one is therefore approximately $d = 30$ nm. It should be realized that the resulting diffusion

coefficient is directly correlated to the lithium diffusion distance d , and the assumption that the Li-diffusion occurs from the center of a $\text{Li}_6\text{PS}_5\text{Br}$ particle to the center of the Li_2S particle is most likely an overestimation due to the poor conductivity of the Li_2S grains, thereby leading to an overestimation of the diffusion coefficient. To compare the Li-ion dynamics in $\text{Li}_6\text{PS}_5\text{Br}$ obtained using different methods with the conductivity of $\text{Li}_6\text{PS}_5\text{Br}$ measured at 298 K using impedance spectrometry, this obtained jump rate was roughly converted into Li-ion conductivity using both the Nernst-Einstein equation and the Einstein-Smoluchowski equation.^{5,6} A comparison of the various Li-ion conductivities determined is given in Figure 4.

References

1. Schmidt-Rohr, K. & Spiess, H. W. *Multidimensional Solid-State NMR and Polymers*. (Academic Press, 1994).
2. Wagemaker, M., Kentgens, A. & Mulder, F. Equilibrium lithium transport between nanocrystalline phases in intercalated TiO_2 anatase. *Nature* **418**, 397-399 (2002).
3. Mousa, M., Oei, Y. & Richtering, H. NMR investigations of cation diffusion in some solids with antiferroite structure. *J. Phys. Colloq.* **41**, C6-223-C226-226 (1980).
4. Yang, Y. *et al.* High-capacity micrometer-sized Li_2S particles as cathode materials for advanced rechargeable lithium-ion batteries. *J. Am. Chem. Soc.* **134**, 15387-15394 (2012).
5. Kuhn, A. *et al.* Li ion dynamics in Al-doped garnet-type $\text{Li}_7\text{La}_3\text{Zr}_2\text{O}_{12}$ crystallizing with cubic symmetry. *Z. Phys. Chem.* **226**, 525-537 (2012).
6. Buschmann, H. *et al.* Structure and dynamics of the fast lithium ion conductor " $\text{Li}_7\text{La}_3\text{Zr}_2\text{O}_{12}$ ". *Phys. Chem. Chem. Phys.* **13**, 19378-19392 (2011).

Summary

The presented thesis aims at understanding the relationship between the synthesis procedure of argyrodite $\text{Li}_6\text{PS}_5\text{X}$ ($\text{X}=\text{Br}, \text{Cl}$) solid electrolytes and the resulting structure, morphology, and solid-state battery performance. Specifically, argyrodite solid electrolytes in combination with Li_2S positive electrodes were investigated using X-ray and neutron diffraction, impedance spectroscopy and solid state NMR. The conclusions are organized in three parts following the scientific questions in Chapter 1.

(1) Synthesis and electrochemical performance

The argyrodite $\text{Li}_6\text{PS}_5\text{X}$ ($\text{X}=\text{Br}, \text{Cl}$) solid electrolytes were prepared by mechanical milling, followed by an annealing process, reaching an ionic conductivity of up to 10^{-3} S/cm at room temperature. Simultaneous Rietveld refinement of X-ray and neutron diffraction data show that the halogen dopants are well distributed over the S_{4a} and S_{4c} crystallographic sites, which as a consequence will lead to a well-distributed charge, compensating Li-ion vacancies, a prerequisite for high conductivities. Cyclic voltammetry measurements demonstrate that both Li metal and Li-Al are not suitable as negative electrode materials for the $\text{Li}_6\text{PS}_5\text{Cl}$ based solid-state cell. The best negative electrode tested for $\text{Li}_6\text{PS}_5\text{X}$ ($\text{X}=\text{Cl}, \text{Br}$) is Li-In or In displaying relatively good reversibility and cyclability combined with S or Li_2S positive electrodes in solid-state cells. Pressed C-S/ $\text{Li}_6\text{PS}_5\text{Cl}$ /Li-In cells deliver initial capacities above 1300 mAh/g and retaining 400 mAh/g after 20 cycles. Using Li_2S as a positive electrode material requires nanosizing of the Li_2S particles. Nanosized Li_2S in combination with $\text{Li}_6\text{PS}_5\text{Cl}$ shows an initial charge and discharge capacity of approximately 1200 and 634 mAh/g respectively,

Summary

corresponding to a coulombic efficiency of only 52.8% within the optimal (dis)charge window between 0.4 and 3.5 V vs. In (1.0 to 4.1 V vs. Li/Li⁺), which was determined by Cyclic voltammetry (CV) measurements. Impedance spectroscopy indicates that the poor initial coulombic efficiency and cyclability of the solid-state cells may be caused by an increase in the interface resistance between the solid-electrolyte and the cathode electrode during cycling. Potential contributors to an increased interface resistance include oxidation of the solid electrolyte as well as loss of contact occurring due to the large volumetric changes in S or Li₂S positive electrodes.

For Li₆PS₅Br materials with different post-synthesis treatments, annealed Li₆PS₅Br (AN-Li₆PS₅Br) followed by mechanical milling exhibits the highest ionic conductivity, as determined by impedance spectroscopy. Cyclic voltammetry (CV) measurements of nano-Li₂S/AN-Li₆PS₅Br/In solid-state batteries show optimal cycling between 0 and 3.5 V vs. In (from 0.6 to 4.1 V vs. Li/Li⁺). When the AN-Li₆PS₅Br material is ball-milled again to smaller particle sizes with an average crystallite size of 22 nm, the capacity retention improves resulting in a capacity of approximately 500 mAh/g retained over 25 cycles. The smaller crystallite sizes and intimate mixing are suggested to facilitate interfacial contacts with the nanostructured Li₂S. This results in a lower interfacial resistance and hence lower overpotentials during cycling. These results present the different demands for the solid electrolyte, which in the positive electrode mixture requires abundant interfaces, while in the electrolyte separator region requires the maximum total conductivity. Impedance spectroscopy does not provide conclusive evidence of the origin of the poor cycling exhibited. It is however expected that the interface between the solid electrolyte and the positive electrode is the largest contributor to the internal resistance in these solid-state batteries. To utilize a majority of the Li₂S capacity, a large overpotential is required, even at low currents. This most likely

challenges the electrochemical stability of the $\text{Li}_6\text{PS}_5\text{Br}$ solid electrolyte, resulting in oxidation products, which may increase the interfacial impedance.

(2) Bulk Li-ion diffusion in argyrodite $\text{Li}_6\text{PS}_5\text{X}$ (X=Br, Cl) solid electrolytes

The bulk conductivity in argyrodite $\text{Li}_6\text{PS}_5\text{Cl}$ is investigated by a combination of ^7Li NMR relaxation experiments and First Principle DFT based Molecular Dynamics simulations. This reveals two clearly distinguishable Li-ion motional processes: (1) Local transitions within the cage-like structure formed by Li-ion positions around the S_{4c} or Cl_{4c} atoms and (2) inter-cage transitions that in combination of the cage-like transitions are responsible for the macroscopic diffusion of Li-ions in the crystalline bulk $\text{Li}_6\text{PS}_5\text{Cl}$ structure. In addition, a good quantitative agreement is established between the bulk conductivity probed by NMR experiments and predictions by DFT Molecular Dynamics simulations. A comparison with the macroscopic conductivity measured by impedance spectroscopy suggests a significant lowering of the conductivity due to the $\text{Li}_6\text{PS}_5\text{Cl}$ - $\text{Li}_6\text{PS}_5\text{Cl}$ grain boundaries.

For $\text{Li}_6\text{PS}_5\text{Br}$ materials, the impact of the post-synthesis treatment on the bulk conductivity is investigated. The AN-BM- $\text{Li}_6\text{PS}_5\text{Br}$ obtained by annealing the milled $\text{Li}_6\text{PS}_5\text{Br}$ shows the highest Li-ion conductivity determined by impedance spectroscopy. The conductivity is higher than both the material before annealing and the annealed material (AN- $\text{Li}_6\text{PS}_5\text{Br}$). NMR relaxation results show that the bulk Li-ion mobility is only marginally improved. The increase in conductivity should mainly be attributed to the larger fraction of mobile Li-ions. This is in turn most likely due to the larger crystalline fraction observed by both XRD and TEM. Assuming that the amorphous fraction of the solid electrolyte is located at the grain boundaries between neighboring particles, this suggests that an amorphous fraction is not beneficial for Li-ion transport over the interfaces between neighboring

Summary

particles, of either the solid electrolyte or the electrode material. This combined with the conclusion that the solid electrolyte in the electrode mixture should be nano-sized to provide abundant interfaces means that these nano-sized particles should be highly crystalline.

Simultaneous refinement of the neutron and X-ray diffraction data of the various post-synthesis treated $\text{Li}_6\text{PS}_5\text{Br}$ materials suggest that the Br dopant is inhomogeneously distributed over the two S_{4a} and S_{4c} crystallographic sites from the core to the surface of the particles. It is proposed that this results in an inhomogeneous conductivity, which is larger in the surface region of annealed materials (AN- $\text{Li}_6\text{PS}_5\text{Br}$ and AN-BM- $\text{Li}_6\text{PS}_5\text{Br}$). This motivates future research towards an understanding role of these distributions in the performance of solid-state batteries and developing synthesis routes to control the site distribution of the halogen dopant.

(3) Li-ion transport over the solid electrolyte-electrode interface

Electrochemical impedance spectroscopy (EIS) is commonly applied to determine the interface resistance between the electrode and electrolyte for lithium ion batteries with liquid electrolytes. However, for solid-state batteries, available EIS equivalent circuit models are not successful in unraveling charge transport kinetics. To be able to distinguish Li-ion bulk transport in the solid electrolyte from the Li-ion transport over the interface between the solid electrolyte and the electrode material, ^7Li solid state exchange NMR was employed. For $\text{Li}_6\text{PS}_5\text{Cl}$, the difference in static ^7Li line width allows the determination of spontaneous transport between the $\text{Li}_6\text{PS}_5\text{Cl}$ solid electrolyte and Li_2S positive electrode phases in positive electrode mixtures. This 1D exchange NMR experiment allows quantitative determination of Li-ion transport over these interfaces, proving that the electrolyte-electrode $\text{Li}_6\text{PS}_5\text{Cl}$ - Li_2S interface is the major hurdle for Li-ion

transport in all-solid-state batteries, limiting the power performance. For the $\text{Li}_6\text{PS}_5\text{Br-Li}_2\text{S}$ positive electrode mixtures, the ^7Li chemical shift difference induced by Br atom makes it possible to perform 2D exchange NMR experiments that quantify the Li-ion transport over the $\text{Li}_6\text{PS}_5\text{Br-Li}_2\text{S}$ interfaces. This approach is used to investigate the influence of preparation conditions and cycling on the Li-ion transport over the $\text{Li}_6\text{PS}_5\text{Br-Li}_2\text{S}$ interfaces. The results indicate that nanosizing Li_2S and intimate mixing of nano- Li_2S with $\text{Li}_6\text{PS}_5\text{Br}$ are essential to provide significant Li-ion conductivity over the $\text{Li}_2\text{S-Li}_6\text{PS}_5\text{Br}$ interface, simply by providing abundant interfaces. The activation energy for Li-ion transport over the $\text{Li}_2\text{S-Li}_6\text{PS}_5\text{Br}$ interface is slightly larger than that for bulk $\text{Li}_6\text{PS}_5\text{Br}$ conductivity, indicating that in the pristine, uncycled positive electrode mixtures the barrier for Li-ion transport over the interface is small. However, the much smaller interface conductivity compared to the bulk conductivity suggests that there is poor wetting between Li_2S and $\text{Li}_6\text{PS}_5\text{Br}$. Therefore, there is little electrode-electrolyte contact area present where Li-ion transport can take place. After two full charge-discharge cycles, between 0.62-4.12 V vs. Li^+/Li , the Li-ion exchange is significantly lowered, resulting in a drop in conductivity of almost one order of magnitude. Additionally, the cycling increases the activation energy for Li-ion transport over the $\text{Li}_2\text{S-Li}_6\text{PS}_5\text{Br}$ interface by a factor of three from 0.13 to 0.39 eV. This may be due to (1) large volumetric changes of Li_2S upon charge and discharge causing a loss of contact between Li_2S and $\text{Li}_6\text{PS}_5\text{Br}$ and (2) redox instabilities at the $\text{Li}_2\text{S-Li}_6\text{PS}_5\text{Br}$ interfaces leading to an interfacial layer that poses a higher barrier for Li-ion transport. We anticipate that both play a role at the $\text{Li}_2\text{S-Li}_6\text{PS}_5\text{Br}$ interface where (1) is responsible for the drop in interface conductivity because of loss of interfacial contact and (2) for the increase in activation energy due to an interfacial layer increasing the diffusion barrier. Estimation of the resistances based on exchange NMR provides a consistent picture of the role of the electrode-electrolyte interface on the solid-state battery performance. For positive electrode mixtures,

Summary

nanosizing of both $\text{Li}_6\text{PS}_5\text{Br}$ solid electrolyte and Li_2S electrode materials are essential to achieving an initial low interface resistance compared to the bulk solid electrolyte resistance. However, only two charge-discharge cycles result in a large increase of the interface resistance, which is suggested to be responsible for the observed increase in polarization during cycling, and resulting in the observed capacity fading. This work demonstrates the ability of exchange NMR to unambiguously quantify the amount and timescale of Li-ion transport over the solid electrolyte-electrode interface between distinguishable Li-ion sites in the electrode and the solid electrolyte, which is impossible by using any other technique up to date.

Concluding remarks

For argyrodite $\text{Li}_6\text{PS}_5\text{X}$ ($\text{X}=\text{Br}, \text{Cl}$) solid-state electrolytes, the impact of the synthesis conditions on the conductivity and battery performance are investigated. Crystallinity, particle size and the position of the halogen dopant on the crystallographic sites are shown to be important in both the bulk Li-ion conductivity and effective Li-ion transport in positive electrode mixtures with Li_2S . This demonstrates the different demands for solid electrolytes in the positive electrode mixtures and in the solid electrolyte separator region, giving direction to the design of future argyrodite solid electrolytes for solid-state batteries. Using $\text{Li}_2\text{S}-\text{Li}_6\text{PS}_5\text{X}$ ($\text{X}=\text{Br}, \text{Cl}$) solid-state batteries as an example, the present experimental results demonstrate that Li-ion interfacial transport over electrode-electrolyte interfaces is the major bottleneck to Li-ion transport through all-solid-state batteries. Both the preparation conditions and battery cycling, affect the interfacial transport considerably. Therefore, realizing high energy density all-solid-state batteries will require interface design to prevent the large increase in impedance during cycling, where in particular volumetric changes and redox instabilities appear responsible.

Samenvatting

Dit proefschrift richt zich er op het verband te begrijpen tussen de procedure voor de synthese van argyrodiet $\text{Li}_6\text{PS}_5\text{X}$ ($\text{X}=\text{Br}, \text{Cl}$) vaste-stofelektrolyten en de resulterende structuur, morfologie en prestatie van vaste-stof batterijen. Meer in het bijzonder werden argyrodiet vaste-stof elektrolyten bestudeerd in combinatie met Li_2S positieve elektroden met behulp van Röntgen- en neutronenverstrooiing, impedantiespectroscopie en vaste-stof NMR. De conclusies zijn verdeeld in drieën naar de wetenschappelijke vragen in Hoofdstuk 1.

(1) Synthese en electrochemische prestatie

De argyrodiet $\text{Li}_6\text{PS}_5\text{X}$ ($\text{X}=\text{Br}, \text{Cl}$) vaste-stof elektrolyten werden bereid door mechanisch malen, gevolgd door annealen, waarmee een ionengeleidbaarheid tot 10^{-3} S/cm bij kamertemperatuur werd bereikt. Simultane Rietveldverfijning van Röntgen- en neutronenverstrooiingsdata toont dat de halogeenatomen goed verdeeld zijn over de S_{4a} en S_{4c} kristallografische posities, wat leidt tot een goede ladingsverdeling ter compensatie van Li-ion vacatures, een voorwaarde voor hoge geleidbaarheden. Cyclische voltammetrie metingen tonen aan dat zowel Li metaal als Li-Al niet geschikt is als materiaal voor de negatieve elektrode van de op $\text{Li}_6\text{PS}_5\text{Cl}$ gebaseerde vaste-stofcel. De beste negatieve elektrode, die getest werd voor $\text{Li}_6\text{PS}_5\text{X}$ ($\text{X}=\text{Cl}, \text{Br}$) is Li-In of In, die relatief goede reversibiliteit en gedrag bij herhaling van de ladingscyclus vertonen in combinatie met S of Li_2S positieve elektroden in vaste-stofcellen. Geperste C-S/ $\text{Li}_6\text{PS}_5\text{Cl}$ /Li-In cellen leveren initiële capaciteiten boven 1300 mAh/g en meer dan 400 mAh/g na 20 cycli. Gebruik van Li_2S als materiaal voor de positieve elektrode vereist nanoschaal van de Li_2S deeltjes. Li_2S op nanoschaal gecombineerd met $\text{Li}_6\text{PS}_5\text{Cl}$ toont een initiële ladings-

Samenvatting

en ontladingscapaciteit van ongeveer 1200 en 634 mAh/g respectievelijk, wat correspondeert met een coulombische efficiëntie van slechts 52.8% binnen het optimale (ont)ladingsvenster tussen 0.4 en 3.5 V vs. In (1.0 tot 4.1 V vs. Li/Li⁺), wat werd bepaald door cyclische voltammetrie (CV) metingen. Impedantiespectroscopie geeft aanwijzingen dat de slechte initiële coulombische efficiëntie en gedrag bij herhaling van de ladingscyclus van de vaste-stofcellen veroorzaakt zouden kunnen worden door een toename in de grensvlakweerstand tussen de vaste-stof elektrolyt en de kathode gedurende de ladingscyclus. Potentiele bijdragers tot een verhoogde grensvlakweerstand zijn oxidatie van de vaste-stofelektrolyt evenals verlies van contact door de grote volumeveranderingen in de S of Li₂S positieve elektroden.

Voor Li₆PS₅Br materialen met verschillende post-synthese behandelingen, vertoont annealed Li₆PS₅Br (AN- Li₆PS₅Br) gevolgd door mechanisch malen de hoogste ionengeleidbaarheid, zoals bepaald uit impedantiespectroscopie. Cyclische voltammetrie (CV) metingen aan nano-Li₂S/AN-Li₆PS₅Br/In vaste-stofbatterijen tonen een optimale ladingscyclus tussen 0 en 3.5 V vs. In (van 0.6 tot 4.1 V vs. Li/Li⁺). Als het AN-Li₆PS₅Br materiaal met de kogelmolen weer op kleinere deeltjesgrootte gebracht wordt met een gemiddelde kristallietgrootte van 22 nm, verbetert het capaciteitsbehoud resulterend in een capaciteit van ongeveer 500 mAh/g behouden over 25 cycli. Van de kleinere kristallietgrootten en grondige menging wordt geopperd dat zij oppervlaktecontacten met Li₂S op nanoschaal faciliteren. Dit resulteert in een lagere grensvlakweerstand en daarmee lagere overpotentialen gedurende de ladingscyclus. Deze resultaten presenteren de verschillende vereisten voor de vaste-stofelektrolyt: in het mengsel voor de positieve elektrode volop oppervlakken, terwijl het elektrolytseparator gebied maximale totale geleidbaarheid eist. Impedantiespectroscopie geeft geen doorslaggevende evidentie voor de oorsprong van de verslechtering van het gedrag

na meerdere cycli. Er wordt echter verwacht, dat het grensvlak tussen de vastestofelektrolyt en de positieve elektrode de grootste bijdrage levert voor de interne weerstand in deze vaste-stofbatterijen. Om het grootste deel van de Li_2S capaciteit te gebruiken is een grote overpotentiaal vereist, zelfs bij lage stroom. Dit tast hoogstwaarschijnlijk de elektrochemische stabiliteit aan van de $\text{Li}_6\text{PS}_5\text{Br}$ vastestofelektrolyt, resulterend in oxidatieproducten, die de grensvlakimpedantie kunnen verhogen.

(2) Volume Li-ion diffusie in argyrodiet $\text{Li}_6\text{PS}_5\text{X}$ (X=Br, Cl) vastestofelektrolyten

De volume geleidbaarheid in argyrodiet $\text{Li}_6\text{PS}_5\text{Cl}$ is onderzocht met een combinatie van ^7Li NMR relaxatie experimenten en ab initio op DFT gebaseerde Moleculaire Dynamica simulaties. Dit onthult twee duidelijk onderscheidbare bewegingsprocessen voor het Li-ion: (1) Lokale overgangen binnen de kooiachtige structuur gevormd door Li-ionenposities rond de S_{4a} of Cl_{4c} atomen en (2) overgangen tussen de kooien die in combinatie met de overgangen binnen de kooien verantwoordelijk zijn voor de macroscopische diffusie van Li-ionen in de kristallijne $\text{Li}_6\text{PS}_5\text{Cl}$ structuur. Bovendien is goede kwantitatieve overeenkomst gevonden tussen de volumegeleidbaarheid gemeten met NMR experimenten en voorspellingen met DFT Moleculaire Dynamica simulaties. Vergelijking met de macroscopische geleidbaarheid gemeten met impedantiespectroscopie suggereert, dat een significante verlaging van de geleidbaarheid te danken is aan de $\text{Li}_6\text{PS}_5\text{Cl}$ - $\text{Li}_6\text{PS}_5\text{Cl}$ korrelgrenzen.

Voor $\text{Li}_6\text{PS}_5\text{Br}$ materialen wordt de impact van de post-synthese behandeling op de volumegeleidbaarheid onderzocht. Het AN-BM- $\text{Li}_6\text{PS}_5\text{Br}$ verkregen door annealing van het gemalen $\text{Li}_6\text{PS}_5\text{Br}$ vertoont de hoogste Li-ionengeleidbaarheid zoals bepaald door impedantiespectroscopie. De geleidbaarheid is hoger dan zowel

Samenvatting

die van het materiaal vóór annealing als het geannealde materiaal (AN-Li₆PS₅Br). NMR relaxatieresultaten tonen dat de volume Li-ionenbeweeglijkheid slechts marginaal verbeterd is. De toename in geleidbaarheid zou hoofdzakelijk toegeschreven moeten worden aan de grotere fractie beweeglijke Li-ionen. Dit is op zijn beurt hoogstwaarschijnlijk te danken aan de grotere kristallijne fractie zoals waargenomen zowel met XRD als TEM. Aangenomen dat de amorfe fractie van de vaste-stofelektrolyt gelokaliseerd is op de korrelgrenzen tussen naburige deeltjes, suggereert dit dat een amorfe fractie niet gunstig is voor Li-ionentransport over de grensvlakken tussen naburige deeltjes, van ofwel de vaste-stofelektrolyt danwel het elektrodemateriaal. Dit gecombineerd met de conclusie dat de vaste-stofelektrolyt in het elektrodemengsel van nanoschaal dient te zijn om volop in grensvlakken te voorzien betekent, dat deze nano-deeltjes sterk kristallijn zouden moeten zijn.

Simultane verfijning van de neutronen- en Röntgenverstrooiingsdata van de verschillende post-synthese behandelde Li₆PS₅Br materialen suggereert, dat Br inhomogeen verdeeld is over de twee S_{4a} en S_{4c} kristallografische posities van het centrum naar het oppervlak van de deeltjes. Er wordt voorgesteld dat dit resulteert in een inhomogene geleidbaarheid, die groter is in de oppervlakteregio van geannealde materialen (AN-Li₆PS₅Br en AN-BM-Li₆PS₅Br). Dit motiveert onderzoek in de toekomst om de rol te begrijpen van deze verdelingen in de prestatie van vaste-stofbatterijen, en synthesepaden te ontwikkelen om de verdeling van de halogeenatomen over de posities te beheersen.

(3) Li-ionentransport over het vaste-stofelektrolyt-elektrode grensvlak

Elektrochemische impedantiespectroscopie (EIS) wordt gewoonlijk toegepast om de weerstand van het grensvlak te bepalen tussen de elektrode en de elektrolyt voor lithium-ionenbatterijen met vloeibare elektrolyten. Voor vaste-stofbatterijen, echter, zijn beschikbare EIS equivalente circuitmodellen niet succesvol in het

ontrafelen van de kinetiek van het ladingstransport. Om in staat te zijn het Li-ionenvolumetransport in de vaste-stofelektrolyt te onderscheiden van het Li-ionentransport over het grensvlak tussen de vaste-stofelektrolyt en het elektrodemateriaal werd ^7Li vaste-stof exchange NMR gebruikt. Voor $\text{Li}_6\text{PS}_5\text{Cl}$ laat het verschil in statische ^7Li -lijnbreedte de bepaling toe van spontaan transport tussen de $\text{Li}_6\text{PS}_5\text{Cl}$ vaste-stofelektrolyt en Li_2S positieve-elektrodefasen in positieve-elektrodemengsels. Dit 1D exchange NMR experiment laat kwantitatieve bepaling toe van Li-ionentransport over deze grensvlakken, waarmee het bewijst dat het elektrolyt-elektrode $\text{Li}_6\text{PS}_5\text{Cl}$ - Li_2S grensvlak de hoogste horde is voor Li-ionentransport in volledig vaste-stofbatterijen en dus de spanningsprestatie beperkt. Voor de $\text{Li}_6\text{PS}_5\text{Br}$ - Li_2S positieve elektrodemengsels, maakt het verschil in ^7Li chemical shift geïnduceerd door het Br atoom het mogelijk 2D exchange NMR experimenten uit te voeren, die het Li-ionentransport over de $\text{Li}_6\text{PS}_5\text{Br}$ - Li_2S grensvlakken kwantificeren. Deze aanpak wordt gebruikt om de invloed te onderzoeken van bereidingsomstandigheden en het aantal cycli op het Li-ionentransport over de $\text{Li}_6\text{PS}_5\text{Br}$ - Li_2S grensvlakken. De resultaten tonen aan dat Li_2S op nanogrootte en grondig mengen van nano- Li_2S met $\text{Li}_6\text{PS}_5\text{Br}$ essentieel zijn om significante Li-ionengeleiding over het Li_2S - $\text{Li}_6\text{PS}_5\text{Br}$ grensvlak te verkrijgen, eenvoudigweg door volop grensvlakken aan te bieden. De activatie energie voor Li-ionentransport over het Li_2S - $\text{Li}_6\text{PS}_5\text{Br}$ grensvlak is enigszins groter dan die voor volume $\text{Li}_6\text{PS}_5\text{Br}$ geleiding, wat aangeeft dat in de oorspronkelijke positieve elektrodemengsels vóór de cycli de barrière voor Li-ionentransport over het grensvlak klein is. Echter, het feit, dat de grensvlakgeleiding veel kleiner is dan de volumegeleiding, suggereert dat er slechte bevochtiging is tussen Li_2S en $\text{Li}_6\text{PS}_5\text{Br}$. Daarom is er weinig elektrode-elektrolyt contactoppervlak waar Li-ionentransport kan plaatsvinden. Na twee volledige lading-ontladingscycli, tussen 0.62-4.12 V vs. Li^+/Li , is de Li-ionenuitwisseling significant verlaagd, resulterend in een verlaging van de geleiding met bijna een orde van grootte. Bovendien

Samenvatting

verhogen de cycli de activatie energie voor Li-ionentransport over het Li_2S - $\text{Li}_6\text{PS}_5\text{Br}$ grensvlak met een factor drie van 0.13 tot 0.39 eV. Dit kan komen door (1) grote volumeveranderingen van Li_2S bij lading en ontlading, die verlies van contact veroorzaken tussen Li_2S en $\text{Li}_6\text{PS}_5\text{Br}$ en (2) redox instabiliteiten aan de Li_2S - $\text{Li}_6\text{PS}_5\text{Br}$ grensvlakken, die leiden tot een grensvlaklaag die een hogere barrière voor Li-ionentransport vormt. Wij verwachten dat beide een rol spelen op het Li_2S - $\text{Li}_6\text{PS}_5\text{Br}$ grensvlak waar (1) verantwoordelijk is voor de val in grensvlakgeleiding door het verlies aan oppervlaktecontact en (2) voor de toename in activatie energie veroorzaakt door een oppervlaktelaag, die de diffusiebarrière verhoogt. Schatting van de weerstanden gebaseerd op exchange NMR leidt tot een consistent beeld van de rol van het elektrode-elektrolyt grensvlak op de prestatie van de vaste-stofbatterij. Voor positieve elektrodemengsels is het op nanogrootte brengen van zowel de $\text{Li}_6\text{PS}_5\text{Br}$ vaste-stofelektrolyt als Li_2S elektrodematerialen essentieel om een initieel lage grensvlakweerstand vergeleken met de volumeweerstand van de vaste-stofelektrolyt te bereiken. Maar slechts twee lading-ontladingscycli resulteren in een grote toename van de grensvlakweerstand, waarvan wordt gesuggereerd dat die verantwoordelijk is voor de waargenomen toename in polarisatie gedurende de cycli en resulteert in de waargenomen capaciteitsvermindering. Dit werk toont de geschiktheid van exchange NMR om ondubbelzinnig de mate en tijdschaal van Li-ionentransport over het vaste-stofelektrolyt-elektrode grensvlak tussen onderscheidbare Li-ionenposities in de elektrode en de vaste-stofelektrolyt te kwantificeren, wat tot nu toe niet mogelijk is met enige andere techniek.

Afsluitende opmerkingen

Voor argyrodiet $\text{Li}_6\text{PS}_5\text{X}$ ($\text{X}=\text{Br}, \text{Cl}$) vaste-stofelektrolyten, zijn de impact van de synthese omstandigheden op de geleidbaarheid en batterijprestatie onderzocht. Voor kristalliniteit, deeltjesgrootte en de bezetting van de kristallografische posities

door het halogeenatoom wordt aangetoond, dat zij belangrijk zijn voor zowel de volume Li-ionengeleiding als effectief Li-ionentransport in positievelektrodemengsels met Li_2S . Dit belicht de verschillende eisen aan vastestofelektrolyten in de positieve elektrodemengsels en in het vastestofelektrolytseparator gebied en geeft de richting aan voor het ontwerp van toekomstige argyrodiet vastestofelektrolyten voor vastestofbatterijen. Met $\text{Li}_2\text{S-Li}_6\text{PS}_5\text{X}$ ($\text{X}=\text{Br, Cl}$) vastestofbatterijen als voorbeeld, laten de huidige experimentele resultaten zien dat Li-ion grensvlaktransport over elektrode-elektrolyt grensvlakken het voornaamste knelpunt is voor Li-ionentransport door volledige vastestofbatterijen. Zowel de bereidingsomstandigheden als ladingscycli van de batterij hebben een aanzienlijke invloed op het grensvlaktransport. Daarom zal realisatie van volledige vastestofbatterijen met hoge energiedichtheid grensvlakontwerp vereisen om de grote toename in impedantie gedurende ladingscycli te voorkomen, waarvoor in het bijzonder volumeveranderingen en redox instabiliteiten verantwoordelijk lijken.

Acknowledgements

Finally, it is my great pleasure to write this part. I would like to take this opportunity to thank all those people who have helped me about my research and life in the past four and half years. I would not have finished this thesis without their help.

First of all, I would like to thank my supervisor Dr. ir Marnix Wagemaker and promoter Prof. dr. Ekkes Brück for having accepted me as a PHD candidate in the Fundamental Aspects of Materials and Energy (FAME) group. Thanks for all their continuous encouragement and valuable advices. I am very grateful for their useful comments about my thesis. My special thanks to my daily supervisor Marnix Wagemaker, who has been an very inspiring guide for my research. You taught me so many skills in exploring science and gave me so many good suggestions about the research. It was you, who taught me how to write the introduction part of a manuscript and to get useful information from the data. You gave me the flexibility to choose those research topics I am really interested in and never pushed me when I was stopped by those obstacles. Because of your patience, I can achieve some good results about sold-state batteries. Marnix, thanks for all of those suggestions, discussions, flexibility, and support. I would like to thank Ekkes, for you advice and efficiency of correcting my thesis, which helped me a lot. I have been inspired by your vision and attitude in scientific research during the time I am studying here.

I would like to express my gratitude to Swapna Ganapathy and Ernst R.H. van Eck for their help about solid-state NMR measurements. They taught me how to perform the measurements and analyze the data. Ernst was actively involved in

designing the experiments, setting up the measurements, and data analysis. Without your help, we would not have finished all of those measurements. My special thanks go to Swapna Ganapathy, one of my best friend and teacher in the Netherlands, who taught me everything about scientific research. I cannot imagine without your help how to finish the research work in the battery group. You taught me everything about NMR, what are the meaning of “ T_1 ” and “ T_2 ”, how to set the measurements, how to do the data analysis, how to get information from 1D and 2D ion exchange NMR, and so on. Moreover, you helped me a lot to improve my English, both oral English and writing English. You gave me encouragement to practice more and do not afraid to make mistakes. Your efficiency of correcting of our manuscripts helped us to get those publications in a short time. It’s my great pleasure to work together with you. Hope in future you can visit me in China and I can be your guide for touring. I also would like to express my gratitude to Erik and Fokko for their good suggestions during the work discussion time of battery group.

Working at Fundamental Aspects of Materials and Energy (FAME) was a fantastic experience for me. Interactions with Ekkes, Niels, Stephan and other group members during the coffee breaking time at 11:00 and the working discussion on Tuesday morning were really helpful for my research. I was really enjoying the time working in the FAME group in the past four years. I want to give my particularly grateful to Bert Zwart for helping me to seal so many quartz tubes. Without his help, I could not have finished numerous sulfide-based solid electrolytes synthesis work. I would like to thank Michel P. Steenvoorden and Frans Oostrum for their daily helps in the laboratory and for their efforts in the battery testing laboratory. My gratitude also goes to Kees Goubitz and Lambert van Eijck for their helps about the diffraction measurements work. Thanks to Anton J. E. Lefering for his assistance about the furnace settings. I am also grateful for Nicole Banga, Ilse van der Kraaij and Trudy Beentjes for their supports taking

care of my administrative staff. I also want to express my gratitude to Jouke Heringa for his support in numerous computer-related issues, and also for his kind help about solving the non-work related Dutch documentary explaining work. I would also want to thank him for the translation into Dutch of the summary and the propositions of my thesis. Also I want to express my thanks to Hans Janssen, Gerrit Janssen and Jan Schoonbrood for their technical assistance of solid-state NMR measurements. I would like to thank Shibabrata Basak (TNW) for his help with the TEM measurements. I would also like to express my gratitude to my friend Prof. Long Zhang (Yanshan University, China) for his support in the SEM measurements and cooperation work about the $\text{Li}_6\text{PS}_5\text{X}$ ($\text{X}=\text{Cl}, \text{Br}$). Thanks to Jart Hageman for his help about the XRD and neutron diffraction refinements of the $\text{Li}_6\text{PS}_5\text{X}$ ($\text{X}=\text{Cl}, \text{Br}$) electrolytes.

I want to thank all of my former and present colleagues in the battery group: Dr. Swapna Ganapathy, Michel P. Steenvoorden, Frans Oostrum, Dr. Kun Shen, Dr. Deepak Pratap Singh, Dr. Xiaoyu Zhang, Dr. Alexander Lyedovskykh, Dr. Chandra George, Dr. Heng Wang, Yaolin Xu, Zhaolong Li, Alexandros Vasileiadis, Tomas Varhallen, Niek de Klerk, Peter-Paul Harks, Martijn van Hulzen, Violetta Arszelewska, Chao Wang, Shasha Lyu, Kun Qian, Yibo Zhang, Remco van der Jagt, Frieda Davey, Bo Peng. Thanks for their help during the last four years and I really enjoyed the time to work with all those guys. Moreover, I am also grateful to people in the FAME and NPM2 group: Dr. Anca Anastasopol, Dr. Zhiqiang Ou, Dr. Zhou Zhou, Dr. Francois Guillou, Dr. Shasha Zhang, Dr. Lei Ma, Dr. Bole Yi, Dr. Michael Maschek, Dr. Xuefei Miao, Dr. Fengjiao Qian, Dr. Thang Nguyen, Dr. Maurits Boeije, Wenqin Shi, Prasad Gonuganta, Haixing Fang, Bawei Huang, Jiawei Lai, Xinmin You, Bei Tian, Chuanqin Shi. I also want to express my special thanks to Yueting Liu, one of my best friends, for his suggestions and supports.

I gratefully acknowledge the financial support by the European Research Council under the European Union's Seventh Framework Programme (FP/2007-2013)/ERC Grant Agreement No. [307161].

Last but not least, I would like to express my deepest love to my whole family who has always supported me in any case. I want to thank my parents for their support in my entire life. They raised me with their truly love, cared my health, and encouraged to overcome all the challenges both in my research and daily life. Finally, I would like to thank my beloved wife, Xiaocui Chen (Cathy), for everything you have done for me, to raise my young son Muchen Yu (Andy) and take care of my parents. You are always being there with me both the great and difficult moments. Life is fantastic with you and our son, Muchen.

List of Publications

Publications Related to This Thesis

1. **Chuang Yu**, Swapna Ganapathy, Ernst R.H. van Eck, Lambert van Eijck, Shibabrata Basak, Yanyan Liu, Long Zhang, Henny W. Zandbergen, Marnix Wagemaker, “Revealing the effects of annealing on Li-ion mobility in the $\text{Li}_6\text{PS}_5\text{Br}$ solid electrolyte synthesized by a mechanical milling route”, [Journal of Materials Chemistry A](#), accepted. (chapter 5)
2. **Chuang Yu**[#], Swapna Ganapathy[#], Ernst R.H. van Eck, Heng Wang, Shibabrata Basak, Zhaolong Li, Marnix Wagemaker, “Accessing the bottleneck in all-solid state batteries, Li-ion transport over the interface between the solid-electrolyte and electrode”, [Nature Communications](#), accepted. (chapter 6)
3. **Chuang Yu**, Lambert van Eijck, Swapna Ganapathy, Marnix Wagemaker, “Synthesis, structure and electrochemical performance of the argyrodite $\text{Li}_6\text{PS}_5\text{Cl}$ solid electrolyte for Li-ion solid state batteries”, [Electrochimica Acta](#), **215**, 93 (2016). (chapter 3)
4. **Chuang Yu**, Swapna Ganapathy, Niek J. J. de Klerk, Irek Roslon, Ernst R. H. van Eck, Arno P. M. Kentgens, and Marnix Wagemaker, “Unravelling Li-ion transport from pico-seconds to seconds, bulk versus interfaces in an argyrodite $\text{Li}_6\text{PS}_5\text{Cl}$ - Li_2S all solid state Li-ion battery”, [Journal of The American Chemical Society](#), **138**, 11192 (2016). (chapter 4)

Other Publications

5. **Chuang Yu**, Swapna Ganapathy, Niek J. J. de Klerk, Ernst R.H. van Eck, Marnix Wagemaker, “Na-ion dynamics in tetragonal and cubic Na_3PS_4 , a Na-ion conductor for solid state Na-ion batteries”, [Journal of Materials Chemistry A](#), **4**, 15095 (2016).
6. **Chuang Yu**, Swapna Ganapathy, Jart Hageman, Ernst R.H. van Eck, Lambert van Eijck, Long Zhang, Heng Wang, Chao Wang, Marnix Wagemaker, “Synthesis of $\text{Li}_6\text{PS}_5\text{Cl}$ by a simple solid-state method and its application to all-solid-state batteries”, [Journal of Power Source](#), under review.

7. **Chuang Yu**, Swapna Ganapathy, Ernst R.H. van Eck, Marnix Wagemaker, “Investigation of Li-ions transfer in $\text{Li}_7\text{P}_3\text{S}_{11}$ and solid state lithium batteries”, in preparation.
8. **Chuang Yu**, Swapna Ganapathy, Long Zhang, Marnix Wagemaker, “Investigation of synthesis conditions for $\text{Li}_6\text{PS}_5\text{X}$ ($\text{X}=\text{Cl}, \text{Br}$) with solid-state reaction method”, in preparation.
9. **Chuang Yu**, Swapna Ganapathy, Jart Hageman, Ernst R.H. van Eck, Lambert van Eijck, Yanyan Liu, Tammo Schwietert, Long Zhang, Marnix Wagemaker, “Revealing structure differences and Li-ion transport properties for $\text{Li}_6\text{PS}_5\text{Cl}_x\text{Br}_{1-x}$ ($x=0, 0.25, 0.50, 0.75, 1.00$) prepared by solid-state methods”, in preparation.
10. Heng Wang[#], **Chuang Yu**[#], Swapna Ganapathy, Ernst R.H. van Eck, Lambert van Eijck, Marnix Wagemaker, “Li-ions transport in all-solid-state battery based on $\text{Li}_6\text{PS}_5\text{Cl}_{0.5}\text{Br}_{0.5}$ electrolytes: the influence of bulk vs interface”, in preparation.
11. **Chuang Yu**, Swapna Ganapathy, Ernst R.H. van Eck, Heng Wang, Marnix Wagemaker, “Synthesis, Phase transitions, Structure and ion motions of lithium garnet $\text{Li}_7\text{La}_3\text{Zr}_2\text{O}_{12}$ ”, in preparation.
12. **Chuang Yu**, Swapna Ganapathy, Ernst R.H. van Eck, Heng Wang, Marnix Wagemaker, “Improving Li-ion mobility in cubic $\text{Li}_7\text{La}_3\text{Zr}_2\text{O}_{12}$ by Nb-doping: Structure, Li-ion dynamics, Chemical Stability, and solid-state battery applications”, in preparation.
13. **Chuang Yu**, Swapna Ganapathy, Ernst R.H. van Eck, Marnix Wagemaker, “Revealing the Na-ion motions in Cl-doped cubic Na_3PS_4 and the effects of annealing”, in preparation.
14. **Chuang Yu**, Swapna Ganapathy, Ernst R.H. van Eck, Long Zhang, Marnix Wagemaker, “Na-ion dynamics in tetragonal and cubic Na_3SbS_4 probed by ^{23}Na Solid state NMR and their solid-state Na-ion batteries applications”, in preparation.
15. Dechao Zhang, Long Zhang, Xiaoting Cao, Di Xu, Ning Wang, **Chuang Yu**, Wentao Hu, Xinlin Yan, Jianli Mi, Bin Wen, Limin Wang, “Synthesis of cubic Na_3SbS_4 solid electrolyte with enhanced ion transport for all-solid-state sodium-ion batteries”, *Electrochimica Acta*, under review.

16. Dechao Zhang, Long Zhang, Kun Yang, Hongqiang Wang, **Chuang Yu**, Di Xu, Bo Xu, Li-Min Wang, “*Superior Blends Solid Polymer Electrolyte with Integrated Hierarchical Architectures for All-Solid-State Lithium Ion Batteries*”, *ACS Applied Materials & Interfaces*, under review.
17. **Chuang Yu**, Heng Wang, Xiangfeng Guan, Jing Zheng, Liping Li, “*Conductivity and electrochemical performance of composites $x\text{Li}_2\text{MnO}_3 \cdot (1-x)\text{LiMn}_{1/3}\text{Ni}_{1/3}\text{Co}_{1/3}\text{O}_2$ ($x=0.1, 0.2, 0.3, 0.4$)*”, *Journal of Alloys and Compounds*, **546**, 239 (2013).
18. **Chuang Yu**, Guangshe Li, Xiangfeng Guan, Jing Zheng, Liping Li, Tianwen Chen, “*Composites $\text{Li}_2\text{MnO}_3 \cdot \text{LiMn}_{1/3}\text{Ni}_{1/3}\text{Co}_{1/3}\text{O}_2$: Optimized synthesis and applications as advanced high-voltage cathode for batteries working at elevated temperatures*”, *Electrochimica Acta*, **81**, 283 (2012).
19. **Chuang Yu**, Guangshe Li, Xiangfeng Guan, Jing Zheng, Liping Li, “*Composites $\text{Li}_{1+x}\text{Mn}_{0.5+0.5x}\text{Ni}_{0.5-0.5x}\text{O}_2$ ($0.1 \leq x \leq 0.4$): Optimized preparation to yield an excellent cycling performance as cathode for lithium-ion batteries*”, *Electrochimica Acta*, **61**, 216 (2012).
20. **Chuang Yu**, Guangshe Li, Xiangfeng Guan, Jing Zheng, Dong Luo, Liping Li, “*Impacts of upper cut-off voltages on the electrochemical behaviors of Composite Electrode $0.3\text{Li}_2\text{MnO}_3 \cdot 0.7\text{LiMn}_{1/3}\text{Ni}_{1/3}\text{Co}_{1/3}\text{O}_2$* ”, *Physical Chemistry Chemical Physics*, **14**, 12368 (2012).
21. **Chuang Yu**, Guangshe Li, Xiangfeng Guan, Jing Zheng, Liping Li, “*A novel approach to composite electrode $0.3\text{Li}_2\text{MnO}_3 \cdot 0.7\text{LiMn}_{1/3}\text{Ni}_{1/3}\text{Co}_{1/3}\text{O}_2$ in lithium-ion batteries with an anomalous capacity and cycling stability at 45.4°C* ”, *Scripta Materialia*, **66**, 300 (2012).
22. **Chuang Yu**, Guangshe Li, Xiangfeng Guan, Jing Zheng, Liping Li, “*Composite $\text{Li}[\text{Li}_{0.11}\text{Mn}_{0.57}\text{Ni}_{0.32}]\text{O}_2$: Two-step molten-salt synthesis, oxidation state stabilization, and uses as high-voltage cathode for lithium-ion batteries*”, *Journal of Alloys Compounds*, **528**, 121 (2012).
23. Xinhui Zhang, **Chuang Yu**, Xiangdong Huang, Jing Zheng, Xiangfeng Guan, Dong Luo, and Liping Li, “*Novel composites $\text{Li}[\text{Li}_x\text{Ni}_{0.33-x}\text{Mn}_{0.47}\text{Co}_{0.19}]\text{O}_2$ ($0.18 \leq x \leq 0.21$): Synthesis and application as high-voltage cathode with improved electrochemical performance for lithium ion batteries*”, *Electrochimica Acta*, **81**, 233 (2012).

24. Dong Luo, Guangshe Li, **Chuang Yu**, Liusai Yang, Jing Zheng, Xiangfeng Guan, Liping Li, “Low-concentration -donor-doped LiCoO_2 as high-performance cathode materials for Li-ion-batteries to operate in a wider temperature range”, *Journal of Materials Chemistry*, **22**, 22233 (2012).
25. Dong Luo, Guangshe Li, Xiangfeng Guan, **Chuang Yu**, Jing Zheng, Xinhui Zhang, Liping Li, “Novel synthesis of $\text{Li}_{1.2}\text{Mn}_{0.4}\text{Co}_{0.4}\text{O}_2$ that shows an excellent electrochemical performance from $-10.4\text{ }^\circ\text{C}$ to $45.4\text{ }^\circ\text{C}$ ”, *Journal of Materials Chemistry*, **1**, 1220 (2013).
26. Xinhui Zhang, Dong Luo, Guangshe Li, Xiangfeng Guan, **Chuang Yu**, Jing Zheng, Chaochao Fu, Xiangdong Huang and Liping Li, “Self-adjusted oxygen-partial-pressure approach to the improved electrochemical performance of electrode $\text{Li}[\text{Li}_{0.14}\text{Mn}_{0.47}\text{Ni}_{0.25}\text{Co}_{0.14}]\text{O}_2$ for lithium-ion batteries”, *Journal of Materials Chemistry A*, **1**, 9721 (2013).

Chapter

1. Xiangfeng Guan, Guangshe Li, Jing Zheng, **Chuang Yu**, Xiaomei Chen, Liping Li and Zhengwei Fu, “Chapter III: Heterogeneous Nanostructured Electrode Materials for Lithium-Ion Batteries-Recent Trends and Developments”, *Lithium Ion Batteries - New Developments*, ISBN 978-953-51-0077-5.

Conference Presentations

1. Oral presentation: **Chuang Yu**, Swapna Ganapathy, Ernst R.H. van Eck, Lambert van Eijck, Marnix Wagemaker, “Probing Li-ion transport in $\text{Li}_6\text{PS}_5\text{X}$ ($\text{X}=\text{Cl}, \text{Br}$)-based solid-state batteries”, *The third National solid-state battery conference*, Wuxi, China, 2017.
2. Oral presentation: **Chuang Yu**, Swapna Ganapathy, Ernst R.H. van Eck, Lambert van Eijck, Marnix Wagemaker, “Probing Li-ion Dynamics in Sulfide Electrolytes and Solid-State Batteries by ^7Li Solid-State NMR”, *The 18th National Conference on Solid State Ionics and International Forum on Electrochemical Energy Storage Technologies*, Guilin, China, 2016.
3. Poster presentation: **Chuang Yu**, Swapna Ganapathy, Niek J. J. de Klerk, Irek Roslon, Ernst R.H. van Eck, Marnix Wagemaker, “Unravelling Li-ion transport from pico-seconds to seconds, bulk versus interfaces in an argyrodite

Li₆PS₅Cl-Li₂S all solid state Li-ion battery”, [The 18th International Meeting on Lithium Batteries, Chicago, Illinois, USA, 2016.](#)

4. Poster presentation: **Chuang Yu**, Swapna Ganapathy, Ernst R.H. van Eck, Arno P.M. Kentgens, Marnix Wagemaker, “*Improving the Li-ion Mobility in Cubic Li-ion Garnet Conductors by Nb-Doping*”, [The 67th Annual Meeting of the International Society of Electrochemistry, The Hague, The Netherlands, 2016.](#)

5. Poster presentation: **Chuang Yu**, Swapna Ganapathy, Niek J. J. de Klerk, Ernst R.H. van Eck, Arno P.M. Kentgens, Marnix Wagemaker, “*Li dynamics in the Li₆PS₅Br solid electrolyte studied by ⁷Li NMR and DFT Based Molecular Dynamics Simulations and its solid-state battery applications*”, [The 67th Annual Meeting of the International Society of Electrochemistry, The Hague, The Netherlands, 2016.](#)

6. Poster presentation: **Chuang Yu**, Swapna Ganapathy, Niek J. J. de Klerk, Irek Roslon, Ernst R.H. van Eck, Arno P.M. Kentgens, Marnix Wagemaker, “*Unravelling Li-ion transport from pico-seconds to seconds, bulk versus interfaces in an argyrodite Li₆PS₅Cl-Li₂S all solid state Li-ion battery*”, [Ampere NMR School, Zakopane, Poland, 2016.](#)

7. Poster presentation: **Chuang Yu**, Niek J. J. de Klerk, Swapna Ganapathy, Ernst R.H. van Eck, Marnix Wagemaker, “*New prospects in studying Li-diffusion in Li₆PS₅Br and solid-state cell via NMR spectroscopy*”, [Theory and practice in Spectroscopy & Electrochemistry Summer School, Groningen, The Netherlands, 2016.](#)

8. Poster presentation: **Chuang Yu**, Swapna Ganapathy, Niek J. J. de Klerk, Ernst R.H. van Eck, Marnix Wagemaker, “*Synthesis, phase transition and dynamics investigations in tetragonal and cubic garnet Li₇La₃Zr₂O₁₂*”, [The 1st International Symposium on Energy Chemistry & Materials \(ISECM\), Shanghai, China, 2015.](#)

9. Poster presentation: **Chuang Yu**, Swapna Ganapathy, Niek J. J. de Klerk, Ernst R.H. van Eck, Marnix Wagemaker, “*Synthesis and dynamics of cubic and tetragonal Na₃PS₄*”, [The 1st International Symposium on Energy Chemistry & Materials \(ISECM\), Shanghai, China, 2015.](#)

Curriculum Vitae

Chuang Yu

Born on 18 November, 1985

Macheng, Hubei, China

Sept. 2005 – July. 2009

Bachelor in Materials Chemistry, Harbin Engineering University, Heilongjiang, China.

Sept. 2009 – June. 2012

Master in Natural Science, Physical Chemical (including Chemical Physics), Fujian Institute of Research on the structure of Matter, Chinese Academy of Sciences, Fuzhou, China.

June.2012 – Dec. 2012

Work experience in Ningbo Jinhe New Materials Co., Ltd., Ningbo, China.

April. 2013 – April. 2017

PHD candidate in the group Fundamental Aspects of Materials and Energy (FAME), Faculty of Applied Science, Delft University of Technology, Delft, the Netherlands.

